ISBN 978-82-326-5980-7 (printed ver.)
ISBN 978-82-326-5424-6 (electronic ver.)
ISSN 1503-8181 (printed ver.)
ISSN 2703-8084 (electronic ver.)

NTNU
Norwegian University of
Science and Technology

Doctoral theses at NTNU, 2022:117

Gara Quintana Díaz

In-orbit Radio Measurements using Software-Defined Radios in Small Satellites

Doctoral thesis

Gara Quintana Díaz

Doctoral theses at NTNU, 2022:117

NTNU

NTNU
Norwegian University of
Science and Technology
Thesis for the degree of
Philosophiae Doctor
Faculty of Information Technology
and Electrical Engineering
Department of Electronic Systems

NTNU
Norwegian University of
Science and Technology

Gara Quintana Díaz

In-orbit Radio Measurements using Software-Defined Radios in Small Satellites

Thesis for the degree of Philosophiae Doctor

Trondheim, April 2022

Norwegian University of Science and Technology
Faculty of Information Technology
and Electrical Engineering
Department of Electronic Systems

NTNU
Norwegian University of Science and Technology

Thesis for the degree of Philosophiae Doctor

Faculty of Information Technology
and Electrical Engineering
Department of Electronic Systems

© Gara Quintana Díaz

ISBN 978-82-326-5980-7 (printed ver.)
ISBN 978-82-326-5424-6 (electronic ver.)
ISSN 1503-8181 (printed ver.)
ISSN 2703-8084 (electronic ver.)

Doctoral theses at NTNU, 2022:117

Printed by Skipnes Kommunikasjon AS

In theory, theory and practice
are the same.
In practice, they are not.

ALBERT EINSTEIN

Abstract

Environmental monitoring of the oceans and the Arctic is important to understand the impact of global warming and climate change. The use of different types of assets, such as satellites and autonomous agents, can contribute to this task at different spatio-temporal scales. However, the collection and distribution of scientific data from sensors or robotic agents in these remote places are challenging due to limited infrastructure. Thus, a new communication system is needed to obtain faster and easier access to the data. To design a robust satellite communication system for energy-limited sensors, measurements of the communication channel and the interference environment are necessary.

In addition to the mission design activities, the main contribution of this thesis is the analysis and characterisation of the in-orbit interference in two different relevant frequency bands in VHF and UHF for small satellite systems. The first band is the UHF amateur radio band (430–440 MHz), selected due to its common use for small satellite communication. This band was measured with payloads on board the Serpens and the LUME-1 satellites. Another contribution of this work is the design and development of an on-board measurement algorithm for small satellites with limited resources. We built a Software-Defined Radio (SDR) testbed similar to the actual satellite setup for testing before uploading the algorithm to LUME-1. In addition, we explored the uplink interference from more than 300 measurement locations all over the world. Band-limited pulsed interference was detected in areas where ground radars are located and wide-band pulsed interference was measured over central Europe.

The other frequency band measured was the lower leg of the VHF Data Exchange (VDE)-SAT system (157 MHz band). This band was selected to explore the performance of a new communication system that is currently being demonstrated, the VDE-SAT, which will operate in the Arctic. We analysed the uplink interference environment of this system by analysing

recordings from an SDR payload on board the NorSat-2 satellite over the Arctic. Pulsed interference of high power was also detected in this band. The pulse length and period were detected using a second algorithm developed in this thesis. The algorithms and software implemented in this thesis can be used in any frequency band to detect the frequency and time variability of different signals in any satellite with an SDR.

Preface

This thesis is submitted in partial fulfillment of the requirements of the Philosophiae Doctor (PhD) degree at the Norwegian University of Science and Technology (NTNU). The candidate has been employed at the Department of Electronic Systems (IES). Professor Torbjörn Ekman has been the main supervisor. Professor Egil Eide and Professor Fernando Aguado Agelet have been co-supervisors.

This PhD thesis was supported by the Research Councial of Norway (RCN) through the Centers of Excellence funding scheme, Center for Autonomous Marine Operations and Systems (AMOS) with the grant 223254, and the Research Council of Norway through the IKTPLUSS programme with the project Mission-oriented Autonomous Systems with Small Satellites for Maritime Sensing, Surveillance and Communication (MASSIVE), grant number 270959. In addition, the Norwegian Space Agency (NOSA) supported work performed within the thesis and the project TIN21024.

Acknowledgements

When I moved to Norway four years ago to do a PhD, little did I know what it meant. It has been a challenging time, not only technically, but also psychologically. Therefore, I want to express my gratitude to everyone who has supported me through these years in one way or another. I am extremely glad for all the new people I have met, who have made this experience unforgettable, and for all the things I have learnt.

I would like to thank my supervisors for their support and help. All the never-ending discussions with Torbjörn Ekman about new ideas and problems we could find on the way ended up in a work I am proud of. He challenged

the constraints we had and inspired me to push the limits and find feasible solutions. Egil Eide always showed interest in how the experiments were going and how we could improve the ground station. His explanations about radars were very useful and his good mood was contagious. I also want to thank Fernando Aguado, a later addition to my supervisor team. He enabled the cooperation with the University of Vigo and work with two satellites. It certainly boosted my research work and motivated me to design new experiments.

I am very grateful for the collaboration with the University of Vigo and Alén Space to work with the Serpens satellite data and the experiments on board the LUME-1 satellite. I would especially like to thank Diego Nodar and Alberto González for helping me understand the experiments performed in Serpens and explaining the possibilities and constraints of LUME-1, Diego Hurtado de Mendoza for the software development expertise on the TOTEM SDR, and José Miguel Lago, for the operations with LUME-1. Thanks to all of you, I launched my software into space. The highlight of the PhD work was receiving confirmation of the on-board software installation and messages from José Miguel saying there was a new measurement.

Another fruitful collaboration I am grateful for is with Space Norway since it enabled my work with the NorSat-2 satellite. I would like to thank Lars Løge, Even Andersen, and Anton Bolstad for the discussions on the experiments, the operations on the satellite, the acquisition of the raw data, and discussions of the results.

The people at the SmallSat Lab have also been of great support. I want to thank Elizabeth, Alberto, Roger, Mariusz, Milica, Evelyn, João, Amund G., Sivert, Marie, Joe, Bjørn, and Dennis for all the help and social activities. Especially Roger, for always motivating me and pushing for more publications. I have really valued all the technical discussions and quick solutions during the lockdown. I also appreciated the help of Julian Veisdal, his passion for his work and engagement inspired me. Thanks to Terje Mathiesen I debugged the problems in the lab testbed which were difficult to solve remotely and with short visits to the lab during the pandemic lockdown.

I also enjoyed working with bachelor and master students. I admired the enthusiasm and engagement of Emilie. I wish we had time to test the

Arctic system in Svalbard. Supervising Erik Olav, Bjørn-Marius, Hans-Robert, and Simen B. taught me a lot about error correction codes. Erik B., Mikolaj, and Amaury showed me the challenges of working with GNU Radio when implementing software for satellite communication. Supervising Stian and Isaac was also an enriching experience, and I hope the software they developed is the next one to upload to LUME-1.

I am glad Jens moved into my office sometime after I started. All the radio discussions have been extremely useful in my PhD, in addition to all the other long conversations in the office and other more fun settings. I hope you keep coming, at least to water the plants. I also want to thank Nicolás, the other radio person who has always been there when I needed help.

Other activities at work that are more social, like coffee breaks, lunches, and lønnøls, have been vital to recharge batteries and motivation. I really miss the library lunches where a lot of ideas were discussed and I learnt a lot of important Norwegian concepts, such as *koselig* and *syden*. This was possible because of some of the people I have mentioned but also the company of Silje, Torstein, Anders, Einar, Jakob (thank you for all the help in Latex!), Fredrik, Ambjørn, Karolina, Sam, Bettina, Ashkan, Hannah, Kristoffer, Magnus, Asgeir, Nina, Ine Mari, Hans Olaf, Ida Marie, Astrid, Erik F., Jens H., Jostein, Farrokh, Dominik, Olivia, Jon, Reza N., Veslemøy, Sandra, Florian, and Milica L.

I would also like to mention Sven, Maria, Ragnhild, and Ole for their patience and positive attitude in PhD discussions. Together with Elizabeth, they have helped me to find new perspectives while eating nice dinners or running in the cold. They were always open to listening and shining a positive light on the problems I encountered.

Apart from all my colleagues and friends, my family has been very important in this adventure, especially my mum, dad, and sister. They have supported me since the moment I decided to travel up north to the Norwegian University of Science and Technology (NTNU). They have always motivated me in challenging times and distracted me when needed. Home trips have recharged my vitamin D and helped me to come back ready to work. I also want to thank Petter for listening to my challenges over and over, always with the patience of the first time. He supported me throughout the PhD and his positive attitude towards everything in life is admirable.

List of publications

The following publications are included in this thesis:

A Software-Defined Radios in Satellite Communication
Small Satellites System & Services Symposium (4S): Sorrento, Italy, 28 May-1 June 2018.
G. Quintana-Diaz, and R. Birkeland.
G. Quintana-Diaz and R. Birkeland conceptualised and performed the study. G.Q-D. prepared and wrote the original draft. Both authors reviewed and edited the manuscript.

B An SDR mission measuring UHF signal propagation and interference between small satellites in LEO and Arctic sensors
33rd Annual AIAA/USU Conference on Small Satellites: Logan, USA, 3-8 August 2019.
G. Quintana-Diaz, R. Birkeland, E. Honoré-Livermore, and T. Ekman.
G. Quintana-Diaz, R. Birkeland, E. Honoré-Livermore conceptualised the paper. G.Q-D. prepared and wrote the original draft. T. Ekman supervised the work. All authors reviewed and edited the manuscript.

C Development of a multi-purpose SDR payload for the HYPSO-2 satellite [Accepted]
IEEE Aerospace Conference: Big Sky, USA, 5-12 March 2022.
R. Birkeland, G. Quintana-Diaz, E. Honoré-Livermore, T. Ekman, F. Aguado Agelet, and T. A. Johansen.
R. Birkeland, G. Quintana-Diaz, E. Honoré-Livermore conceptualised the paper. G.Q-D. and T. Ekman designed the radio applications. G.Q-D. implemented and tested the radio applications. R.B. and G.Q-D. integrated the SDR setup into the HYPSO framework. R.B. and G.Q-D. prepared and wrote the original draft. T.E., F. Aguado Agelet and T.A. Johansen supervised the work. All authors reviewed

and edited the manuscript.

D A Satellite-USV system for Persistent Observation of Mesoscale Oceanographic Phenomena
Remote Sensing, vol. 13, no. 16, p. 3229, Aug. 2021.
DOI: 10.3390/rs13163229
A. Dallolio, G. Quintana-Diaz, E. Honoré-Livermore, J. L. Garrett, R. Birkeland, and T. A. Johansen.
A. Dallolio, G. Quintana-Diaz, E. Honoré-Livermore and R. Birkeland conceptualised the paper. A.D., G.Q-D., E.H-L. and R.B. applied the theory to simulations. G.Q-D implemented and performed the simulations and A.D. conducted the field experiments. All authors contributed to the involved activities through discussions and revisions. All authors wrote and prepared the original draft and T.A. Johansen supervised the work.

E Detection of radio interference in the UHF amateur radio band with the Serpens satellite
Advances in Space Research, vol. 69, no. 2, p. 1159, Jan. 2022.
DOI: 10.1016/j.asr.2021.10.017
G. Quintana-Diaz, D. Nodar-López, A. González Muíño, F. Aguado Agelet, C. Cappelletti, and T. Ekman.
A. González Muíño, D. Nodar-López and F. Aguado Agelet conceptualised and designed the experiments. A.G.M. and D.N-L. implemented and validated the measurement software. G. Quintana-Diaz and T. Ekman analysed the measurement method and G.Q-D. performed the formal analysis of the data. A.G.M., D.N.-L and F.A.A. performed the experiments and the data collection. F.A.A., A.G.M., D.N.-L, C. Cappelletti and provided the satellite and operations resources. G.Q.-D. performed the data curation process, and wrote and prepared the original draft. C.C., F.A.A. and T.E. supervised the work. All authors reviewed and edited the manuscript.

F In-Orbit Measurements and Analysis of Radio Interference in the UHF Amateur Radio Band from the LUME-1 Satellite
Remote Sensing, vol. 13, no. 16, p. 3252, Aug. 2021.
DOI: 10.3390/rs13163252
G. Quintana-Diaz, T. Ekman, J. M. Lago Agra, D. Hurtado de Mendoza, A. González Muíño, and F. Aguado Agelet.

G. Quintana-Diaz, T. Ekman and F.Aguado Agelet conceptualised and designed the experiments. G.Q.-D. and T.E. created the design methodology. G.Q.-D. implemented the measurement software and code for analysis. G.Q-D and D.H.d.M validated the flight software. G.Q.-D and T.E. performed the formal analysis of the data. G.Q.-D., J.M. Lago Agra, A. González Muíño and F.A.A. performed the experiments and the data collection. F.A.A., A.G.M., D.H.d.M. and J.M.L.A. provided the satellite and operations resources. G.Q.-D. performed the data curation process, and wrote and prepared the original draft. G.Q.-D., T.E., F.A.A., J.M.L.A. and D.H.d.M. reviewed and edited the manuscript. T.E. and F.A.A. supervised the work.

G In-orbit Interference Measurements and Analysis in the VDES-band with the NorSat-2 Satellite [Accepted]
IEEE Aerospace Conference: Big Sky, USA, 5-12 March 2022.
G. Quintana-Diaz, R. Birkeland, L. Løge, E. Andersen, A. Bolstad, and T. Ekman.
G. Quintana-Diaz, R. Birkeland, L. Løge and T. Ekman conceptualised and designed the experiments. G.Q.-D. and T.E. created the design methodology. G.Q.-D. implemented and tested the measurement software and code for analysis. G.Q.-D and T.E. performed the formal analysis of the data. L.L., E. Andersen and A. Bolstad performed the experiments, the data collection, provided the satellite and operations resources. G.Q-D. and E.A. performed the data curation process. G.Q-D. wrote and prepared the original draft. T.E., R.B. and L.L. supervised the work. All authors reviewed and edited the manuscript.

Contents

Acronyms

ACDS	Attitude Control and Determination System
ACM	Adaptive Coding and Modulation
ADC	Analogue to Digital Converter
ADCS	Attitude Control and Determination System
AGC	Automatic Gain Control
AIS	Automatic Identification System
AIT	Assembly Integration and Test
AOI	Area of Interest
API	Advanced Publication Information
ASM	Application Specific Messages
AUV	Autonomous Underwater Vehicle
AWGN	Additive White Gaussian Noise
AZFP	Autonomous Zooplankton and Fish Profiler
BPSK	Binary Phase Shift Keying
CAD	Computer Aided Design
CAN	Controlled Area Network
CDMA	Code Division Multiple Access
CDR	Critical Design Review
CERTO	Coherent Electromagnetic Radio Tomography
CMCC	Coordinated Mission Control Centre
CoNNeCT	Communications, Navigation, and Networking reConfigurable Testbed
CONOPS	Concept of Operations
COTS	Commercial-Off-The-Shelf
CS	Constituent System
CSP	CubeSat Space Protocol
CV	coefficient of variation
CW	Continuous Wave
DAC	Digital to Analogue Converter
DFT	Discrete Fourier Transform
DSA	Delay Sensitive Application
DTA	Delay Tolerant Application
ECDF	Empirical Cumulative Density Function

EESS	Earth Exploration Satellite Service
EIRP	Effective Isotropic Radiated Power
EMC	Electro Magnetic Compatibility
EO	Earth Observation
EPS	Electrical Power Subsystem
ESA	European Space Agency
ESEO	European Student Earth Orbiter
FC	Flight Controller
FDD	Frequency Division Duplex
FFSS	Fractionated and Federated Satellite Systems
FIR	Finite Impulse Response
FOV	Field of View
FPGA	Field-Programmable Gate Array
GNSS	Global Navigation Satellite System
GS	Ground Station
HAB	Harmful Algal Bloom
HIL	hardware-in-the-loop
HSI	Hyperspectral Imager
HUMPL	HUMsat PayLoad
HumSat	Humanitarian Satellite constellation
HYPSO	HYPer-spectral Smallsat for Ocean observation
IAF	International Astronautical Federation
IALA	International Association of Lighthouse Authorities
IARU	International Amateur Radio Union
IF	Intermediate Frequency
IGBP	International Geosphere-Biosphere Program
IoT	Internet of Things
IP	Internet Protocol
IQ	In-Phase and Quadrature
ISS	International Space Station
ITU	International Telecommunication Union
LEO	Low Earth Orbit
LEOP	Launch and Early Orbit phase
LME	Local Mean Envelope
LNA	Low Noise Amplifier
LO	Local Oscillator
M2M	Machine to Machine
M6P	Multipurpose 6U Platform
MAC	Medium Access Control
MASSIVE	Mission-oriented Autonomous Systems with Small Satellites for Maritime Sensing, Surveillance and Communication

MBSE	Model-Based Systems Engineering
MCC	Mission Control Centre
MIMO	Unmanned Aerial Vehicle
NASA	National Aeronautics and Space Administration
NCA	Norwegian Coastal Administration
NEMO	Next-Generation Earth Monitoring
NOSA	Norwegian Space Agency
NTNU	Norwegian University of Science and Technology
ONION	Operational Network of Individual Observation Nodes
OS	Operating System
PAVE	Precision Acquisition Vehicle Entry
PAWS	Phased Array Warning System
PC	Payload Controller
PDR	Preliminary Design Review
POPEs	platforms for optical, physical and ecological sensors
PSK	Phase Shift Keying
QPSK	Quadrature Phase Shift Keying
RCN	Research Councial of Norway
RF	radiofrequency
RFI	Radio Frequency Interference
RS	Remote Sensing
RSSI	Received Signal Strength Indicator
SALSAT	Spectrum AnaLysis SATellite
SAMS, UK	Scottish Association of Marine Sciences
SAR	Search and Rescue
SBD	Short Burst Data
SDR	Software-Defined Radio
SMO	Secondary Mission Objective
SoC	System on Chip
SoS	System of Systems
SSH	Secure SHell
SSO	Sun-synchronous orbit
TDD	Time Division Duplex
TEC	Total Electron Content
TLE	Two-Line Element
TM/TC	Telemetry and Telecommand
TT&C	Telemetry, Tracking and Command
TU Berlin	Technische Universität Berlin

UART	Universal Asynchronous Receiver-Transmitter
UAV	Unmanned Aerial Vehicle
UHF	Ultra High Frequency
UK	United Kingdom
UNOOSA	United Nations Office for Outer Space Affairs
US	United States
USA	United States of America
USV	Unmanned Surface Vehicle
UTIAS	University of Toronto Institute for Aerospace Studies
UVigo	University of Vigo
VDE	VHF Data Exchange
VDES	VHF Data Exchange System
VHF	Very High Frequency
WCRP	World Climate Research Program

Part I

Summary

1 Introduction

In this chapter, the context of the thesis is explained. The objectives are defined as research questions which motivate the literature review. Finally, the thesis outline is presented.

1.1 Context

It is predicted that 500 billion Internet of Things (IoT) devices will be installed all over the world by 2030 [1]. The sensors in these IoT devices generate a large amount of data and information, contributing to the well-known *big data*. Depending on the sensor network under consideration, different communication systems are used to retrieve the generated data. If the sensors are placed in remote locations, such as the Arctic, data collection and distribution are more challenging due to the lack of infrastructure [2]. In this case, there are no plug-and-play communication solutions due to the harsh environment and difficulty to make a business case in a sparsely populated area.

The Arctic is an important area to monitor since it is one of the regions where the consequences of global warming are observed early [3], [4]. Ocean observation is also relevant to understanding how the climate evolves and its effects on marine ecosystems, as 71% of the Earth's surface is water [5]. Gathering data from sensors in remote locations, like the Arctic and oceans, is crucial and requires a reliable communication link which currently is deficient [2], [6].

Using diverse assets, such as autonomous vehicles and satellites, for remote sensing is beneficial, as each asset can cover different time scales and spatial variability for ocean observation [7]. The combination and coordination of

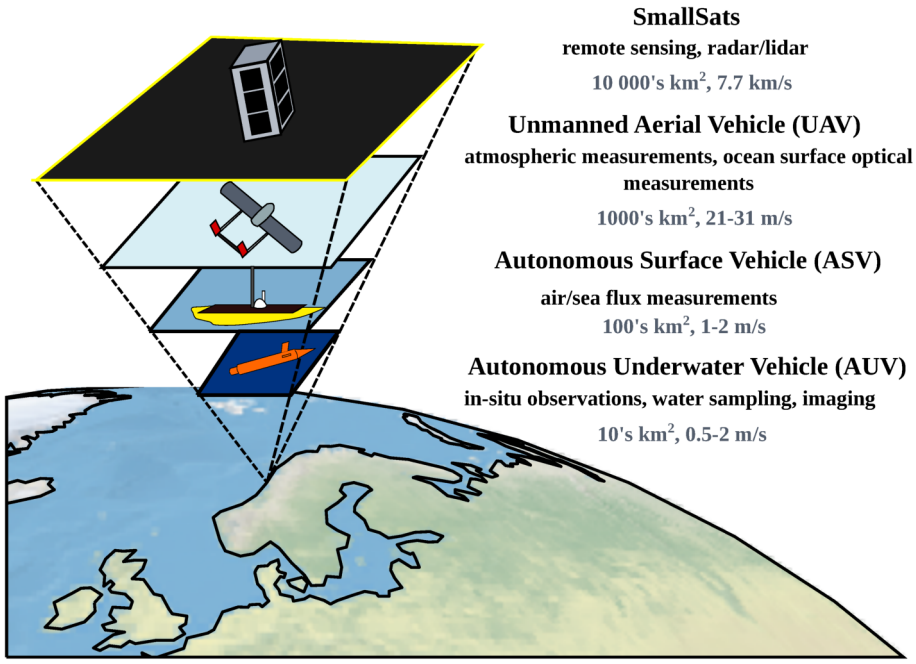

Figure 1.1: Robotic agents and small satellites for ocean observation (observation pyramid), from Paper C [13].

robotic agents and satellites can be valuable to enhance ocean observations (Figure 1.1) and is an important topic of research [8]–[11]. Distribution and sharing of resources among different satellites using Fractionated and Federated Satellite Systems (FFSS) is also a promising concept to improve Earth Observation (EO) missions [12]. Efficient coordination between agents requires robust communication to exchange information between assets.

The Norwegian University of Science and Technology (NTNU) together with the Center for Autonomous Marine Operations and Systems (NTNU-AMOS) launched a research project in this field in 2017. It focuses on designing, building, and operating small satellites (or SmallSats) as parts of a system of autonomous robots and agents for maritime sensing, surveillance, and communication. The combination of SmallSats and autonomous agents can enhance monitoring methods or even replace expensive human expeditions. The project is called Mission-oriented Autonomous Systems with

Small Satellites for Maritime Sensing, Surveillance and Communication (MASSIVE). The goal is to launch two SmallSats for ocean observation and communication: HYPer-spectral Smallsat for Ocean observation (HYPSO)-1 and HYPSO-2. The main part of the work presented in this thesis is funded by the MASSIVE project.

In order to coordinate different robotic agents and satellites for oceanographic observations, a robust communication system must be in place. The communication requirements vary depending on the type of data to be transmitted and the agents involved in the link, such as satellite-to-Unmanned Surface Vehicles, satellite-to-drone, or satellite-to-Ground Station (GS). The amount of the data to be downlinked to the ground station will be high if it is raw data. However, the amount of data transmitted from the satellite to a robotic agent can be reduced with on-board processing.

The communication channel between the satellite and the ground station is different from the one between a drone and a satellite, and between an Unmanned Surface Vehicle (USV) and the satellite. The frequency bands are not the same, resulting in a different amount of free space loss. The Doppler shift generated due to the movement of the assets varies with the relative speed between the nodes. For maritime scenarios, the ocean waves will generate reflections of the signal, causing multipath effects. Sea reflections will not occur in the ground station link. In the case of a drone, the reflections will be impacted by the flying altitude and its variations. Since the channel behaves differently depending on the conditions of the link, a unique robust communication system that maximises data throughput for all cases is not possible.

The selection of frequency band is important because it impacts the data rate, the physical size of antennas, and the energy consumption of the system. High-frequency bands, such as S-band, require advanced antenna pointing [14] and big terminals that may not fit in some autonomous vehicles. In order to use simple antennas, limit energy consumption, and have better link budgets, lower frequencies, such as Very High Frequency (VHF) and Ultra High Frequency (UHF) are desired.

In addition, interference signals transmitted by other sources can degrade the channel further. Interference signals can be narrow-band or wide-band, in-band or out-of-band, and continuous or discontinuous. The International

Telecommunication Union (ITU) is the organisation responsible for frequency coordination and defines the allowed services within a specific frequency band. In most bands, there are several services but sometimes it is difficult for them to co-exist because they interfere with each other. Although the radiofrequency (RF) spectrum is crowded, its real usage is difficult to estimate unless it is measured. The investigation of the interference environment on board small satellites is the main objective of this thesis.

Communication systems are often designed for the worst-case scenario or the design is adjusted based on trial and error. However, the selection of communication parameters in a system should be based on real radio measurements of both the communication channel and the interference environment [15] to maximise the throughput of the system and achieve better performance. A flexible satellite communication payload that enables measurements using different parameters (carrier frequency, bandwidth, time resolution, etc.) is an advantage. Measurements can be adapted after analysing preliminary results and more measurements can be performed with the same equipment.

Software-Defined Radios (SDRs) are flexible communication platforms that enable functional changes by modifying the software and keeping the same hardware. Using an SDR on a satellite allows for in-flight updates of the software functionality, such as channel and interference measurements, relaying sensor data from remote locations, and communicating to robotic agents. SDRs have become very popular in the last years, and many have been flown in space [16]–[22].

This thesis focuses on measurements and characterisation of the radio interference environment in relevant communication bands in VHF and UHF. New knowledge on this interference paired with communication channel characterisation in these frequency bands enables the design of suitable countermeasures and appropriate access protocols to improve the quality of the satellite link. The Medium Access Control (MAC) protocols are an important part of the communication system design and need to be studied in detail for the use case as in [23]. However, radio propagation characterisation (including ionospheric effects), mitigation techniques, and protocol design and selection are outside the scope of the thesis.

1.2 Research questions

To summarise the objectives of this work and limit the scope, the following research questions (RQ) are defined. In order to make a robust communication system for environmental research in the ocean and the Arctic (RQ1.1), measurements of the satellite interference environment are needed, motivating RQ2.1 and RQ2.2.

1. Mission design (Part II).

    - RQ1.1. *How can we define a flexible communication satellite mission and architectures for ocean and Arctic environmental research?* (Paper A, B, C and D).

2. Interference measurements (Part III).

    - RQ2.1. *How can the time and frequency characteristics of radio interference be measured from a small satellite with limited resources?* (Paper E and F).

    - RQ2.2. *How is the uplink interference environment for small satellites in Low Earth Orbit (LEO) in relevant communication bands in VHF and UHF?* (Paper E, F and G).

1.3 Literature review

In this section, the Arctic sensor data collection use case is described and an overview of the radio environment in satellite links is provided. In addition, the state-of-the-art of satellite RF measurements, Radio Frequency Interference (RFI) detection and mitigation techniques and SDR platforms is summarised.

1.3.1 Data retrieval from sensors in the Arctic

The temperature in the Arctic has risen at unprecedented rates in the last 400 years, according to a study performed in 1997 [24]. The trend continues to increase in this century, resulting in more ice melting. Summers with no ice in the Arctic region have been predicted to occur in this century [25]. The decrease in ice areas has an impact on the ecosystems living there [26], [27]. Therefore, monitoring the Arctic region is important to understand climate change and its effects.

There are several projects addressing the importance of environmental monitoring of the Arctic area, such as the Passive Microwave Satellite Mission for EU Copernicus[1], the Arctic Weather Satellite mission[2], the Arktika satellites [3] and the Operational Network of Individual Observation Nodes (ONION)[4] project. The ONION project is part of the European Horizon 2020 funding programme that started in 2016 and lasted two years. This project ranked the Marine Weather Forecast in polar regions and the Arctic Sea Ice Monitoring as the two use cases with the highest priority to be addressed in future EO satellite missions (2021-2027) [12]. Even though sea ice phenomena is not usually considered a natural disaster, it is a use case in a study of monitoring requirements for natural disasters [23]. As part of the ONION project, a polar EO mission for the Copernicus programme to complement the monitoring gaps in the Arctic was presented to address the previous use cases and some others [12]. A detailed system architecture study, identification of technologies needed, and payload selection study were performed [12], [28]. This EO mission can contribute significantly to the gaps in Arctic monitoring.

The "*Arctic Ocean ecosystems - Applied technology, Biological interactions and Consequences in an era of abrupt climate change*" (Arctic ABC) is a project that develops instrumentation to study ecosystems under the Arctic ice and analyses the data. The project partners are the University of Tromsø (Norway), NTNU (Norway), the University Center in Svalbard (UNIS, Norway), and the Scottish Association of Marine Sciences (SAMS,

[1] https://cimr.eu/node/34
[2] https://www.esa.int/.../Contract_signed_to_build_Arctic_weather_satellite
[3] https://arctic.ru/infrastructure/20210303/991583.html
[4] https://cordis.europa.eu/project/id/687490

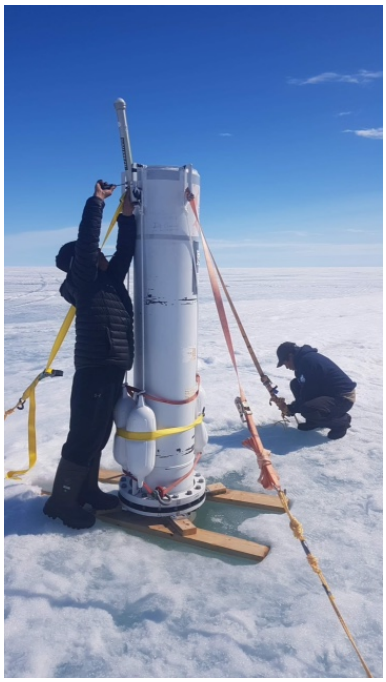

Figure 1.2: Photo provided by Maxime Geoffroy showing the deployment of an Acoustic Zooplankton and Fish Profiler ice tethered buoy (AZFP POPE for short) in the Canadian Arctic [Arctic ABC Development national infrastructure project funded by the Norwegian Research Council PN245923].

UK). In the Arctic ABC project, several ice-tethered platforms for optical, physical and ecological sensors (POPEs) have been designed for research [29]. Buoy prototypes have been developed and deployed in the Arctic [30] as in Figure 1.2. One of the sensors used for plankton and fish research under the ice is the Autonomous Zooplankton and Fish Profiler (AZFP) which can generate 3–8 MB of data per day [30]. The Arctic ABC project is an example of a project in need of better communication infrastructure in the Arctic.

Instrumentation to be deployed in the Arctic has specific constraints due to the harsh environment and limited infrastructure [2]. The equipment has restricted power since solar energy is unavailable to charge the batteries in

winter. Maintenance is limited because it involves expensive expeditions. Furthermore, mechanical structures must be fixed to avoid problems with icing. Thus, mechanically steered antennas, like high gain dishes used in high data link satellite communication, are not feasible in an Arctic scenario. The gain and the size of the antennas depend on the frequency band selected. Higher frequencies allow for a higher gain and a narrow antenna beamwidth requiring strict pointing and steering. Antennas for lower frequencies have a lower gain and a wider beamwidth, thus, pointing requirements are more relaxed or not needed for some antenna designs.

All these constraints make retrieving data from the sensors in the Arctic challenging. Arctic ABC has used two main methods: sending messages through the Iridium Short Burst Data (SBD) service, and flying an airplane over the nodes to establish a radio link. Both alternatives are costly. The data generated is in the order of megabytes per day [30], which requires many SBD messages. Renting an airplane every couple of months does not provide fast access to the data. Expeditions also involve a high cost, not providing faster data access. Satellite services are also limited in the Arctic [2], [6].

There are emerging IoT-over-satellite systems using single messages, such as Astrocast Nanosatellite Network, Lacuna Space, Myriota, Kineis, Kepler Communications, OQ Technology, and Swarm Technologies [31]. However, these systems typically only allow for a small data volume for the sensors to transfer, about 100 bytes a few times per day [32], [33]. Broad-band systems use high frequencies that require high power and high-gain tracking antennas. Iridium offers different solutions that can be relevant for some of these scenarios. In addition, natural disaster monitoring requirements for IoT networks have been reviewed, with a specific use case of sea ice monitoring [23]. MAC protocols have been studied and analysed for different natural disaster monitoring use cases depending on their monitoring requirements [23]. The design and configuration of MAC protocols are important to improve the performance of a communication system. For example, in a communication link with high power interference packet retransmissions are vital.

However, systems that operate in lower frequency bands, such as VHF and UHF, are better candidates for energy-constrained equipment. The lower the frequency, the lower the free space loss in the communication link.

Hence, transmitted power and antenna gain can be lower, loosening the pointing requirements since the antenna beamwidth is wider. The VHF Data Exchange System (VDES) is an emerging system that will provide two-way communication between ships and satellites in the Arctic and other areas. This system has a satellite component that is studied in this thesis. Nevertheless, there is a research gap for flexible Arctic communication systems using small satellites to retrieve moderate data amounts from sensor nodes [34].

1.3.2 Radio environment in satellite links

Measuring the radio environment that affects satellite communication systems is important both to: 1) design a new robust communication system for sensors in remote locations and 2) to improve or assess the performance of emerging systems. In this context, the radio environment involves the channel and the interference signals. A better knowledge of this environment enables the selection of appropriate communication parameters, such as modulations and error correction codes, which can be useful to increase the data throughput with Adaptive Coding and Modulation (ACM) techniques.

Satellite signals are affected when travelling through the atmosphere. Ionospheric effects, such as Faraday rotation, time delays and excess rotations, dispersion, and ionospheric scintillation, affect communication in frequencies below 1 GHz [35]. There are several satellite missions designed to study these ionospheric effects [36]–[38]. In general, the satellite communication channel has been measured in the UHF band, at 435 MHz and 435.128 MHz, in 1980-1999 [39], [40]. A channel model was proposed by Chu et al. using satellite measurements [39]. Different error correction codes were tested in simulations using the model developed, but not in orbit.

Further degradation of the link can be experienced due to interference signals in different areas of the world. The RF spectrum used for radiocommunication is a scarce resource regulated by the ITU. Satellite operators using radiocommunication need to write an Advanced Publication Information (API) notice. The API document is used to apply for a frequency assignment to the ITU. For applications covering frequencies in the amateur

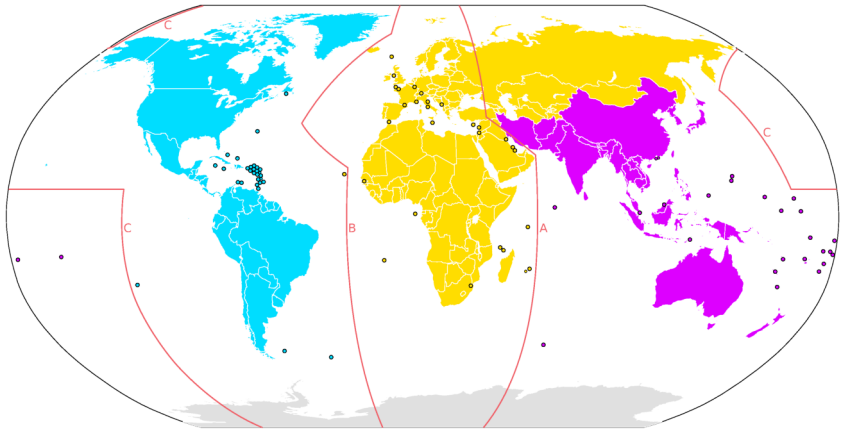

Figure 1.3: International Telecommunication Union regions with dividing lines by Maximilian Dörrbecker under the CC BY-SA 2.5 license. Region 1 is yellow, region 2 is blue and region 3 is magenta.

radio band, the International Amateur Radio Union (IARU) is involved in the process [41]. This frequency coordination process is important to reduce the amount of interference between systems.

Different frequency bands are used for different radiocommunication services (satellite operations, maritime mobile, radiolocation, etc.) depending on the ITU region [42]. The ITU regions are shown in Figure 1.3. The services are divided into primary and secondary services. The latter services are not protected from interference generated by primary services and should not interfere with the primary services. This means that some services must be robust against interference to co-exist with primary services, like amateur radio in some ITU regions. Some common satellite frequency bands are summarised in Table 1.1 based on [43].

1.3.3 Radiolocation in the UHF amateur radio band

Radiolocation (420–450 MHz), the Earth Exploration Satellite Service (432–438 MHz), and the UHF amateur radio band (430–440 MHz) share the same UHF band. Amateur radio is a primary service only in ITU region 1. For

Table 1.1: Common satellite frequency bands for small satellites.

Service	Band	Frequency range
Amateur satellite	UHF	435–438 MHz
Earth exploration-satellite	UHF	401–403 MHz
Space operation	UHF	401–402 MHz
Space operation	L-band	1 427—1 429 MHz
Earth exploration-satellite Space operation Space research	S-band	2 025—2 110 MHz
Earth exploration-satellite Space operation Space research	S-band	2 200—2 290 MHz
Space research	S-band	2 290—2 300 MHz
Earth exploration-satellite	X-band	8 025–8 400 MHz

regions 2 and 3, radiolocation is the primary service. The UHF amateur radio band has been a popular choice for small satellite communication [41] because it is unlicensed and there is no cost for frequency filing.

In the radiolocation service (420–450 MHz), there are three types of ground radars that can transmit high power and time-variable signals (chirps) [44]. Type-A radars are used for space object tracking, type-B for surveying high altitudes, and type C are for surface and search. The characteristics of these radars are summarised in Table 1.2. Since type-A radars can transmit 1–5 MW of peak power, operate all year round, and track space objects, they can cause severe interference in satellite uplinks. These radars transmit chirp signals with variable pulse duration, pulse period, and chirp bandwidth. For search mode, the chirp bandwidth is 100–350 kHz, and for tracking, 1 or 5 MHz linear chirps. The identified locations of type-A radars are shown in Figure 1.4.

More information on the Precision Acquisition Vehicle Entry (PAVE) Phased Array Warning System (PAWS) radars located in Cape Cod (Massachusetts), Beale (California), and Clear (Alaska) can be found in [47]. In this case, the pulse width for the tracking mode can be 0.25, 0.5, 1, 2, 4, 8, and 16 ms, and for surveillance, 0.3, 5, and 8 ms. The pulse repetition rate can be between 18 and 72 pulses per second.

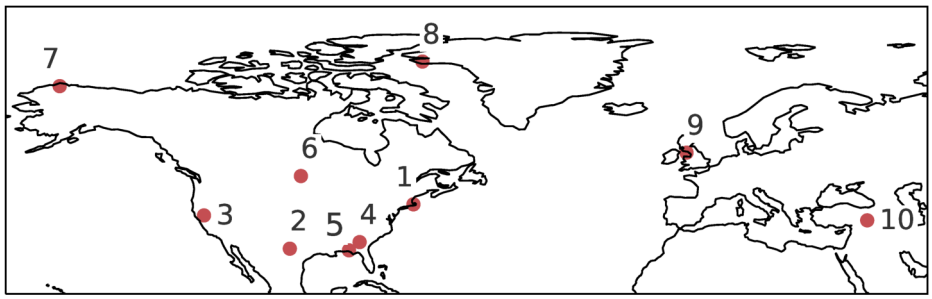

Figure 1.4: Type-A radar locations identified in [44], [45]. 1: Massachusetts (United States of America (USA)), 2: Texas (USA) , 3: California (USA), 4: Georgia (USA), 5: Florida (USA), 6: North Dakota (USA), 7: Alaska (USA), 8: Thule (Greenland), 9: Fylingdales Moor (United Kingdom (UK)), 10: Pirinclik (Turkey). Adapted from Paper E [46].

1.3.4 Satellite radiofrequency measurements

RF measurements are important to design or improve communication systems, but also because it is difficult for the ITU to control the real use of the spectrum [48]. Satellite launches have increased in the last ten years and are expected to continue increasing [49], especially small satellites with 1-10 kg mass. Only 31.4% of the nanosatellites and picosatellites launched in the period 2003-2014 had sent an API to the ITU [41]. In-orbit radio measurements from satellites are needed to know the actual use of the RF spectrum.

The European Space Agency (ESA) has promoted projects to perform in-orbit spectrum monitoring and analyse the interference environment [50]–[53]. ESA also has a satellite that can monitor the spectrum in-orbit, OPS-SAT [54]. Furthermore, in the last years, some companies have started to work on this topic and launch their own satellites to monitor the spectrum and localise RF emitters (Table 1.3). Some examples are HawkEye 360 [55], Aurora Insight [56], Kleos Space [57], Umbra [58], and Horizon Technologies (Amber) [59].

In the UHF amateur radio band, the University of Würzburg, the Technische Universität Berlin (TU Berlin) and the University of Vigo (UVigo) en-

Table 1.2: Characteristics of ground radars in the 420–450 MHz band [44]. Adapted from Paper E [46].

Parameters	Radar A	Radar B	Radar C
Peak output power (MW)	1–5	0.3	0.01
Pulse duration (ms)	0.25, 0.5, 1, 2, 4, 8, 16	0.01–16	0.001–1
Pulse frequency modulation	Search: 100–350 kHz chirp Track: 1 or 5 MHz linear chirp	2 MHz linear chirp	1 or 3 MHz linear chirp
Pulse repetition frequency (Hz)	up to 41	15–400	100–3000
Antenna beamwidth in azimuth (°)	2.2	1.8 typical	80
Antenna beamwidth in elevation (°)	2.2	1.8 typical	60

countered interference signals when trying to operate some of their satellites and started measuring the spectrum [48], [60], [61]. Starting in November 2013, strong pulsed interference was measured from the HumSat-D satellite (UVigo). In the same year, communication problems with the TUBSAT satellite from TU Berlin were experienced. High-power interference was measured over central Europe from the UWE-3 satellite (University of Würzburg). In 2019, TU Berlin launched an SDR to the International Space Station (ISS) to start thorough spectrum monitoring activities in the band. A year after, the SALSAT satellite was launched to continue those activities without the ISS orbit constraints. The ISS orbit has an inclination of 51.6°, limiting the spacecraft footprint to ±51.6° latitude.

In the VHF Data Exchange (VDE)-SAT band, the satellite component of the emerging VDES system that can be used in the Arctic, different studies have been performed. Channel modelling has been presented by Giambene et al. [62] and Bråten et al. [63]. An ON-OFF model including sea reflections based on downlink VDES measurement data was

Table 1.3: Satellite spectrum monitoring companies.

Company	Country	Band	Launched/Planned
HawkEye 360	USA	VHF, UHF L/S/X-band	9/30
Aurora Insight	USA	2G/3G/5G, LTE, IoT, Wi-Fi, TV,	3/-
Kleos Space	Luxembourg	VHF, X-band	8/80
Umbra	USA	-	1/20
Horizon Technologies	UK	VHF L/S/X-band	0/13

developed by Giambene et al. using the gamma distribution [62]. Bråten et al. modelled fading caused by ionospheric scintillation and incoherent sea reflections in the VDE-SAT downlink using Nakagami-Rice envelope distributions [63]. Haugli et al., Eriksen et al. and Bråten et al. analysed satellite downlink measurements transmitting Continuous Wave (CW), Binary Phase Shift Keying (BPSK)/Code Division Multiple Access (CDMA), $\pi/4$-Quadrature Phase Shift Keying (QPSK) and 8-Phase Shift Keying (PSK) signals [64]–[66]. The initial analysis by Haugli et al. showed that transmitting BPSK/CDMA signals from NorSat-2 provided a larger link margin, as compared to 8PSK [64]. The Doppler shift and the downlinked CW power was analysed by Eriksen et al. for more than a 100 passes and the typical received power was -118 dBm [65]. The analysis performed by Bråten et al. showed that the received carrier-to-noise ratio had a dynamic range of 25 dB and the peak-to-peak fading measured followed a normal distribution behaviour [66]. In addition, time-variable interference was measured. However, the focus of all these measurements has been on the downlink performance of the system, but the uplink was not analysed.

Knowledge of the real uplink and downlink interference environment can help to improve satellite communication system performance for satellite operations in the UHF amateur radio band and the VDE-SAT band, and can also be extrapolated to other bands. In the amateur radio band, public measurements have been provided only by three universities (UVigo, University of Würzburg and TU Berlin) and have focused on average power levels, and not on the time variability of the signals [48], [60], [61]. In the

VDE-SAT band, since all measurements were performed on the downlink, uplink interference remains to be analysed.

In this thesis, the author studies the interference environment in the VHF and UHF bands since it is relevant for communicating between satellites and sensors in remote locations. For the UHF band, the focus is on the UHF amateur radio band (430-440 MHz) because it has been a popular band for Telemetry, Tracking and Command (TT&C) operations of small satellites. Uplink interference analysis and measurements from the Serpens and the LUME-1 satellites are presented in Paper E and Paper F. For the VHF band, the lower leg of the VDE-SAT frequency band (centered at 157 MHz) is explored to evaluate the uplink interference of an emerging communication system that could be used in the Arctic (Paper G).

1.3.5 Radio Frequency Interference detection and mitigation techniques

From a traditional communication perspective, RFI degrades the quality of the link between a transmitter and a receiver. Similarly, RFI also affects other fields that measure radio waves, such as radioastronomy and microwave remote sensing. RFI in different frequency bands is a growing problem for microwave remote sensing radiometry, so a considerable effort has been put into implementing RFI detection and mitigation techniques in microwave remote sensing [67]–[70].

Depending on the domain where the algorithms operate, the RFI detection and mitigation techniques can be grouped into the following categories [67], [69], [70]:

- **Temporal**. The average received power is compared to a detection threshold in the time domain. These algorithms are useful for detecting pulsed interference, especially when the integration period to calculate the average power matches the pulse length. The simplest mitigation technique against pulsed interference is pulse blanking, where In-Phase and Quadrature (IQ) samples above a power threshold are removed.

- **Spectral**. In this case, the power of frequency bands is compared

to a threshold to detect RFI. The power measured depends on the bandwidth. These algorithms are useful to detect CW RFI. An example of a mitigation technique in this domain is frequency blanking, where subbands with detected RFI are eliminated.

- **Spatial**. These algorithms compare pixels in an image to detect RFI and are useful for interference that is localised in a specific area [69]. Adaptive antennas that use null steering and beamforming techniques can mitigate the RFI spatially. The null steering technique points the antenna in the direction that minimises the received energy because RFI power is expected to be higher than the desired signals. If the RFI source is not in the same direction as the desired signal, beamforming can be used to adjust antenna pointing to maximise the signal-to-noise ratio.

- **Polarimetric**. The majority of natural targets are not polarised, and if so, they have a weak signature. The polarisation of the received signals can be measured by calculating the third or fourth Stokes parameters. If the received signals have a high polarimetric signature, they are detected as RFI.

- **Statistical**. The implementation of these algorithms is not simple but they can detect low power interference. The statistical characteristics of the received signals are used to detect RFI. Higher-order moments are calculated to measure how close the distribution of the signal received is to a Gaussian distribution with zero mean and normality tests are performed. The most common algorithm is the Kurtosis method which requires the second and fourth-order moments of the distribution. This method can be applied in the time (time kurtosis) or frequency domain (spectral kurtosis).

There are other methods that combine domains, such as time-frequency algorithms (the short-time Fourier transform and the Wigner-Ville distribution), or use other transform domains (Wavelet Transform and Principal Component Analysis) [67]. However, these algorithms are generally computationally complex.

In this thesis, a new time-domain algorithm is implemented to detect RFI in the measurements with the NorSat-2 satellite (more details in Section 2.2.3).

Spectral techniques can provide part of the interference characterisation estimating the power levels in different bands, but the time properties of the signals are ignored. The time and frequency characterisation of RFI is important for countermeasures that can easily be implemented on Cubesats. Spatial algorithms have limited applicability for single antenna systems common on small satellites in UHF and VHF. Heatmaps are a low-resolution spatial description of RFI that has been used to give an overview of the interference environment in the UHF amateur band in the literature [48], [60] and in this thesis (Paper E). Polarimetric methods have limited use in communication as the desired source has polarised characteristics too. Higher-order statistics, such as kurtosis, imply a complex implementation and require large data sets. After some preliminary testing with simulated interference, emulating the data collected using the LUME-1 satellite (Paper F), it was discarded because too many samples were needed to reduce the random fluctuation as kurtosis is a noisy measure [68]. The Local Mean Envelope (LME) interference measurement algorithm designed in this thesis (see Section 2.2.2) combines the frequency domain with simple statistical algorithms where only the first and second-order moments of the distribution are calculated. This method reduces the random fluctuations in shorter integration times compared to kurtosis and generates little data to downlink.

1.3.6 Software-Defined Radios

Analysing the interference for both the UHF amateur radio and the VDE-SAT band, serves as a preparation for the communication activities on HYPSO-2 (Paper C). Measurements and characterisation of the interference environment in the 400 MHz band are planned for HYPSO-2. Knowledge of the radio environment will aid the communication system design to demonstrate a communication link to sensors in remote locations (Paper C), such as the Arctic (Paper B), and to robotic assets for ocean monitoring (Paper D). SDRs can be used as flexible communication payloads because they can adapt their communication parameters to enable different missions.

An SDR is a flexible radio communication device where most components (modulators/demodulators, error coding/decoding, etc.) are implemented in software using the same hardware platform. Ideally, the antenna would

be connected directly to an Analogue to Digital Converter (ADC) (for the receiver) and a Digital to Analogue Converter (DAC) (for the transmitter). After the A/D and D/A conversion, the signal would be digitally processed. However, due to the limited sampling rate of ADCs/DACs, limited speed of processing units and difference in interfaces an RF front-end is needed after the antenna. A generic SDR architecture is depicted in Figure 1.5.

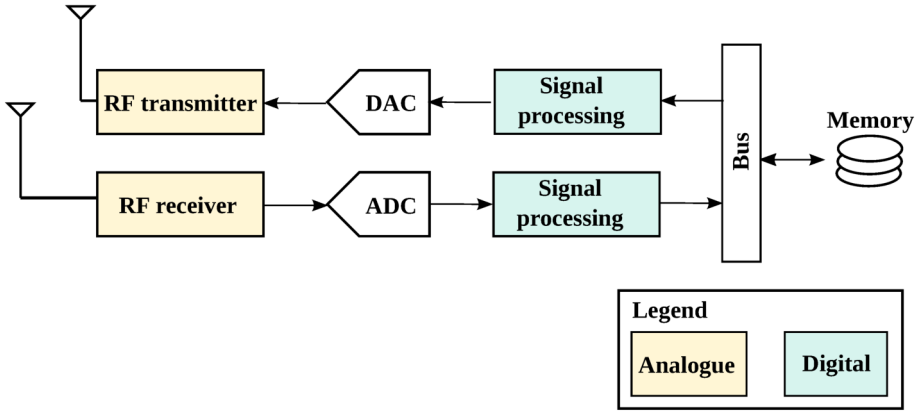

Figure 1.5: Architecture of a generic SDR platform.

In the transmitter chain, the signal to be transmitted is generated in software, and then, converted to an analogue signal by the DAC. The analogue signal is fed to the RF transmitter. The RF transmitter consists of power amplifiers to increase the power of the signal, filters to limit the bandwidth, and mixers and local oscillators to up-convert the signal to the RF carrier frequency. The antenna sends the signal after up-conversion.

In the receiver chain, the signal is received at the RF carrier frequency by the antenna and fed to the RF receiver. The RF receiver contains Low Noise Amplifiers (LNAs), filters, mixers and oscillators to down-convert to the baseband. The LNA amplifies the signal to a suitable level for the ADC, noise is filtered and the signal is down-converted to the frequency range needed for the ADC. The RF receiver front-end can have different architectures. The most common architectures in commercial devices are *superheterodyne* and *direct conversion* [71]. In a superheterodyne receiver, the frequency conversion is done in multiple stages. For example, in double conversion, the RF carrier is down-converted to the first Intermediate

Frequency (IF). Then, the first IF frequency is down-converted to a second IF before down-converting to baseband. In the direct conversion (zero-IF) architecture, the RF frequency signal is directly converted to baseband in IQ signals [71]. After the frequency down-conversion, the analogue to digital conversion is done by the ADC. In this process, the Nyquist–Shannon sampling theorem should be applied to avoid aliasing. The theorem states that the sampling frequency should be at least twice the signal bandwidth for band-limited signals [72]. Afterwards, other digital signal processing is performed.

When selecting an SDR platform for a space mission, some of the most important drivers are mass, size, cost, power consumption, and flight heritage. The author considers a mass of 200 g, size of 1/4 of a 1U (10 cm x 10 cm x 10 cm), €500 (in the order of €10 000 for space-proven) and 2 W idle power consumption as low values desired for an SDR payload for a CubeSat mission. Flight heritage proves that the platform has functioned or successfully operated in space. To reduce the need for adaptation of the platform and risk of the mission, space-ready SDRs, such as the TOTEM SDR (Alén Space) [17], the GomSpace SDR (GomSpace) [16], the Astro SDR (Rincon Research Corporation) [19] and the newly released SDR-1001 (CesiumAstro) [73] are desired. Another option is to modify existing SDR platforms to tailor the needs and make them space suitable. The LimeSDR from Lime Microsystems was modified by TU Berlin and installed on the ISS for spectrum monitoring experiments [48]. The Myriad-RF 1 board, also from the same company, has flown in the OPS-SAT satellite from ESA [54]. Some of the SWIFT SDRs (L/S/X-band models) achieved flight heritage in the last years but there is not much information on their architecture [74]. The datasheet of the SDR-1001 also lacks information. A summary of the most relevant space SDRs is shown in Table 1.4.

To design the communication payload of the HYPSO satellites, it is important to know the characteristics of the SDR platforms on the market. Cost increases dramatically when the equipment is space-ready or space-proven, which is the case for the GomSpace SDR and the Totem SDR. Those two platforms and the Astro SDR have a reasonable mass and size, that could fit CubeSat applications. The SWIFT models are also in a similar mass range but are slightly bigger (still fitting in a small CubeSat). Other SDRs with

[5] A modified version was sent to the ISS by TU Berlin.

Table 1.4: Space-ready SDRs, some with flight heritage.

SDR	Band (MHz)	Transceiver	Proc. Unit
TOTEM	70 – 6 000	AD9364	Zynq-7020
GomSpace SDR	70 – 6 000	AD9361	Zynq-7030
Astro SDR	70 – 6 000	AD9361	Zynq-7045
LimeSDR USB [5]	0.1 – 3 800	LMS7002M	Altera Cyclone IV EP4CE40F23
SWIFT UTRX	370 – 750	-	-
SWIFT HB	-	-	Zynq 7030
SWIFT XTS	1 700 – 2 500 7 000 – 8 500	-	-
SDR-1001	300 – 6 000	-	-

lower mass and lower cost are the Lime Microsystems SDRs [20], FUNcube models [75], and RTL-SDR [76], but they are not made for space so they need some modifications to be flight-ready. The USRPs from Ettus Research are not space-ready, and come at a higher cost, making them less attractive for space applications. However, the USRP E310, part of the Embedded Series [18], is lighter and smaller so it can be an interesting option. EPIQ Solutions also provides some SDR models (Matchstiq and Sidekiq) with a reasonable mass and a size that enables integration onto small CubeSat [77]. This is also the case of the HackRF One [21], BladeRF [78], and ADALM-PLUTO [79].

The frequency band and main components of some relevant space and non-space proven SDRs are summarised in Table 1.4 and Table 1.5. Many of the SDRs platforms mentioned use the Analog Devices AD936x (AD9361, AD9364) transceiver chip family [16]–[19] for part of the RF stage and ADC/DAC. The AD9361 has two transceiver chains and the AD9364, just one [80], [81]. The LMS6002 and LMS7002M transceiver chips are mainly used by Lime Microsystems SDRs, but also for BladeRF [20], [78]. The FUNcube Pro uses a Silicon tuner as the RF front-end and the RTL-SDR, a Rafael Micro R820T transceiver chip. The transceiver chips used in the SDRs platforms limit the frequency band for the platform. For the AD936x and LMS7002M, the frequency range is from tens of MHz to a few GHz. In the case of the SWIFT SDR, each model targets a different frequency band. For the processing unit, the Zynq Z System on Chip (SoC)

is a popular choice, often using the variants 7020, 7030 or 7045 [16]–[19], [82]. The software development tool needed to program each SDR is also important. GNU Radio programming can be used in the USRPs, LimeSDRs, FUNcube, ADALM PLUTO, and HackRF, for example. The USRPs can also be controlled using LabVIEW communications. The GomSpace SDR and TOTEM SDR enable software development flexibility on the platforms. Totem SDR allowed Python programming using GNU Radio libraries, C and C++ programming.

Table 1.5: SDRs not designed for space, with no flight heritage.

SDR	Band (MHz)	Transceiver	Proc. Unit
LimeSDR mini	0.1 -– 3 500	LMS7002M	Altera MAX 10
FUNcube Pro	TX: 0.64 – 1 100 RX: 1.27 – 1 700	Silicon tuner	PIC24FJ32 GB002
FUNcube Pro+	TX: 0.15 – 240 RX: 420 – 1 900	Silicon tuner	PIC24FJ32 GB002
RTL-SDR	RX:0.5 – 1 766	Rafael Micro R820T	-
USRP N210	DC – 6 GHz	WBX Daughterboard	Xilinx Spartan3A DSP 3400
USRP E310	70 – 6000	AD9361	Zynq-7045
Matchstiq S10/S11	70–6 000	AD9361	Zynq 7020
Matchstiq Z3u	<1 – 6 000	AD9361	Xilinx Zynq Ultrascale+
Sidekiq Z2	70–6 000	AD9364	Zynq 7010-2i
Sidekiq NV100	30 – 6 000	ADRV9004	Xilinx Artix 7 XC7A50
HackRF One	1 – 6 000	RFFC5072	LPC4320
Blade RF	300 – 3 800	LMS6002D	Altera Cyclone IV
ADALM PLUTO	325 – 3 800[6]	AD9363	Zynq Z-7010

Power consumption should also be considered when using an SDR platform as a small satellite payload, especially the idle power consumption. From

[6] It can be extended to 70–6 000 MHz.

the space-proven SDRs, the one with the lowest standby power consumption is the TOTEM SDR (1.4 W), followed by Gomspace SDR with 3 W, and Astro SDR and SWIFT SDRs with 4 W. The Matchstiq SDRs consume 2–6 W and the USRPs 2–6 W.

To reduce the development time of the SDR payload for the HYPSO satellites and limit the risk of the mission, a space-proven SDR was selected. The TOTEM SDR provided a mass of about 150 g, volume less of 1/4U (depending on the connector used), the lowest idle power consumption (1.4 W), lower cost than GomSpace SDR and complete access to the firmware framework. The selection of TOTEM SDR for the communication missions is described in Paper B, as well as its architecture.

1.4 Thesis outline

The thesis is divided into three parts. Part I is the summary of the thesis, Part II contains the mission-oriented publications, and Part III, the interference measurement articles.

Part I consists of the introduction, the description of the satellites used, thesis contribution and conclusion and future work. Part II contains the publications related to mission design (Paper A, B, C and D). Paper A studies the state-of-the-art of SDR platforms for space applications. Paper B defines two small satellite SDR missions for HYPSO-1. Paper C generalises these missions for HYPSO-2. Paper D discusses possible system architectures to enhance oceanographic observations using small satellites and USVs. Part III includes the publications about the in-orbit interference environment. Paper E and F focus on the uplink interference in the UHF amateur radio band (430–440 MHz) using the Serpens and LUME-1 satellites. Paper G analyses the uplink interference environment in the VDE-SAT system (157 MHz band) from the NorSat-2 satellite.

2 Satellite descriptions

In this chapter, the satellite platforms involved in this research and the interference measurement algorithms used are described.

2.1 Satellite platforms

The work in this thesis has involved the use of five satellites for different purposes (Figure 2.1). A summary of the different characteristics of the satellites mentioned and the work performed with each of them in the thesis is presented in Table 2.1. A preliminary mission design for Arctic communication using a Software-Defined Radio (SDR) payload was done for the HYPer-spectral Smallsat for Ocean observation (HYPSO)-1 satellite. In the end, this payload was not included in HYPSO-1, but is planned to be on HYPSO-2. Hence, the mission design was updated and generalised for a flexible communication mission for HYPSO-2.

A collaboration with University of Vigo (UVigo) provided the opportunity to analyse uplink interference measurements from the Serpens satellite and to define new measurements and software for the LUME-1 satellite, as well as to analyse the results.

The last satellite used is NorSat-2. Thanks to a collaboration with Space Norway, measurements in the VHF Data Exchange (VDE)-SAT band were defined for NorSat-2 and analysed using the software developed on the ground. Measurement definition, ground processing software development, and analysis were performed by the author.

Table 2.1: Satellites used in the thesis.

	HYPSO-1	**HYPSO-2**	**Serpens**	**LUME-1**	**NorSat-2**
Thesis scope	Mission and payload design	Mission and payload design	Interference analysis	Algorithm implementation and interference analysis	Algorithm implementation and interference analysis
Research questions	RQ1.1	RQ1.1	RQ2.1, RQ2.2	RQ2.1, RQ2.2	RQ2.2
Paper	**B**	**C**	**E**	**F**	**G**
Launched	Yes	No	Yes	Yes	Yes
Still in-orbit	Yes	-	No	Yes	Yes
Owner	NTNU	NTNU	Brazilian universities	UVigo	NoSA
Orbit	500 km 97.8° SSO	-	400 km 51.6°	500 km 97.2° SSO	600 km 97.6° SSO
Downlink data rate	1 Mbps	4 Mbps	1.2 kbps	4.8/9.6 kbps	1 Mbps
Communication payload	-	TOTEM SDR	Configurable radio	TOTEM SDR	Kongsberg Seatex SDR
Measured frequency band	-	400 MHz	435–438 MHz	435 MHz	157 MHz
Measuring antenna	-	Turnstile	Turnstile	Turnstile	8 dBi Yagi Uda
Antenna pointing	-	Yes	No	No	Yes
Measurement algorithm	-	LME (on-board)	Sustained interference (on-board)	LME (on-board)	LME and pulse detection (on ground)

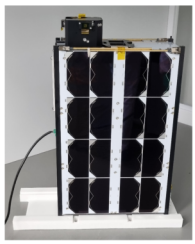

(a) HYPSO-1.

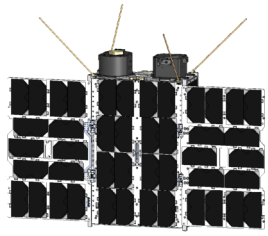

(b) Current Computer Aided Design (CAD) model of the HYPSO-2 satellite bus. Credit: Nanoavionics[1].

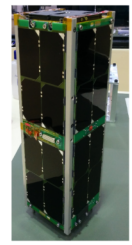

(c) Serpens. Credit: UVigo.

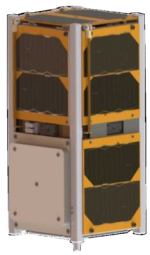

(d) LUME-1. Credit: UVigo.

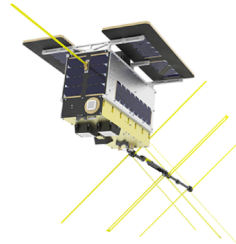

(e) NorSat-2. Credit: University of Toronto Institute for Aerospace Studies (UTIAS)[2].

Figure 2.1: Satellites used in this thesis.

A description of the characteristics of each satellite is provided in the following sections.

2.1.1 HYPSO-1

HYPSO-1 is a Norwegian satellite that was launched 13$^{\text{th}}$ January 2022 in a 500 km and 97° Sun-synchronous orbit (SSO) orbit [83]. The satellite bus is a Multipurpose 6U Platform (M6P) built by NanoAvionics. The SmallSat Lab at Norwegian University of Science and Technology (NTNU)

[1] https://nanoavionics.com
[2] https://www.utias-sfl.net/?page_id=2312

provided one payload with two instruments: a hyperspectral and an RGB camera. The main mission objective is to monitor ocean colour events both spatially and temporally, to be able to mitigate effects from Harmful Algal Blooms (HABs), for example. HYPSO-1 has an S-band system capable of downlinking 1 Mbps using a patch antenna and two UHF radios using a turnstile antenna and a monopole antenna as a backup. The UHF system will use the 400 MHz band to communicate.

Initially, this satellite was going to host an SDR in addition to the optical payloads. In Paper A, the author investigates the possible SDR platforms that could be used for this case, and in Paper B, the author describes a preliminary mission design for Arctic communication. In the end, this payload was not included in HYPSO-1, but integration onto HYPSO-2 has started.

2.1.2 HYPSO-2

HYPSO-2 will be the second satellite of the SmallSat Lab at NTNU and is based on the M6P from NanoAvionics, like its predecessor. The satellite will have an S-band transceiver that enables a downlink data rate of up to 4 Mbps and a UHF communication system as a backup. The satellite mission will be similar to the HYPSO-1 mission, especially for the optical instruments. In addition, a TOTEM SDR will be included to enable a flexible communication mission.

The definition of the communication mission for HYPSO-2 has been part of this work. The first objective of the mission is to perform spectrum monitoring measurements to characterise the radio interference in the 400 MHz band. It can be achieved by listening to the in-orbit radio environment from the satellite. The Secondary Mission Objective (SMO) is to characterise the channel effects in this band. One way to perform channel measurements (second SMO) is to transmit a pseudorandom sequence from the satellite and receive it on the ground. By comparing the transmitted and received signals, the impulse response of the channel can be obtained. These two mission objectives will help to design a robust communication system for the next objective. The last objective is to demonstrate a two-way communication system between the satellite and sensor nodes in remote locations,

such as the ocean and the Arctic. The Arctic ABC project is the use case for collecting and relaying data from the sensors in the high north. The optical observations with the Hyperspectral Imager (HSI) integrated into a heterogeneous system with the satellite and robotic agents is the other use case. In addition to defining the flexible communication mission, the integration of the TOTEM SDR into the HYPSO software framework and hardware-in-the-loop testbed has been part of this thesis and is described in Paper C. However, there is more work to be done with the SDR payload to be prepared for next project reviews, such as Preliminary Design Review (PDR) and Critical Design Review (CDR).

2.1.3 Serpens

Serpens was a Brazilian satellite that was built in a project led by a consortium of universities in Brazil (Sistema Espacial para Realização de Pesquisa e Experimentos com Nanossatélites) [84]–[86]. It was a 3U Cubesat that was launched in an International Space Station (ISS) orbit (400 km, 51.6°) in September 2015 and reentered the atmosphere in March 2016. The satellite was divided into two independent sectors that had different missions. Sector A was part of an educational project led by the Brazilian universities and sector B was led by the UVigo (Spain). Sector B hosted an amateur radio payload to demonstrate a UHF Machine to Machine (M2M) communication system for the Humanitarian Satellite constellation (HumSat) project. The communication payload in sector B included four parallel receivers (Figure 2.2) configurable via telecommands, allowing the relay of messages from sensor nodes in remote areas in a store-and-forward system. The antenna connected to this payload was a turnstile antenna. An algorithm to measure the power of received packets was implemented by the UVigo team on the payload to analyse the performance of the system.

During spacecraft operations at the ground station in Vigo (Spain), challenges in the uplink of commands were experienced and M2M payload operations in the northern hemisphere were not possible. The Telemetry, Tracking and Command (TT&C) radio included Reed Solomon error correction and could operate in both hemispheres despite the difficulties. To investigate the problems with the M2M payload, the algorithm settings were modified to study the payload communication issue. Different in-orbit

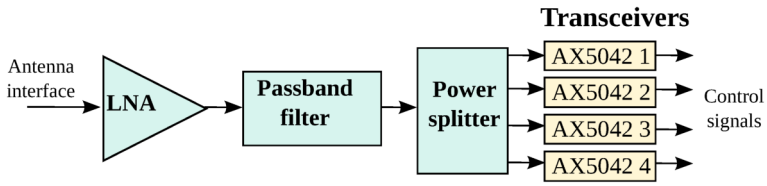

Figure 2.2: Communication payload architecture used in Serpens. Adapted from [46].

interference power measurements in the 435–438 MHz band were performed. As part of the collaboration between NTNU and UVigo, the measurement data obtained by UVigo was shared with NTNU. In this thesis, the author describes the algorithm used and analyses the measurement results from 2015-2016 (Paper E). In order to complement these measurements and overcome the limitations (satellite footprint constrained to ISS orbit and algorithm limitations), a new interference measurement campaign was designed, and then executed on the LUME-1 satellite.

2.1.4 LUME-1

LUME-1 is a 2U Cubesat launched in a 97.2° and 510 km SSO in December 2018. The satellite was developed by UVigo for the European project Fire RS where they collaborated with The Laboratory for Analysis and Architecture of Systems (France) and the University of Porto (Portugal) [87]. The goal of the project was to detect and monitor forest fires using an SDR (TOTEM) as the satellite communication payload. The LUME-1 mission for the Fire RS project ended in June 2019 and was available for other research afterwards.

The collaboration between NTNU and UVigo (Spain) provided the opportunity to perform interference measurements on board LUME-1. In this case, the author designed and developed new measurement software, uploaded it to the SDR on-board the satellite, planned the measurements, and analysed the results. The measurement algorithm is called the Local Mean Envelope (LME) and measures the time and frequency variability of the spectrum (more information in Section 2.2 and in Paper F). The target frequency band

is the UHF amateur radio band (435–438 MHz) and it is measured with an on-board turnstile antenna on LUME-1. Radio amateurs from UVigo and supported by Alén Space operate the satellite at 437 MHz, uplinking the schedule to run the measurement software and downlinking the results. The software is designed considering the constraints of the satellite and the payload. The gross data rate can be configured to 4.8 kbps and 9.6 kbps at 437.06 MHz, but the net rate is lower due to overhead and interference in the uplink. A downlink throughput of 1 kbps continuously for 5 min and 200 bps for 5 min in the uplink proves to be a realistic estimate for the 4.8 kbps configuration. The uplink is more limited due to the in-orbit interference the author wants to characterise, and affected the time it took to upload the measurement software implemented.

The main drivers for the measurement algorithm design are to generate as little data as possible and to have a fast implementation and testing cycle, as the satellite is in the extended part of its life cycle. The software implementation includes the development of a transmitter that generates different signals and a receiver. The algorithm on the receiver is the LME. The development process consists of the following steps:

1. High-level programming language implementation (Matlab).
2. GNU Radio implementation.
3. Automatic translation into Python using GNU Radio Companion.
4. Translation into C++ using GNU Radio libraries.

The first implementation step was to build a high-level programming framework that includes both a transmitter and a receiver. The transmitter generates four types of signals that simulate relevant interference. An Additive White Gaussian Noise (AWGN) model is used when there are many independent random signals. As an example of a simple stationary signal, a Continuous Wave (CW) can be generated. Pulses and chirps are a way of representing the interference that can be experienced because of radiolocation services (primary service in the 420–450 MHz band). The LME measurement algorithm is implemented on the receiver part of the software as it is on the satellite. The software framework was first built in Matlab and then in GNU Radio since GNU Radio libraries are available on the TOTEM SDR on LUME-1. These first two steps were key to simulations. Simulations imply that signal generation (interference) and the receiver

LME algorithm are executed on the same hardware to validate the algorithm. The last two steps of the development process start as simulations and later are moved on to execution on TOTEM.

The author built an SDR testbed in the SmallSat lab at NTNU, where a copy of the TOTEM SDR is used as a receiver (Figure 2.3). The TOTEM SDR consists of two boards: the radiofrequency (RF) front-end and the motherboard (see Paper B). The front-end includes an antenna switch, a power amplifier, filters, a transmitter/receiver switch, and a Low Noise Amplifier (LNA). The main components of the motherboard are the Zynq 7020 System on Chip (SoC) and the AD9364 transceiver, but it also contains some peripherals like Ethernet, Universal Asynchronous Receiver-Transmitter (UART) and Controlled Area Network (CAN) [17]. An embedded Linux operating system is installed on the motherboard and the firmware is built using Buildroot. The TOTEM SDR on LUME-1 can run shell commands, C and C++ scripts (including GNU Radio libraries). The TOTEM on the lab setup at NTNU is a more advanced version of the SDR flying on LUME-1 and can run Python code.

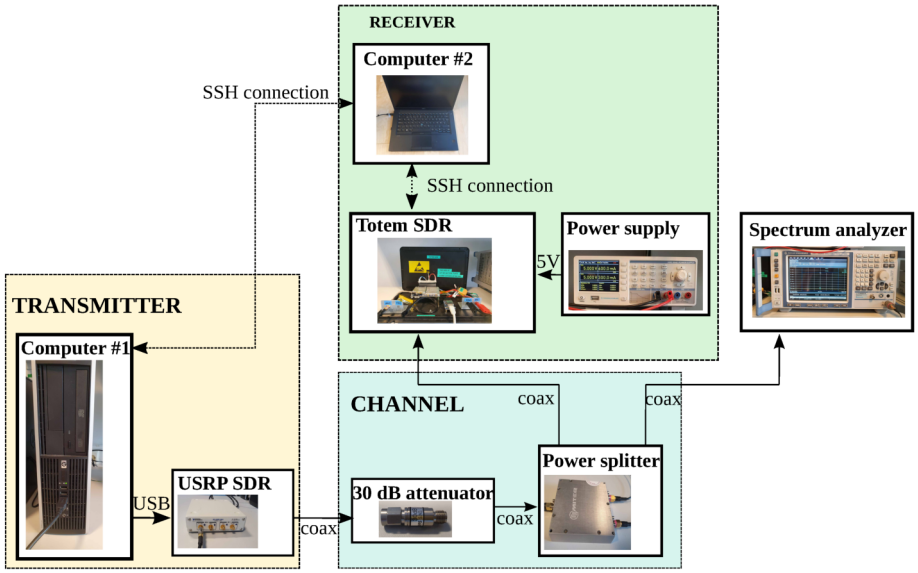

Figure 2.3: SDR testbed in the lab. The USRP transmits interference signals and the TOTEM SDR runs the measurement algorithm. Adapted from [88].

To move on to executing on TOTEM, the software is split into the transmitter and the receiver part. Transmitter programmes in GNU Radio are implemented to generate different RF signals and are run on another SDR (USRP 2901) using Computer #1 in Figure 2.3. These programmes can also be run remotely via Secure SHell (SSH) from, for example, Computer #2. The signals transmitted simulate the four types of in-orbit interference mentioned above. The USRP SDR is connected to an attenuator to protect the receiver. The attenuator is connected to a power splitter to divide the signal into 1) TOTEM SDR, and 2) a spectrum analyser for debugging purposes. The TOTEM SDR measures the transmitted signals with the LME algorithm (measure.cpp script) as it does on LUME-1. Furthermore, a shell script is developed to control the execution of the C++ algorithm (interf_service.sh script). The TOTEM SDR is connected to the power supply and controlled remotely via SSH using Computer #2. Operational tests are performed on the software to simulate 24 h measurements, as well as shorter tests. After testing at NTNU, the software is sent to UVigo with the support of Álen Space to test with the engineering model of LUME-1 and then uplink the software to the satellite.

The author developed a framework for planning the measurements and processing them. The Python library *Pyorbital* is used to propagate the orbit of the satellite using the Two-Line Elements (TLEs) from Celestrak and obtain relevant measurement locations and dates. The configuration of the measurement software and specific dates and times to execute the software are sent to the operators to create the schedule for LUME-1 and execute the measurements. After the operators downlink the data generated, the author processes and analyses the results. The description of the measurement algorithm, its validation with theoretical analysis, simulations, hardware-in-the-loop testing, execution of measurements on board LUME-1, and analysis of results are explained in Paper F.

2.1.5 NorSat-2

NorSat-2 is a Norwegian small satellite launched in July 2017 in a 97.6°, 600 km SSO [64]. The satellite was built by UTIAS for the Norwegian Space Agency (NOSA) using the Next-Generation Earth Monitoring (NEMO) bus (measuring 20 × 25 × 44 cm without solar panels) [89]. NorSat-2 has two

payloads. One payload is an Automatic Identification System (AIS) receiver to forward AIS data to Norwegian authorities. The other is an SDR-based payload (developed by Kongsberg Seatex and owned by Space Norway) to demonstrate the use of VDE-SAT. The antenna used for VDE-SAT is a VHF Yagi-Uda folded dipole with 8 dBi gain and its pointing can be controlled by changing the satellite attitude. The satellite also has an S-band feeder link that allows a downlink data rate of 1 Mbps.

A collaboration with Space Norway allowed for performing and analysing interference measurements in the VDE-SAT frequencies. In this case, the software cannot be uploaded to the on-board SDR payload. However, due to the higher downlink data rate, raw In-Phase and Quadrature (IQ) is downlinked and can be processed on the ground. The author planned interference measurements in the Arctic, and Space Norway prepared the satellite schedule to execute the measurements and downlinked them. The author ported the LME algorithm to Python and applied it to the raw samples. Additionally, a simple method to detect pulses and their characteristics (length and repetition period) was implemented and run on the data. The analysis of these results, obtained in May 2021, can be found in Paper G.

2.2 Measurement algorithms

Three algorithms have been used for interference analysis in this thesis: the sustained interference method, the LME, and pulse detection. The sustained interference algorithm was defined and implemented by UVigo for Serpens and its results are analysed in this work. The LME and pulse detection algorithm were designed by the author (Paper F and G). The sustained interference method and its results from Serpens are discussed in Paper E, the LME is described in Paper F and results are explained in Paper F (for LUME-1) and Paper G (for NorSat-2).

2.2.1 Sustained interference

The sustained interference algorithm was initially designed to measure the power of received packets but was adjusted in-orbit, within its capabilities,

to measure interference power. By using a maximum-minimum method, the output result is the sustained interference power that lasts at least 24 ms for different frequency carriers. This method provides some insight into the time characteristics of the interference, as well as discrete frequency information.

The input samples of the measurement algorithm are the Received Signal Strength Indicator (RSSI) measurements from the AX5042 chips [90]. There are four parallel transceivers tuned at different frequencies, and the process is the same for the four chains. The power samples, $P[n]$ with $n \in \{1, ..., L-(M-1)\}$, are stored in a circular buffer whose length is $M = 8$ samples (determined empirically during payload development). Since the power sampling frequency is 333 samples per second, the buffer length is 24 ms. The total number of samples of a measurement (L) is: $L = 666$, for 2 s measurements (shortest possible); and $L = 4000$, for 12 s measurements.

The circular buffer acts as a sliding window on the power samples and is represented as columns in the power matrix ($\bar{\bar{P}}$) in Equation (2.1) (adapted from Paper E).

$$\bar{\bar{P}} = \begin{bmatrix} P[1] & P[2] & ... & P[L-(M-1)] \\ P[2] & P[3] & ... & P[L-(M-1)+1] \\ P[3] & ... & ... & ... \\ ... & ... & ... & ... \\ P[M] & P[M+1] & ... & P[L] \end{bmatrix} \tag{2.1}$$

Calculating the minimum of each column in $\bar{\bar{P}}$, a vector ($\bar{P}_{min}$) of length $L-(M-1)$ is obtained. The maximum of all samples in $\bar{P}_{min}$ is the output power of the algorithm.

2.2.2 Local Mean Envelope

The LME method is designed to analyse both the time and frequency characteristics of the interference within the constraints of the LUME-1 satellite. The data to be downlinked has to be minimised due to the limited data throughput while keeping the computational complexity low to reduce power consumption. The LME method is implemented and uploaded to

the LUME-1 satellite and is used for on-ground processing of the raw data downlinked from NorSat-2. The LME method is a low-complexity algorithm that generates very little data and measures the time variability of the local mean envelope using a Discrete Fourier Transform (DFT) and different averaging windows. It also provides the average envelope and average power over the frequencies studied. The LME algorithm improves the time-frequency characterisation of the interference [48], [60], [61].

A software block diagram depicting the algorithm is shown in Figure 2.4. The input of the algorithm is the IQ samples of the signal received. Every M samples, a DFT with M frequency bins is performed on the input data [91] and the magnitude (envelope) is calculated, $|X_k|$. The average envelope of the measurement m_{1k} (first-order moment) is estimated as the mean of the magnitude for the measurement duration as in Equation (F.1). Similarly, the average power m_{2k} of the measurement (second-order moment) is obtained by calculating the mean of $|X_k|^2$ as in Equation (F.2). Both the m_{1k} and m_{2k} are M frequency bins long and are downlinked for further analysis on the ground. The average power is the measure needed to plot the heat maps of interference as performed by the University of Würzburg [60] and the Technische Universität Berlin (TU Berlin) [48]. The ratio between m_{1k} (mean) and m_{2k} (standard deviation) are used to calculate the overall coefficient of variation (CV) and estimate the dispersion of the data during the measurement duration as in Equation (F.7).

To measure time variability shorter than the measurement duration, time windows of different lengths are used. The total number of DFTs in a measurement is denoted with T and the number of DFTs in a time window is T_i. In the algorithm implemented, the shortest window length (T_1) is configurable, and the rest of the windows are a multiple (T_{step}) of the first one to allow for an efficient implementation of the algorithm. In this thesis, the step is set to two. The local mean is the mean envelope for a particular time window ($m_{1k}^{T_i}$), corresponding to one M long vector every T_i number of DFTs during the measurement duration. The variability of the local mean indicates how stationary the data is. It is measured with the second-order moment of the local mean $m_{2k}^{T_i}$, generating one M long vector for each time window. The $m_{2k}^{T_i}$ for each window is downlinked. The $m_{2k}^{T_i}$ and the average envelope of the measurement m_{1k} is used to calculate the CV of the local mean and estimate the first-order stationarity window. This stationarity

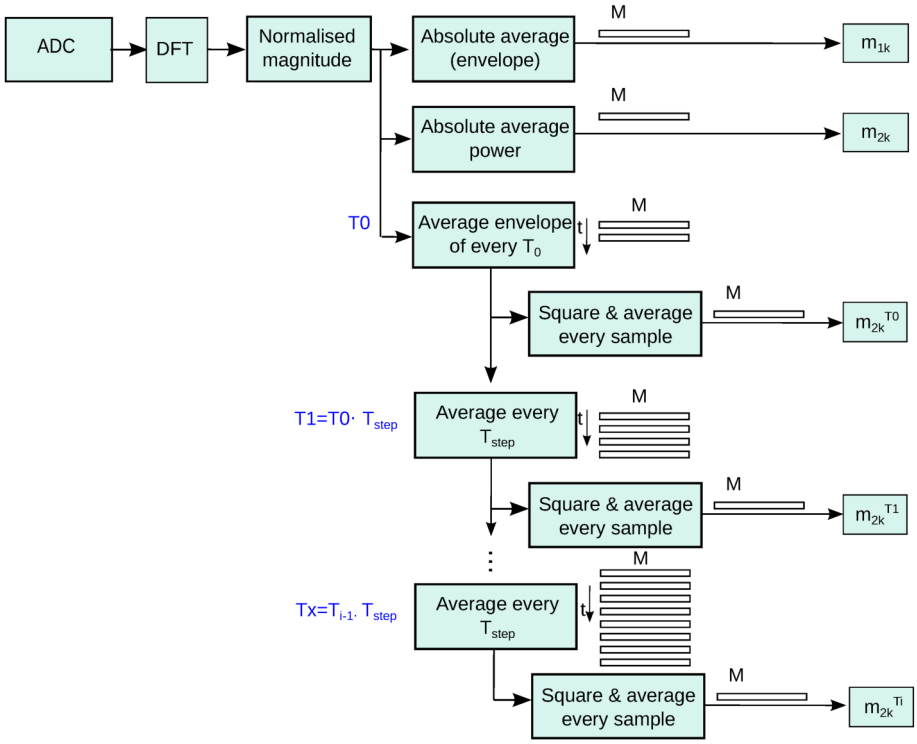

Figure 2.4: LME software diagram.

window is defined in this thesis as the shortest window whose CV is less than -10 dB.

2.2.3 Pulse detection

The pulse detection algorithm was developed for NorSat-2, since it is the only satellite in this thesis that provided raw IQ samples. The algorithm is a simple method used to detect pulses and their characteristics (pulse length and period). The IQ samples downlinked from the satellite are used to create the complex signal. The first step of the algorithm is to calculate the envelope of the incoming signal in the time domain by calculating the absolute value (Figure 2.5a). Second, to smoothen the signal, a median filter is applied to the data (Figure 2.5b). Lastly, the pulses are detected using a peak detection

function from the *scipy.signal* library in *Python* (Figure 2.5c). This peak detection function uses a time-domain Radio Frequency Interference (RFI) detection method, where the peaks are detected by calculating local maxima comparing neighbouring samples.

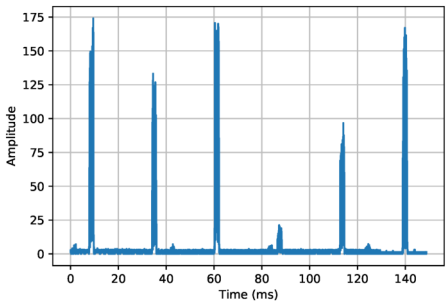

(a) Absolute value of the complex signal.

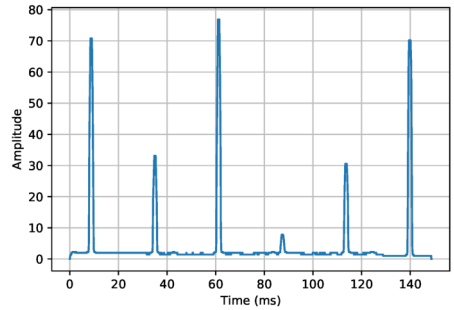

(b) Median filter applied to absolute value of signal.

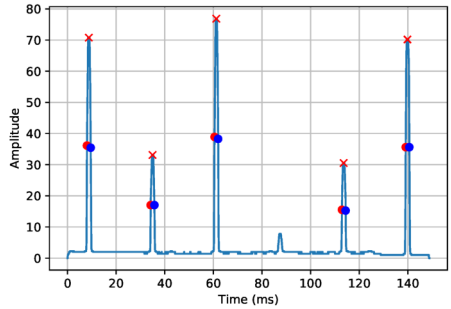

(c) Peak detection the signal after median filter (red circle indicate start of the pulse, blue circles the end the pulse, and red crosses the highest peak).

Figure 2.5: Pulse detection algorithm steps on the received IQ samples.

This function provides the start (red circle in the figure) and stop (blue circle) indexes of the pulses and their highest value (peak) and index (red cross), which are used to estimate the pulse characteristics. The length of the pulses is calculated by subtracting the pulse stop and start index. The pulse period is estimated by differentiating the indexes of the peaks. The periods with silence between pulse trains are considered long pulse periods as they are not filtered out in this implementation. Due to the configuration

of the *Python* function, the minimum detected pulse length is 7 μs and the minimum detected period is 0.7 ms.

3 Thesis contribution

This chapter describes the main contributions of the thesis, related to published and accepted papers. Additionally, all articles included in this work are summarised.

3.1 Key contributions

In this thesis, the publications are grouped into two parts: mission design (Part II) and interference measurements (Part III).

The author's key contributions in Part II are:

- A survey on relevant Software-Defined Radio (SDR) platforms for space missions and their use in university projects, as well as selection of the SDR platform for the HYPer-spectral Smallsat for Ocean observation (HYPSO) satellites (Paper A and B).

- Preliminary mission designs for different communication missions were performed. The focus was on radio environment research, communication between low power devices and small satellites, and robotic agents and small satellites. These missions can be demonstrated using one satellite with a flexible communication payload by updating the software in flight (Paper B and C).

- Payload design and initial integration and testing for HYPSO-2 (Paper C).

- Proposal and high-level analysis of three system architecture designs for oceanographic observations using an Unmanned Surface Vehicle

(USV) and a satellite, including an assessment of the communication latency of each design (Paper D).

In Part III, uplink interference is investigated for two different bands: UHF amateur radio (430–440 MHz) and the lower leg of VHF Data Exchange (VDE)-SAT (centered at the 157 MHz band). The contributions of the author in this part are:

- Analysis of the in-orbit sustained uplink interference in the UHF amateur radio band using Serpens (Paper E).
- Design and implementation of a low complexity algorithm, Local Mean Envelope (LME), to measure time and frequency characteristics of interference on board satellites with a limited downlink throughput (Paper F).
- Development of an SDR hardware-in-the-loop setup for testing interference software, and integration of an SDR platform to the HYPSO framework (Paper C and F).
- Analysis of the time-frequency characteristics of uplink interference in the UHF amateur radio band for selected regions (Paper F).
- Analysis of the time-frequency characteristics of uplink interference in the VDE-SAT band over the Arctic, including the development of the pulse detection algorithm (Paper G).
- In-orbit validation of an interference algorithm relevant for HYPSO-2 (Paper F).

3.2 Summary of included papers

In this section, all the articles included in this thesis are summarised. The first four papers belong to mission design (Part II) and the next three, to interference measurements (Part III).

3.2.1 Paper A. Software-Defined Radios in Satellite Communications

In this article, the need for flexible communication missions, addressing RQ1.1, at the Norwegian University of Science and Technology (NTNU) using an SDR is introduced. A survey on different SDR platforms and satellite programmes that have worked with SDRs is described.

The main design drivers for small satellite missions are mass, size, energy consumption, and cost. The SDR platforms with higher cost are the GomSpace SDR, the Matchtiq Series (EPIQ Solutions), and the USRPs (Ettus Research). The lighter platform of the previous ones is the GomSpace SDR, and the rest has an increasing mass in the same order. More inexpensive platforms are the RTL-SDR, FunCube, and LimeSDR models from Lime Microsystems, having a lower mass than the previous group. The most common transceiver chips in these designs are the AD936x (Analog Devices) and the Lime Microsystems chips. For the processing unit, a popular choice is the Xilinx Zynq 70xx System on Chip (SoC). Another important aspect is flight heritage. From the SDR platforms studied in this paper, only the GomSpace SDR was space-proven at the time.

Furthermore, there are many universities that have developed SDRs for space applications. The Aerospace Corporation and the University of Michigan-Flint built an SDR to use Adaptive Coding and Modulation (ACM) and increase data throughput. Istanbul Technical University developed SDRs for the space and ground segment. Johns Hopkins University built Frontier Radio, an SDR for space applications. National Aeronautics and Space Administration (NASA) has also been interested in this technology and developed three different SDRs for the Communications, Navigation, and Networking reConfigurable Testbed (CoNNeCT) project. The University of Surrey also developed an SDR system in-house. For the ground segment, the University of Bologna and National Cheng Kung built a ground station using an SDR.

Comparing commercial SDRs is not trivial, but an overview is provided for the community. After this survey, the TOTEM SDR (Alén Space) was found and chosen as the communication payload for HYPSO-2.

3.2.2 Paper B. An SDR mission measuring UHF signal propagation and interference between small satellites in LEO and Arctic sensors

This paper provides a preliminary description of two satellite communication missions in the NTNU SmallSat research programme to address RQ1.1. The preliminary integration of the payload for these missions for the HYPSO-1 satellite is described.

The Arctic ABC programme deployed sensor prototypes in Arctic ice to monitor environmental parameters. However, since communication infrastructure in the Arctic is limited, a possible solution to retrieve sensor data is addressed in this article. A communication mission using SmallSats with SDRs and other assets to retrieve scientific data from sensor nodes in the Arctic is defined. The stakeholders identified are Arctic researchers, sensor equipment, environment, suppliers, and regulatory organisations. The frequency band selected for the system is UHF to reduce power consumption.

In order to design a robust Arctic communication system, a precursor mission to measure the channel and in-orbit interference characteristics of the link is defined. The user requirements include spatial-frequency heatmaps of interference, time and frequency statistics, and the downlink impulse response. A demonstration of a communication link between the satellite and a sensor node prototype is considered a secondary objective, to move a step closer to the Arctic communication mission.

The opportunity to perform the precursor mission as a secondary mission on HYPSO-1 is presented. The system architecture proposed is composed of a ground station network, sensor node prototypes, and the satellite. After the survey in Paper A was completed, a new SDR platform was found to be the best fit for the satellite: TOTEM SDR from Alén Space (Spain). A preliminary mechanical interface design, a mass budget, and the antenna placement for the precursor mission are presented in this article.

Adding a secondary payload to a mission is challenging, especially when it is not included from the beginning. The SDR payload should minimise the impact on the primary mission. In the end, the SDR was not included as a payload for this satellite but is planned to be on HYPSO-2 (Paper C).

3.2.3 Paper C. Development of a multi-purpose SDR payload for the HYPSO-2 satellite

This article expands on the missions in Paper B and explains the development and integration of an SDR payload on the HYPSO-2 satellite, addressing RQ1.1. There are three main mission objectives for the communication part of the mission for HYPSO-2. The first objective is to measure the in-orbit uplink interference received by satellites in the 400 MHz band to investigate the time and frequency characteristics. The second objective is to measure channel effects that can degrade the signal. The last objective focuses on the ocean and Arctic environmental research of RQ1.1, building on the observational pyramid in Figure 1.1. It includes both the Arctic communication mission to retrieve scientific data from sensor nodes (defined in Paper B) and sending Earth Observation (EO) satellite data to robotic agents for ocean monitoring (further explored in Paper D).

The selected communication payload is based on the SDR survey in Paper A and its update in Paper B. The same payload, TOTEM SDR, is selected to be on HYPSO-2 and is integrated into the HYPSO software framework. An SDR lab testbed is built to test radio applications in a realistic scenario. A USRP-2901 SDR transmits simulated interference and the TOTEM payload measures it with the developed application (further explained in Paper F). This SDR setup is integrated into the HYPSO hardware-in-the-loop framework with the optical payloads of HYPSO-2 and the ground station system. It enables thorough testing of the radio applications.

Two radio applications were implemented for the SDR payload and tested in the SDR hardware-in-the-loop testbed. The first application was also uploaded to the LUME-1 satellite and uses the LME algorithm to estimate time-frequency characteristics of in-orbit interference (Paper F). The second radio application measures the time variability of the interference. It obtains a distribution of how often and how long time windows have lower interference power. These windows are candidates for transmission.

The main advantage of using an SDR as the communication payload is its flexibility. The communication missions do not need to be fully defined before launch and other missions can be designed after launch if they adhere to the constraints of the system.

3.2.4 Paper D. A Satellite-USV System for Persistent Observation of Mesoscale Oceanographic Phenomena

In this article, a system integrating small satellites and robotic agents for oceanographic observations is proposed and analysed. Three different architectures are evaluated to address RQ1.1.

In scenario 1, data from existing EO satellites is retrieved by the Coordinated Mission Control Centre (CMCC). The data is processed on the ground to detect phenomena that should be investigated by robotic assets. If a relevant phenomenon is detected, the CMCC creates a navigation plan and sends it to the USV. This scenario was tested in 2021 and the images were obtained from four EO satellites. The delay between a satellite observation and the reception of the navigational plan by the USV is 3 to 24 h.

In scenario 2, there is a dedicated satellite for ocean monitoring, like HYPSO, that observes a specified area. The images acquired are processed on board the satellite, interesting phenomena are detected and sent to the CMCC using Ground Stations (GSs). The CMCC sends a navigation plan for the USV. The delay between a satellite observation and the CMCC receiving the data is simulated for a sparse GS network (one GS in Svalbard) and a dense one (six GS). For the sparse case, the mean delay is about 30 min (worst case). For the dense case, it is less than 16 min.

In scenario 3, the dedicated satellite performs an observation, processes the data, and sends the USV a navigation plan. Assuming the USV is in the vicinity of the Area of Interest (AOI), the observation and the processing time will be the main contribution to the time delay. Simulations for all target areas are carried out to analyse the feasibility of the communication architecture. Considering the operations planned for HYPSO-1, the total delay is less than 3 minutes.

The appropriate architecture variant depends on the mission goal and requirements. Scenario 1 is currently available but does not enable a flexible definition of AOI or real-time monitoring. Scenario 2 allows control of monitoring areas, but to reduce delays the last scenario is needed. Scenario 3 requires robust communication between satellites and robotic agents, and more on-board processing capabilities.

3.2.5 Paper E. Detection of radio interference in the UHF amateur radio band with the Serpens satellite

In this article, the UHF amateur radio band for satellite communication is investigated, addressing RQ2.1 and RQ2.2. In-orbit interference measurements from the Serpens satellite in the 435–438 MHz band are analysed.

In 2015-2016, University of Vigo (UVigo) experienced similar communication problems to University of Würzburg and Technische Universität Berlin (TU Berlin) when testing Machine to Machine (M2M) communication. Thus, an algorithm to measure sustained interference was applied on Serpens. A 24 ms long sliding window was applied to the Received Signal Strength Indicator (RSSI) samples measured by four transceivers at different frequencies. The minimum of each window is calculated and the maximum of all minima over a 2 s measurement represents the sustained interference power analysed.

The heat maps of sustained interference show high power over the east and west coasts of North America and central Europe. The highest power measured is -70 dBm, which is 10–21 dB higher than the expected desired signal. The power distribution over non-populated areas (noise floor) is very similar to the distribution over South America, where the maximum sustained interference power is -107 dBm.

The sustained interference power measured over Europe, Africa, and the Middle East is divided into four geographical regions. The power distribution in the northern regions has higher power than the noise floor. The measurements over North America are divided into six regions. More power is received in the northern regions than the southern ones. The dependability of the power measured in one carrier with respect to another is also analysed. Most of the interference has at least 200 kHz bandwidth. Some points indicate that the interference levels vary with frequency over a 1.2 MHz bandwidth.

Some measurements show the variation of the sustained interference expected from ground radars. These high-power radars can be the cause of the interference. These measurements complement [48], [60], [61]. To mitigate the impact, effective counter-measures are needed. Collaborating with ground stations in the southern hemisphere can be another solution.

3.2.6 Paper F. In-Orbit Measurements and Analysis of Radio Interference in the UHF Amateur Radio Band from the LUME-1 Satellite

This work continues the interference measurements of Paper E with a different satellite (LUME-1) and algorithm (LME), but the same band (centered at 435 MHz) and RQs. Due to the orbit of LUME-1, measurements in the polar areas are possible, overcoming the limitations of Serpens.

Since the satellite has an on-board SDR, new software designed within the satellite's constraints can be uplinked. The algorithm uses a Discrete Fourier Transform (DFT) on the received In-Phase and Quadrature (IQ) samples and measures its average envelope spectrum, average power spectrum, and the variability of the LME for different time windows. To validate the software on the ground, the results of theoretical analysis, simulations, and hardware-in-the-loop testing are compared and show consistency. The testing signals are Additive White Gaussian Noise (AWGN), Continuous Wave (CW), pulses and chirps. The author built a hardware-in-the-loop setup in the lab with the same SDR as in the satellite. This is the setup integrated in the HYPSO framework in Paper C.

A total of 300 measurements were executed over the world. The measurements over non-populated areas are used as a relative noise floor. Both the frequency and temporal behaviour are similar to the results of AWGN, justifying the use of heat maps in these areas. Over populated areas, the average interference power is higher. Pulsed interference with a bandwidth of approximately 300 kHz is detected over regions where there are known type A ground radars. This bandwidth matches the chirp bandwidth used for the search mode of these radars (100–350 kHz). In addition, wideband pulsed interference with time structure is measured over Europe. In this case, the bandwidth cannot be estimated. The first-order window of stationarity estimated for the 434.75–434.83 MHz band is 14 ms for most regions and cases. In the 434.83–435.19 MHz band, windows longer than 27 ms are estimated for some areas in the Arctic, America, and Europe.

The results give an indication of the time and frequency variability in different regions of the world, including the poles. However, more measurements are needed to provide reliable statistics over more areas and time scales.

3.2.7 Paper G. In-orbit Interference Measurements and Analysis in the VDES-band with the NorSat-2 Satellite

This manuscript focuses on the uplink interference of an emerging Arctic satellite communication system, VDE-SAT. The results of a preliminary interference measurement campaign in the lower leg of VDE-SAT (157.2875–157.3375 MHz) using NorSat-2 are analysed to address RQ2.2.

The capabilities and constraints of NorSat-2 are less limiting than for LUME-1, but the measurements are also performed without transmitting. The spacecraft bus is bigger, has a different SDR on board, and higher data throughput. Thus, raw IQ samples can be downlinked and processed on the ground. Two different processing algorithms are applied to the data: the LME developed for LUME-1 and a pulse detection method.

Ten measurements tracks with the satellite's antenna pointing towards the horizon above Bjørnøya were recorded in May 2021. The instantaneous power received on board the satellite reaches -70 dBm and its distribution is similar for all tracks. The LME method is applied to one-second segments using a different number of frequency bins for the DFT to analyse time variability. The coefficient of variation is higher than for AWGN within the bandwidth studied and higher for shorter DFTs. It indicates that there is a high time variability within one second and even within 15 ms. The measurements tracks are divided into regions to compare the average power (over one second) distribution. The difference between the lowest interference region and the highest is about 20 dB. The length of the first-order stationarity window of most measurements is longer than 122 ms, except for the low interference region which is 0.95 ms. Using the pulse detection algorithm on the IQ samples, a pulse length of 1.6 ms and different pulse periods (13, 26, 41, and 52 ms) are detected.

High power pulsed interference causes bit errors and can cause loss of packets, reducing the performance of the VDE-SAT system. Thus, interference mitigation techniques and appropriate configuration of the communication system would improve its performance. Longer measurement campaigns are needed to obtain more statistics and define larger regions to use different waveforms and error correction codes.

4 Conclusions and future work

In this chapter, the conclusions of the thesis are summarised, the research questions are addressed and future work is described.

4.1 Conclusions

In this thesis, we show that in-orbit measurements of radio interference using Software-Defined Radios (SDRs) on board small satellites are useful to characterise the interference in the uplink for Low Earth Orbit (LEO) satellites. Radio interference has been detected in both the UHF amateur radio band and the VHF Data Exchange (VDE)-SAT band. Future satellite missions can avoid interference by selecting a different frequency band. Keeping the same band, interference effects can be mitigated by using protocols that allow for retransmissions, protecting the packet header, adding error correction codes and interleavers. The packet header can be protected by making it long enough and using appropriate error corrections codes. The specific design of these codes and the interleavers depend on the interference length, period, and duty cycle. This thesis makes initial steps in defining and performing interference measurements needed for the countermeasure design in satellite communication systems.

SDR platforms enable in-flight updates of measurement software to modify parameters and functionality. Algorithms for limited platforms provide a richer characterisation of the time and frequency behaviour of the interference, complementing existing measurements [48], [60], [61]. More measurements are necessary to provide reliable statistics over a larger period of time in the different frequency bands and for more locations.

New measurements will help to progress further in the design of new robust

communication systems for ocean observation and Arctic monitoring. In this work, we define a flexible communication mission for radio environment research and for a two-way communication system between sensors in remote locations and a small satellite, HYPer-spectral Smallsat for Ocean observation (HYPSO)-2. The sensors will help monitor the ocean and the Arctic for environmental research. Furthermore, the author designed and integrated an SDR payload for the HYPSO-2 satellite for the flexible communication mission. A hardware-in-the-loop setup was built and is ready to be used in further development and testing.

RQ1.1. *How can we define a flexible communication satellite mission and architectures for ocean and Arctic environmental research?*

Small satellites can be part of a heterogeneous network of assets for ocean observation at different spatio-temporal scales. A robust communication infrastructure to relay data from satellite observations to robotic agents in or on the ocean for rapid response is not currently available. This application is explored in this thesis (Paper D). Three different system architectures for forwarding Earth Observation (EO) data from satellites to autonomous agents are proposed using HYPSO-1 and an Unmanned Surface Vehicle (USV) as assets. The communication delay varies from a couple of minutes to 24 h depending on the architecture used. Depending on the level of integration between robotic agents and satellites, the exact application targeted and the delay tolerated, one alternative would be better than the others.

Furthermore, operational communication systems in the Arctic that enable moderate data retrieval from low-powered sensor nodes, such as the ones deployed by the Arctic ABC project, are limited. A small satellite mission to target the lack of communication systems has been defined in this work (Paper B). Frequency monitoring and channel measurements from small satellites in LEO are necessary to design new communication systems and improve existing ones [15]. A survey of possible SDRs platforms for space applications is performed (Paper A). The author defined a flexible communication mission that encompasses the above-mentioned applications and designed an SDR payload to fulfill the missions (Paper B and C).

RQ2.1. *How can the time and frequency characteristics of radio interference be measured from a small satellite with limited resources?*

We have explored two algorithms to measure interference on constrained platforms. The first one, the sustained interference algorithm, measures the sustained interference over a 24 ms window and is run on Serpens (Paper E) for four frequency carriers. The main contribution of analysing data with the sustained interference method is the identification of regions where there is high-power interference. The main limitation is that it only detects high-power interference that lasts for at least 24 ms and not shorter. Also, the method did not measure a full frequency band, but rather four individual frequencies. Hence, important temporal and frequency information is lost.

The second algorithm, the Local Mean Envelope (LME), measures the variability of the local mean to analyse the time-frequency characteristics and was used in the LUME-1 satellite (Paper F). The LME method provides spectrum measurements at the same time as time variability measures so that interference can be characterised in both domains. Three types of time behaviours can be distinguished using the LME: Additive White Gaussian Noise (AWGN), Continuous Wave (CW) and pulsed. Furthermore, the settings of the algorithm can be modified to increase the time or frequency resolution, especially if the satellite data throughput is larger than for LUME-1. The design and implementation of the LME algorithm is an important contribution because it can be used in any satellite platform, but especially in those with limited data throughput. The main limitations are set by the configuration used that constrains the time and frequency resolution.

RQ2.2. *How is the uplink interference environment for small satellites in Low Earth Orbit (LEO) in relevant communication bands in VHF and UHF?*

The main contribution is the analysis of the measurement data from Serpens and LUME-1. Strong uplink interference is detected over Europe, the coasts of North America, and the Arctic. The data explains the difficulties

encountered in satellite operations over Berlin [48], Würzburg (Germany) [60] and Vigo (Spain) [61]. Band-limited pulsed interference is detected in the 435 MHz band with LUME-1, in areas where known type-A ground radars are present, supporting the cause suggested with the Serpens measurements. The bandwidth measured was 300 kHz, which is consistent with the chirp bandwidth of these radars in search mode. Furthermore, high power pulsed wide-band interference was observed over Europe. Over the South Pacific and South Atlantic, the time behaviour of the signals measured was similar to AWGN.

To analyse the performance of the VDE-SAT system in terms of uplink interference over the Arctic region, measurements were performed on board the NorSat-2 satellite. The frequency band studied is the lower leg of VDE-SAT (157.2875–157.3375 MHz). In this case, the processing of the raw data is performed on the ground. High power pulsed interference is detected reaching instantaneous powers of -70 dBm. Pulse characteristics are estimated using a pulse detection algorithm that requires raw In-Phase and Quadrature (IQ) samples and is not suited for satellites with limited resources. The pulse length is about 1.6 ms and the period varies throughout the measurements, but the most common periods are 13, 26, 41, and 52 ms. The VDE-SAT communication system should be able to cope with this type of interference either with a worst-case design or changing settings depending on satellite location.

4.2 Future work

In this thesis, we focus on the investigation of the uplink interference of small satellites in LEO and the analysis of the measurements has been published. It is important to be able to compare interference measurements from different satellites in the same and different bands. Knowledge of the actual usage of the frequency spectrum can be helpful to manage frequency filings and to design and improve communication systems. Moreover, the community should agree on comparable measures to characterise the interference. An open-source repository of interference analysis algorithms that any satellite operator can upload to their satellite can be the first step. It can also be a way of validating algorithms in different platforms and setups and obtaining more

measurements. Additionally, to improve satellite communication systems, the downlink interference and channel degradation should be measured. Some of these measurement activities can continue on HYPSO-2, LUME-1, and NorSat-2.

The integration and testing of the SDR payload on the HYPSO-2 spacecraft needs to be continued until it is ready for launch. This requires finalising all the necessary software for the three missions defined in Paper C: spectrum monitoring, channel measurements, and two-way communication to sensor nodes in the ocean and the Arctic. More measurements will add more knowledge about the environment making it easier to design a robust communication system for sensor applications. The implementation and demonstration of such a system will aid environmental research both in the ocean and in the Arctic.

More measurements can be performed on LUME-1 to extend the work of this thesis. Global measurements during a full day to cover more areas of the world should be planned. To keep the data output of the software limited, the time and frequency resolution should be reduced by changing the configuration parameters. To facilitate the comparison of LUME-1 data with Serpens data, and to have absolute power units, power calibration campaigns are needed. These can be performed by transmitting known signals from a ground station and using the LME algorithm on the satellite at the same time. All the measurements that have been carried out in this thesis and those suggested here can be repeated with different carrier frequencies, such as the operating frequency for LUME-1 (437 MHz). Furthermore, the second radio application, briefly described in Paper C (developed in a master thesis co-supervised by the author [92]) can be tested on LUME-1. Radio measurements with this software will improve the knowledge of the time variability of the interference, within the constraints of LUME-1, and complement the measurements already performed.

For the interference in the VDE-SAT band, more measurements are needed over the Arctic and new measurements over the Antarctic. Measurements with the same configuration should be performed in the Arctic to observe a larger time scale than the two days analysed in this thesis. Antarctic measurements can be used as calibration of the noise floor, as it was done with LUME-1 in Paper F. Additionally, measurements with higher bandwidth are encouraged to investigate the interference bandwidth and

analyse the pulse characteristics in a wider frequency range. Moreover, the measurements can be performed with a different type of antenna pointing to characterise the interference in different directions. Finally, since the data collected with NorSat-2 are raw IQ samples, there are other algorithms that can characterise the interference better, both in time and frequency, such as the short-time Fourier transform, the Wigner-Ville distribution, and the S-method [93].

Part II

Publications on mission design

A Software-Defined Radios in Satellite Communication

The text of the following paper is added as a chapter and re-formatted for better readability:

G. Quintana-Díaz and R. Birkeland, 'Software-defined radios in satellite communications,' in *Small Satellites, System & Services Symposium (4S)*, 2018

Abstract A Software-Defined Radio (SDR) is a flexible technology that enables the design of adaptive communications systems. A generic hardware design can be used to address different communication needs, such as changing frequencies, modulation schemes and data rates. Applied to small satellites, some of the implications are increased data throughput when down-linking or up-linking by varying communications parameters and making use of one hardware design and implementation for communicating for many missions, just by updating the software. Therefore, development time for small satellite communication systems can be reduced in the future. This one of the reason why many universities and other organisations around the world are investing in this type of space technology. The technology can support different kinds of applications, such as Earth observation and communication services. This paper analyses various hardware and software platforms and includes a survey on SDRs that have been designed and developed for satellite communications in the last years. In the survey both ground stations and satellites using SDR have been included. Furthermore, a short discussion on SDR designs have been included.

A.1 Introduction

The interest in small satellites (or SmallSats) is continuously growing, both in CubeSats and other customised platforms. Many universities and other organisations around the world are investing in this type of space technology for various applications, such as space exploration and Earth observation. When observing our planet there are two especially relevant areas to focus on: oceans, as 71 % of the Earth is water [5], and Arctic monitoring, because of the dramatic effect of global warming. In-situ monitoring of these extremely harsh areas is difficult, expensive and they are not fully covered by communication systems [6]. This is one reason why it is important to research new solutions in order to improve ocean and Arctic monitoring. One possibility is to deploy a coordinated infrastructure composed of different types of vehicles and platforms, such as Autonomous Underwater Vehicles (AUVs), Unmanned Aerial Vehicles (UAVs) and small satellites [6].

The Norwegian University of Science and Technology (NTNU) together with the Center for Autonomous Marine Operations and Systems (NTNU-AMOS) have recently launched a new research programme. It has a concerted and unified cross-disciplinary focus on designing, building and operating small satellites (or SmallSats) as parts of a system of autonomous robots and agents for maritime sensing, surveillance and communication. These activities should contribute to fundamental and interdisciplinary research on autonomous systems in marine applications. The programme is associated with the Faculty for Information Technology and Electrical Engineering's strategic research area Coastal and Arctic Maritime Operations and Surveillance (CAMOS) and has planned two missions. The first is to acquire high quality images for oceanographic studies using a Hyperspectral Imager (HSI) and the second one to provide Arctic researchers with easier and faster access to scientific data by using a flexible communications system.

One important aspect to consider when building any type of satellites is communications. Communication systems enable data transfer between sensor systems, satellites and end users. Most kinds of communications systems are designed for worst-case scenarios, and satellite channel characteristics are highly variable due to atmospheric and ionospheric effects, especially in Low Earth Orbits (LEO). Designing for worst-case leaves an expensive and overly designed system that does not maximise channel capacity. To

compensate for this, there is a need to develop enhanced communications systems that can adapt to variable characteristics, for instance changing modulation, power levels or carrier frequency on-the-fly.

SDR is a flexible technology which enables the design of an adaptive communications system. This means that a generic hardware design can be used to address different communication needs, with varying frequencies, modulation schemes and data rates [95]. Applying this concept to small satellites can increase data throughput, add the possibility to perform software updates over-the-air and make it possible to reuse the hardware platform for multiple missions with different requirements [96]. Therefore, development time for future small satellite communication systems can be reduced, even though the development time of the first implementation might be longer than for a traditional radio system.

However, this idea of launching SDR into space is not new. There are many universities, agencies and companies that are currently addressing this issue and some have already launched their own designs. Various SDR platforms and designs are analysed for use in small satellites in challenging scenarios, data retrieval from diverse Arctic sensors or multi-agent communications, for instance. This paper also studies the state-of-the-art of SDR both for spacecraft and ground stations developed by different universities and organisations.

A.2 Available hardware platforms

In addition to requirements for frequency, bandwidth and regulations found in every communication system, SDRs are highly dependent on the hardware platform used to run the software. In small satellites, the main design drivers are size, mass, cost and power consumption.

In Figure A.1 an overview of some SDRs platforms is shown. The vertical axis is *cost* whereas the horizontal axis is *mass*. These are two important aspects to consider when choosing a radio suitable for a small satellite mission. Ideally, the best platform would be the one on the lower left corner of the graph: an inexpensive and light solution. In our comparison,

GomSpace SDRs is the most expensive, and it has an average mass. However, it is also the only space-qualified hardware platform. While decreasing the cost, the next platforms is the different EPIQ and USRP models. The inexpensive platforms, with a cost of less than 300 €, are the ones from FunCube, Lime and RTL. All with average to low mass.

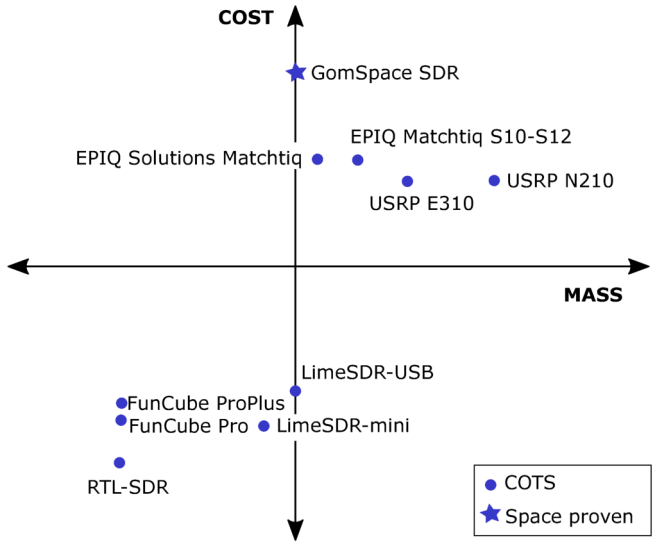

Figure A.1: SDR platform overview (cost vs mass).

Each of the platforms are described briefly below.

A.2.1 GomSpace SDR

The SDR system is built by combining three standalone components: GomSpace NanoCom TR-600 (transceiver), NanoMind Z-7000 (processor/Field-Programmable Gate Array (FPGA)-unit) and the NanoDock SDR [16]. There is shielding added to the components and the size of the system is 22 x 16 x 5 mm. The RF capabilities are provided by the AD9361 transceiver that deals with the phase (I) and quadrature (Q) samples. Xilinx Zync 7030 System on Chip (SoC), which includes dual core ARM Cortex A9 processors and FPGA logic, performs the processing. However, there is no possibility of using GNURadio to program the transceiver at this moment. The noise figure of the NanoCom TR-600 receiver ranges from 5.1-7.8 dB and the

power consumption is 3 W (idle).

Technical characteristics of AD9361 [80] are shown in Table A.1. The frequency range of this component is what limits the GomSpace SDR to 70 MHz - 6 GHz. In addition, AD9361 has two channels for Unmanned Aerial Vehicle (MIMO) and supports Time Division Duplex (TDD) and Frequency Division Duplex (FDD).

Features	**AD9361**
Transmitter frequency band	47-70 MHz
Receiver frequency band	70 MHz - 6 GHz
Channel bandwidth	200 KHz- 56 MHz
Noise figure	2 dB at 800 MHz LO
Operation modes	TDD and FDD

Table A.1: AD9361 technical characteristics

A.2.2 USRP from Ettus Research

USRP E310 is part of the Embedded Series platform, which uses an OpenEmbedded framework and can be programmed with GNURadio [18]. The transceiver is also AD9361 and the processing unit is the Xilinx Zynq 7020 SoC (including dual core ARM Cortex A9 processors and a FPGA). The size of this SDR is 133 x 68 x 26.4 mm. The noise figure of the overall receiver is 8 dB and power consumption ranges from 2-6 W.

USRP N210 from Networked Series has a higher performance, as the Analogue to Digital Converters (ADCs) and Digital to Analogue Converter (DAC) have higher resolution and sample frequency, at the expense of increasing its mass and size (220 x 160 x 50 mm) [22]. It can also be programmed using GNURadio. The RF frontend consists of a daughterboard, and the processing unit is based on a Xilinx Spartan3-DSP. The frequency range is from DC to 6 GHz and the receiver has a noise figure of typically 5 dB.

A.2.3 EPIQ

EPIQ Solutions Matchstiq has a few SDR models, namely the S10-S12, with similar cost and characteristics as the USRPs [82]. It uses Xilinx Zynq 7020 SoC and the same transceiver as most of the SDRs, the AD9361, so it has same RF capabilities. The noise figure of the receiver is also 8 dB. Moreover, the size is 112 x 50.8 x 36.3 mm and the power consumption 2-6 W.

A.2.4 Lime microsystems

Lime microsystems offers two transceiver chips similar to Analog Devices one, the LMS6002D and LMS7002M. In Table A.2 both transceivers are compared.

Features	LMS6002D	LMS7002M
Transmitter frequency band	47-70 MHz	30 MHz-3.8 GHz
Receiver frequency band	70 MHz-6 GHz	30 MHz-3.8 GHz
Channel bandwidth	0-28 MHz	Up to 48[1], 96[2], 160 MHz[3]
Noise figure	3.5-10 dB	2-3.5 dB
Operation modes	TDD and FDD	TDD and FDD

[1] Through digital interface (MIMO). [2] Through digital interface (SISO).
[3] Through analogue interface.

Table A.2: Lime microsystems transceivers technical characteristics

LimeSDR-USB has a smaller frequency band than the previous mentioned SDRs, from 0.1 MHz to 3.8 GHz, and a maximum bandwidth of 61.44 MHz [97]. It uses an Altera Cyclone IV EP4CE40F23C8N and LMS7002M transceiver chip (noise figure of 2-3.5 dB). The size is 60 x 100 mm. In addition, it can be programmed using GNURadio framework. Compared to the USRP embedded series and the Matchstiqs, this radio does not come with an integrated processor.

LimeSDR-mini is similar, also programmable with GNURadio, but has fewer features [20]. The frequency range is from 0.01 MHz to 3.5 GHz and the maximum bandwidth is 30.72 MHz. The RF transceiver is the same chip but the FPGA is Altera MAX 10 (10M16SAU169C8G). The main advantage is that is smaller, 69 x 31.4 mm and inexpensive.

A.2.5 FunCube

FunCube Pro is a very small SDR which uses a Silicon tuner as RF frontend and a PIC24FJ32 GB002 as microprocessor. The transmitter frequency range is from 0.64 MHz-1.1 GHz, whereas from receiving is from 1.27 - 1.7 GHz.

FunCube ProPlus is a similar SDR. It covers from 150 KHz-240 MHz and from 420 MHz to 1.9 GHz and has a maximum bandwidth of 56 MHz. Both FunCube models where made to support HAM radio satellite missions.

A.2.6 RTL SDR

RTL SDR is also a very small SDR, limited to receiving only. The frequency band covered is from 0.5 MHz to 1.766 GHz, with a maximum channel bandwidth of 2.4 MHz. It consists of a Rafael Micro R820T chip, a transceiver chip with 3.5 dB noise figure, and a digital modulator.

A.2.7 Others

There are many other SDRs available. BladeRF uses an Altera Cyclone IV and LMS6002D transceiver [78] and HackRF One uses an NXP microcontroller MAX2837 transceiver [21], both programmable using GNURadio. SWIFT has several SDR models with ongoing small satellites designs [74] such as SWIFT-UTX, SWIFT-SLX, SWIFT-WRX. Finally, AstroSDR [19] is a Space Plug-and-Play CubeSat SDR which uses Xilinx Zynq Z-7045 and

the AD9362 transceiver, and therefore covers similar bands, and has a power consumption of 4-40 W.

In Figure A.2 maximum channel bandwidth of the platforms mentioned above is plotted against frequency in a qualitative way. As it can be seen most of the SDRs work in many bands.

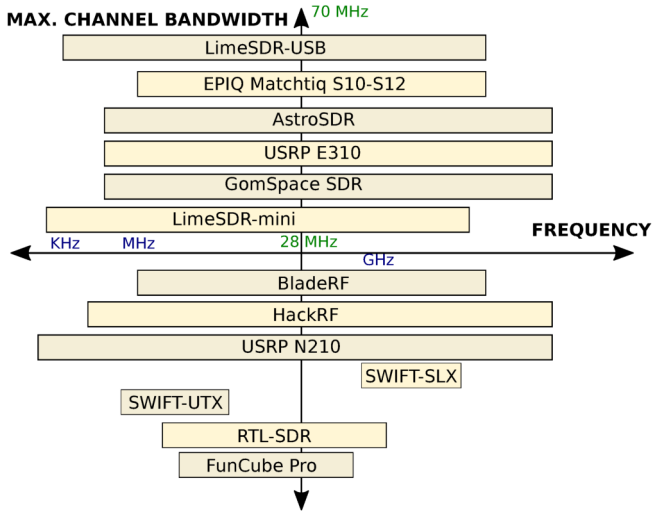

Figure A.2: Maximum channel bandwidth vs frequencies covered in SDR platforms.

Another aspect to be considered when choosing an SDR is the software development tools. Some platforms are GNURadio compatible, like the USRP, Lime SDR, FUNCube, HackRF and others. This gives the users and developer access to a well-know open source ecosystem to base the software development on. This can be used both for ground stations and for the space segment. The USRPs also support the National Instruments LabView, thus a LabVIEW interface could be used to program them. However, due to the need for extra hardware and software to run LabView, this interface can reduce the development time but it can only be used in the ground station. One alternative would be to develop programs from scratch, for example in C for the microcontroller, or VHDL/Verilog for the FPGA. The programming language required for the SDR platform is definitely a factor to take into account.

A.3 SDR survey

This section showcases a survey of SDRs that all have been designed and developed for satellite communications over the last years. We present an analysis of various hardware and software platforms. In the survey both ground stations and satellites using SDR are included.

A.3.1 Space Segment

The Aerospace Corporation and the University of Michigan-Flint have described a SDR design for their pipeline of small satellites, the Aerocubes [98]. The purpose of using this flexible technology was to increase the data throughput by using Adaptive Coding and Modulation (ACM) technique and changing the error encoding characteristics and modulation depending on the channel variation. Simulations were carried out for a typical AeroCube pass over a ground station. By changing modulation (BPSK, QPSK, 16APSK, 32APSK) and code rates (from 1/4 to no encoding at all) without modifying the symbol rate, the throughput was increased by a factor of two if compared to QPSK at 1/2-rate coding. Looking at the SDR design, they adapted the firmware from an earlier SDR implementation and used a Zynq7020 board as the processing unit. The LMS6002D transceiver was used as RF frontend. The carrier frequency of the first generation design is 914 MHz (1 MHz of bandwidth), whilst the second generation transceiver will work on 26.1 GHz. The power consumption is 1.2 W when receiving and 2.5 W when transmitting 30 dBm.

Istanbul Technical University has also contributed to the development of space SDRs using Components Off-The-Shelf (COTS). In [99] two SDRs are described: one for the ground station and one for a CubeSat. The SDR for space is half-duplex and it is implemented in three boards: the transmitter, the receiver and a FPGA board, containing an Altera EP3C25E144I7N. It uses UHF Industrial Scientific and Medical (ISM) band, 433.92 MHz, and a 2FSK modulation. In addition, the power consumption is quite low; 2 W when transmitting and 0.7 W when receiving. The ground station SDR used two USRPs, a computer, one Low Noise Amplifier (LNA)

and a power amplifier. Even though their project was carried out by undergraduate students, components for the CubeSat SDR were tested under space conditions. This small satellite is called HavelSat [100] and was launched in April 2017 [101].

University of Vigo in Spain and University of Porto [102] have been working for several years in the HumSat project, supported by the United Nations office for outer space affairs (UNOOSA), the European Space Agency (ESA) and the International Astronautical Federation (IAF). This project is a collaboration between multiple universities and centres, and its objectives are: to develop a data communications system for areas where there is not enough infrastructure for humanitarian purposes and to have sensors in remote areas. The SDR is a transmitter built on a board with a RF stage, a control stage and a power stage. The frequency ranges used from 440-470 MHz, with GMSK modulation and the power consumption when transmitting 30 dBm is 3.2 W. In stand-by mode the power consumption is 0.14 W. The first version of this SDR was launched in 2013 in a 1 unit CubeSat, called Xatcobeo. The next version is planned to be launched in December 2018.

Applied Physics Laboratory from Johns Hopkins University has built a TRL-9 SDR which has flown in the Van Allen Probes mission from NASA (National Aeronautics and Space Administration) with an S-band configuration (an X-band and Ka-band link can be possible too) [103], [104]. This SDR, called Frontier Radio, enables the possibility of changing to multiple modulation schemes, such as, BPSK, QPSK, PM/subcarrier for reception and up to 64PSK and 16QAM for transmission. Frontier radio is and FPGA-based design that uses RTAX4000 for the processing part and has different exciter slices depending on the frequency band used.

NASA has a huge interest in pushing SDR technology forward. Their objective is that an SDR may provide a flexible transceiver platform that can be tailored to several missions, just by changing software or hardware logic [95]. This is one of the reasons that can explain why there are several student satellites in the Educational Launch of Nanosatellites (ELaNa)

programme planning to launch SDRs. For instance, LinkSat from Buffalo University; Space Hauc from University of Massachusetts; STF1 from West Virginia University and other member of a consortium; VCC A, B, C from Old Dominion University, Virginia Tech and University of Virginia; and OPEN from University of North Dakota. In addition, in 2012 NASA launched a Space Communications and Navigation (SCAN) testbed to provide with an on-orbit SDR facility. Earlier than same year, NASA published a paper which describes three different SDR developments for CoNNeCT (Communications, Navigation, and Networking reConfigurable Testbed) project [105]. In the first two cases the waveform and platform provider were General Dynamics and Harris. In the last case, JPL (Jet Propulsion Laboratory) and Cinnati Electronics developed the platform. Regarding frequency bands, Harris SDR was Ka-band and GD and JPL developed an S-band SDR. All of them using at least one Xilinx Virtex FPGA for the processing section and some radiofrequency (RF) converters and power amplifier for the RF frontend.

A.3.2 Ground Segment

SDRs are not only being utilised in the space segment, but also as part of ground stations.

University of Bologna built an SDR-based ground station suitable for ESA's European Student Earth Orbiter (ESEO) project [106]. As previously mentioned, SDRs enable the possibility of adding new waveforms by updating the software. Therefore, it is easier to update all ground stations in a network, just by sharing the updated software. In this development, the USRP N210 with an RF daughterboard is used as the SDR platform and the RF frontend. The ground station uses the UHF band, particularly radio-amateur frequencies (437 MHz for downlink and 435.2 MHz for uplink).

University of Surrey has focused on SDRs for concurrent multi-satellite communications. In [107] it has been developed a flexible system that can receive different types of signals of different satellites on a ground station using SDR technology. The transceiver board used is AD-FMCOMMS3-EBZ

and for the processing part a Xilinx Zynq 7020 FPGA to achieve parallel architectures. The frequency band covered is limited by the transceiver, being 70 MHz - 6 GHz.

National Cheng Kung University is another university that has developed an SDR-based ground station to track small satellites [108]. The hardware used includes a ADLink PXI-3710 system controller and receiver blocks are implemented on Matlab/Simulink. Frequency bands considered are amateur VHF (140-150 MHz), UHF (430-440 MHz) and ISM band (2.4 GHz). Several bands can be received at the same time due to the implementation of an interference cancellation approach.

The Norwegian University of Science and Technology is also working on a GENSO-compatible station [109]. In addition to having developed an SDR-based ground station using a USRP2 and NGHam [110].

A.4 Discussion

This study of SDR state-of-the-art comes from the need to use this technology to support several missions at the NTNU Small Satellite programme. In addition to set up a versatile SDR ground station, the main aim is to support science data collecting missions where there is poor communications infrastructure, like in the Arctic. To provide Arctic researchers with easier and faster access to scientific data harvested by sensor nodes, the payload should be flexible, so that physical retrieval of the data from sensors can be less frequent. In order to make better use of the resources available (bit rate, power, link properties, timing and delay, and the amount of data), the payload should be re-configurable and adaptable in-flight. This is where SDR technology comes into play.

The SDR payload is meant to be an experimental system with two purposes: The first is demonstrating re-programming of the SDR in-flight, the second is to demonstrate simple ACM capabilities. Employing ACM, the bit rate and modulation can change within one pass, or at least between passes,

based on the predicted "quality" of the pass. The re-programmable features can comprise a selection of frequency bands, channel bandwidths, bit rates, modulation and power levels. Depending on available frequency bands (for uplink and/or downlink), the payload should support at least two frequency bands; for example VHF or UHF, and L-band or S-band. The SDR alternatives available support two separate RX/TX paths, so each antenna system can be individually mated to one RXTX interface. If more than a frequency bands are required, then filter banks/diplexer must be used.

Three main options considered for the payload design are:

1. Buy and integrate space proven hardware platforms, such as GomSpace SDR.

2. Buy and integrate no-space proven COTS hardware (URSPs, LimeSDR, EPIQ Solution SDRs,...)

3. Make an in-house design and integration of a custom SDR. Based on the AD9361 transceiver chip and an FPGA, for example.

On the one hand, the first option is safe for the mission. However, it is very expensive. Also, buying a complete SDR implies less control of the mission. On the other hand, making a custom design would increase the team's knowledge of SDR and enable full control of the SDR. Most universities in this study have done that, but it is less reliable as the components are not space-qualified and the system has to be developed from scratch. It seems like the second option is the best compromise. A trade-off study will be carried out to help decide which design approach is going to be followed.

Another important aspect is how to design the RF front-end. In order to be able to communicate using multiple bands, both the SDR hardware platform and also the RF front-end must support the bands. More than one antenna will be needed to receive both UHF and S-band. This means that a diplexer is needed between the SDR and the antennas. The SDR platforms usually have an internal LNA, but an additional one may be needed. In this case, there are two possibilities: to use a broadband LNA (designed for both bands) or two different LNAs, one for each band. Using

multiple bands can add complexity and cost to the system but enhances communication (enabling different data rates and providing redundancy, for instance), therefore a trade-off analysis must be made.

Most of the radios presented in Section A.2 can be used as part of a ground station design, as long as it fits the frequency bands of the mission. Since one usually has access to computers at the ground station, the fully embedded solutions (USRP E-series, Matchstiq and HackRF) might not be desirable, as it will be easier to work on a regular computer both during development and operations.

For the space segment, the opposite is true. In this case, both size and power are major concerns. Therefore, highly integrated embedded solutions are preferable. This can point in the direction for the USRP E-series or the Matchstiqs. The Lime SDR could also be used, however it must be integrated with a processor running Linux. These radios can be used in a *hybrid* COTS solution. The processor is included in the USRP E and Matchstiq. It is important that the radio chosen has a good quality, is frequency stable and have good RFI (radio frequency interference) and EMC (ElectroMagnetic Compatibility) properties.

A.5 Conclusion

This survey attempts to give insight into SDRs for small satellites and ground stations. It became clear that it is not an easy task to compare the platforms, because not all of them provide the information needed for a coherent analysis. It is also challenging to find information about university projects and figure out they have launched the satellites described in their papers. Nevertheless, there is no doubt that a lot of research groups have worked on developing space SDRs. There are already a lot of small satellites using this technology for science applications, radio measurements, navigation, communications and technology demonstrators.

Most of the university projects studied seem to use a custom SDR solution based on FPGAs. The Zynq board and the AD9361 transceiver chip from Analog Devices are very commonly used in these implementations. The

transceiver chips from Lime microsystems has also been utilised a few cases. This suggests to conclude that the AD9361 can be used to reduce the risk. The component has been flown in space several times in different SDRs implementations.

Choosing an SDR platform depends on many factors and the risk of component failure is very important to consider. GomSpace SDR seems to be the safest choice. Nevertheless, it is the most expensive one and the team working with would not have so much control over the hardware nor software. The URSPs can be a reasonable choice, especially for the ground station segment. There are no requirements for size or weight, and experience with these platforms are available.

EPIQ Solutions Matchtiq and LimeSDR could also be considered both for the space and ground segments. However the LimeSDR must be integrated with an external processor capable of running Linux. FunCube and RTL-SDRs can be used for the first time because they are inexpensive, but may be limiting the performance of a production system. HackRF and BladeRF are interesting platforms but have not been used in space so far. SWIFT SDRs seem very attractive, but there is no enough information about them available. Finally, AstroSDR is an SDR designed for CubeSat but its power consumption may be too much for a 3 unit (3U) or 6U CubeSat.

The need to develop flexible satellite communications systems, particularly for small satellites, has been described. Different hardware implementations of this technology have been highlighted and their technical characteristics have been explained. In addition, a survey on SDR technology developments by several universities was carried out. Their mission or goal was described, as well as the main components used and the radio parameters of their design. Finally, how to approach an SDR development for NTNU's communications mission was briefly discussed.

B An SDR mission measuring UHF signal propagation and interference between small satellites in LEO and Arctic sensors

The text of the following paper is added as a chapter and re-formatted for better readability:

G. Quintana-Díaz, R. Birkeland, E. Honoré-Livermore and T. Ekman, 'An sdr mission measuring uhf signal propagation and interference between small satellites in leo and arctic sensors,' in *33rd Annual AIAA/USU Conference on Small Satellites*, 2019

Abstract Enabling communication to sensor systems in the Arctic is a challenge due to the harsh climate, limited infrastructure and its remote location. In this paper a communication system for Arctic back-haul serving low-power devices to complement existing services is discussed and two small satellite missions are defined. The communication mission objective is to provide Arctic researchers with faster access to scientific data. However, a precursor mission is needed to gather data about the UHF communication channel and interference in the Arctic to design a reliable communication system between Arctic sensors and LEO (Low Earth Orbit) satellites. An SDR (Software Defined Radio) payload is proposed to fly on a small satellite as a secondary payload in order to carry out the radio measurements in a flexible way. The challenges of being a secondary payload are also outlined.

B.1 Introduction

The areas where global warming effects are most dramatic are the Arctic, Antarctica and the Tibetan Plateau. Monitoring of these places is very important to the World Climate Research Program (WCRP) and International Geosphere-Biosphere Program (IGBP) [3]. The specific use-case addressed in this paper is based on The Arctic ABC programme [111], working on the deployment of sensor nodes in Arctic ice to measure various parameters, such as temperature and light in the water column [30].

However, collecting data from those nodes is challenging as there is not sufficient telecommunication infrastructure in this area [112]. Researchers that make long and expensive expeditions to retrieve their data face the dangers and the cold of this region. Thus, reducing the frequency of their trips, and maintaining or increasing measurement data collection is beneficial. Some satellite service providers can offer a communication service in the Arctic depending on the requirements [113].

An emerging alternative to complement existing data retrieval methods is to deploy a coordinated infrastructure. It can be composed by different types of vehicles and platforms, such as Autonomous Underwater Vehicles (AUVs), Unmanned Aerial Vehicles (UAVs) and small satellites [6].

This paper describes how to approach the design of this Arctic communication system. First, identifying the stakeholders and their needs, defining the problem statement and outlining the current alternatives to collect sensor data in the Arctic. Second, two small satellite missions are defined: the Communication Mission and the Precursor or Measurement Mission. Third, since there may be a flight opportunity for the precursor mission, some mission and design parameters have been adapted to it. The system architecture, the impact of the potential orbit, mass and volume considerations, placement of antenna ad challenges as a secondary payload are described. Finally, a short conclusion is included.

B.2 Identification of stakeholders and needs

The stakeholder analysis is a vital part of developing a mission to ensure that the system satisfies the needs and requirements of the interested parties [114]. The stakeholders for the long-term goal of the Arctic communication system have been identified in Table B.1 and classified as primary or secondary according to their involvement in the project. The stakeholder analysis is updated continuously through the project and is important especially during critical design decisions to maintain a focused system design.

Table B.1: System stakeholders.

Stakeholders	Involvement	Needs
Arctic researchers	Primary	-Need frequency access to scientific data -Affordable service
Sensor equipment	Primary	-Antennas and transceivers that fit in the structure - Low power transceivers
Environment	Primary	-Mechanical structures must be fixed -No solar energy during winter
Suppliers	Primary	Exchange of models and requirements in a simple format. Usually a known, standardized format
Regulatory organizations	Secondary	Compliance

The Arctic researchers are the primary stakeholders in this system because they are the ones who need the data. Furthermore, the Sensor equipment influences the type of system architectures and design parameters such as frequency, data budget, mission and concept of operations (CONOPS) design. The Environment and Regulatory organizations impose the limiting constraints for the system, such as frequency band, operating temperature range, maintenance limitations, etc. Researchers (communication researchers) need to learn about the communication channel to be able to develop a feasible solution and to publish results. The needs of these researchers are the reason why a precursor mission is suggested before the communication mission.

B.3 Problem statement

Communication infrastructure in the Arctic is limited [112]. The harsh climate has a direct impact on system implementation. The equipment must be designed for power efficiency as in the winter there is no sun to charge the batteries with solar power. In addition, the structures must deal with icing of mechanical parts which makes mechanical design challenging.

To achieve high data rate links in satellite communications, it is common to use dishes as high gain antennas. They close the link and achieve high data rates, but they are steered mechanically. Due to this issue, antennas need to be either omnidirectional or steered electrically to track a satellite. Since robust energy efficient high gain antennas are unavailable for sensor nodes in the Arctic, lower frequencies bands such as Very High Frequency (VHF) and Ultra High Frequency (UHF) are desired.

B.4 Current alternatives

The traditional ways of retrieving scientific data are (1) to go on expeditions to physically collect sampled data from the sensors, or (2) to use existing satellite services. Expeditions are costly due to the harsh conditions of the area. There is extreme cold and dangerous local fauna. In these remote areas existing satellites services are also quite expensive and dependent on service providers. Iridium is a satellite service that is commonly used. It has coverage in the poles and offers services to transmit short data messages from monitoring equipment to host computers. Data rates are quite low, energy consumption for the data transmitted has room for improvement and the cost per gigabyte is high. Iridium NEXT is meant to increase the data rate with speeds of 22 Kbps to 1408 Kbps [115] with Iridium Certus. It should be operational in 2019, but there is no publicly available information about the specifications of the transceivers, such as size and power consumption. Low power consumption is an important constraint in this scenario.

The use of a flexible communication system for heterogeneous network

using small satellites and AUVs can complement expeditions and existing satellite services [116]. This solution can be more tailored to the problem using Arctic ABC as a use case. Currently, this Arctic programme uses Iridium Short Burst Data (SBD) messages and an airplane solution [30]. They rent a Dornier DO-228 (Lufttransport AS, Norway) and establish a communication link between the radio of the sensor node and another radio in the aircraft to retrieve large amounts of data. Both alternatives are costly. Data requirements for Arctic sensors are shown in Table B.2.

Table B.2: System stakeholders.

Sensor nodes	Data size per year	Data size per month
AZFP 1	1 GB	83 MB
AZFP 2	2.84 GB	236 MB
Echosounder	100 GB	8,333 MB

B.5 Communication mission

The Communication Mission is described in the following section. It is a mission that fulfills the problem with the architecture described in the previous sections.

A flexible communication mission can be carried out using a Software-Defined Radio (SDR) as payload. Measurement software can be upgraded in-flight after analyzing results to maximize capacity when possible. Communication parameters can also be modified in-flight and Adaptive Coding and Modulation (ACM) may be developed in software. The capability of reprogramming the SDR both for measurements and communication makes it a key component in the design of the mission.

The mission statement is: a space-based SDR system shall provide Arctic researchers easier and faster access to scientific data products. This mission is a technology demonstrator. It will prove concept and system viability by acquiring sensor data where there are harsh environments that induce high operational risk and costs.

Table B.3: Communication mission objectives.

MO-001	Spacecraft shall gather data of different types from ground sensor nodes in the Arctic.
SMO-001	Reduce or eliminate the need of manned expeditions, by enabling access to data from sensors in the Arctic.
SMO-002	Maximize data throughput by using ACM depending on current channel characteristics

Satellite communication using UHF frequencies gives lower data rates than S-band and X-band. In addition, there is a lot of interference in this band due to the growing number of small satellites launched [117]. Thus, to maximize data throughput both the channel and the interference should be measured and characterized.

B.6 Precursor mission

The first part of the mission consists of channel and interference measurements to be analyzed and considered for the design of the communication system. The results obtained will narrow down possible communication parameters (modulation, protocols, ...) to be used.

The second part of the mission will deal with the communication link to the sensor nodes. This operational mode will include a technology demonstration for retrieval of scientific data from sensor nodes in the Arctic.

In Table B.4 user needs for the precursor mission are specified as user requirements. The first three requirements are related to the data products needed to learn about the channel and the interference. The technological demonstration aspect is reflected on SDR-UR-004. The last two requirements come from the Arctic use case, the area of interest and the target frequency bands. Even though the communication mission is focusing on the Arctic, measurement further south, starting from 60 degrees north (southernmost part of Norway), are still relevant. The specific band of 400-440 MHz is selected because: there are bands for Earth Exploration Satellite Service

(EESS) in 401-403 MHz for uplink, a band in 400.15-401 MHz for space research and space operation for downlink, and amateur service within 430-440 MHz [42]. Amateur band can be measured since many small satellites are using for operations and the other bands can potentially be used for the communication mission.

Table B.4: Precursor mission user requirements.

SDR-UR-001	Create spatial-frequency heat maps of radio interference.
SDR-UR-002	Estimate time and frequency statistics of radio interference.
SDR-UR-003	Estimate downlink channel impulse response.
SDR-UR-004	Establish a communication link with a sensor node prototype.
SDR-UR-005	The area of interest is north of 60 degrees north.
SDR-UR-006	The frequency band shall be UHF: 400-440 MHz.

The precursor mission objectives are less ambitious, as the main goal is to learn. The new objectives are described in Table B.5. The first two objectives are purely for measurements and learning, whilst the following two are oriented towards the technology demonstration. In order to test different communication schemes depending on measurement results, SDR-SMO-004 was added.

Table B.5: Precursor mission objectives.

SDR-MO-001	To measure radio interference and perform downlink channel measurements for future communications in the Arctic.
SDR-SMO-001	To measure downlink channel in UHF using sensor node antennas.
SDR-SMO-002	To establish a basic communication link to a sensor node prototype.
SDR-SMO-003	To demonstrate communication in the Arctic.
SDR-SMO-004	The system shall allow for update in flight.

To achieve the first objectives (SDR-MO-001 and SDR-SMO-001), three types of measurements will be performed with the SDR payload. The purpose of these measurements is to understand channel characteristics and interference so that they can be used in future missions. Measurement types are:

- Interference calibration. Reference signals will be transmitted from our ground station to calibrate the measurements for real interference.
- Interference. SDR payload will sense the radio environment for interfering signals.
- Channel measurements. SDR payload will transmit a specific training sequence that when received on ground is used for downlink channel impulse response estimation.
- As stated in Table 5, a secondary objective (SDR-SMO-002 and SDR-SMO-003) is to establish of a communication link between the satellite and a sensor node. The sensor node can be a lab prototype or even a buoy in the Arctic to demonstrate the whole system. An antenna has been designed for the sensor considering the constraints imposed by the Arctic environment. This objective is planned to be tested in future updates of the SDR software.

B.7 Flight opportunity

The HYPer-spectral Smallsat for Ocean observation (HYPSO) mission [83] will be launched in a sun-synchronous polar orbit to observe ocean color along the coast of Norway. Its specific mission is to detect and characterize ocean color features such as algal blooms, phytoplankton, river plumes. etc. The spacecraft will be a 6U CubeSat structure, provided by NanoAvionics LLC. The CubeSat is equipped with a hyperspectral push-broom imaging payload (hereafter called Hyperspectral Imager (HSI)) which has on-board processing capabilities. The volume of the HSI payload, requires a 6U satellite bus, but the HSI payload does not occupy the full space.

The SDR payload can be a part of this CubeSat mission, where the SDR functions as a secondary payload. The SDR can fit in the extra space of the HYPSO mission to "fill in the whole space" and ensure maximum utilization of the launch opportunity. The secondary mission of HYPSO can then be the Precursor Mission.

The established HYPSO mission requirements will be considered constraints and the SDR payload, including the antenna, will be adapted to fit HYPSO. The chosen SDR platform is a design decision from which some of the requirements are derived from. The requirements have been developed through workshops using the software CORE9 from Vitech Corp, VA, USA supporting Model-Based Systems Engineering (MBSE). The requirements have gone through several iterations, with the focus of being lean by limiting the number of requirements and making them usable to the designers. The following gives a short background from the HYPSO mission parameters that influence the SDR mission.

B.7.1 System architecture

The system architecture of the SDR (Figure B.1) mission consists of the ground segment and the space segment.

In the ground segment there will be a ground station network and sensor node prototypes for the future Arctic communication system. The S-band ground station will be used as main Telemetry, Tracking and Command (TT&C) for the HSI, and to downlink interference measurement data. The UHF ground station is a backup for TT&C and it is also used to perform downlink channel measurements and transmit reference signals for calibration. Sensor nodes prototypes for future Arctic communications will be used to do channel measurements for the use case and to demonstrate a communication link.

The space segment is formed by the satellite. The SDR payload will measure both radio interference and communication channel. It will also demonstrate a communication link with sensor nodes prototypes. The S-band communication components will be used for the same as the S-band ground station. The UHF radio and turnstile antenna will be TT&C backup. The SDR payload will use the UHF monopole antenna for the measurements

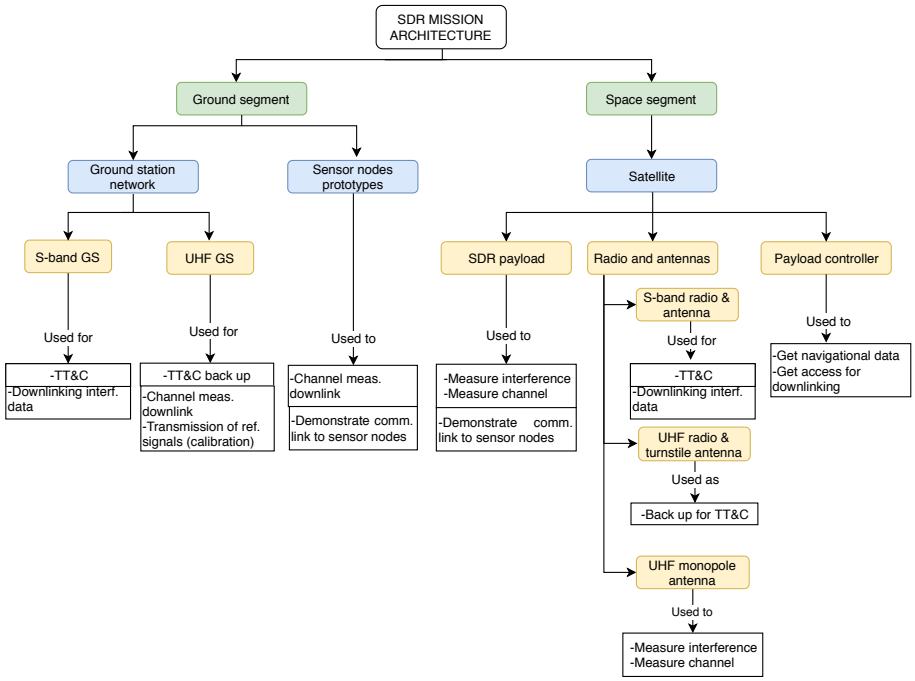

Figure B.1: System architecture.

to avoid interfering with main communications or data link of the spacecraft. The SDR payload must communicate with the payload controller of the satellite bus to downlink data through S-band and get navigational data.

The main constraints for the design of the payload are cost and development time. Schedule constraints are very important in the trade-offs for the secondary mission to be compatible with HYPSO project.

A total of 21 SDR platforms have been analyzed and have been part of a high level assessment in [94]. An extra alternative was found after that study, TOTEM SDR from Alén Space. Power consumption is quite low compared to the alternatives, it includes the Radio-Frequency (RF) front-end and its noise figure is 2 dB. The transceiver chip has only one transmitter and one receiver chain. Nevertheless, as cost is reasonable, and it provides high level of flexibility it was decided that this platform will be the SDR payload of the mission. Since SDR-UR-006 states that the frequency band should be between 400-440 MHz, but the front-end filters have a bandwidth of 10 MHz,

a bypass was included. Signals in this branch (additional RF I/O in the picture) will not pass through the filters and amplifies of the front-end. This was the only solution found to avoid connecting another front-end board.

More detailed characteristics can be found in Table B.6.

Table B.6: TOTEM characteristics..

Extra components required	None.
Interface to CubeSat bus	CAN.
Space readiness	Space proven.
Power consumption	TX: 5.1 W @30 dBm RX: 2 W Idle: 1.4 W.
Dimensions	22.93 x 89.3 x 93.3 mm (PC104).
Shielding	Included.
Mass	150 g.
Frequency range	70-6,000 MHz.
Bandwidth	0.2-56 MHz.
Transceiver	AD9364.
Noise figure	2 dB (front-end).
Processing unit	Based on Zynq-7020 SoC -Dual ARM Cortex-A9 -FPGA
SDR framework	Access to low (VHDL) and high-level programming (C, C++, GNURadio).

In Figure B.2 the architecture of TOTEM platform and how it can be connected to the antenna is shown. This platform is formed by two boards: RF front-end (analogue part) and SDR motherboard (analogue stage, analogue/digital conversion and digital processing). The SDR motherboard consists of an RF transceiver (AD9364) and a System on Chip (SoC) based on Xilinx boards, which has a Zynq 7020.

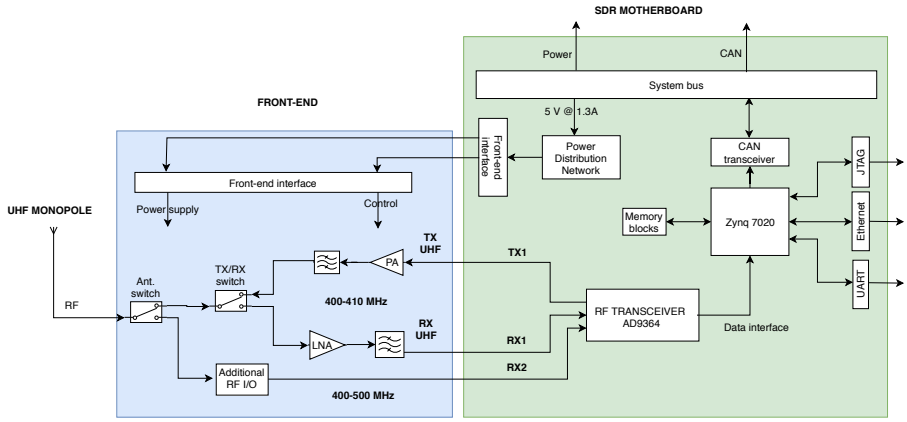

Figure B.2: SDR payload architecture.

B.7.2 Orbit

The orbit in the flight opportunity is the same as for the HYPSO mission. The chosen orbit for HYPSO is a morning Sun-synchronous orbit (SSO) at 500 km altitude because of a preferred observation area on the coast of Mid-Norway, and ground infrastructure in Trondheim and Svalbard. It is expected that the inclination will be 96-98°.

The area of interest of the SDR measurements are north of 60°. Having a polar orbit is the only requirement needed to do so. Given the orbit characteristics above, the satellite will fly over the area of interest 15 min per pass approximately.

B.7.3 Mass/volume

The volume of the spacecraft is 6U, leaving room for the SDR payload in conjunction with the HSI payload. Because the SDR payload radio does not require much mass nor volume, the constraints imposed by the HYPSO mission do not influence the radio module itself. Except for the choice of antenna and antenna placement, described in the next section. The SDR radio has masses that influence the spacecraft's moment of inertia and center of gravity, but the internal configuration and the arrangement of subsystems

within the spacecraft do not influence the mission significantly.

In addition, a mechanical interface for TOTEM is required. The SDR has a PC104 form factor, but due to the placement of the HSI and other components in the bus, the SDR has no available space to be mounted on stacking rings used for PC104. Therefore, an alternative mounting assembly had to be designed. The custom hardware interface (Figure B.3) consists of: mounting plate, base plate as a platform for mounting, cylinder spacers to extend the support from the base plate to the SDR and provide a stable base and a support plate to provide support for the rods and reduce the moment that the SDR may impact on them.

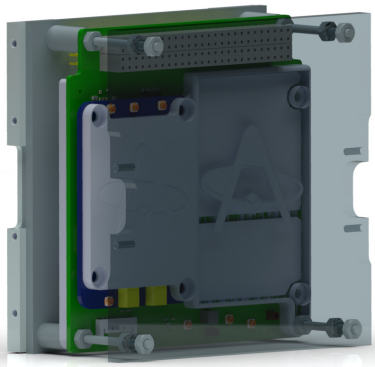

Figure B.3: Mounting assembly for the SDR payload.

The SDR mission designers must work closely to ensure transparent and up-to-date communication with the HYPSO spacecraft designers not to compromise the main mission of the spacecraft. Thus, a mass budget for the secondary payload is required. The payload mass budget of the SDR payload is shown in Table B.7. The UHF monopole antenna is not included in the payload budget as it is included in Nanoavionics satellite bus.

Table B.7: System stakeholders.

Subsystem	Nominal mass (g)	Margin (%)	Mass with margin (g)
SDR front-end (TOTEM)	20	20	24
SDR mother-board (TOTEM)	130	20	156
SDR mounting assembly	299.7	20	359.64
Total (payload)	449.7	20	539.64

B.7.4 Antenna

The HYPSO mission is equipped with two imaging payloads that need a specific Field of View (FOV) to operate. These parameters give the main constraint on the antenna design for the SDR: SDR antenna placement shall not interfere with any of the imaging payloads. The FOV of the HSI is assumed to be $\pm 4.22°$ and the RGB camera has a FOV of $\pm 35°$. The HSI will be placed in the middle of the 2U side of the satellite (3U axis aligned with Earth radius) and the RGB in the middle of one the 1U in the same side.

The satellite bus has three antennas: one S-band patch antenna, one UHF turnstile and one UHF monopole antenna. For channel measurements a turnstile antenna with an omnidirectional pattern would be desired to easily distinguish the effect of the antenna pattern from the channel or interference effects. However, the turnstile antenna in the bus is used for communication during Launch and Early Orbit phase (LEOP) and as a backup for TT&C. Thus, the SDR can only utilize the UHF monopole which may only be deployed if it does not interfere with the FOV of the imagers.

Figure 4 shows a placement of the antenna to get compromise between an omnidirectional antenna pattern and camera FOVs. Assuming a 15 cm monopole, the antenna must be placed so that $\Delta x_1 > 1.1$ cm and $\Delta x_2 > 10.5$ cm, shown in Figure 4. Monopole will be placed 11 cm from the center

of the RGB camera.

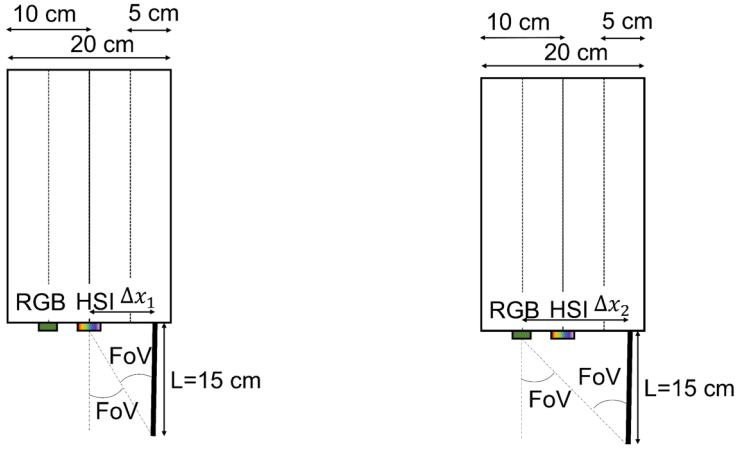

(a) Impact on the HSI.

(b) Impact on the RGB camera.

Figure B.4: Antenna placement.

B.7.5 Challenges as a secondary payload

If a secondary payload is added to the satellite after the satellite bus is selected, this payload must be adapted to the bus. The most important requirement for a secondary payload in this case is to limit the impact on the primary mission. This must be ensured during integration, thermal analysis, system budgets and testing.

Integration of a payload consists of mechanical, electrical and software integration. The secondary payload must be mounted in the satellite bus. A custom mechanical interface may be required to attach it, as has been explained in Section B.7.3. Secondary payload software should be integrated with primary payload to ensure compatibility and consistence. Control software to communicate with the bus and to downlink payload data could be reused from the primary payload if properly adapted to the secondary payload. Software development time can therefore be decreased. In addition, electrical interfaces of the secondary payload must comply with the interfaces of the bus for electrical integration. Thus, the secondary payload can only

use the types of interfaces that the satellite bus can offer, reducing the flexibility of operations.

Thermal analysis must be carried out both for the secondary payload alone and the complete satellite. Turning the payloads on and off during operations will have a high impact in the thermal analysis. The temperature of a component that has no power supply will be very low. The contrast with a payload that is transmitting signals, for example, can be drastic. Thermal simulations should consider all payloads modes.

System budgets must be modified to include another payload. Not only the mass increases in the mass budget, but the center of gravity and moment of inertia are also altered. The power budget is critical since both payloads will consume power. The depth of discharge of batteries should not decrease below the recommended threshold. Thus, idle power consumption may become a problem. In HYPSO a solution that is under consideration is to turn off the secondary payload during primary mission operations. Not being capable of turning off secondary payload after operations or turning it on by accident become new risks to the mission. The data budget is also affected by adding a new payload, since more data must be downlinked. Primary payload data will have priority, and this must be accounted for in secondary mission operations. Furthermore, the pointing budget must be revised. Mapping and pointing errors should be calculated again because they depend on the spacecraft assembly, for example on thermal distortion and mechanical jitter.

Operations should also be updated. The scheduling of operations, automatic generations of commands and telemetry data must accommodate for both payloads. Operations from secondary payload shall not interfere with primary mission. In addition, the Mission Control Centre (MCC) must be modified. Its software must include a new database and new graphical user interface for the secondary payload operations. New frequency filings may be required to control the new payload.

The main mitigation of all risks is for the secondary payload to undergo thorough testing including environmental testing and Electro Magnetic Compatibility (EMC) tests. Furthermore, automatic tests should be run on all software. A proper Assembly Integration and Test (AIT) plan should be developed including two payloads.

B.8 Conclusion

To complement some expeditions and existing satellite services, a coordinated infrastructure with different types of vehicles including small satellites is proposed. The long-term goal is to provide Arctic researchers with easier and faster access to scientific data.

Through systematic stakeholder analysis needs and requirements for an SDR-based communication system are established. Following this, a Communication Mission aiming to fill the gap in the Arctic is described and a Precursor Mission is required to learn more about the communication channel.

A flight opportunity in HYPSO may be granted to the Precursor Mission to characterize the UHF satellite channel and interference to enable the design of the Arctic communication system. This is the first step to improve data retrieval for Arctic researchers. The SDR-based communication system can act as a secondary mission to the main HSI mission, and the mission design must be adapted accordingly. HYPSO mission parameters and the interactions with the SDR have been outlined. It is very challenging to add a secondary payload in a mission, especially if it is not included from the start. The secondary payload may impact the success of the primary mission, thus more work must be carried out if the SDR payload flies on HYPSO.

Future work will include a full system design breakdown of the SDR secondary mission, development of the software needed for performing measurements, verification and validation activities, and AIT activities to integrate the SDR platform with the satellite bus. It is assumed that there will be more user requirements added as the prototype is being developed, in close collaboration with the Arctic ABC project.

Acknowledgements This work is supported by the Norwegian Research Council (Grant No. 270959), the Norwegian Space Center, and the Centre of Autonomous Marine Operations and Systems (NTNU AMOS). The authors want to thank Henrik Galtung, Tuan Tran and Tord Hansen Kaasa for the design of the SDR mechanical interface.

C Development of a multi-purpose SDR payload for the HYPSO-2 satellite

The text of the following paper is added as a chapter and re-formatted for better readability:

R. Birkeland, G. Quintana-Díaz, E. Honoré-Livermore, T. Ekman, F. A. Agelet and T. A. Johansen, 'Development of a multi-purpose SDR payload for the HYPSO-2 satellite,' in *IEEE Aerospace Conference [accepted]*, 2022

Abstract Recent developments in flexible Software Defined Radio (SDR) platforms provide researchers with a framework for small satellite missions that combine several parallel objectives. A part of the mission for the HYPer-spectral Smallsat for ocean Observation (HYPSO-2) satellite from the Norwegian University of Science and Technology (NTNU) is to provide a responsive and agile service to the users where the on-board application software can be updated in flight. The radio-oriented part of the mission objectives spans radio frequency interference measurements and channel characterization in the selected frequency band – 400 MHz UHF – as well as a demonstration of communication services between the satellite and terrestrial sensor nodes and robotic agents. Energy-constrained sensor nodes in remote areas, such as the Arctic, is one of the application scenarios that would benefit from a tailored communication service. Even with services from emerging mega-constellations, traditional satellite communication systems, and new Internet of Things (IoT) over satellite services, there is a service gap for long-range-long-endurance robotic agents and Arctic sensor networks. Therefore, a better understanding of the radio frequency environment, including in-orbit interference as well as channel characteristics, can aid the design of responsive and robust communication links connecting individual assets of a larger System-of-Systems. Instead of just focusing on average spectrum interference levels, the frequency monitoring software

enables the estimation of the interference dispersion and temporal variability. The HYPSO-2 is an evolution of the HYPSO-1 satellite, thus leveraging an already implemented mission software framework. Parts of the SDR payload have been tested on-board another satellite, and the in-orbit results from those measurements will be used as input for the next generation of the radio interference application.

C.1 Introduction

In this paper, we outline the research motivation and the design of a flexible Software-Defined Radio (SDR) payload for radio channel research and communication experiments in the polar regions. The payload is based on a Commercial-Off-The-Shelf (COTS) SDR platform, the Totem from Alén Space (Spain) and will be launched with the HYPer-spectral Smallsat for Ocean observation (HYPSO)-2 satellite. The goal is a payload design that can adapt to system requirements and environmental constraints, such as varying radiofrequency (RF) propagation and interference environments. An SDR payload can be designed for different sub-missions (radio environment research and communication to robotic agents and remote sensor systems) and fulfill various mission objectives, including missions conceived after launch.

Firstly, the research motivation is presented, then the mission design and how this is linked to related work and background. Lastly, we describe how the payload is integrated into the HYPSO-2 satellite, a CubeSat being developed at the Norwegian University of Science and Technology (NTNU) together with Nanoavionics. The HYPSO-2 satellite will also have a Hyperspectral Imager (HSI) payload for ocean monitoring, which is described in detail in [119], [120] and will not be covered in this article.

C.1.1 A need for more communication infrastructure

Monitoring the polar regions and the surrounding oceans is fundamental for understanding the Earth's evolving climate. Despite their extreme environment, several research cruises visit these regions to collect in-situ

measurements [121]. However, due to the vast area and lack of infrastructure [2], it is difficult to obtain good sampling coverage of environmental parameters.

The use of autonomous sensor agents with on-board processing capacity and the emergence of System of Systems (SoS) [122] for environmental monitoring [123], [124] may relieve this situation. In this context, the sensor agent is either a remote sensing satellite, an in-situ stationary sensor buoy or a moving vehicle, such as an Unmanned Aerial Vehicle (UAV) or Unmanned Surface Vehicle (USV). The UAV and USV may also perform remote sensing tasks. The traditional approach to gather continuous in-situ sensor data from remote areas with no communication infrastructure is to deploy a sensor system and then, either collect the system after a given time or relay raw data to an operations center for processing and analysis. Smart sensors with on-board processing (edge processing) can do parts of the data processing in real-time, and then make decisions based on processing results. This includes selecting the most important information to relay to other agents or to the operators [125], [126], saving bandwidth and decreasing system latency and response time.

However, to enable utilization of edge processing and to realize a responsive SoS, there must be a way for the different Constituent Systems (CSs) to communicate with each other. Ideally, this communication should take place in near real time, especially for delay critical systems. This is lacking today, and motivates research on novel communication systems, both on the network layer, but also on new enabling components such as UAV antenna systems [6], [30], [116], [127], [128].

C.1.2 Emerging satellite services and service gaps

There are many new and emerging satellite based communication services that enable connecting sensor systems together in remote areas. Some examples are the operational systems such as Iridium NeXt, the emergence of Starlink and OneWeb mega-constellations, in addition to the many satellite based Internet of Things (IoT) services of various properties. The properties and performance of those different systems vary, and may meet user requirements for various scientific missions.

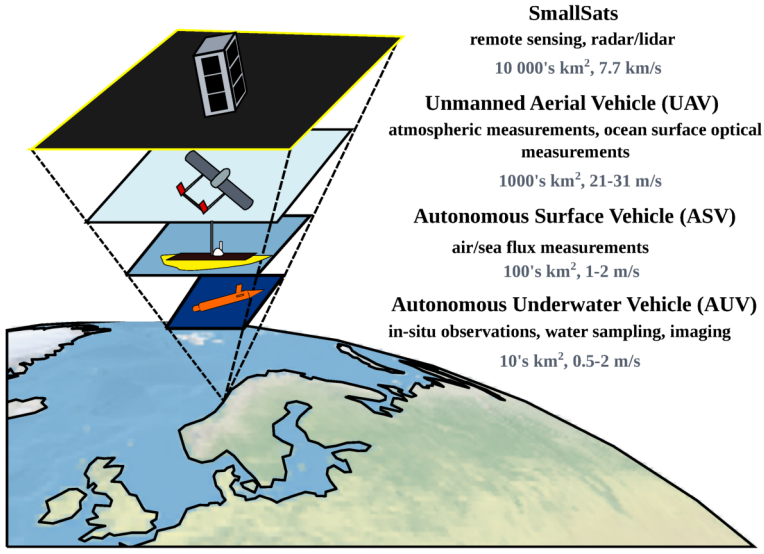

Figure C.1: The observation pyramid. A selection of agents observing a target with different spatial, temporal and spectral resolutions.

However, there are gaps worth researching, when it comes to *long duration, low energy* missions that require more than the low throughput provided by emerging IoT-over-satellite systems, but do not require a full broadband connection. For example, sensors deployed in the Polar areas or autonomous USVs. Another benefit is to provide distributed computing, where the different CSs can optimize in which asset the computation happens, depending on energy, data links, data latency, etc. Additionally, operating many different assets adds resilience in providing the capabilities, as one asset may take over if there is a fall-out. For Delay Tolerant Application (DTA) systems [127], like forwarding sensor data from in-situ sensors by satellite [30], it is possible to relay information through each CS' inherent communication system (as shown in [123]). However, for Delay Sensitive Application (DSA) systems [127], the direct communication becomes important. Time-critical Search and Rescue (SAR) and disaster management applications are important examples of such DSA systems.

Figure C.1 shows how using sensor assets with different spatio-temporal

properties, sensing instruments and field of view can be combined together to provide a more complete situational understanding. An overview can be obtained using remote sensing satellites and UAVs, and slowly moving robots with in-situ sensors can provide more detailed information. Effective and efficient relay of sensor data and metadata between the various assets help fusion of data from cameras and oceanographic sensors, such as temperature, salinity and bio-optics to better understand the biological phenomena.

Sensor agents are typically constrained in several ways, such as range, duration, energy, and size. Such constraints limit the use of otherwise efficient communication systems, as it is vital to adapt to the individual requirements for each asset. To meet the trade-offs between energy, physical size and usable data throughput, the choice of the frequency band is essential. Low frequencies, like VHF or UHF, provide better link budgets for simple antennas and enable low power applications to close the link between the satellite and the sensor agents. Higher frequency systems (broadband systems) require advanced antenna pointing and larger terminals [14], which may not be suited for small sensors and UAVs. The emerging IoT constellations target thousands or millions of sensor units, making the effective throughput for each of the sensors too small to be practical in a scientific operational context. For all these reasons, we argue that research on tailored communication services is needed, targeting the best possible utilization of the RF spectrum.

In the next section, we describe the mission, its objectives and the preliminary concept of operations. In Section 3, we explain the related work, background and motivation for the research of the different sub-missions. In Section 4, we describe the implementation and integration of the payload into the HYPSO-2 satellite, as well as the hardware-in-the-loop setup for testing the communication missions. Finally, the findings and conclusions are outlined.

C.2 Communication mission descriptions

Improvement of communication systems for harsh environments has been a topic of research at NTNU for several years [46], [88], [129]–[131]. At the

NTNU SmallSatLab[1], the development of a flexible communication mission is an important objective [13].

This mission will be carried out through the second satellite from NTNU SmallSatLab. The main objective of the HYPSO-2 mission is to demonstrate a flexible in-orbit platform for near real-time oceanographic observations in coastal areas. It builds on the knowledge generated through the HYPSO-1 mission. The satellite will be an edge computing node. Autonomously processed data will be shared between assets in an SoS, seeking to enable a concert of robotic agents through different communication architectures [123]. The flexible communication platform will also be used to characterize the RF environment, and to provide communication links between the satellite and other assets. In this paper, we will only address the communication-related parts of the HYPSO-2 mission.

The first satellite, HYPSO-1, will be launched in Q1 2022. The satellite is part of a science oriented mission featuring an HSI instrument that will observe ocean color. Analyzing the data will derive the presence of algal blooms [119]. Harmful Algal Blooms (HABs) can cause dramatic loss of live-stock in fish pens. Data from hyperspectral satellites can be a part of a monitoring and warning system alleviating this problem. For HYPSO-1, on-board processed data will be transmitted to the ground segment of the system, where data will be further processed and distributed to end users. Further improvement of this system is possible by allowing direct communication between the sensing satellite and sensor agents on or in the ocean [123], which is part of the objectives for HYPSO-2. A *system-of-systems* [132] consisting of multiple levels of sensor systems will be able to investigate the nature of an algae bloom more closely, compared to utilizing only Remote Sensing (RS) or in-situ measurements. As discussed above, the UHF band at 400 MHz is selected for this study.

C.2.1 Communication mission objectives

From the start, the communication payload on HYPSO-2 supports three main objectives, in a consecutive step-wise approach, where the final object-

[1] http://ntnu.edu/ie/smallsat

ives build on the first two. Due to the flexible nature of the mission, new or changed objectives may be added at a later stage. The first objective is the most mature, and the last two will be further developed before and after launch of the satellite:

- **MO1**: Spectrum monitoring in the UHF (400 MHz) band.
- **MO2**: Characterization of the satellite channel for the UHF (400 MHz) band.
- **MO3**: Demonstrate two-way communication with sensor nodes (stationary or moving) in remote areas, including the oceans and the Arctic.
  - **MO3a**: Relay sensor data from remote sensor networks through the satellite.
  - **MO3b**: Forward Earth Observation (EO)-data from the satellite to autonomous in-situ sensor agents.

Spectrum monitoring

With HYPSO-2, we will be able to measure the time and frequency variability of the interference to contribute to the public state-of-art and use this information to design better communication systems.

A low complexity algorithm to measure the time and frequency characteristics of interference in the UHF radio amateur band has been designed, implemented and executed on-board the LUME-1 satellite in 2020 and 2021 [88]. An algorithm designed to detect opportunity windows in between interference events has been tested in the lab [92]. This is planned to be tested on-board a satellite in the near future. These two algorithms will be the first radio applications to run on HYPSO-2. The long-term goal is to implement an adaptive system capable of: 1) sensing the radio environment, and 2) perform Adaptive Coding and Modulation (ACM) to maximize the data throughput.

Channel characterization

While **MO1** considers measuring in-orbit RF interference, it is also important to characterize the channel from the satellite to the ground stations and sensor nodes. The first step is to estimate the impulse response of the communication channel by transmitting a known pseudorandom sequence to the different sensor nodes and correlating it with the received signal at the nodes. This will enable a characterization of the individual links in the system.

Direct communications to sensor assets

The final mission objective (**MO3**) is to enable direct communication between sensor agents and the satellite, either stationary sensors or moving robotic agents. There are two cases, the first one (**MO3a)** is where a terrestrial sensor has data to be distributed or relayed through the satellite. The second (**MO3b**) is where the satellite, HYPSO-2 as an example, makes observations that should be forwarded to in-situ sensors.

Since the communication payload is co-hosted with an HSI instrument, **MO3b** is given more consideration in this project. Distributing recent satellite sensor data to in-situ agents will aid real time planning of responsive in-situ measurements in the same area that the satellite observed. In order to reduce the response time and ease the requirements for terrestrial infrastructure (e.g., dedicated RF links, 4G, 5G or similar), the satellite should have a direct link to sensor agents. The agents can be informed by the satellite without first having to send satellite data to the Mission Control Centre (MCC) through a ground station. This can reduce latency and increase the responsiveness of the system [123]. The mission research challenge is to design a robust and efficient communication link between the agents, based on the actual interference and channel characterization from **MO1** and **MO2**. This communication link needs to be implementable on the in-situ agents, within the constraints of a CubeSat and complying with the limitations on energy, mass and volume for the sensor terminals.

Suitable packet structures, modulations, effective error correction coding

and interleavers will be implemented and tested. Furthermore, sensing the RF environment and adapting the communication to the channel and interference will enable the increase of the data throughput using ACM techniques.

The aim is not to create a generic IoT service, but rather show the possibility of making a mission-tailored communication system to support projects in need of responsive communication. This, within a reasonable cost and lifetime, compared to the overall project. A small satellite launched into an orbit of 500-550 km altitude will have an orbital lifetime of a few years, on the same order of a research project and expected lifetime of COTS electronics in space.

C.2.2 Operational concept

The operational concept for the different mission objectives are presented in the following:

Frequency monitoring and channel measurements

A simplified sequence for the frequency monitoring mission is shown in in Figure C.2. The steps are:

1. **Upload measurement parameters**: When a ground station is within reach of the satellite, measurement parameters will be uplinked or added in the satellite schedule using a S-band communication link.

2. **Measurements**: The communication payload performs the scheduled spectrum monitoring measurements, pre-processes and saves the results.

3. **Downlink results** The satellite will downlink the measurement results to the ground station using the S-band link.

For channel measurements the concept will be similar. First, a schedule

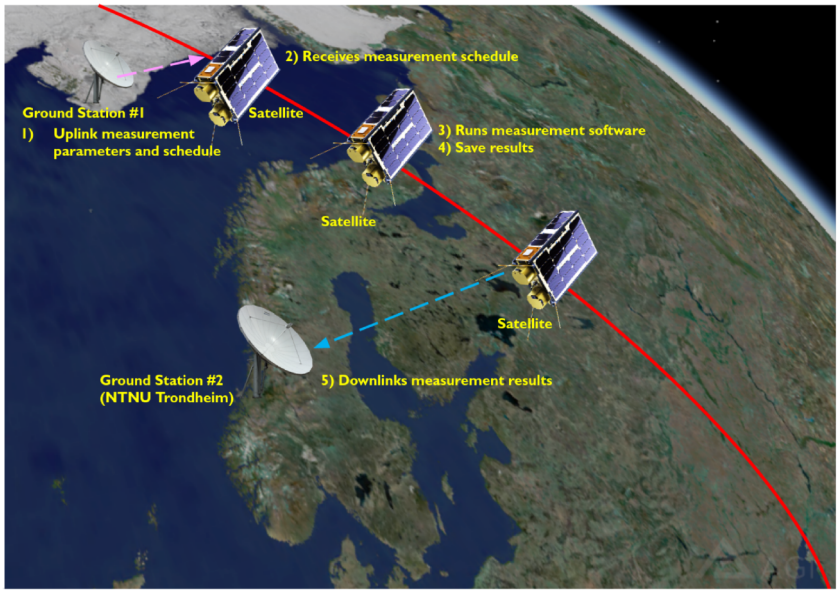

Figure C.2: Operational concept for frequency monitoring.

and plan is uploaded, but instead of performing measurements, the satellite transmits a data sequence when it is over a ground station or terminal.

Test of communication link

In Figure C.3, the operational concept of the direct communication between the satellite and sensor agents are shown.

For **MO3a** – relay measurement data from terrestrial sensors to mission operations:

1. **Listen for sensors**: The satellite will power on the payload and enable listening mode when it approaches an area with deployed sensor systems.

2. **Receive sensor data**: The satellite receives sensor data from sensors, and stores it.

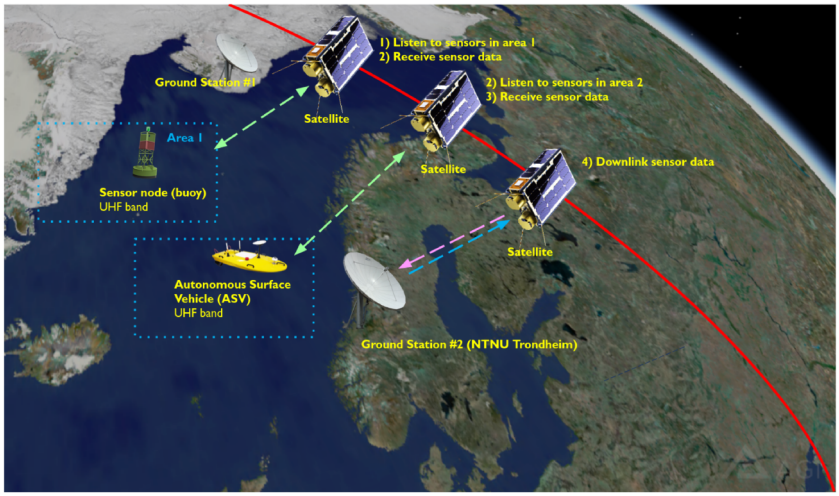

Figure C.3: Operational Concept for direct communication with sensor assets.

C

3. **Downlink sensor data**: When the satellite is over a ground station, retrieved data from sensor nodes is downlinked and relayed to the mission operations center.

For **MO3b** – instruct in-situ agents based upon in-orbit processed EO measurements:

1. **Upload parameters:** Location and observational parameters for HSI-observations are uploaded when the satellite is over a ground station.

2. **Perform observation:** When the satellite is over the selected coordinates the observation is recorded.

3. **Process data:** After an observation the satellite processes data. If specific events or features are detected in the data, the satellite prepares instructions for the remote agent.

4. **Instruct remote agent:** The satellite forwards a measurement plan to the remote agent.

5. **In-situ measurement:** Based on the plan received from the satellite, the in-situ agent navigates to the area of interest and performs in-situ data collection

6. **Send data to operations:** The in-situ agent sends data about the observation to the mission operations (either through the satellite again, or through its designated network for command and control).

C.3 Research motivation and related work

The two research areas that the communication payload will address are radio environment measurements and communication with robotic agents. The first area includes both channel measurements and in-orbit frequency monitoring. The term frequency monitoring refers to interference signals and channel measurements refers to other degradation in the signal quality. Each research area has a different motivation and background, which are explained in this section.

C.3.1 Radio environment research

Link budgets are used in satellite communication system design to estimate the performance of the system. Depending on the frequency band selected, different effects must be considered. For frequencies below 1 GHz, ionospheric effects become more important than effects in other parts of the atmosphere [35]. These ionospheric effects are: Faraday rotation due to the Total Electron Content (TEC), time delays and excess rotations caused by ionospheric irregularities, dispersion because the effects mentioned above are not linearly dependent with frequency, and ionospheric scintillation that affects the amplitude, phase and angle-of-arrival of the signal [35]. There are models to estimate the ionospheric losses for satellite systems [35], but ionospheric physics are complex phenomena. Satellite measurements are important to validate and improve models. The TEC and radio scintillation can be measured by transmitting radio beacons from Low Earth Orbit (LEO) satellites, as in the Coherent Electromagnetic Radio Tomography (CERTO) constellation [36], [37] and analysing the signal received [38]. More

general LEO satellite channel measurement campaigns in the UHF band were carried out in the end of the 20th century at 435.128 MHz [40] and 435 MHz [39]. In the second study, the measurements were used to model the channel and simulate the performance of different error correction codes. This approach can be taken a step further by testing the error correction codes in-orbit after measuring the channel to improve the system design.

In addition to the channel effects, interference signals can degrade the system performance further. Measuring interference through in-orbit frequency monitoring is important for several reasons. There has been an increase of satellite missions in the last years, such as the IoT-over-satellite constellations [133], [134], and the satellites from these missions need to communicate with the Earth not only for operations, but also to provide their service in the case of communication missions. In most cases, this communication uses the RF spectrum and requires frequency coordination with the International Telecommunication Union (ITU) and with the International Amateur Radio Union (IARU) for radio amateur purposes [46]. However, not all satellites apply to these organizations for frequencies and therefore, it is difficult to know the real availability in the frequency spectrum unless it is measured. In addition, satellite operations in certain bands have been challenging due to unexpected interference [46], [48], [60], [88].

Both universities and companies working with small satellites have identified the need to perform spectrum measurements. University of Würzburg, University of Berlin, University of Vigo and NTNU have published interference measurements in the UHF amateur radio band (430–440 MHz) in the last years [46], [48], [60], [88]. The European Space Agency (ESA) launched the OPS-SAT satellite, a flying laboratory capable of supporting many on-board experiments, including interference measurements [54]. In 2020, University of Berlin launched a satellite to continue spectrum monitoring activities. Companies like HawkEye 360, Aurora Insight, Kleos Space, Umbra and Horizon Technologies also work with RF spectrum monitoring and geolocation of interfering emitters.

Knowing the current status of the channel and interference characteristics allows for ACM, increasing the throughput of the system. This is especially useful for narrow-band communication where the bandwidth is already limited. In an SoS, where there are several communication nodes, the channel can differ from node to node, thus a system that can measure the

status and adapt the link to that specific channel would be also be beneficial. The individual CSs in the SoS thus can be able to share information and adapt and re-configure in response to events [132], [135].

C.3.2 Communication with robotic agents and remote sensor systems

In-situ data obtained by different robotic agents is important for environmental monitoring, as RS has limited use in some cases. RS may not be able identify the signatures, or measure concentration, of all biological or chemical components in the water column, or measure under the ice. In addition, comparison of in-situ data and EO satellite data is important to validate the EO-data from satellites. A combination of both RS and in-situ measurements is beneficial to enable the scientific community to better understand environmental phenomena.

Kodheli et.al [136] and other studies discuss the various roles satellites may play in current and future heterogeneous communication systems, including 5G and beyond. Kodheli et al. discuss multiple use cases like back-haul of data from IoT networks. It is also discussed how new technologies including edge computing and prototyping based on SDRs may allow for flexible platforms where functionalities can be updated when needed. This also plays a role for creating enabling technologies for connecting UAVs and satellites [127], [128].

Enabling a near real-time integrated sensor agent concept as shown in Figure C.1, depends on a communication link between the agents that currently is not available. In this case, *real-time* means that there is a link between the different assets so sensor data can be forwarded between CSs directly, not relayed through other ground systems. By exploiting existing communication systems to maintain a near real-time communication link latencies down to 30 minutes or below are possible [123]. Currently, there are no turnkey solutions for enabling the direct connection between a satellite and an in-situ robotic agent. The architecture shown in Figure C.4 does currently not exist, and thus, is one of the research lines we pursue.

In the case of remote sensors (on ground, in water or on ice), they operate

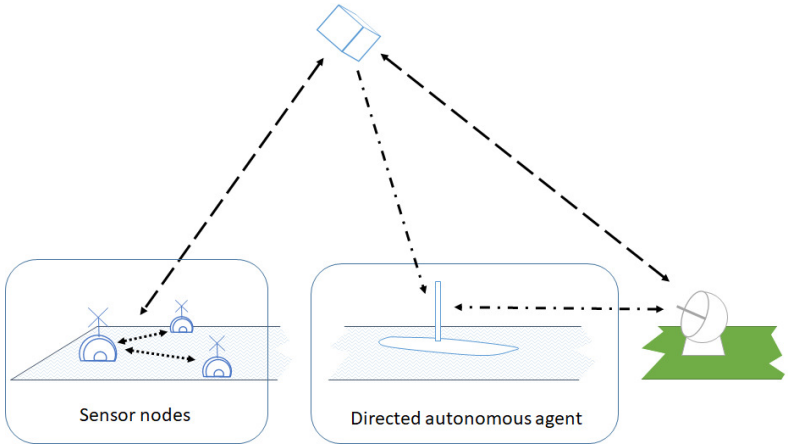

Figure C.4: A flexible small satellite: The satellite can relay data from sensor nodes to a ground station, or it can direct an autonomous agent to an area of interest, based on observations made by, for example, a camera on-board the satellite.

in energy-constrained environments with batteries that may or may not be recharged by solar energy. Sensor nodes in the Arctic will not get any solar energy during the winter. Hence, they must consume as little energy as possible to maximize sensor operational time. A direct link to satellites will enable relaying of sensor data back to the researchers (or other end-users of the data). Such sensors generate a varying amount of data [29], [30]. In some scenarios on the order of a few megabytes per day. Further environmental constraints for sensors deployed in extreme environments, such as Arctic areas, call for no moving parts, i.e., mechanically tracking antennas. To summarize, there are common constraints to consider when mounting radio terminals on constrained sensor platforms (both stationary and moving):

- No moving parts (excludes terminals with mechanical tracking antennas).
- Moderate battery capacity (excludes high power and broad-band solutions).
- The communication link must support a moderate data volume, on

the order of megabytes per day [30].

Usability of existing or planned systems

For relaying sensor data from remote sensor (networks) to the operators or end-users through a satellite, there exist several solutions with different characteristics. These can be classified into three types (systems not covering the polar regions are excluded, and the list is not exhaustive[2]):

1. Broad-band
    - Existing examples: Iridium, Inmarsat
    - Emerging examples: Kepler, Starlink, OneWeb
2. Narrow-band (stream of data)
    - Existing examples: Iridium
    - Emerging examples: VDES
3. IoT-over-satellite (single messages)
    - Existing examples: Iridium
    - Emerging examples: Astrocast Nanosatellite Network, Lacuna Space, Myriota, OQ Technologies, Swarm

The broadband solutions operate on higher frequencies, requiring higher transmit power or high gain tracking antennas. Therefore, they are of little use for many robotic agent applications and also individual sensors. The IoT constellations may trigger a revolution in accessing environmental data, health data for livestock and various forms of tracking data directly from a small sensor, by sending the data through a satellite network and deliver

[2]Information about the systems has been found on company web-pages or community databases such as [101], [137], [138].

this information to the customer in near real-time. However, one of the common features of those systems, is the low data volume allowed for each sensor, which is on the order of 100 bytes a few times per day [32], [33]. This means that none of the IoT systems seem suitable if it is desired to transmit several megabytes per day.

Iridium has been used for stationary sensors and drones, both for command and control and to relay small amounts of sensor data [30]. Thus, Iridium can fulfill mission requirements in some cases, but more energy-efficient solutions operating on VHF or UHF bands may be desired [14]. These solutions represent a viable trade-off between energy requirement, non-moving antennas and the possibility of a large enough throughput if used in a dedicated, tailored system.

C.4 Payload Implementation and Integration

The following sections describe the mission implementation, including the satellite platform, the selected communication payload, and the framework for development and hardware-in-the-loop (HIL) testing.

C.4.1 The HYPSO-2 spacecraft

The HYPSO-2 satellite is based on a similar platform to HYPSO-1, namely the Multipurpose 6U Platform (M6P) satellite bus from NanoAvionics (Lithuania) [119], and features the SDR communication payload in addition to a similar HSI payload as on the HYPSO-1.

The subsystems of the satellite include a Flight Controller (FC) for onboard data handling in cooperation with the Payload Controller (PC), that also acts as a router between the subsystems and the payloads. The FC also manages the pointing and orientation of the satellite through hosting the Attitude Control and Determination System (ADCS) functions. One important part of that system is a SatLab Global Navigation Satellite System (GNSS) for orbit determination and time synchronization. Furthermore, the satellite is equipped with an Electrical Power Subsystem (EPS) for power management

and a UHF radio for Telemetry and Telecommand (TM/TC) and basic communications. The internal communications bus is based on CubeSat Space Protocol (CSP) over Controlled Area Network (CAN), where each subsystem is a network node with its dedicated CSP address. The satellite will be equipped with a SatLab SRS-4 S-band transceiver, capable of up to 4 MBps downlink and up to 200 kbps uplink transfer rates. Compared to HYPSO-1, there will upgrades of the power system, such as deployable solar panels providing extra power and energy for the payloads. In addition, there will be an upgraded communication link between the HSI payload processor and PC and a higher downlink speed.

In order to enable flexible missions, the payload itself must be adaptive and re-configurable in-flight. Hence, an SDR is the best payload implementation for this type of missions. The key feature with an SDR is that it is re-programmable and can be used to run very different radio applications. The payload shall be a platform and framework suitable for ensuring mission success for different communication missions using the same payload but acting as different virtual payloads. Also, this flexibility enables re-organising and changing mission objectives throughout the full spacecraft lifetime, adapting to in-flight experience and newly discovered to research needs.

C.4.2 Selected communication payload

An SDR survey was performed in 2018 [94] and complemented in 2019 [13] to choose the right platform for the HYPSO satellites. The most suitable SDR was the *Totem* SDR from Alén Space (Spain).

The Totem physically consists of two main parts: 1) the motherboard with the processing system, based on the Xilinx 7020 Zynq System on Chip (SoC), which includes both ARM processors and an Field-Programmable Gate Array (FPGA) [139]; and 2) a radio front-end with filters and amplifiers for the selected frequency band. The system runs an embedded Linux operating system. Radio applications on Totem can be developed on different abstraction levels from high-level Python, C programming to low-level FPGA-implementations. In addition, the SDR has flight heritage through the LUME-1 mission [87] and frequency monitoring research activities carried out from the same satellite [88].

C.4.3 Payload software architecture

The HYPSO software stack mainly consists of two parts: an operator interface named `hypso-cli` and the payload service program called `sdr-services`. The operator interface is run on ground on a computer with a communication interface to the satellite. This may be either directly through the CAN bus for testing in the lab, or through the mission control system including a radio link. For the operator, this connection is nearly transparent. The service part runs on the payload processor as a normal program.

The HYPSO-1 payload software architecture is described in [140]. For HYPSO-2 this architecture is expanded so that the architecture supports multiple payloads. Much of the basic on-board software services share a common base code, with some adaptations and tailoring to the specific payload systems. In practice, this means that each payload hosts its own Linux-based operating system, and individual services related to the *payload functions*, such as operation of cameras or the radio applications for the SDR. Other common services, such as telemetry, file transfer, CSP interface and Operating System (OS) service are similar and share a common base code. Through this architecture, it is easy to add different types of payloads to future satellites with a high degree of code reuse with little effort. The SDR software payload architecture is shown in figure C.5. The *Radio service* serves as the interface to the SDR functions, and is used as an interface layer between an operator and the SDR. Strictly speaking, the SDR interface may be directly accessed through the use of the *File Transfer Service* and the *OS service*, but the *Radio service* wraps functionality and operations into a more user-friendly environment.

C.4.4 Payload functions (radio applications)

The main advantage of an SDR payload is its flexibility and re-programability. Programs can be uploaded in-flight as soon as they are developed and tested. There are two radio applications for frequency monitoring that have been developed for the LUME-1 satellite that will be used as a base for the first applications in HYPSO-2. These applications were designed to conform with the constrained downlink data rate from LUME-1, but the program

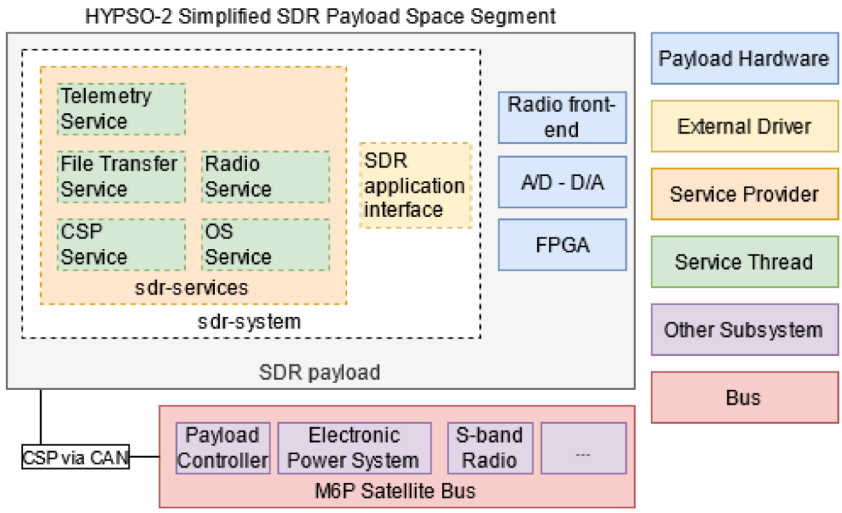

Figure C.5: Payload software architecture.

can be modified to take advantage of a better downlink. Due to the capacity of the S-band radio link that will be used in HYPSO-2, a lot more data can be downloaded, as the gross downlink rate increases from 4.8-9.6 kbps from LUME-1 to up to 4 Mbps for HYPSO-2. Future work will involve the development of new radio applications for channel characterization and communication with sensor nodes and robotic agents.

Local Mean Estimator (LME) algorithm

The first application measures the time-frequency characteristics of the in-orbit radio environment using a Discrete Fourier Transform (DFT) and a Local Mean Envelope (LME) estimator [88]. The application consists of: 1) a shell script that manages individual measurements, and 2) a C++ program based on GNURadio. The script calls the measurement program at the set time, compresses and prepares the generated files for download. The measurement program acquires the raw In-Phase and Quadrature (IQ) samples from the transceiver, calculates the magnitude of the DFT of the number of samples specified and estimates the LME. The second order moment (m_2) of the mean for different window lengths is calculated. By

analysing how the m_2 varies depending on the length of the window, the time variation of the interference can be estimated. The number of time windows can be four, six or eight, and the length of the first window and the step between them can be specified. The center RF frequency, bandwidth, sampling rate, duration of measurements and number of frequency bins can also be configured. By doing this processing in orbit, it is possible to measure over a larger area while still keep the generated data volume manageable for download.

Opportunity window algorithm

The second application has a similar software architecture and focuses on the time characteristics of the interference. A shell script controls the timing of execution of the measurement program, and then, compresses the resulting processed files. The program is written in C++ and estimates when there are time windows with low interference level. The power of the received signal is calculated from raw IQ samples. An opportunity window is detected when the power is below a certain threshold continuously for a defined time (configurable). The signal will spend time in opportunity windows of different lengths, and these windows can be grouped in intervals. Furthermore, the opportunity windows can be estimated for different power thresholds. The output of the program is the opportunity distribution that estimates how long the signal is in windows of opportunity of different lengths for different power thresholds. The opportunity windows indicate time slots where transmissions can be performed to avoid loss of packets due to high power interference.

C.4.5 Testing and Hardware-in-the-loop

The development and testing of the radio application followed a step-wise methodology. First, the applications were developed in a high-level programming language (Matlab). Interference signals were generated in software and the algorithms were tested in the simulation framework. Second, the software was ported to C++, and executed on a computer. The program collected raw IQ samples from the Totem using a remote connection over

Internet Protocol (IP). The third step involved porting the software to the Totem platform and run it on the Totem itself. The full testbed for functional testing consisted of two SDRs (see Figure C.6). A USRP-2901 SDR was connected to a computer to transmit simulated in-orbit interference (different test signals). This was achieved by running GNURadio programs on the USRP. The USRP is connected to both the Totem SDR to receive the input test signals for the radio applications, as well as to a spectrum analyser for debugging purposes. At this stage, the Totem SDR operated independently of the rest of the satellite system, remotely controlled via Secure SHell (SSH) and powered by a stand-alone power supply.

At a later stage of the project development, the Totem SDR was integrated into the FlatSat for HYPSO-1, to aid sub-system integration. This was achieved by replacing the external power supply and connecting Totem directly to one of the EPS output channels. The CAN interface of the Totem was connected to the payload CAN bus of the FlatSat, as shown in Figure C.6. In addition to the sub-systems physically in-house at NTNU, the FlatSat has a network connection to the satellite suppliers site, giving remote access to other subsystems, such as the FC. For all subsystems and the operator, the physical location of the subsystems does not matter, as in the end they are all connected to the same physical CAN network. This setup enables parallel system integration and a full hardware-in-the-loop testbed, where SDR applications can be run from the FlatSat. Furthermore, multiple students can work with the same system at the same time. This process builds on, and extends, the work described in [141].

C.5 Main findings and discussion

In this paper we have described the development of a flexible smallsat communication platform that can enable multiple missions, spanning three main mission objectives. The selection of a COTS SDR platform and the preparation of the implementation for the first mission objective are described. Furthermore, we show how the SDR was integrated into an existing satellite platform and software framework with little effort.

The main advantage of an SDR, reprogrammability, is exploited to define

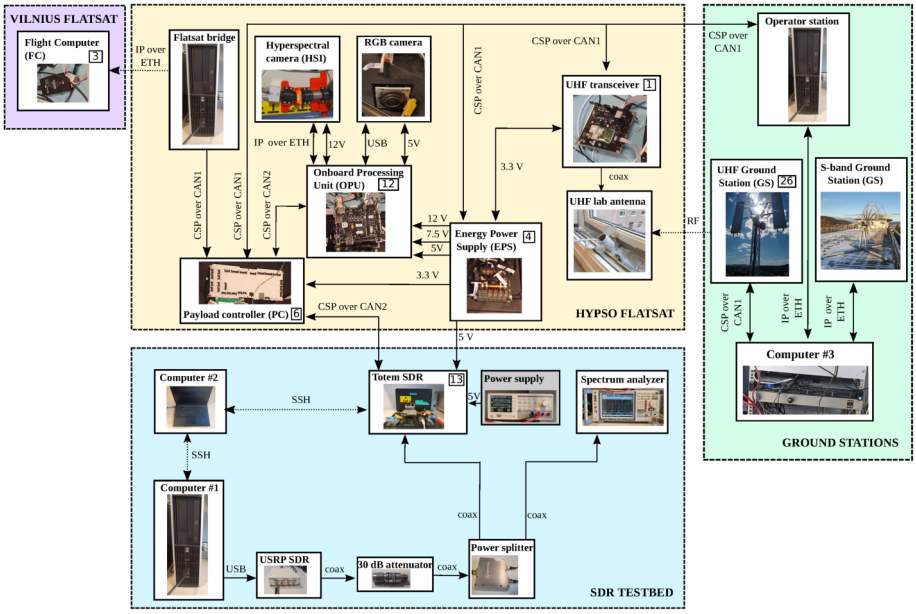

Figure C.6: The HYPSO-2 testbench and FlatSat architecture. CSP addresses are indicated with a small square inside the component.

multiple flexible missions using one satellite payload. The main mission objectives should be defined early, but the specific functionality can be specified at a later stage. Since the radio applications can be updated throughout the mission it is possible — and desired — to design the mission in such a way that functionality for the first mission objective is completed by launch. Development of radio applications to fulfill the other objectives rely on outcomes and results from the previous mission, and will therefore be developed iteratively while the satellite is in orbit. Frequency monitoring measurement methods and processing algorithms have been tested in orbit on the LUME-1 satellite [88], and will be further developed and adapted for the HYPSO-2 satellite with different downlink and power constraints. The HYPSO software framework was extended and refactored to accommodate a second payload with little effort [140], and the SDR was incorporated in the common HIL framework.

Results from this satellite project may contribute with more and global

in-orbit interference measurement data in the 400 MHz band. It will also make a framework for incorporating channel estimation into an adaptive radio link that can bind sensor agents, such as the satellite itself and in-situ agents, together to deliver a more complete picture of environmental factors in selected areas. This is a vital enabler for resilient and responsive SoS for environmental monitoring. The 400 MHz UHF band is selected as non-moving antennas and low power devices can be used while still closing the link between a remote agent and a satellite. We argue that the emerging IoT constellations do not fit the use case of relaying moderate amounts of data from remote sensors, nor enabling connectivity between an EO-satellite and an in-situ agent. A tailored communication service, adapted to the specific needs of a mission should be the goal, and this can be realized by utilizing the flexibility of an SDR platform to maximize the system data throughput using limited RF spectrum.

Acknowledgments This work was supported by the Research Council of Norway through the Centers of Excellence funding scheme, Grant 223254 - Center for Autonomous Marine Operations and Systems (AMOS) and the Research Council of Norway through the IKTPLUSS programme grant 270959 (MASSIVE). Further, the authors want to thank all HYPSO team members for their joint efforts in this project. Sivert Bakken, Tuva Moxnes and Dennis Langer from the software team and Amund Gjersvik from the electronics team deserve special thanks for their help.

D A Satellite-USV system for Persistent Observation of Mesoscale Oceanographic Phenomena

The text of the following paper is added as a chapter and re-formatted for better readability:

A. Dallolio, G. Quintana-Diaz, E. Honoré-Livermore, J. L. Garrett, R. Birkeland and T. A. Johansen, 'A satellite-usv system for persistent observation of mesoscale oceanographic phenomena,' *Remote Sensing*, vol. 13, no. 16, 2021, ISSN: 2072-4292. DOI: 10.3390/rs13163229. [Online]. Available: https://www.mdpi.com/2072-4292/13/16/3229

Abstract Traditional tools and methodologies for mesoscale observation of oceanographic phenomena are limited by under-sampling and data latency. In this article we evaluate three different scenario variants of an architecture for how heterogeneous sensor nodes can be integrated with satellite remote sensing. Independent space and marine sensing platforms are interconnected either directly or by means of a ground-based mission control center responsible for data processing, relay, and coordination of the assets. A wave-propelled unmanned surface vehicle (USV) persistently collects in-situ data of the targeted phenomenon. In two variants of the architecture, a dedicated small satellite acts as a sensor node, a data processing facility and a communication node. We have used a System-of-Systems (SoS) modeling approach coupled with operational simulations in different locations on Earth, in order to support the proposed methodology and investigate quantitatively the reduction the data latency to end-users. Through a combination of field experiments and simulations we estimate how the different scenarios perform with respect to providing remote sensing data that are used to create a measurement and navigation plan for the autonomous

vessel.

D.1 Introduction & Motivation

Human activity near and in oceans is strongly affecting our environment through the warming of the planet and increased eutrophication, causing substantial loss of sea-ice in the Arctic region [142] and represents a profound threat to biodiversity. With a focus on the ocean as the primary sink for greenhouse gases, ocean science, and the study of climate change has become critical to understanding our planet [143]. In particular, continuous observation of oceanographic phenomena as a stepping stone for understanding the impact of human activity on the world's oceans is hampered by under-sampling and data latency. Unlike the atmosphere, the ocean is not continuously monitored or sampled, so the only way to learn its dynamic processes is to collect measurements with boats or diving platforms. However, such systems are expensive, and by only providing a glimpse of large phenomena cause short-term events to remain undetected. Current monitoring methodologies rely on both terrestrial and space-based remote sensing platforms. While most common terrestrial platforms and sensors are often constrained by proximity to ship or shore and by limited on-board energy, ocean color remote sensing based on optical imagery from space is limited by cloud coverage and weather phenomena.

The frequency of Harmful Algae Blooms (HABs) is increasing in step with increased human activity and eutrophication, and depending on the type of bloom, in some cases with the increased temperature of the oceans ([144], p. 17). HABs occur in oceans and lakes and can be highly toxic to aquatic and non-aquatic life, or cause harmful effects by anoxia (oxygen depletion). These effects reduce the water quality that leads to significant recreational, economic, and ecological impacts [144]. Because the HABs typically occur in dynamic and optically complex water systems, and space-based remote sensing systems are desired to provide radiometry services multiple times a day [145]. Accordingly, the International Ocean Color Coordinating Group (IOCCG) state that "it is necessary to take a multi-layered approach to HAB studies, amalgamating information from multiple satellites, multiple sensors, and multiple adjunctive data sources to form a multidimensional

understanding of the nature and dynamics of HABs ([144], p. 11).” Global environmental changes happen at large temporal and spatial scales. The study of phenomena evolving at smaller scales can provide valuable insights and enhance our understanding of the global, slow-changing dynamics of our planet.

The mesoscale variability (<1000 km^2) can be best observed with mobile platforms that can sample a wide range of properties such as chlorophyll concentration, oxygen concentration, biomass, anthropogenic runoffs, temperature, salinity, vertical current structure, seafloor topography, and turbulence. Unmanned vehicles (such as Unmanned Underwater Vehicle (UUV), Unmanned Surface Vehicle (USV), Unmanned Aerial Vehicles (UAV)) are flexible assets that can individually observe and acquire data from various target areas [146]. However, no single platform is ideal for full coverage of oceanographic mesoscale phenomena [144]. Furthermore, to gain useful insights based on observations from different assets, they should be coordinated to observe the same patch of the ocean near-simultaneously, within time scales that fit the observed phenomena, i.e., synoptic observations [147]. The physical and operational diversity across such mobile platforms may result in complementary spatial and temporal sampling capabilities.

Figure D.1 from [7] shows spatial and temporal scales of the most common marine and aerial systems employed in ocean studies. Small satellites and gliders operate at scales that mostly overlap in space and time and can as such enable synoptic measurements of the same phenomena. The cooperation of both systems indicates coverage of phenomena in the range of 100 m to 1000 km in space, while from hours up to one year in time. Ship-based ocean observation also involves similar scales and points to well-consolidated methods ocean studies have relied on in the last decades. However, these involve higher operational cost and risk (for example, personnel costs, humans exposed to harsh environments) and, most importantly, they cannot scale across space and time and are therefore not suitable for the study of slow-changing oceanographic phenomena. Combining multiple different autonomous agents in a heterogeneous ocean sampling network has been demonstrated [8], [148], [149] to increase the amount of information and, therefore the observation quality of physical phenomena beyond what each platform can achieve individually.

Sea gliders, both on the surface and sub-surface are extensively employed as

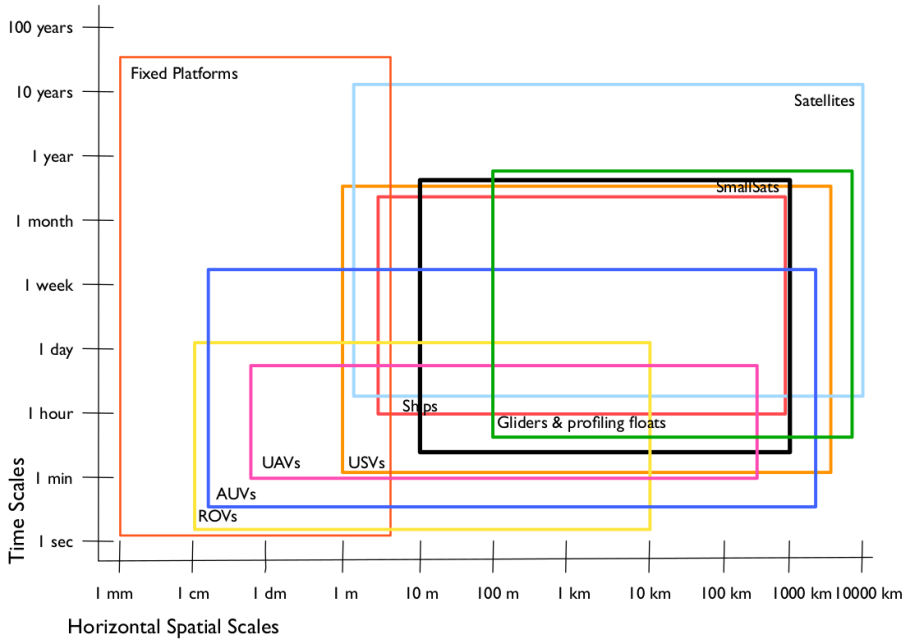

Figure D.1: Temporal and spatial scales of marine systems. Figure modified from [7].

ocean observation platforms [150]–[152] because of their extended operational autonomy. Some works show the possibility to utilize such platforms to validate satellites measurements [153], [154]. Nevertheless, the current state of the art lacks detailed modeling of marine operations in which the science-driven objectives for unmanned assets are based on processed data from small satellites.

In this paper, we discuss how to enhance the study of oceanographic phenomena using satellites together with in-situ terrestrial assets, as compared to using each platform independently. The proposed architecture is composed of a space segment with a mission-specific small satellite and "traditional" Earth Observation (EO) satellite data, a ground mission control center and a long-endurance wave-propelled USV, as shown in Figure D.2. The satellite offers an overview of an area where the sea glider collects detailed in-situ measurements and transmits them to shore. In one variant of the system architecture, we make use of EO-data from existing satellites, whereas in the

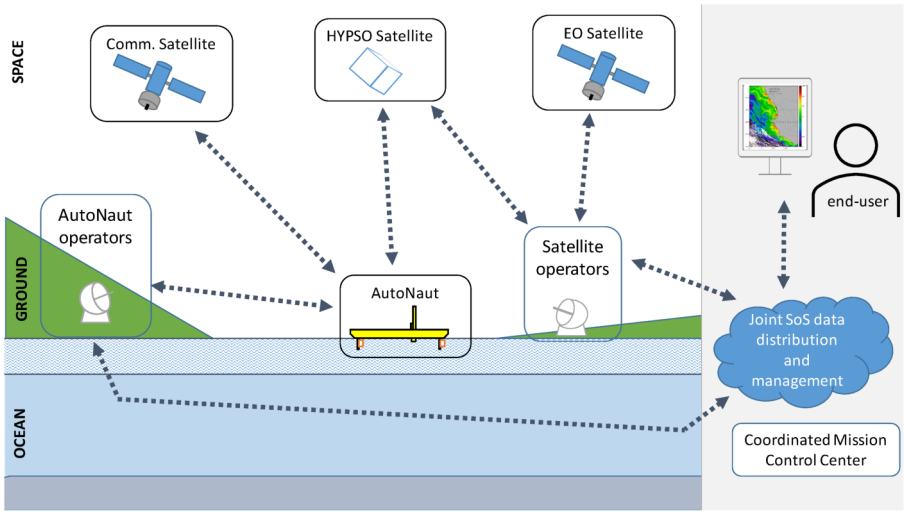

Figure D.2: Proposed system architecture.

two other variants we model how the architecture would benefit from using a dedicated small satellite, such as the HYPerspectral small Satellite for Oceanographic observations (HYPSO)-1 satellite developed at Norwegian University of Science and Technology (NTNU).

The sea surface glider considered in this work is the AutoNaut, a commercially available wave-propelled USV equipped with a passive propulsion system that converts waves energy into forward thrust, see Figure D.3.

To best exploit the capabilities of each asset; we propose a method for optimizing the information flow between the nodes of the architecture. We have employed a System-of-Systems (SoS) approach [155] for modeling and development and the solution presented can be classified as an *acknowledged SOS*. The use of an SOS approach has already been applied to other studies involving unmanned vehicles [156]–[158]. In particular, Ref. [87] describes the application of an SOS approach for the detection and monitoring of forest fires involving forest-based infrared sensors, CubeSats providing early warning and communication services, and UAVs for high-resolution mapping. In our work, the acknowledged SOS has recognized objectives, *providing a better information system for observing mesoscale phenomena*, dedicated management, *the research team*, but the Constituent Systems

Figure D.3: NTNU AutoNaut during operations in Trondheimsfjord.

(CS) have different development lifecycles, individual objectives, and a need for coordinating interfaces and operations to achieve the common goals. The authors postulate that architectures promoting tight cooperation between satellites and surface marine vehicles can improve the observation of oceanographic mesoscale phenomena and contribute to increasing the data available on HABs, both qualitatively and quantitatively, and provided data of a higher value and timeliness to end-users. Our analysis shows that while integrating existing systems will provide added information with little effort, making use of new tailor-made assets such as small satellites will improve the timeliness and the adaptivity of the observational system because the users can select their Area of Interests (AoIs) to a greater extent than currently possible.

The paper is structured as follows: In Section D.2 we describe approaches for persistent observation of oceanographic phenomena, in Section D.3 the constituent systems and scenarios are presented, followed by the methods applied in Section D.4. In Section D.5 we present the results. We present a discussion in Section D.6. Finally, in Section D.7, we summarize our findings and suggest areas for future studies.

D.2 Using Robotic Platforms to Support the Persistent Observation of Oceanographic Phenomena

The oceans are continuously surveyed on a global scale by remote sensing satellite systems like Copernicus [159], [160], and even systems like Landsat provide data products, including monitoring of inland waters [161]. In addition, oceans are populated with measurement buoys (drifters) that continuously sample their surrounding environment and transmit collected data to shore for further analysis and processing [162]. Constrained by fixed position, short sensor range, lagrangian motion or limited payload energy, the network created by remote sensing buoys is expanded by remotely controlled platforms able to exploit the environment to achieve an intended navigational behavior [150]–[152], [163]. These platforms are usually equipped with a wide-range sensor suite [164] that samples both near-surface atmospheric parameters (such as wind speed, pressure, temperature) [165] and features of the upper water column (for example, water salinity and temperature, sea currents, oxygen concentration) [166]. From ecological and biological perspectives, such systems are able to quantify natural phenomena related to animal primary productivity (by collecting chlorophyll and Dissolved Organic Matter (DOM) concentration), to assess the health of the ecosystem [167] (such as algal blooms, toxins concentration) or to study fish behavior and migrations via acoustic hydrophones [168], for example. Enhanced endurance and bigger payloads come, however, with a number of challenges related to the maneuverability and operational capabilities of such platforms, as described in Section D.3.4.

The control of such robotic systems and the communication with them are challenging tasks due to the unpredictability of the environment. Goal-driven intent for scientific measurements will require careful balancing between the value of information related to the observed phenomenon and the ability to be at the right place at the right time. Moreover, communication challenges such as the limited bandwidth of satellite links influence the ability to provide valuable data to shore.

In Ref. [154], a Wave Glider is used to persistently collect chlorophyll data for several months and validate satellite measurements. This work

demonstrates that in-situ measurements provided by long-endurance marine systems can be used, in combination with satellite observations, to provide a better understanding of the natural phenomena and climate changes of the planet. The Wave Glider was also used to validate winds measured by satellites in orbit[153] that use microwave sensors to observe the sea surface backscatter. Despite the important contributions of these works, their main objective was to validate quantitatively and qualitatively the existing satellite-based ocean monitoring methods. In Ref. [169], a HAB detection system is proposed using existing satellites (MODIS Aqua and Terra, NASA) and gives some indications on how predictions of HAB can be carried out. The 2021 IOCCG report [144] provides more examples of HAB warning systems and how the data can be collected.

Our work addresses the observation of mesoscale phenomena in the short time range, i.e., phenomena detection from satellite and its in-situ observation using terrestrial assets within the time scale of the phenomenon itself. Communication latency is assessed with simulations that provide insight on the spatial and temporal coordination that is needed among the involved assets. This coordination can increase the quality and amount of collected data, and contribute to our understanding of the targeted phenomena.

D.3 System and Scenario Description

To overcome the limitations affecting current ocean observation systems, we advocate the development of integrated systems harvesting the specific benefits from each sensor platform. One of the current limitations in space-based remote sensing is that several maritime areas of scientific and economic interests are not covered well enough. Examples are the Norwegian sea and Arctic areas, the coast of Chile, Canadian waters, and areas in Scotland because of aquaculture installations [144]. Small satellites in Low Earth Orbit (LEO) equipped with instruments selected for each mission and use-case can target specific AOIs with greater spectral and spatial resolution than large EO satellites at higher altitudes. The temporal resolution can also be determined by the user to a greater extent, by scheduling observations on-demand and by selecting an orbit suitable for the AOI, such as polar orbits for Arctic areas.

The following sections describe the constituent systems in our SOS shown in Figure D.2 and the scenarios foreseen to support the collection of HAB data and other oceanographic data.

The system consists of a space segment and a ground segment. The ground segment includes the wave-propelled USV AutoNaut, ground stations to communicate with the satellite, and a Coordinated Mission Control Center (CMCC). Note that there is a clear distinction between the ground stations and the CMCC; the ground stations encompass the antenna and infrastructure needed to establish the radio link to the satellite, while the operator is located at the CMCC.

D.3.1 The HYPSO Satellite and Ground Segment

The small satellite HYPSO is a 6U CubeSat equipped with a HyperSpectral Imager (HSI) payload featuring onboard processing of hyperspectral data based on a push-broom acquisition of data to support coordinated missions with unmanned vehicles [119]. The HSI telescope uses a Commercial-Off-The-Shelf (COTS) image sensor, COTS optical components, and in-house designed machined interfaces [120]. The design results in an unbinned Signal-to-Noise Ratio (SNR) of 180, detects wavelengths between 400–800 nm with a Full-Width at Half-Maximum (FWHM) of approximately 4 nm. The onboard processing unit is built on a Zynq-7030 Xilinx PicoZed System-on-a-Chip with a Field Programmable Gate Array (FPGA) and a two-core ARM processor. This processing unit provides a configurable platform for onboard processing and software, which can be tailored to suit the mission's needs while in orbit. The FPGA enables rapid processing of large datasets, such as the hyperspectral data, and utilizes CCSDS-123 lossless compression for image processing [170]. The configurable onboard processing of images can provide target detection and classification services to direct unmanned asset data collection. In addition, the HYPSO-1 CubeSat features an S-band radio link, a UHF radio link, and an Attitude Determination and Control System (ADCS) that allows for slew maneuvers to increase the SNR and improve the ground sampling distance [119].

While HYPSO-1 features a high spectral resolution, its spectral range and observations are limited by cloud cover, and payload operating time is

limited by energy constraints. There is a plan to complement HYPSO-1 with more satellites carrying an upgraded payload to improve operational availability.

The space segment also includes commercially available communication systems that may be compatible with those onboard the AutoNaut. The ground segment supporting the HYPSO-1 spacecraft consists of commercially available ground communication services and an in-house ground station that communicates with HYPSO-1 and can be configured for other asset communication. These systems are interconnected through a CMCC and cooperate to deliver the requested data to the end-users. When operational, the HYPSO-1 satellite can deliver two types of data products: "raw" HSI data and "operational" data. The former can be downloaded to the CMCC for further processing, see Figure D.2. However, transmitting raw data to the CMCC involves some challenges. The large data volume each observation generates, combined with a limited downlink capacity, leads to a time needed for data download spanning several Ground Station (GS) passes. Thus, the resulting age of data will add up to hours and may limit the operational utility of the data itself. Instead, operational data derived by onboard processing can be tailored to different uses, such as information about the location and characteristics of a current or future phenomenon. The data budget for HYPSO-1 can be found in [119], and the assumptions and constraints for the communication links are discussed in Sections D.3.3 and D.3.3.

D.3.2 AutoNaut: A Wave-Propelled USV

The AutoNaut is a wave-propelled long-endurance USV equipped with a wide-range scientific payload, whose typical speed over ground (SOG) is in the range of 0–3 knots depending on the sea state and the ocean currents and wind. We employ a version of the AutoNaut, shown in Figure D.3, in which navigation, communication, and payload control systems are publicly documented (http://autonaut.itk.ntnu.no) and are designed and developed by NTNU as described in [164]. The AutoNaut operates according to navigation and scientific plans containing one or multiple destinations and an indication of what sensors and data to collect and when. The choice of employing the AutoNaut in this work is motivated by its ability to perform

sustained operations in the ocean without the need for human intervention. This unique feature makes the USV suitable to sample persistently oceanographic phenomena. Moreover, the AutoNaut is equipped with radio and satellite communication links, allowing the operators to retrieve data from remote locations and therefore assess the evolution of the targeted phenomenon.

D.3.3 Operational Concept

To illustrate how satellite observations can aid in-situ observations from unmanned vehicles like the AutoNaut, we explore three scenarios that model the information flow between the assets. Scenario 1 makes use of data from existing EO-sources, while Scenario 2 and 3 rely on a dedicated satellite, represented by HYPSO-1. Furthermore, Scenarios 1 and 2 involve the CMCC as a coordinating entity, whereas Scenario 3 does not, until the final collection and presentation of collected data from both the satellite and the AutoNaut. In Scenarios 2 and 3, HYPSO-1 monitors an area and uses the onboard detection algorithms to determine whether the observation is a natural phenomenon of interest or not. If the retrieved information is classified as such, the satellite forwards directives to the USV. Depending on the scenario and communication mode, the information may be either relayed through an existing ground segment to the CMCC (Scenario 2), or directly to the AutoNaut employing a dedicated communication system (Scenario 3). Despite that direct communication between the satellite and the USV could decrease latency and enable faster in-situ response; it comes with challenges related to employing a communication link and the amount of data transmitted. The downlink capabilities onboard the USV might depend on the sea state and the amount of data to be downlinked. Those limitations are negligible if data are first downlinked to ground, post-processed, and then transmitted to the USV in the form of a navigation and data collection plan. This process means that the data forwarded to the AutoNaut by the satellite in the second scenario must be processed operational data including a navigational plan. Once data are received onboard the AutoNaut, the onboard software modifies the goals of its current mission to steer the vehicle towards the desired location and sample the targeted phenomenon.

The three different scenarios, shown in Figure D.4, describe how the inform-

ation flow above can be achieved:

- **Scenario 1**: the CMCC retrieves data from existing space assets, like Copernicus Sentinels and other EO-satellites, and processes them to detect phenomena that should be investigated in-situ. The age of data and the predicted behavior of the phenomena must be included in the processing. In case of detection, the CMCC creates a navigation and sensors usage plan and forwards it to the AutoNaut.

- **Scenario 2**: a dedicated satellite such as HYPSO-1 monitors a selected AOI and forwards (processed) data to the CMCC. If processed data indicate an ongoing or potential phenomenon of interest, a dedicated mission is built and dispatched to the USV from the CMCC.

- **Scenario 3**: following an observation from the AOI, a dedicated satellite like HYPSO-1 processes the acquired data onboard and communicates a mission plan directly to the AutoNaut.

Physical events in the oceans are dynamic and constantly changing, and the timelines of information delivery and data latency are important metrics to consider to assess the utility of the system. The lowest data latency and age is achieved through scenarios where onboard processing extracts the important information from the data at an early stage to minimize the data volume to downlink, and hence the time for this data transfer. Scenario 3 has the potential of providing data with virtually no delay between the satellite and the AutoNaut, given some assumptions that are discussed in detail in Section D.3.3. The three data distribution strategies are explored, compared and discussed in this paper.

Scenario 1: Satellite Imagery from Existing Infrastructures

In the first scenario, we exploit existing technologies and infrastructures to gather satellite imagery of a selection of AOIs and commanding in-situ assets for data collection, as shown in the top path of Figure D.5. Specifically, in the spring of 2021, we used the Sentinel database [171] to retrieve processed imagery of Frohavet in mid-Norway and coordinate in-situ observation and sampling of coastal areas typically affected by HABs, as discussed in

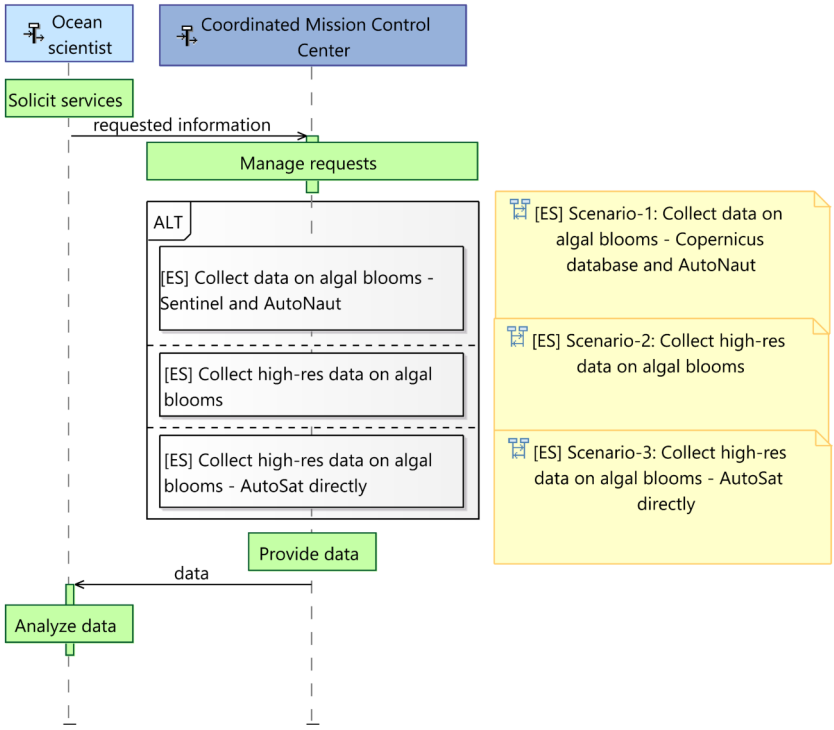

Figure D.4: Exchange scenario ([ES]) overview in a lifeline format. The dashed lines indicate the lifeline of the actor, and the solid lines indicate a functional exchange between a source and a target actor. A green box indicates a function, the grey box with [ALT] indicates choices between different ES. The yellow sticky notes are there for linking between diagrams for the user. The figure is modeled using Capella.

Section D.5.

Based on information from the available satellite observations, a user or data processing tool selects an area of interest for the AutoNaut to investigate. The latency of satellite data varies between 3 h and a day, depending on the chosen infrastructure (e.g., Copernicus Sentinels or other). The data spectral and spatial resolution may vary depending on the satellite source used.

This scenario requires a processing pipeline to be available. The data latency

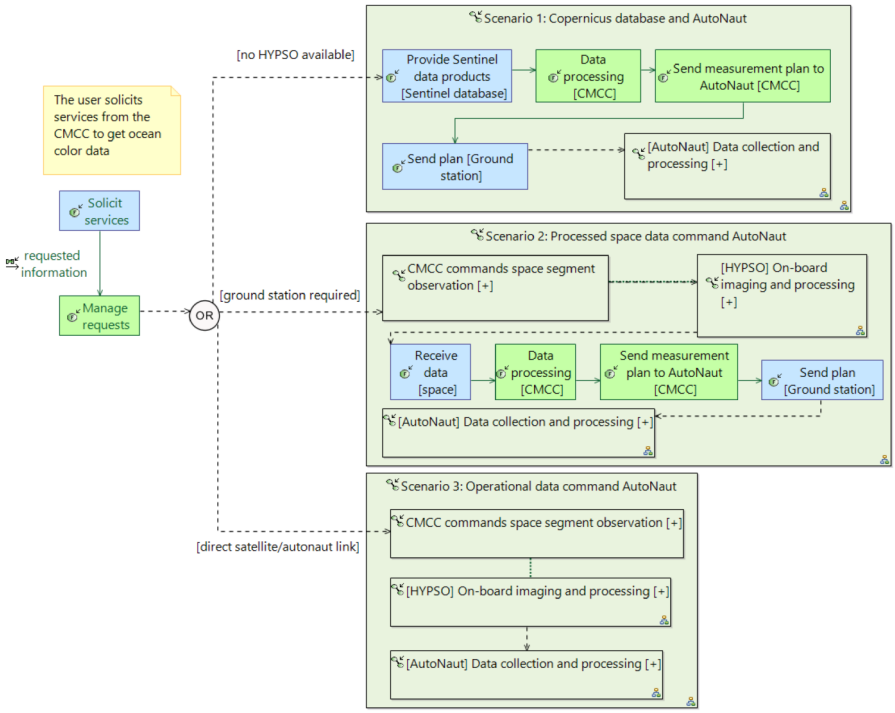

Figure D.5: Information flow in the different scenarios is shown as functional chains. Dashed lines signify sequenced exchanges, while solid lines signify functional exchanges. The blue boxes represent functions allocated to actors, and green boxes allocated to the system-of-interest (here, the CMCC). The [+] indicates that an element can be expanded but was not in this diagram to maintain the high-level perspective and clarity.

will be the sum of the age of satellite data products, the processing and commanding time, and the time needed for data collection and communication to shore from the sampling site. Whereas the time periods for information retrieval using existing infrastructures are usually known, the time required to retrieve to shore data collected in-situ depends on several factors as described in Section D.3.4.

Assumptions for Scenario 1 For Scenario 1, information about the AOI is made available to the AutoNaut based on the EO data processing at the

CMCC. This means that the data age is determined by the service level of the data provider, t_{dataage}. Assuming a well-programmed processing pipeline, the time for processing selected data, $t_{\text{processing}}$, will be very short compared with the data age. Furthermore, since this scenario uses existing infrastructure the communication delay, t_{transmit}, can be approximated to zero, since the communication delay through a 4G network or Iridium is negligible if compared to the time scale of the USV navigation capabilities (the distance covered in time) and to the time scale of the observed phenomenon. Hence, the only factor determining the freshness of the data product is the age and availability of EO data. A typical value for this parameter is in the range of 6 to 24 h.

Scenario 2: Dedicated Small Satellite—CMCC—AutoNaut

Small EO satellites, such as the HYPSO-1 satellite [119], enable more agile and customized operations. The use of such systems enhances the flexibility of the operations, such as the choice of the area to be monitored and use of reconfigurable and adaptive algorithms for compression and processing of the data to be downlinked. The satellite can transmit processed information directly to the CMCC obtained from single or multiple observations. The CMCC is responsible for the definition of the mission plan that should be communicated to the AutoNaut, and hence their communication to the USV, as shown in the middle path of Figure D.5.

After making an observation, the satellite must transit from the AOI to the next available ground station until it can transmit data to the CMCC. Similar to the previous scenario, the data product latency is a sum of response time needed for image processing, downlink, ground data processing and the time relaying the connected data and mission plan to the AutoNaut. The response time of the image processing includes uplinking to the satellite, the time it takes for the target to become observable and processed on board.

Assumptions for Scenario 2 For Scenario 2, we use a model simulated in Python utilizing the *PyOrbital* library for propagating the satellite that is set to observe a selection of AOIs. For each AOI pass, we compute the time until the satellite passes over a ground station and use that as an estimate

for when processed data can be delivered to the AutoNaut. The AOIs are defined by their center location to simplify simulations. In this case too, t_{transmit} can be neglected as the navigational plan data is assumed to be around 100 bytes transmitted over either 4G or Iridium, with a minimum bitrate of 1200 bytes per second for Iridium.

1. Since the HYPSO-1 is not launched yet, LUME-1 is used as a representative model. Two Line Elements (TLEs) are automatically obtained from Celestrack.

2. Minimum elevation for optical target observation: 20°.

3. Minimum elevation for radio communication to ground station: 0°.

4. Only daylight passes are considered: from 8:00 to 19:00 local time.

5. Only onboard processed data are considered to reduce the data size needed for downlinking.

6. Ground station locations from the KSAT Lite network are considered, see Figure D.7. Two simulations are compared; either using one station only, or the full network.

7. The downlink is based on S-band with 1 Mbps raw data rate.

The impact of assumption 2 is that the most extreme slant range passes are ignored, so every target is only observable one to three times a day. If omitting assumption 5, transmitting raw data from the satellite, we would need multiple passes to download the relevant data, which may take hours or days to complete ([119], Table VII), heavily affecting the t_{dataage}. The total time to download data will depend on the length of the observation. Transmitting on-board processed data, such as a target position, will take only seconds under the same conditions. The satellite used for simulations is LUME-1, built for the European project Fire RS from the joint efforts of the University of Porto (Portugal), LAAS-CNRS (France), Universidade de Vigo (Spain), and Alén Space (Spain) [87]. This satellite is in a representative orbit for HYPSO-1, thus simulation results are expected to be similar to what HYPSO-1 will experience.

For some targets, the satellite will see both the target and a ground station simultaneously. The simulations take this into account. Cases where the ground station contact ends at least four minutes after the observation ends to allow for processing time and downlinking are included in the simulation results. For these occurrences, both maximum, minimum and mean delays are set to zero. This also assumes that booking and scheduling of ground station passes are available so that the satellite can transmit data to the first ground station it passes over.

Scenario 3: Dedicated Small Satellite—AutoNaut

In the third and last scenario (shown in the bottom path of Figure D.5), we envisage a flow of information that makes no use of ground communication infrastructure. After a small satellite, such as the HYPSO-1, makes an observation, data is processed onboard, and instructions and a navigation plan are communicated to the terrestrial assets such as the AutoNaut directly. For example, target detection can be used to create a map showing the most likely locations of a particular spectral signature [172], [173]. Either the map can directly inform the path planning or be expressed in a simpler form, such as the most probable location of a bloom. HYPSO-1 plans to use the Adaptive Cosine Estimator for target detection, but Constrained energy Minimization and the Matched filter have also been developed.

The response time and data latency will, in this case, be the sum of the response time for imaging of the selected area, the processing time, the downlinking time, and sampled data transmission to shore. A central topic in this scenario is how to enable the communication infrastructure between the assets. This brings forth challenges with both the physical infrastructure needed (radios and antennas) and network management. This scenario requires that both assets know their location and the location of the other so that communication can be scheduled accordingly.

Assumptions for Scenario 3 We are considering the same target list and simulations as for Scenario 2. In addition, the satellite must reach the AutoNaut in a time-window that both allows on-board data processing and

transmission of the navigation plan to the AutoNaut before the satellite is out of view.

The data preparation (on-board processing) time after observations is assumed to be less than one minute. Furthermore, the resulting data volume is assumed small enough to be transmitted over a 10–100 kbps link for less than one minute. The size of the navigational plan and other needed information is assumed to be similar to what is the case today, which is around 100 bytes (see the assumptions for Scenario 2 above). The complete specification of this link is the topic of future work. This requires the AutoNaut to be in the AOI and within satellite coverage for at least one minute after data preparation for downlinking.

D.3.4 Constraints

Optical sensors operating in the visible range are affected by cloud coverage and, therefore, may have limited detection capabilities. The AutoNaut can be impacted by storms or other weather conditions that both can degrade the data quality and the maneuverability and response time of the AutoNaut. The encompassing system and services must consider CS constraints when defining the SOS operational scenarios and CS requirements.

In this section, we describe the high-level constraints that affect all architectural variants of the proposed system, namely, general constraints that affect the execution of the information flow and that are common to all scenarios.

Wave-Propelled USV Constraints

As most of the marine vehicles whose propulsion is produced by environmental forces, the AutoNaut capabilities depend on the sea state. The velocity of such vehicles is not controllable and therefore, to predict future locations, one must rely on estimates based on present and forecasted sea state. Situational awareness is achieved via onboard sensors that sample physical environmental properties and provide the vehicle control system

an estimated present sea state used to adapt the navigation control parameters. Stable course control can also be a challenge whenever the forces exerted by the environment dominate on steering and propulsion mechanisms, preventing the vehicle from following an intended path. The USV's speed and course are affected by waves direction, height, and frequency, and by surface currents and winds. This has a considerable impact on the AutoNaut capability to monitor oceanographic phenomena that occur far from its current location, as the time needed to reach a destination depends on the surrounding environments.

A second major limitation is the onboard energy available. The onboard battery bank is constantly harvesting solar energy produced by deck-mounted solar panels providing the necessary power to sensors and electric steering. Significant power limitations are experienced in winter at high latitudes, where light is not sufficient to recharge the batteries, and the time span of the mission may be reduced. This impacts the possibility of observing specific phenomena as too little energy might prevent the activation of a specific sensor. Moreover, power should not only suffice for sampling specific features but also to allow data transmission to shore (e.g., via Iridium, 4G or VHF) and navigation control.

Communication is the third constraint that affects operational flexibility. The USV is equipped with three communication links that are used depending on the type and amount of information to be transmitted and the location of the vehicle. Satellite communication (for example, through Iridium) constitutes a reliable link proven to work in most areas of the globe. However, this is costly and limited by the amount of data that can be transmitted. 4G/LTE communication allows transmitting a much larger amount of data even though it is limited by distance to shore. Finally, the VHF radio link, mainly used for telemetry and emergency situations, has a range of tens or hundreds of kilometers depending on the sea state and antennas location.

Data acquired onboard can be stored and transmitted over the mentioned links depending on the type of data and the vehicle location. For example, sea current information for the whole upper water column involves a large amount of data that can be easily transferred over Internet or WiFi, but cannot be sent over satellite. It is thus possible to transfer only key information over Iridium or, alternatively, let the USV navigate close to shore within

4G/LTE coverage. For example, key information about a specific water property could be the temporal average of the collected numeric values over predefined time periods.

Based on field experience, it is observed that the USV speed in the ocean fluctuates between 0 and 3 knots, depending on the sea state. Therefore we can safely assume that the vehicle is capable of traveling in average 30 km per day. Based on the time period of the phenomenon to be observed, the vehicle proximity to the targeted area is a constraint that must be considered during the mission planning phase.

Constraints for Small Satellites

Small satellites can be an agile tool since they are relatively cheap and have a short development time [174]. As satellites such as HYPSO-1 are small, they are influenced by physical constraints leading to system constraints impacting the power/energy availability due to a limited solar array area. Moreover, the size of the satellite may restrict antenna sizes, especially in the VHF and UHF-bands.

The power constraint comes into play in the sense that only a limited part of the Earth can be actively covered at the time because there is limited energy for payload operation and data downlink. A dedicated small satellite has the agility to accept any area of interest defined by the mission operators on short notice. Additionally, in EO missions that generate a large volume of data, both energy for operating the downlink radio leading to a time limitation, and data rates are constrained by physical antenna sizes and the availability of ground stations limits the amount of data possible to download every day. The challenge of data volume is mitigated by performing onboard payload processing, thus compressing the data and effectively reducing the data volume by several orders of magnitude. The limitations in coverage, the revisit time over a given area, is a function of the number of satellites in the network and can be mitigated by increasing the number of satellites and orbital planes.

For single satellites, there are some limitations in coverage and agility. The coverage area and accessibility at a given time of day are constrained but

well known and defined by the satellite orbit. This can be mitigated by adding more satellites, for example, in different orbital planes. The selection of the AOI must also be done in due time before the satellite passes over a ground station prior to a target pass, so the satellite can prepare for the observation. Initially, operators will determine the AOI by selecting a coordinate for the center of the image, but the development of more sophisticated AOI geometries is a topic of future research. Moreover, adding more ground stations at suitable locations will improve agility.

The integration of autonomous sensor agents into heterogeneous networks together with satellites either as independent sensors or communication relays has been studied in several surveys and proposals [102], [116], [124], [175], [176]. Networking principles enabling the network integration encompassing a multitude of agents, by employing standard toolchains and efficient network protocols as well as location-aware smart routing principles are discussed in [131], [177], [178].

Communication Technologies and Analysis

Scenario 1 will only make use of existing communication infrastructure; both between the EO-satellites and ground systems, as well as between the CMCC and the AutoNaut.

For Scenario 2, we can utilize existing radio links between the satellite and the ground stations. Correspondingly, the existing infrastructure for command and control for the AutoNaut can be used. To bind these two constituent systems together, a middleware layer with a messaging protocol must be developed and implemented.

For Scenario 3, the direct communication between the satellite and the AutoNaut must be based on new infrastructure. This is a research topic that should be further explored. It should be mentioned that the recent years have seen an increase in deployments of new satellite-based communication infrastructure, such as IoT-constellations [133] and megaconstellations such as Starlink, OneWeb or Kupier. However, the use of the megaconstellations is considered not relevant for our scenarios, as their ground terminals will be too big for the AutoNaut. Moreover, the available IoT solutions may

still not fill the gap created by low throughput, one-way data traffic, and their method of dealing with multiple access, like providing channel access for users at random time intervals. A limited number of communication channels suitable for each proposed scenario exists.

D.3.5 Other Architecture Variants

In addition to our suggested architectures discussed as Scenario 1 and Scenario 2; there are options for how the satellite and robotic agents such as the AutoNaut can be interconnected. The satellite could be equipped with equipment creating an Inter-Satellite-Link (ISL) between the small satellite and other space-based infrastructure instead of transmitting its observations to a GS. Possible options include "traditional" satellite phone/Machine-to-Machine communication (M2M) systems such as Iridium, Globalstar and OrbComm, "traditional" broad-band satellite systems as Inmarsat and Intelsat based on Geostationary Orbit (GEO) satellites, in addition to the new megaconstellations as well as new IoT-satellite constellations. The work behind this paper does not aim to evaluate and compare these options in full, but a brief discussion on the alternatives follows.

Previous studies encompassing mostly Iridium and Globalstar options have shown that such methods will allow for the transmission of a small amount of data, most likely to be adequate to direct the AutoNaut to an area of interest. Rodriguez et al. [179] have summarized several studies in their paper. Several activities are supported by NASA, for example, through their PhoneSat series. In 2021, Riot et al. presented results from an on-orbit experiment which found that an LEO satellite equipped with an Iridium transmitter will be able to deliver low volumes of telemetry within a 30-min delay, for about 90% of the time [180]. This result is comparable to our results for sparse ground stations, see Section D.5.2.

Making use of networks meant for terrestrial use on-orbit, also means that we will have similar constraints for parameters as Doppler shift and maximum usable range, limiting the usable service area from, i.e., the Iridium satellites [180]. In addition, more constraints follow from the combination of orbits, where the inclination has the largest effect. This leads to the case that ISL to low-inclined services (such as OrbComm, Globalstar) are not

ideal for polar-orbiting satellites. The same will be the case for crosslinking from LEO to GEO for Inmarsat services, for example.

D.4 Methods

D.4.1 Description of Workflow

We followed a simple workflow shown in Figure D.6 for the research provided in this paper. In the *Modelling and developing operational concept* phase, we applied a combination of a whiteboard, virtual meetings and drawings, and discussions to develop the operational concepts, and used literature to identify relevant AOIs. These operational concepts were modeled in Capella and iterated on through discussions. In *Simulations of scenarios*, we set up the scenarios for the simulations with the assumptions given for each scenario in Section D.3.3, and *Analyzed results* to improve the simulations, the scenarios and ensure that our assumptions were valid. The AutoNaut *Field work* experiences were used to validate the results, and to provide feedback to the assumptions and simulations.

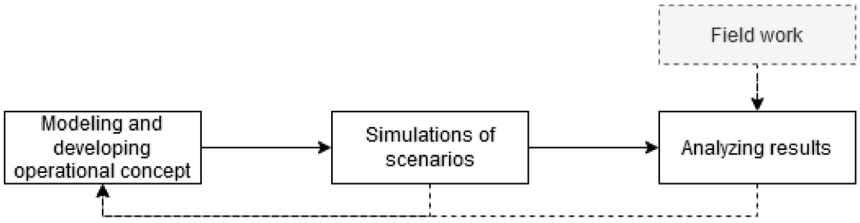

Figure D.6: The workflow applied in this work.

D.4.2 Tools Used

In this analysis, we have used the Arcadia method [181] with the open-source Capella software tool (Web page: `https://www.eclipse.org/capella/`) to support the Model-Based Systems Engineering (MBSE) effort and provide an operational and logical architecture of the SOS [182].

The system model enables the representation of the architecture with different viewpoints, such as "exchange scenarios", "context diagrams," and "architecture diagrams." There are also possibilities for integration with domain-specific tools such as System Tool Kit (STK), that can be used to demonstrate the quantitative performances of the proposed SOS.

The simulations have been performed using Python, in particular using the *pyorbital* library. This library calculates orbital parameters and computes other astronomical parameters from satellites' TLEs. The TLEs are collected from Celestrak [183].

D.4.3 Selection of Areas of Interest

The objective of the SOS is to detect but also sample in-situ oceanographic phenomena remotely. We choose to observe areas that have historically been affected by phenomena such as HABs. Since HABs can result in the death of farmed fish; the targets selected for our simulations are areas where fish farming is common. The selected targets are popular areas for fish farming, and where HABs may occur (see [184] for an overview). These are the Norwegian Atlantic coast near Frøya, the coast of Chile south of Puerto Montt, the coast of Canada near Vancouver Island, the coast of Tasmania in Australia and Lake Erie [185], a fresh-water lake in the US where HABs are common. These locations and the considered ground stations are shown in Figure D.7.

D.4.4 Communication Delay Estimation

One of the key metrics for evaluating the performance of the data flow and utility of the SOS is the data delay, meaning the time from observation to the data is available for the AutoNaut. In this case, the "data" is the navigational plan and all information needed for the AutoNaut to perform its operations. The time for returning samples and analysis from the AutoNaut will be the same for all three scenarios, so this duration is omitted in further discussion.

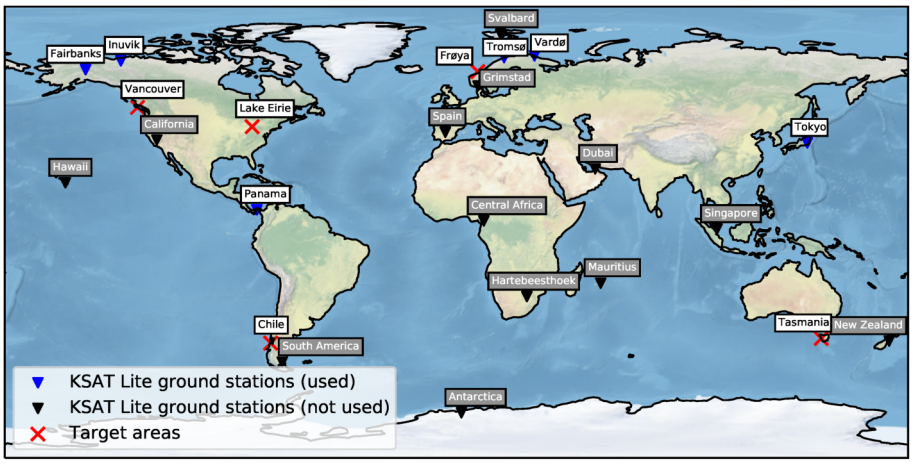

Figure D.7: Areas of Interest and considered ground stations. The ground stations with blue symbols and white labels were selected by the simulator, the stations with black symbols and grey labels were available but not used. The areas of interest are indicated with a red cross.

Equation (D.1) shows how we estimate the total delay in time (t_{total}) between when an observation of an oceanographic event of an AOI is made, to when the AutoNaut is notified and commanded to investigate this event in-situ. t_{dataage} is the age of the observation data until it is processed either on ground or in-orbit, $t_{\text{processing}}$ is the time spent for data processing and t_{transmit} is the time it takes to transmit a set of commands to the AutoNaut.

For Scenarios 1 and 2, t_{transmit} is assumed to be equal since both cases rely on using the same communication infrastructure from the CMCC to the AutoNaut. The value for this delay is in the range of hundreds of milliseconds to a few seconds, based upon 4G or Iridium. The range for the processing time, $t_{\text{processing}}$, is from seconds to a few minutes. The value for t_{transmit} is assumed to be less than two minutes. This is based upon the assumptions for the communication links listed above and the size of the navigational plan, which is about 100 bytes.

$$t_{\text{total}} = t_{\text{dataage}} + t_{\text{processing}} + t_{\text{transmit}} \tag{D.1}$$

D.4.5 Simulations

Based on the above assumptions, a short Python program was implemented to generate a set of times for when the satellite can observe the targets, and deliver the observational data either to the CMCC through a ground infrastructure (Scenario 2), or directly to the AutoNaut (Scenario 3). For Scenario 2, two different simulations were performed, one with only one ground station, and one with all the ground stations of the KSAT Lite network available.

The function called *get_next_passes* from *pyOrbital* library was used to estimate when the satellite was over the ground stations and the target areas. The main parameters specified for the simulations are: start date [exact date and time to start the simulations], number of hours to simulate, coordinates of observation location [longitude and latitude] altitude above sea level and minimum elevation for contact between location and satellite [minimum elevation for a pass]. The simulation start date was set to 2021-06-09 16:00 and the time to simulate for a week. First, all possible passes over the targets and the ground stations are computed. The passes over the targets are limited to those during daylight [between 8:00 and 19:00 local time]. For each target pass, the delay is estimated as the difference between the start time of each ground station pass and the end time of the target pass. When the difference between the end of a ground station pass and the end of a target pass is longer than a minimum communication window, the delay is saved. The ground station whose pass offers the minimum delay after an observation of a target is considered the first ground station used. The maximum delay and the mean delay are calculated for each target pass. The simulations are performed both for a sparse ground station network [just one ground station] and dense ground station network [where six ground stations are used].

D.5 Results

In this section, the different scenarios and their utility are explored.

D.5.1 Scenario 1: Coordinated Observation of HABs

The information flow described in Scenario 1 was tested in the field in Spring 2021, in the context of HAB coordinated observation involving both aerial and terrestrial platforms. This experiment involved several manned and unmanned robotic assets for a duration of over one month and the objective of the field campaign was to study the algal bloom at different space and time scales, from satellite observations of the whole Frohavet region down to the underwater sampling of the epipelagic (upper) water column. In particular, satellite-based imagery was acquired from Sentinel-3, Terra and Aqua (MODIS data) and PRISMA (https://www.asi.it/en/earth-science/prisma/) when available. The imagery, see Figure D.8, recorded on 14 March was used to monitor the growth of the algal bloom in the operational area and assist with high-level mission planning and coordination of the involved robotic platforms gathering in-situ measurements.

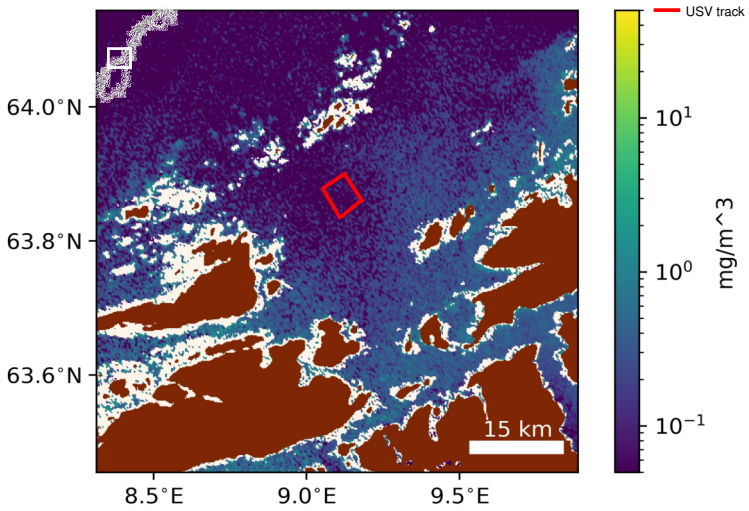

Figure D.8: Sentinel-3 imagery of chlorophyll-a concentration in Frohavet (mid-Norway) on 14 March 2021. The AutoNaut track in Frohavet is shown in red. In the top left corner the location of Frohavet in Norway is depicted.

Among the assets, the AutoNaut was the first deployed, and it provided the overall mission insight into how algae grew and multiplied in the period leading up to the bloom. The wave-propelled AutoNaut was at sea for a

total of 24 days, collecting and transmitting data continuously over 4G and Iridium communication. In addition to providing additional long-term insight into the algal bloom dynamics itself, the wave-propelled USV collected data to be used to validate hyperspectral cameras carried by the involved UAV and airplane.

Figures D.8 and D.9 also show the track covered by the AutoNaut in Frohavet on March 14th and the surface chlorophyll-a data collected in-situ. It can be observed that the surface chlorophyll-a measurements performed by AutoNaut validate the Sentinel-3 observations in the same area.

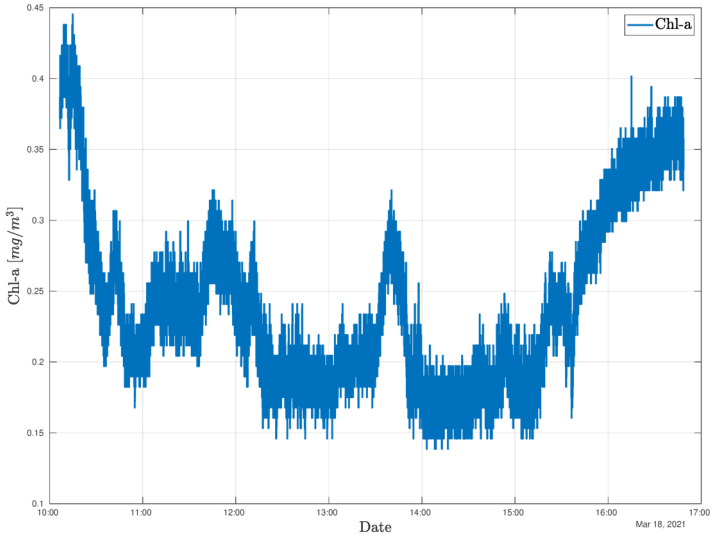

Figure D.9: In-situ chlorophyll-a measurements collected by the AutoNaut in Frohavet.

D.5.2 Scenario 2: Satellite—CMCC—AutoNaut

The delay from an observation to the CMCC was simulated for two different sub-cases; one with only one ground station available. Svalbard is selected as it is seen by all revolutions by a polar orbiting satellite. This is called a *sparse* ground station distribution. The second run where all the ground stations of KSAT Lite network were available is called *dense* ground station coverage. This delay will give an estimate for the t_{dataage} for this scenario.

The simulation is run for one week starting from 9 June 2021. The satellite orbit is based on TLEs for the LUME-1 satellite, received from Celestrack. LUME-1 moves south-to-north over Western Europe during daylight hours. In both cases it is assumed that the AutoNaut is within 30 km of the center of the AOI, as this is the range the AutoNaut may navigate during the day.

Sparse Ground Station Coverage

For Scenario 2, the satellite will acquire and process the data, before it needs to reach a GS to forward the data to the CMCC for final processing and forwarding to the AutoNaut.

With t_{transmit} in this case being similar to Scenario 1, $t_{\text{processing}}$ is similar to Scenario 3, it is again t_{dataage} that will be the driving factor for t_{total}.

From the column named *Delay stats for single GS* in Table D.1, we can see that for a single ground station, the delay (meaning the duration after an observation until the satellite can reach the ground station at Svalbard) varies from about 0 minutes for the Frøya target to about a half hour for Chile and Tasmania targets. This duration/delay corresponds to the value for the parameter t_{dataage} in Equation (D.1).

Table D.1: Statistics for dense and sparse ground station coverage (mm:ss) for one week, showing the delay from end of an observation to the first available ground station.

	Delay Stats for Single GS			Delay Stats for GS Network		
	min	max	mean	min	max	mean
Lake Erie (USA)	06:38	07:59	06:59	01:53	03:34	02:31
Western coast of Chile	29:58	31:08	31:08	05:56	10:40	07:42
Tasmania (Australia)	27:46	28:28	28:09	12:25	15:01	12:22
Vancouver (Canada)	05:40	06:59	06:08	00:00	00:00	00:00
Frøya (Norway)	00:00	00:00	00:00	00:00	00:00	00:00

Dense Ground Station Coverage

Column *Delay stats for GS network* in Table D.1 shows the results for the minimum time after an observation until the satellite reaches a ground station, given the availability of the full KSAT Lite ground station network. From the simulations, we see that the mean time to reach a ground station varies between 0 and less than 13 min, depending on the target location. For all targets with a delay larger than 0, there is a reduction compared to the sparse ground station setup. Tasmania and Chile targets get their mean delays more than halved.

The number of instances for when a ground station was the closest after a target observation is shown in Table D.2. Such mapping can also be used to derive and plan which stations should be utilized, and which stations can be removed to reduce cost, for example. Since the satellite is in an Sun-Syncronious Orbit (SSO) type orbit, where we only are interested in daylight passes, the same ground stations will be utilized every time. From the table, we observe that maximum two stations are needed for each target. In this particular case, we observe that Inuvik is the station that may collect data from the highest number of targets.

Table D.2: Count of first ground station used after each target for the simulated period.

	Inuvik	Panama	Tokyo	Fairbanks	Vardø	Tromsø
Lake Erie	7	0	0	0	0	0
Chile	0	8	0	0	0	0
Tasmania	0	0	7	0	0	0
Vancouver	3	0	0	6	0	0
Frøya	0	0	0	0	4	10

D.5.3 Scenario 3: Direct Communication between Satellite and USV

For Scenario 3, the observation time, including on-board processing, represents the value for t_{dataage}, and is in the range of one to two minutes [119].

The short on-board processing time, $t_{\text{processing}}$, (about one minute) allows for transmission of a short message to the AutoNaut immediately after an observation is made, given that the AutoNaut is in the vicinity of the AOI. The observation time is set to 2 min for all occasions, starting when the satellite is at Acquisition of Signal (AOS). This is following the operational concept of the HYPSO-1-mission [119] plus a one-minute margin. This scenario is depicted in Table D.3. In this case, the value for t_{transmit} will be in the order of seconds for transmission of navigation coordinates and instructions. The total delay, t_{total} is then within two to three minutes, near real-time operation is possible.

Table D.3: Simulations of target observations and communication windows to the AutoNaut.

Target	Target AOS	Target LOS	Target Max Duration	Target obs. End	Autonaut LOS	Avail. Time for Comms
Lake Erie	15:16:35	15:21:15	00:04:40	15:18:35	15:24:34	00:05:59
Chile	13:20:37	13:23:01	00:02:24	13:22:37	13:27:14	00:04:37
Chile	14:53:50	14:56:43	00:02:53	14:55:50	15:00:42	00:04:52
Tasmania	00:44:48	00:48:53	00:04:05	00:46:48	00:52:29	00:05:41
Vancouver	18:50:53	18:55:16	00:04:23	18:52:53	18:58:42	00:05:49
Frøya	07:32:35	07:34:46	00:02:11	07:34:35	07:38:54	00:04:19
Frøya	09:04:29	09:09:19	00:04:50	09:06:29	09:12:35	00:06:06

Table D.3 shows all daylight passes for the 16 April 2021, with times in Universal Time Coordinated Orbit (UTC). The columns indicate when the target is visible which is the time between *Target AOS* and *Target LOS*. This gives a total possible observation time. Furthermore, 2 min was chosen as the actual observation time, leaving a given duration available for processing and communication between the observation end and the AOS-event for the AutoNaut.

D.6 Discussion

We consider the three different architecture variants as introduced, and through simulations and analysis, we present the main findings that were focused on satisfying a HAB use-case. The architecture variants are generic but are exemplified and evaluated through simulations employing properties

of the HYPSO-1 satellite and the AutoNaut as example implementations. The main advantage of the proposed solution is that the multi-asset and multi-sensor approach can enable near real-time coordinated oceanographic observations of HABs, which are challenging to detect and classify.

Main results:

- In Scenario 1, the t_{total} is expected to be 3–24 h, based on the "publishing time" for traditional EO-data. This limits the operational real-time use of this type of data. In addition, the AOIs cannot be selected by the end-user.
- For Scenario 2, the mean value of t_{total} is less than 16 min for a dense ground stations network, and less than 30 min for all selected targets if only a single ground station is used.
- For Scenario 3, the t_{total} is estimated to be on the order of 1–3 min, given the assumptions listed.

Even without direct contact between a satellite and a USV, it is possible to transmit fresh EO-data from a remote sensing satellite to an in-situ vessel as the AutoNaut within 30 min for most cases. The use of on-board processing and existing infrastructure will make this scenario possible with little cost and effort. Depending on resources and delay requirements, one or more GSs from a commercial ground station supplier can be used to enable this. Which GS to use can be decided based on simulations, as shown in this paper. A CMCC must be in place, integrating the communication satellite and the USV(s) through a common middleware layer.

D.6.1 Scenario Evaluation

The three scenarios are analyzed and discussed in the following.

Scenario 1

In Scenario 1, no efforts are needed to ensure periodical delivery of the required imagery. Moreover, several EO data sources are accessible for no cost. Despite these advantages, the chosen services and infrastructures are not configurable, so the end-user cannot select the AOI the EO-satellites will observe and have instead to rely on historical data and a "best-effort" revisit time. Moreover, the age of the observational data is arbitrary and near "real-time" operation with a data age requirement of less than 6–24 h cannot be supported. This would affect the in-situ observation and sampling of targeted phenomena which are commonly defined in a limited time frame.

A processing pipeline for selecting/filtering and processing of the EO data must be created, and can be based on existing frameworks and technologies. In addition, a middleware layer integrating the processing pipeline and the commanding software for the AutoNaut must be developed, but no other infrastructure will have to be developed. An example of this scenario is provided in Section D.5.1, where satellite imagery from existing infrastructure is used to command marine and aerial assets with the purpose of observing a HAB.

Scenario 2

In Scenario 2, we estimate the time from when a dedicated satellite makes an observation until this data can be for instructions and navigation plans for the AutoNaut. Similar to Scenario 1, this scenario also relies on existing infrastructure, except for the need of an CMCC with a processing pipeline and middleware layer able to integrate messages between the satellite and the AutoNaut. A dedicated satellite that can be commanded to observe selected AOIs may deliver information to the AutoNaut 30 min later, even if only one ground station is used (this time will vary depending on the target locations.) If a full GS network is used, this time can be further reduced, down to about 15 min. As shown, targets within Arctic/sub-Arctic areas are close to existing GSs; thus the time between an observation and a downlink pass may be close to zero.

Even with using only one ground station, we see that for the case of Frøya (Norway) the satellite will see both the target area (Frøya) and the ground station (Svalbard) at the same time for part of the observation pass. This means that the data can be downloaded immediately after processing. For the simulation, useful communication passes must end at least 4 min after the observation ended. This in order to have time to do both processing (limited to one minute, similar to Scenario 3) and perform downlinking in a reasonable time. All passes in this simulation leave more than 5 min for downlinking.

When making the full GS-network available for the simulation, the simulator will choose the closest usable ground station in each case. For example, we see that the assumed best station (Svalbard, as it is seen from all satellite orbital passes) is then not used since other stations can pick up the signal from the satellite earlier. In addition to utilizing existing infrastructure, the main advantage of Scenario 2 is that satellite data can be requested and retrieved on-demand. On-board data processing will reduce the size of data to be transmitted to ground, thus reducing energy for operation of the radio system as well as the time to download the data. Selecting the number and locations of GSs will impact the response time of the system, and possibly also influence the cost of ground station lease, depending on the commercial model of the ground station provider (if accessing more than one GS costs more than one, or if it only is the time of access that determines the cost).

Scenario 3

The main advantage of Scenario 3 is that, depending on the communication delays between the satellite and the USV, the closed-loop from space observation to in-situ sampling and data analysis on shore observation of an oceanographic phenomenon can be achieved with lower data latency and time responses compared to Scenarios 1 and 2. Despite such benefits, this implementation comes with some limitations concerning the data processing capabilities on-board both assets, the need of resilient algorithms for human supervision/intervention and a robust communication link between the assets. The possibility of adding onshore processing and data from other sources in Scenario 2, as the CMCC can make use of larger computational capabilities to run complex metocean models on the base of satellite ob-

servations, may outweigh the gain of a faster response in Scenario 3. This could help to optimize the missions commanded to terrestrial assets and thus the quality of data retrieved to shore.

D.7 Conclusions

Our analysis indicates that an architecture like the SOS presented in this paper can be used for tailored and adaptive observation systems, adapted to their specific target areas. The commonality of a generic architecture consisting of satellite(s), a CMCC, and in-situ agents can be utilized to observe a great variety of oceanographic properties and geographic regions. The specific satellite and in-situ platform and instrument can be adapted to season or other properties.

The specific properties of the different architecture variants can be exploited to match different purposes, and they come with different costs for implementation and resources for realization. Scenario 1 is available today, as demonstrated in our field experiment. The real-time constraints of this scenario as well as the limitation in an active selection of AOIs, motivates the exploration and development of Scenarios 2 and 3. Like Scenario 1, Scenario 2 is available with existing technology, or technology available in the near future. Scenario 2 can provide fresh data, both for a dense and sparse ground station topology. The cost of using more ground stations has to be traded against the gain of getting data up to 1 to 20 min earlier. Optimal ground stations can be chosen based on target selection and similar simulations, as shown in this paper. Even though the difference in data delivery times between those scenarios is on the order of 30 min. in favor of Scenario 3, the architecture variant of Scenario 3 represents the possibility of tighter integration between sensor agents, without the need of inclusion of a CMCC.

Author contributions Conceptualization, A.D., G.Q.-D., E.H.-L., R.B.; methodology, A.D., G.Q.-D., E.H.-L., R.B.; software, G.Q.-D.; validation, all authors; data curation, G.Q.-D., J.L.G., R.B.; visualization, J.L.G., A.D., G.Q.-D.; writing—original draft preparation, all authors; supervision, T.A.J.;

project administration, T.A.J.; funding acquisition, T.A.J. All authors have read and agreed to the published version of the manuscript.

Funding This research is supported by the Norwegian Research Council (grant no. 270959), the Norwegian Space Center, and the Centre of Autonomous Marine Operations and Systems (NTNU AMOS, grant no. 223254).

Acknowledgments The authors would like to thank Stéphane Lecrampe for his support for using Capella.

Conflict of interest The authors declare no conflict of interest. The funders had no role in the design of the study; in the collection, analyses, or interpretation of data; in the writing of the manuscript, or in the decision to publish the results.

Part III

Publications on interference measurements

D

E Detection of radio interference in the UHF amateur radio band with the Serpens satellite

The text of the following paper is added as a chapter and re-formatted for better readability:

G. Quintana-Diaz, D. Nodar-López, A. González Muíño, F. Aguado Agelet, C. Cappelletti and T. Ekman, 'Detection of radio interference in the uhf amateur radio band with the serpens satellite,' *Advances in Space Research*, vol. 69, no. 2, pp. 1159–1169, 2022, ISSN: 0273-1177. DOI: https://doi.org/10.1016/j.asr.2021.10.017. [Online]. Available: https://www.sciencedirect.com/science/article/pii/S0273117721007778

Abstract High packet losses when uplinking commands to small satellites have been reported in the UHF amateur band (430-440 MHz) since late 2013. Measurements of the uplink radio environment have shown high levels of in-band interference in previous works, but public measurement results are limited. Average interference levels are usually measured over some time to build heat maps. In this paper, the analysis is focused on sustained interference over a 24 ms time window using a maximum-minimum method. New heat maps and interference power distributions over Europe, Africa, the Middle East and the Americas were obtained using this method on measurements from the Serpens satellite . One of the missions of Serpens was to test an in orbit store-and-forward communication system to exchange short messages with ground sensors for disaster monitoring. The satellite operators had difficulties commanding the satellite due to interference, causing bit errors in uplink packets. Interference power of up to -70 dBm was detected during in-orbit measurements over Europe and North America, while expected received power from the ground stations was not more than

-80 dBm. High power space-object tracking radars on the ground operating in the 420-450 MHz band could be the cause, but further measurements are required to verify this. Characterizing this interference can help develop mitigation techniques for future satellite communication systems.

E.1 Introduction

Telemetry, Tracking and Command (TT&C) operations of small satellites have traditionally been performed in frequency bands below 1 GHz [186]. Most of these satellites have used VHF and UHF amateur radio bands with limited bandwidth (typically 25 kHz) [187]. Operators of this type of satellites experience difficulties when communicating with their satellites using the UHF band, especially when uplinking commands [48], [60]. At Technische Universität Berlin (TU Berlin), loss of commands was experienced with the TUBSAT satellites over certain regions [48]. Uplink of commands to the UWE-3 satellite by the operators at Universität Würzburg was also challenging [60] due to interference in the 435-438 MHz band. In 2014, the average uplink failure rates for UWE-3 were 90-95% and reached 98-100% for some passes. Strong interference levels can prevent the correct demodulation of commands on the satellite receiver leading to limited satellite capabilities and loss of communication on some occasions.

Similar problems were experienced during the Brazilian Serpens mission by the University of Vigo (UVigo) team. The Serpens satellite had two missions: first, to serve as a technological demonstrator in the VHF band, and second, to test a UHF communication system as part of the Humanitarian Satellite constellation (HumSat) project. The latter offered a data store-and-forward system for ground sensor terminals [188], enabling exchange of short messages with a packet-based Machine to Machine (M2M) communication system. The shorter revisit time of small satellites in Low Earth Orbit (LEO) is useful for disaster monitoring efforts and data collection from ground sensors in remote areas [84], both of which benefit from frequent observations to track environmental change over time.

Communicating with the Serpens satellite was challenging due to high packet loss rates on the uplink. In-orbit radio measurements were performed to

investigate the cause of these difficulties. Strong interference signals affecting the uplink were detected over certain areas of the world. Short interference events can cause a high packet loss rate, even if the interference varies over time. Therefore, exploring the duration of the high-power interference signals is important for knowing the usable length of the communication packets. Analysing only average interference levels provides a superficial measure of the impact of the interference in a packet-based system. Strong and short interference bursts can have low average power but can cause enough packet error loss to prevent communication.

The focus of this paper is to estimate the severity of interference for satellites in LEO using the UHF amateur band 430-440 MHz and identify which geographical areas are affected by analyzing in-flight measurements from the Serpens satellite. The next section summarises the radio regulations in the frequency band and the state-of-art of radiofrequency (RF) spectrum measurements in the UHF amateur radio band from space. In Section E.3, the system architecture of the Serpens satellite and the measurement algorithm are described. The measurement results are presented in Section E.4, followed by the discussion and a simple link budget in Section E.5. Conclusions can be found in Section E.6.

E.2 Related work

The frequency spectrum is a scarce resource for radiocommunication and its use is regulated by the International Telecommunication Union (ITU). Satellites use space radiocommunication services, and thus, the operators should send an Advanced Publication Information (API) to notify the ITU of the frequency assignment. If the satellite is part of the radio amateur service, the International Amateur Radio Union (IARU) should also be involved in the frequency coordination process for the amateur radio part of this band [41].

Small satellites are not considered a separate class of satellites with regards to frequency filings, but they are referred to as *short-duration mission* satellites. The number of satellites with a mass between 1-10 kg launched during the past ten years has dramatically increased and is expected to keep

increasing in the next years [49]. However, not all satellites have applied to the ITU for frequencies. Between 2003-2014, there were 341 nanosatellite and picosatellite launches, but only 31.4% had filed an API [41]. Therefore, knowing the real use of the frequency spectrum in space without measuring it is challenging.

The UHF spectrum is divided into many bands and each band is dedicated to one or more types of services depending on the ITU region [42]. In the 430-440 MHz band, there are three services: amateur radio (430-440 MHz), radiolocation (420-450 MHz), and Earth exploration-satellite (432-438 MHz) [42]. Amateur radio and radiolocation are primary services in ITU region 1; Earth Exploration-Satellite service is a secondary service. Secondary services may not create harmful interference to primary services and are not protected from interference generated by primary services. In ITU regions 2 and 3, amateur radio is a secondary service, while radiolocation is a primary service.

The radiolocation service includes high-power ground, airborne and ship-borne radars. Some characteristics of the ground radars are described in the ITU-R M.1462-1 recommendation [44]. There are three types of ground radars: type A (space object tracking), type B (high altitude surveillance), and type C (surface and search). The characteristics of the radar types are summarized in Table E.1. Type-A radars have transmit power of up to 5 MW and could cause interference in satellite uplinks since they are used for space-tracking. These radars operate all year round, scanning the sky from 3° to 60° of elevation and in 120° azimuth sectors. In Figure E.1, the locations of identified type-A radars according to ITU recommendations, are marked with red dots.

Due to the communication problems when uplinking commands to small satellites and the lack of knowledge of the real frequency usage and environment of the UHF band in space, a few universities and companies have started to measure the spectrum using satellites in the last few years [48], [55], [56], [60], [61]. However, there is still a need for continuous spectrum monitoring because of the increase of small satellite launches, the fact that not all satellites file the required API to the ITU, and that public measurement data is limited. So far, the focus of most measurement studies has been to estimate heat maps and average interference values without considering the duration of strong interference or its power distribution.

Table E.1: Characteristics of ground radars in the 420-450 MHz band [44].

Parameters	Radar A	Radar B	Radar C
Peak output power (MW)	1–5	0.3	0.01
Antenna gain (dBi)	38.5	28-40	10
Polarisation	Circular	Circular	Circular
Pulse duration (ms)	0.25, 0.5, 1, 2 4, 8, 16	0.01-16	0.001-1
Pulse frequency modulation	Search: 100-350 kHz chirp Track: 1 or 5 MHz linear chirp	2 MHz linear chirp	1 or 0.3 MHz linear chirp
Pulse repetition frequency (Hz)	up to 41	15-400	100-3000
Antenna beamwidth in azimuth (°)	2.2	1.8 typical	80
Antenna beamwidth in elevation (°)	2.2	1.8 typical	60

Figure E.1: Identified type A ground radar location in the 420-450 MHz band as defined in [44], [45]. 1: Massachusetts (United States of America (USA)), 2: Texas (USA) , 3: California (USA), 4: Georgia (USA), 5: Florida (USA), 6: North Dakota (USA), 7: Alaska (USA), 8: Thule (Greenland), 9: Fylingdales Moore (United Kingdom), 10: Pirinclik (Turkey)

.

The operators of the UWE-3 satellite at Universität Würzburg (Germany) experienced difficulties in the uplink in 2013-2014 and carried out in-orbit measurements in the 435-438 MHz band to investigate the problem. Using Received Signal Strength Indicator (RSSI) levels, the measured interference over central Europe was higher than over the Pacific. During a pass over Würzburg, the interference reached powers of -70 dBm at 437.385 MHz but was not detected at 436.6 MHz. The authors suggested that in-orbit reconfiguration of the carrier frequency could improve the link quality [60].

At UVigo (Spain) some preliminary measurements were performed after detecting strong interference in the test phase of the HumSat-D satellite in 2014. The communication system was based on the HUMsat PayLoad (HUMPL). Strong, pulsed interference was detected over the northern hemisphere in the 430-440 MHz band. The interference source was identified as one of the ground radars operating in the 420-450 MHz band from a site in the United Kingdom (UK) [48]. However, the measurements were limited to predefined frequencies and small areas, so the authors suggested the need to carry out further measurement campaigns and compare results with other satellites [61].

There have also been two projects at TU Berlin (Germany) to monitor the frequency spectrum. In May 2018, a Software-Defined Radio (SDR) payload was sent to the International Space Station (ISS) as part of the MarconiSSta project [189]. The goal was to measure received signals in space for the VHF, UHF, L-band, and S-band frequencies. The resulting heat maps made for the UHF band showed high average interference over both North America and Europe [48]. The payload was removed from the ISS in February 2019. As of the writing of this paper, the data is still being analysed. The use of an ISS-type orbit constrains the area of the sub-satellite points to between -51.6° and +51.6° latitude. In order to carry out measurements without this limitation, TU Berlin launched a small satellite called Spectrum AnaLysis SATellite (SALSAT) in September 2020 [48].

Over the past six years, new businesses have emerged to address the increasing need for spectrum monitoring. Hawk Eye 360 [55] and Aurora Insight [56] are two companies that offer frequency spectrum data services by measuring the radio environment with their satellites. Hawk Eye 360 launched their second cluster of small satellites to geolocate RF emitters on the ground in January 2021, after demonstrating proof-of-concept with their

first cluster [190]. Aurora Insight has also begun commercial measurements of the frequency spectrum with small satellites. Their first satellite was launched in 2018 as an in-orbit demonstration mission and their second satellite was put into orbit in January 2021 [56].

The contribution of this paper is to present a measurement methodology to detect strong sustained uplink interference and radio measurements from the Serpens satellite to complement existing measurement results. New heat maps and the power distribution of measured consistent uplink interference for areas in Europe, Africa, the Middle East and the Americas are estimated. Regions with low levels of consistent uplink interference are identified; these are better suited for M2M communication for collection of ground sensor data compared to regions with higher interference levels. Furthermore, this paper provides lessons learnt from these interference measurements that can be used to tailor future measurement and analysis methods to improve interference characterisation.

E.3 Interference measurements with the Serpens satellite

The Serpens satellite was a Brazilian 3U Cubesat, launched on 17 September 2015 in an ISS-type orbit. The project was led by a consortium of Brazilian universities, with the participation of UVigo and several other international universities [84]. The satellite was divided into two different sectors for the different missions and payloads. Sector A was an educational project to demonstrate technology developed by a group of Brazilian universities. Sector B was developed by UVigo (Spain) and was part of the HumSat system. The HumSat project is an initiative from the United Nations Office for Outer Space Affairs (UNOOSA), the European Space Agency (ESA) and the International Astronautical Federation (IAF) to provide a communication system for remote areas or natural disaster areas. The idea is to provide the service by means of a constellation of small satellites with a store-and-forward communication system [85]. In this paper, the focus is on the UHF communication mission in sector B.

Previously, the HumSat-D satellite was developed by UVigo as part of the

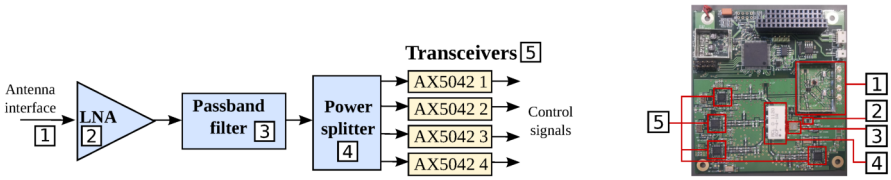

(a) RF payload architecture based on the diagram from [85].

(b) Payload board adapted from UVigo [61].

Figure E.2: HUMPL payload used both in HumSat-D satellite and Serpens satellite.

HumSat project [85]. In 2014, strong interference was detected in the uplink [61]. Lessons learnt from HumSat-D were applied on Serpens to enhance the mission. This included the implementation of an error-correction code in the radio protocol to mitigate the expected interference [85].

E.3.1 RF payload architecture

The communication payload in sector B (HUMPL) was used for in-orbit demonstration of communication between the satellite and ground terminals, and also for the interference measurements described in this paper. A turnstile antenna consisting of four monopoles was shared between TT&C and the payload.

The antenna interface in Figure E.2 consisted of the feeding network to adapt the signal to the monopoles and an antenna switch. The front-end of the payload was connected to the antenna switch to receive the RF signal. The front-end included a Low Noise Amplifier (LNA) from Avago Technologies (MGA-62563), a passband filter from Golledge Electronics Ltd (TA0693A) and a splitter from Minicircuits (SCP-4-1+) as shown in Figure E.2. The splitter was connected to the receiver part of four transceivers from ON Semiconductor (AX5042) [90].

The center frequency and bandwidth of each receiver was configurable. For interference measurements, the payload used an operational mode with different configurations of bandwidth, centre frequency and measurement duration. COMMS mode was used for low-data rate M2M communication

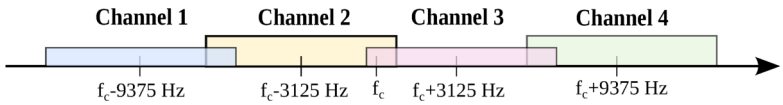

Figure E.3: Overlapping bandwidths of the four receivers in COMMS mode.

and simultaneous power measurements in the four receiver channels. The receiver channels had slightly overlapping bandwidths as seen in Figure E.3.

E.3.2 Interference measurement algorithm

The measurement algorithm used was designed for calculating the power of received packets whose length were hundreds of milliseconds. This algorithm was implemented on the payload before launch. Due to uplink communication challenges experienced during satellite operations, the algorithm was configured, within its limitations, to measure the in-orbit interference environment. The configuration parameters used for the measurement analysis in this paper are summarized in Table E.2. All the measurements presented in this paper were performed while the satellite's transmitter was switched off and were downlinked afterwards using limited data throughput. Power samples were obtained using the RSSI measurements in the AX5042 chips [90]. The right length of the power measurement buffer (M) was calculated empirically during the development of the payload, analysing the error of the RSSI value estimated by the AX5043 transceiver in the laboratory. The value $M = 8$ was the minimum number of samples which yielded a reasonable error in the RSSI measure. These power samples were acquired from the received signal at the antenna port. Hence, the samples included the power of the interference and noise in space and the noise floor of the receiver. The power sampling frequency was 333 samples per second. The measurement duration could be configured.

The algorithm was based on a maximum-minimum approach applied to the power samples. Using the measurement duration and the power sampling rate, the total number of samples of the measurement (L) was calculated. The intention was to perform measurements as short as possible to try to determine the instantaneous power of each measurement, and two seconds was the minimum time the payload could be in reception mode. For this

Table E.2: Measurement parameters.

Parameter	Value
Measurement duration (s)	2-12
Bandwidth of receivers (kHz)	4 or 7.25
Bandwidth overlap (kHz)	1.25
Power sampling rate (samples/s)	333
Power sampling period (ms)	3
Length of power meas. buffer	8 samples (24 ms)

measurement duration, $L = 666$. Longer measurements were carried out for 12 s, $L = 4000$, as a comparison.

The power samples $P[n]$ were added to a circular buffer of length $M = 8$, vector $\bar{P}[n]$ with $n \in \{1, ..., L - (M - 1)\}$. The algorithm estimated the maximum received power of sustained interference that lasted for at least the length of the buffer. The power samples $P[n]$ were added to the buffer as

$$\bar{P}[n] = [P[n] \quad P[n+1] \quad ... \quad P[n+M-1]]^T \tag{E.1}$$

The first vector, for $n = 1$, was $\bar{P}[1] = [P[1] \quad P[2] \quad ... \quad P[8]]^T$ and the next one was, $\bar{P}[2] = [P[2] \quad P[3] \quad ... \quad P[9]]^T$. These column vectors can be seen as the result of applying a sliding window of length M to the power samples. These column vectors can form an $M \times (L/M)$ matrix like

$$\begin{aligned} \bar{\bar{P}} &= \begin{bmatrix} \bar{P}[1] & \bar{P}[2] & ... & \bar{P}[L-(M-1)] \end{bmatrix} \\ &= \begin{bmatrix} P[1] & P[2] & ... & P[L-(M-1)] \\ P[2] & P[3] & ... & P[L-(M-1)+1] \\ P[3] & ... & ... & ... \\ ... & ... & ... & ... \\ P[M] & P[M+1] & ... & P[L] \end{bmatrix} \end{aligned} \tag{E.2}$$

The smallest entry (minimum) in each column formed the vector $\bar{P}_{min}$, where the k^{th} element was $\bar{P}_{min}[k] = min\left(\bar{P}[k]\right)$. The output of the algorithm (P_D) was the largest (maximum) of all smallest power detected (minima),

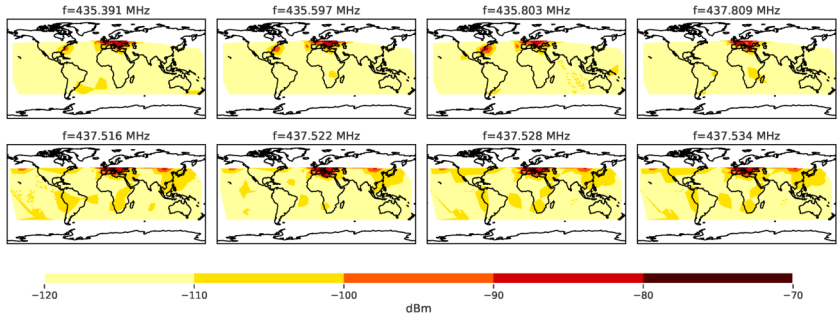

Figure E.4: Interference power measurement [dBm] world plot generated over several orbits (measurement duration of 2 s).

$P_D = max\left(\bar{P}_{min}\right)$, during the measurement duration. This measurement method is an estimation focused on sustained interference levels to investigate how long the packets would be affected by strong interference. The output of the algorithm is the highest power sustained that lasts at least 24 ms and happens at least once in a measurement (in 2 or 12 seconds depending on the specific measurement duration). Therefore, the peak levels could have been higher for some occasions and for shorter periods of time.

E.4 In-orbit measurement results

Noise and interference measurements were carried out from October 2015 to March 2016. The heat maps in Figure E.4 show the interference for four 7.25 kHz sub-bands at different center frequencies in the 435-437 MHz band in October-December 2015. These measurements had a duration of 2 seconds. Sub-satellite points over Europe were strongly affected by the interference with levels up to -70 dBm, which were about 40 dB above the system noise floor.

Another series of measurements were taken at 435.391, 435.597, 435.803 and 437.809 MHz. Each measurement had a duration of 12 seconds. In Figure E.5, a global interference map of the 435 MHz frequencies shows higher levels of interference at the east and west coast of the United States. Since the interference must be higher than a given threshold for at least

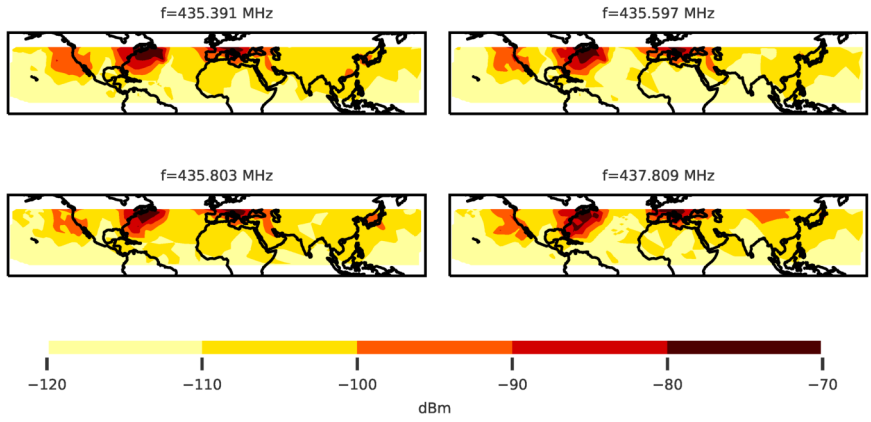

Figure E.5: Interference power measurement [dBm] plot generated over several orbits (measurement duration of 12 s).

24 ms to be stored by the measurement algorithm (Section E.3.2), longer measurements rendered a higher probability of getting 24 ms segments with consistent high power. In Figure E.5, the areas that were the most affected by interference were the east and west coast of North America and central Europe.

In order to investigate how the interference power was distributed—and not just the common heat maps with average values—the Empirical Cumulative Density Function (ECDF) was calculated for different regions. Since the M2M communication system of Serpens was intended to work for South America, initial measurements were carried out in that area (green crosses in Figure E.6a). As a reference for a low interference distribution (also referred to as noise floor measurements in this paper) measurements over non-populated areas in the south Pacific and the south Atlantic were conducted (blue circles in Figure E.6a). There were four values of received power for each point which corresponded to the center frequency of the receive channels (437.516, 437.522, 437.528 and 437.534 MHz). The ECDF was estimated for both areas in Figure E.6. These measurements were taken with 4 kHz bandwidth, which was close to half the bandwidth of the other measurements in this paper (7.25 kHz). Hence, to compare both types of measurements, 3 dB was added to the power received in these cases. The received interference and noise were assumed to have a constant power

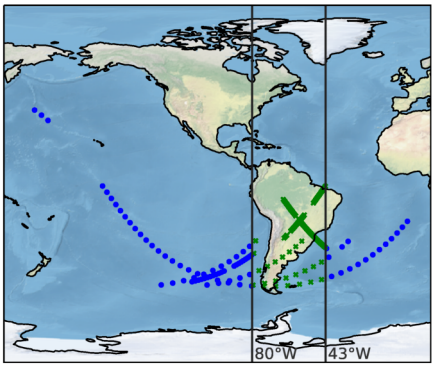

(a) Sub-satellite points for measurements over several orbits over the ocean (blue circles) and South America (green crosses). For each point there were four power values, one per frequency.

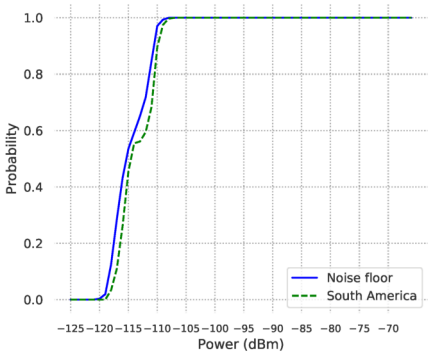

(b) ECDF of received power over the ocean (noise floor) and South America over several orbits. The ECDFs included four frequencies (437.516, 437.522, 437.528 and 437.534 MHz) since their power distributions were similar.

Figure E.6: Comparison of power distribution over the Pacific and south Atlantic ocean used as noise floor measurements, and areas of South America where ground sensor terminals could be located for M2M communication.

density over the bandwidth. The power distribution over South America was similar to the one from the noise floor, but about 1 dB higher for 50% of the points. Two behaviours can be seen from the ECDF of the South American points: around 55% of the points experienced an interference power less than -114 dBm, and the rest reached powers of about -107 dBm. Interference power over South America was low, with received power around 37 dB lower than the maximum interference power detected in the heat maps. Preliminary tests of the M2M communication system were performed in this area with adequate uplink performance.

The ECDF for the interference was estimated for four regions $R1$-$R4$ covering Europe, northern Africa and the Middle East (Figure E.7). In the map shown in Figure E.7a the northern parts of the plot were between 26.5° and 53° (marked with crosses in the map and with dashed lines in the plot) and southern parts were between 0° and 26.5° (circles in the map and continuous lines in the plot). Each region represented 35° of longitude. The

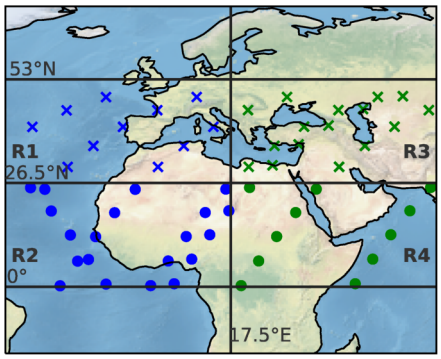

(a) Measurement locations over several orbits. Crosses were used for northern regions and circles for southern regions, blue for western and green for eastern areas. Each region covered 35° of longitude. Four frequencies were measured at each point (435.4, 435.6, 435.8 and 437.8 MHz).

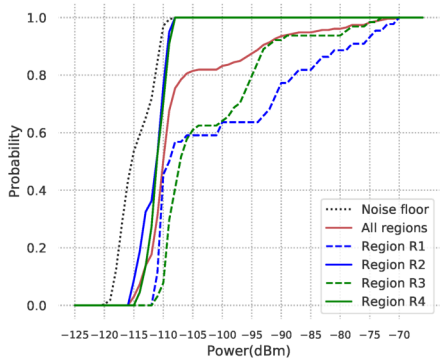

(b) ECDF of received power over the four regions and four frequencies, including the noise floor measurements (black dotted line). Continuous lines were linked to the circles in the map and dashed lines to crosses. Red line was the ECDF of all the points in the map.

Figure E.7: Power distribution over Europe, northern Africa and the Middle East (measurement duration of 12 s).

points in the map represented the sub-satellite points where the satellite measured received power. There were four values of received power for each point, which corresponded to the center frequency of the receive channels (435.4, 435.6, 435.8 and 437.8 MHz). In Figure E.7b each line considered all the frequencies to estimate the ECDF. As a reference, the red curve was the distribution of all regions. There was a clear difference between the interference experienced in the regions in the north ($R1$ and $R3$) and south ($R2$ and $R4$). Regions $R2$ and $R4$ were affected in less than 20% of the points by signals with a power higher than -110 dBm. The power increased 15 dB in $R3$ and more than 22 dB in $R1$ for 20% of the points. In general, the sub-satellite points with a lower latitude experienced less interference because they were acquired over less populated areas and their distribution was closer to the noise measurement distribution (dotted black line).

In Figure E.8 the same procedure was applied to the measurements carried out over North America, redefining the areas of interest. Each region covered an area of 19° of latitude and 38° of longitude. The regions that

were more affected by the interference were the northern regions ($R5$, $R7$ and $R9$). Around 27% of the points in region $R5$ and $R7$ experienced an interference level higher than -94 dBm and in region $R9$ higher than -78 dBm. Furthermore, in region $R9$ two different behaviours were observed: 75% of the points experienced interference levels above -109 dBm, while 25% of points did not. Satellites flying over this region will receive an interference power higher than -82 dBm for 50% of the time, reaching levels of -70 dBm on some occasions. In the southern regions $R6$, $R8$ and $R10$, where there were no known strong ground radars (Figure E.1), the power distributions were similar with a significantly lower mean as compared to the northern regions. These distributions were closer to the noise floor distribution (dotted black line).

The variation in interference power over the region was not due to measurements at different frequencies. In Figure E.8c and Figure E.8d a comparison between received power of two close carriers and two distant ones was plotted. The symbols for the regions were consistent with the ones used in Figure E.8a. The black dashed line showed the behaviour if the power in one carrier was completely dependent on the other and the red dashed lines, a difference of ± 3 dB. In the left corner, the power of the carrier 435.4 MHz was plotted against the power in 435.6 MHz. It can be seen that when there was high power in one carrier, there was also high power in the other one. Hence, the interference seemed to have at least 200 kHz bandwidth. The difference in behaviour of the points in region $R9$ and $R10$ was highly visible. Most points in $R9$ were in the high interference area; the power in one frequency was strongly dependent on the power in the other frequency. In contrast, most points in $R10$ detected power at the noise level for both carriers. In Figure E.8d, the distribution of power was between a carrier at 435.4 MHz and another at 437.8 MHz. In this case, there were more points that were outside the ± 3 dB region. This means that while high power was detected in one carrier, the other one did not detect as much because these points experienced narrow band interference. This interference may be caused by radio amateurs since the maximum bandwidth recommended for those services is 20 kHz.

The communication payload in Serpens was designed for M2M communication but was adapted to perform interference measurements. Despite the limitation in the measurement algorithm to determine signal time structure, there were some measurements that were compatible with the behaviour of

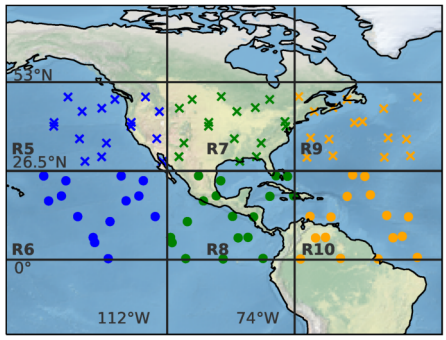

(a) Measurement locations over several orbits. Each region covered 38° of longitude. Four frequencies were measured at each point (435.4, 435.6, 435.8 and 437.8 MHz).

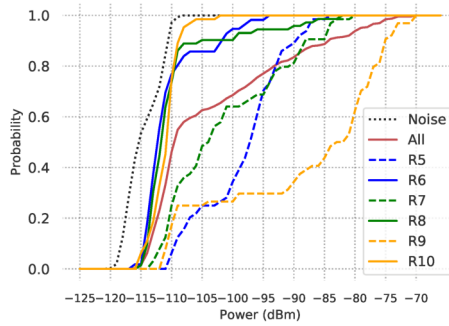

(b) ECDF of received power over the six regions and four frequencies, including the noise floor measurements (black dotted line). Continuous lines were linked to the circles in the map and dashed lines to crosses. Red line was the ECDF of all the points in the map.

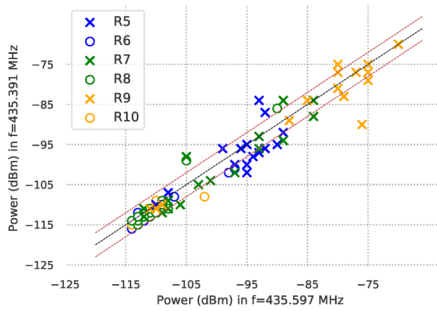

(c) Distribution of power over close carriers. The black dashed line showed the tendency if the power in one carrier was completely dependent on the other and the red dashed lines, a difference of ± 3 dB.

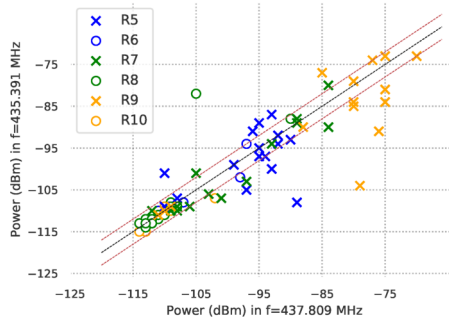

(d) Distribution of power over distant carriers. The black dashed line showed the tendency if the power in one carrier was completely dependent on the other and the red dashed lines, a difference of ± 3 dB.

Figure E.8: Power distribution over North America divided in six regions (measurement duration of 12 s). Crosses were used for northern regions and circles for southern regions, blue for western, green for central and orange for eastern areas.

radar sources. An example of a pass over the ground station in Vigo (Spain) suggested that a radar in the UK could be the cause of high interference. In Figure E.9a the power levels measured by the four receivers were mapped to the sub-satellite points where measurements were carried out, and plotted against the corresponding elevation towards the radar located in Fylingdales Moor. The measurements were 2 seconds long and the bandwidth of each receiver was 7.25 kHz. The PAVE PAWS radar in Cape Cod was used as a reference due to the public availability of specific information about its behaviour. The power levels measured follow the expected behaviour of a space-tracking ground radar changing from surveillance mode (lower elevation) to tracking mode (higher elevation), which is similar to the way the PAVE PAWS radar works [47]. When the satellite was above 10° elevation with respect to the radar, the measured power increases about 40 dB. The cross in the map was where the measured power experienced the first peak of interference. Furthermore, the measured power at the different frequencies was similar in this particular example. The separation between the centre frequencies of the receivers was around 18 kHz. If the interference was from a radar, it would be wide band (1-5 MHz for a type A radar), so all observed frequencies would be affected in a similar way.

Figure E.9b shows another example of a satellite pass over the same region with a different direction. In this case, the satellite was moving towards the south-east and the elevation of the pass with respect to the radar in the UK was below 10°, which means that the radar would not enter tracking mode. Still, an interference event can be seen 25 dB above the noise for a shorter period. This could be due to the radar operating in surveillance mode, where it searches for potential targets and switches between them.

The regions with high interference in the 430-440 MHz band were consistent with occurrences of type-A ground radars in Europe and North America (Figure E.1). However, there could also be other interference sources, such as amateur radio operators and communication with other satellites.

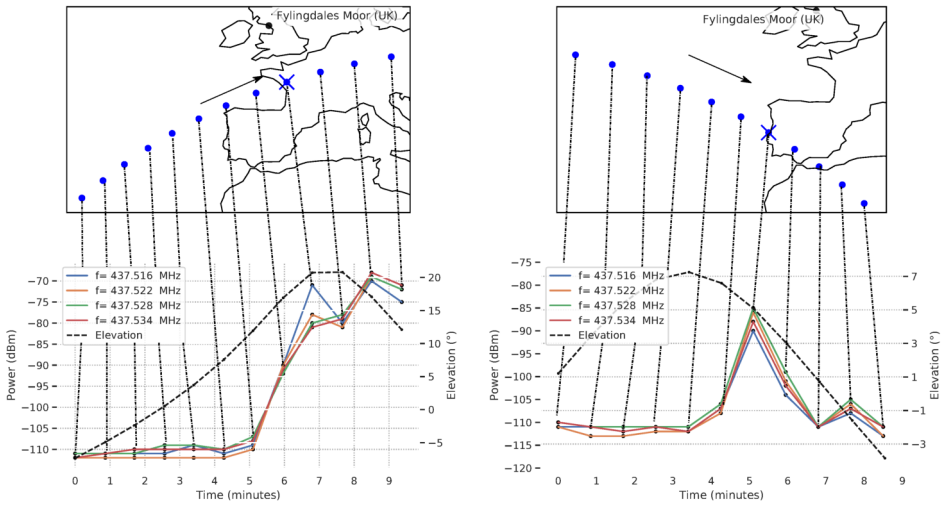

(a) North-east pass.

(b) South-east pass.

Figure E.9: Example of interference measurement of a pass over Vigo (Spain) at four different frequencies and with measurement duration of 2 seconds.

E.5 Discussion

Given the interference measurement results, an estimation of the uplink carrier to interference ratio (C/I) for a generic UHF ground station to a satellite can be done. The considerations are:

- Satellite orbit type: circular
- Satellite orbital height: 400 km.
- Carrier frequency: 437 MHz
- Ground station output power: 25 W (≈14 dBW)
- Ground station cable loss: 2 dB
- Circular polarised antenna.

- Antenna gain: 18 dBi.
- Minimum elevation of pass: 10°
- Maximum elevation of pass: 90°
- Propagation loss: free space and polarisation.

The Effective Isotropic Radiated Power (EIRP) is: $EIRP = 14 - 2 + 18 = 30$ dBW $= 60$ dBm. The free space loss is between approximately 137 dB (90° elevation) and 148 dB (10° elevation). Polarisation loss is 3 dB for a linearly polarised satellite antenna. The power received at the satellite is between -80 dBm and -91 dBm. If the interference power is -70 dBm, it would mean a (C/I) between -21 dB and -10 dB. It is very difficult for a communication system to cope with such a negative (C/I), as it leads to high packet loss in the uplink.

These (C/I) levels are not valid for average interference, but are instead valid for high sustained interference. The measurement method used enables the analysis of the probability that a sample will be over a certain power level for events 24 ms long in the 430-440 MHz band. The power levels measured over non-populated areas were considerably lower than in the rest of the world. Low interference power was detected over South America, making M2M communication for collection of sensor data from equipment on the ground possible. Over the higher latitudes in the European-African-Middle Eastern map, about 20% of the points were 16-24 dB above the noise floor and 18-35 dB for the higher latitudes of North American regions. Half of the points in the regions in Figure E.7a were 5 dB above the noise floor, and all points in Figure E.8a were 6 dB above the noise floor. This reflects how crowded the frequency spectrum is, based on real measurements, and gives an indication of why all the ground stations in Europe will experience difficulties when communicating with their satellites in the UHF-band. In North America, there was also a high level of interference in the higher latitudes shown in Figure E.8a. However, $R9$ is not a highly populated area and interference power was still 33 dB above the noise floor for 50% of the points. It can be an indication that the radar in Massachusetts (Figure E.1) makes a considerable contribution to the interference power such that ground stations in the area will experience an undesirable uplink quality. Due to the low interference levels detected over South America and the African

regions, uplink communication performance will improve considerably if collaboration with ground stations in these areas is established.

Some lessons learnt from this study of interference can help plan future work. Plannning the measurement campaigns based on which parameters will be calculated and the relevant areas of interest is extremely important. When repeating measurements over the different regions, the configuration should be kept the same for a better comparison of results. Noise and interference measurements over non-populated areas are useful to establish the noise floor of the environment, including system noise. Building a hardware-in-the-loop setup that resembles the RF satellite architecture would make noise floor comparisons easier.

Future measurement missions to assess temporal properties of the interference environment could provide valuable information for the proper design of communication systems for small satellites operating in the 430-440 MHz band. Estimating the frequency and time structure of in-band interference from other small satellites in LEO is necessary to improve satellite communications. The results from this analysis can help other research groups to plan future measurements, since they have shown the areas with high consistent interference. The coasts of North America and central Europe, especially Vigo (Spain), are areas of interest for measurements since high interference has been detected. In addition, measurements above 51.6° and below -51.6° latitude should be pursued to get a global view and not be limited to the ISS orbit's constraints. In general, more measurement campaigns are needed to characterize interference thoroughly in both time and frequency to enable proper interference coping communication system design for this band. Spread spectrum techniques can protect from narrow band interference and interleavers can be useful for strong wide band interference. Error-correction algorithms, such as Reed-Solomon, are reliable for burst-noise channels [191].

E.6 Conclusions

In this paper, we presented a method to detect strong consistent uplink interference from satellites and used it in the Serpens satellite. We created

new heat maps and interference power distributions plots in the 430-440 MHz amateur radio band over Europe, Africa, the Middle East, and the Americas. The results show that the regions over South America and specific areas over Africa have low uplink interference levels. Thus, data collection of ground sensor equipment for disaster monitoring over these regions is possible in the 430-440 MHz band.

The results also showed that there is strong interference affecting the uplink over Europe and the coasts of North America, reaching power levels of -70 dBm for at least 24 ms duration. Measurement results support and complement the findings in the works of TU Berlin [48] and Universität Würzburg [60]. The Serpens satellite measured at least 5 dB more power over populated areas than in non-populated areas in half of the measurements, reaching differences of up to 35 dB more power in 20% of the measurement points in some areas of North America. One possible source of interference may be the ground radars used for radiolocation in the band, since high interference was found in scarcely populated areas in regions with type-A radars. Interference counter-measures would not be needed in South America and Africa, thus, uplink communication to small satellites in the 430-440 MHz band can be achieved by establishing cooperation with ground stations in those areas.

In order to better understand the properties of UHF band uplink interference that a satellite can suffer in a LEO orbit in the UHF band, it is necessary to carry out more interference measurements with higher spatial, temporal and frequency resolution. Such measurements can be used to design an optimal communication system that can cope with interference events and increase the link quality.

Acknowledgments The authors thank the Brazilian Space Agency who financed the Serpens project and the Serpens consortium who managed the mission and the international cooperation. The work of UVigo is supported by Ministerio de Ciencia e Innovación in Spain (Grant No. ESP2016-79184-R). The work of Norwegian University of Science and Technology (NTNU) is supported by the Norwegian Research Council (Grant No. 270959), the Norwegian Space Agency, and the Centre of Autonomous Marine Operations and Systems (NTNU AMOS). Gara Quintana Díaz wishes to acknowledge the help of her colleague, Dr. Roger Birkeland.

F In-Orbit Measurements and Analysis of Radio Interference in the UHF Amateur Radio Band from the LUME-1 Satellite

The text of the following paper is added as a chapter. Some typos introduced by the editor's office of the journal (change of milliseconds to seconds) have been updated in this thesis. The paper is re-formatted for better readability.

G. Quintana-Diaz, T. Ekman, J. M. Lago Agra, D. Hurtado de Mendoza, A. González Muíño and F. Aguado Agelet, 'In-Orbit Measurements and Analysis of Radio Interference in the UHF Amateur Radio Band from the LUME-1 Satellite,' *Remote Sensing*, vol. 13, no. 16, 2021, ISSN: 2072-4292. DOI: 10.3390/rs13163252. [Online]. Available: https://www.mdpi.com/2072-4292/13/16/3252

Abstract Radio interference in the uplink makes communication to satellites in the UHF amateur radio band (430–440 MHz) challenging for any satellite application. Interference measurements and characterisation can improve the robustness and reliability of the communication system design. Most published results focus on average power spectrum measurements and heatmaps. We apply a low complexity estimator on an SDR (Software-Defined Radio) to study the interference's dispersion and temporal variation on-board a small satellite as an alternative. Measuring the Local Mean Envelope (LME) variability with different averaging window lengths enables the estimation of time variability of the interference. The coefficient of variation for the LME indicates how much the signals vary in time and the spread in magnitudes. In this article, theoretical analysis, simulations, and laboratory results were used to validate this measurement method. In-orbit measurements were performed on-board the LUME-1 satellite. Band-limited

interference with pulsed temporal behaviour and a high coefficient of variation was detected over North America, Europe, and the Arctic, where space-tracking radars are located. Wide-band pulsed interference with high time variability was also detected over Europe. These measurements show why operators that use a communication system designed for Additive White Gaussian Noise (AWGN) at power levels obtained from heatmaps struggle to command their satellites.

F.1 Introduction

Communication with satellites is required to operate any spacecraft and offer the service planned, no matter what type of service (telecommunication, Internet of Things (IoT), remote sensing, etc.). The choice of communication parameters should be based on the communication channel properties and the actual interference and noise environment [15]. For radiofrequency (RF) communication, the radio environment can be measured on-board satellites and provide information to improve the design of the communication system and increase the data throughput. In-orbit spectrum monitoring is paramount for satellite communication systems and has been supported by the European Space Agency (ESA) [50]. Spectrum monitoring is especially important for IoT-over-Satellite networks and for small satellite communication, where uplink interference levels will rise due to the increasing number of IoT devices deployments [192] and small satellites launched [137]. Actual in-orbit interference measurements can complement existing system models for IoT-over-Satellite systems [192]–[195] to improve their real performance and help to design interference mitigation techniques. Spectrum monitoring can help to solve some of the challenges of future satellite systems, such as efficient spectral usage and interference mitigation capabilities [196].

The UHF amateur radio band (430–440 MHz) is a popular frequency band for Telemetry, Tracking and Command (TT&C) of small satellites [187]. Several operators of small satellites have experienced poor uplink performance in this band and have performed interference measurements to analyse the problem [46], [48], [60], [61]. In 2014, the University of Vigo carried out a set of preliminary measurements with the HumSat-D satellite, where pulsed interference was detected [61]. In the same year, the University of

Würzburg registered high interference levels over central Europe in certain frequencies within the UHF amateur radio band (430–440 MHz) with the UWE-3 satellite [60]. Additional measurements were performed by the University of Vigo using the SERPENS satellite in 2015 and 2016. Strong, consistent uplink interference was detected over North America, Europe, the north of Africa, and the Middle East. Low levels were measured over South America and some regions of Africa [46].

Moreover, Technische Universität Berlin (TU Berlin) has worked on spectrum monitoring in the same band (in addition to VHF, L-band, and S-band) and detected high power interference over North America and Europe using a Software-Defined Radio (SDR) on the International Space Station (ISS) in 2018 [48]. In 2020, TU Berlin launched the SALSAT, a CubeSat to continue their spectrum monitoring activities without the ISS constraints [117], but no results have been published yet. There are also companies, such as Hawk Eye 360 and Aurora Insight, that have started to monitor the spectrum in the last years and are building a constellation to provide frequency spectrum data services, such as geolocation of interference sources [55], [56], [190].

Most of the published results focus on the average interference power over a certain measurement duration [48], [60], [61], omitting the time structure of the interference. In addition, the sub-satellite points of some measurements are limited between $-51.6°$ and $+51.6°$ latitude, specifically, the measurements performed by TU Berlin from the ISS [48] and the SERPENS measurements [84]. Satellite orbits with higher inclination can extend sub-satellite points further north as in Reference [60], [61], [197]. Heatmaps have been the traditional way of showing the average power of interference [48], [60], but they do not show the variability.

The temporal characteristics of the noise/interference impact what type of error correction coding is needed. For example, turbo-codes have a good performance in the presence of Additive White Gaussian Noise (AWGN), but they are weak codes for burst-noise channels [15]. Reed-Solomon error correction coding performs better in burst-noise channels than in AWGN [15]. Channel interleavers can be used in combination with error correction codes for burst noise. A window covering the full temporal dynamics of the interference can be used for the interleaver length since the burst length will be shorter. Moreover, if the interference has a specific time structure, such

as pulsed signals, windows of opportunity could be estimated to transmit in between pulses.

To understand the current issues experienced in the TT&C links to small satellites using the UHF radio amateur band, new measurements that combine time and frequency information are needed. Furthermore, the time variability characteristics of the interference can be exploited to improve the communication system design in the band. Ideally, a continuous spectrogram and the probability density function of the interference should be measured to obtain accurate frequency and temporal dynamics. Due to the limited downlink rate of small satellites using the UHF amateur radio band (430–440 MHz) and their power constraints, a low complexity algorithm is desired to measure time and frequency characteristics.

The UHF amateur radio band (430–440 MHz) is shared with other radiocommunication services, such as radiolocation and Earth Exploration Satellites [42]. As a part of the radiolocation service, there are different types of ground radars (type A, B, and C) in the 420–450 MHz band that transmit up to 5 MW of power [44]. Radar type A is used for space object tracking and could be the source of interference of satellite communication in the amateur radio band. In Reference [48], a strong pulsed interference was identified as the ground radar operating in the United Kingdom (UK). Measurements from the SERPENS satellite [46] also suggest that these ground radars can be interfering in the satellite uplink since high power interference was detected over scarcely populated areas.

These type A radars transmit pulse frequency modulation in the form of linear chirps. For the search mode (when surveying space objects), the chirps have a bandwidth of 100–350 kHz, while, for tracking, the bandwidth is 1 or 5 MHz [44]. The pulse width can be 0.25, 0.5, 1, 2, 4, 8, or 16 ms, the average duty cycle is 25%, and the pulse repetition frequency is up to 41 Hz [44]. In Reference [47], the characteristics of the Precision Acquisition Vehicle Entry (PAVE) Phased Array Warning System (PAWS) early warning radars in the United States (US) are described for an environmental impact statement. These radars are located in Cape Cod (Massachusetts), Beale (California), and Clear (Alaska). For these radars, the pulse width for tracking mode can be 0.25, 0.5, 1, 2, 4, 8, and 16 ms, and, for surveillance, 0.3, 5, and 8 ms. The pulse repetition rate can be between 18 and 72 pulses per second. The 3 dB antenna beamwidth is 2.2°, the same as

in Reference [44]. The PAVE PAWS radars also transmit high power (around 0.5 MW peak power), so they are an expected source of interference in space.

In this article, we present measurements of the radio environment in the 435 MHz band for satellites in Low Earth Orbit (LEO) using the LUME-1 satellite in the spring of 2021 to support interference characterisation. This satellite has an approximately 98° inclination orbit allowing measurements over the polar areas. The LUME-1 is a CubeSat with limited on-board data processing capabilities and low data rates for communication. This called for the development of simple on-board estimation procedures to obtain the time-frequency interference statistics with low downlink data rate requirements. We performed spectrum measurements over five seconds and estimated the time variability of the interference over windows between 0.21 ms and 27.3 ms, measuring the first-order stationarity by estimating the variance of the Local Mean Envelope (LME) with different lengths of averaging windows.

The contributions of this article can be summarised as: (1) development of a low complexity algorithm to measure time-frequency behaviour of interference to be used in low data rate links, (2) validation of the method through theoretical analysis, simulations, hardware-in-the-loop testing and in-orbit measurements on-board a small satellite, and (3) analysis of the in-orbit interference environment measured in the UHF radio amateur band.

The structure of the paper is as follows. In Section F.2, the LUME-1 satellite and its constraints are introduced. The software architecture and measurement algorithm are explained in Section F.3, followed by the description of the setup for simulations, laboratory (flatsat), and satellite measurements in Section F.4. The theoretical, simulation, lab, and in-orbit measurement results are presented in Section F.5 and discussed in Section F.6. Finally, conclusions are presented in Section F.7.

F.2 LUME-1 Satellite

LUME-1 was launched on 27 December 2018 from Vostochny in Russia into a 510 km Sun-synchronous orbit. This 2U Cubesat was part of the European project Fire RS, where the University of Porto (Portugal), The Laboratory for Analysis and Architecture of Systems (France), the University of Vigo (Spain), and Alén Space (Spain) collaborated together [87]. The mission ended in June 2019, but the satellite is still operational and available for other research. LUME-1 has a TOTEM SDR on-board [87], allowing the upload of new software with new functionality.

The Norwegian University of Science and Technology (NTNU) collaborates with the University of Vigo and Alén Space to develop and perform new communication experiments with the satellite. The objective is to estimate the in-band radio interference environment in the UHF radio amateur band (430–440 MHz). New software to estimate the time-frequency characteristics of this radio interference was developed at NTNU during 2020. This software was designed considering the constraints of the LUME-1 satellite. The main limitation is the data throughput and communication window. The default gross data rate configuration is 4.8 kbps, extendable to 9.6 kbps, over the UHF amateur radio band at 437.060 MHz, but the obtained net data rate is significantly lower. When using the 4.8 kbps configuration, given the few daily passes over the Vigo ground station due to latitude (42°) and the high level of interference experienced in the uplink, a continuous 1 kbps downlink rate for 5 min per day is a realistic estimate. For the uplink, the communication is degraded, and the estimated actual data throughput is 200 bps for 5 min per day.

In addition, the satellite is tumbling (at approximately 1 rpm), since the Attitude Control and Determination System (ACDS) is planned to be activated at a later stage. The UHF antenna used is the ANT430 antenna from GomSpace, whose antenna pattern is not completely omnidirectional. According to the total gain measured on the GOMX-1 satellite [198] (a 2U CubeSat), the gain can vary between −1.5 to 1.6 dBi, depending on the pointing. The antenna is circularly polarised only when seen from the top (left-hand) and bottom (right-hand). Additional losses can be experienced when pointing differently.

The measurements were planned so that operations were as simple as possible. The TOTEM SDR on-board can have a maximum duty cycle of 50% due to power budget limitations. The RF front-end can be tuned within the 435–438 MHz band, and the dynamic range is approximately 66 dB. The RF bandwidth can be adjusted between 200–56,000 kHz [17], and the ideal sample frequency can be configured within 521–56,000 kSps. In order to use sample frequencies higher than 2 MSps, some digital signal processing must be ported to the Field-Programmable Gate Array (FPGA), requiring extra development. The interference measurement software was developed using GNURadio libraries in C++ and shell scripting.

If the Automatic Gain Control (AGC) was activated, the gain of the Analogue to Digital Converter (ADC) would adapt to the dynamic range of the signal. As the gain cannot be read in real-time, the AGC was deactivated, resulting in a fixed gain for the measurements in this article. Thus, strong signals may saturate the ADC, and weak signals may be below the resolution threshold.

F.3 Software Architecture and Measurement Algorithm

F.3.1 Software Architecture

The software consists of two different parts: a shell script controlling the measurements, and a C++ program using GNURadio libraries. The first script starts the measurements with the correct parameters and is responsible for the timing of measurements and file storage. The second programme performs the measurements.

F.3.2 Measurement Algorithm

The goal of the algorithm is to measure the time-frequency characteristics of the interference received by the LUME-1 satellite. The window of first-order stationarity of the interference is the shortest time window long enough

to include a sufficiently varied selection of samples to form a local mean close to the mean envelope in that region. For the stationarity window length, the LME has a low coefficient of variation, and it indicates the length over which an interleaver has to spread information to obtain average interference behaviour.

The In-Phase and Quadrature (IQ) samples $x[l]$ are acquired from the ADC at an sample frequency f_s. A Discrete Fourier Transform (DFT) with M frequencies is calculated every M samples of $x[l]$, forming the time frequency representation $X_k[n]$ of the signal. The frequency bin is $k \in \{0, 1, \ldots, M-1\}$, and the time index n denotes that the DFT is applied to $\{x[nM], x[nM+1], \ldots, x[(n+1)M-1]\}$. To estimate the time variability, the magnitude of the DFT, $z_k[n] = |X_k[n]|$, is used [91].

The LME statistics are estimated for each frequency bin. For simplicity, $z_k[n]$ is defined as the time series of the values of the magnitude of the DFT for a particular frequency bin k and $n \in \{0, 1, \ldots, T-1\}$, with T being the total number of DFTs in a single measurement.

The first moment of a distribution is the mean m_1. In the discrete domain, the mean of series $z_k[n]$ with T samples is calculated as the time average

$$m_{1k} = \frac{1}{T} \sum_{n=0}^{T-1} z_k[n]. \tag{F.1}$$

The second moment (m_2) can be seen as the average power of the signal. This can be calculated as

$$m_{2k} = \frac{1}{T} \sum_{n=0}^{T-1} z_k^2[n]. \tag{F.2}$$

In order to measure the stationarity of the signals in the traditional way, it would be necessary to acquire all IQ samples and process them on the ground. However, the downlink data throughput is limited, as described in Section F.2, so an on-board processing method was developed to reduce the data to be downloaded.

A simple method to measure stationarity that generates little data is to compare local statistics using different time windows. In this article, we

analyse the first-order stationarity by measuring the variability of the local mean of the envelope (LME) for different time windows. Short-time windows generally create highly variable local means for stochastic signals. For longer windows, the variability decreases and approaches the mean of the region. If the signal is non-stationary in the region where the data is collected, then no window size smaller than the entire data set gives a LME with small variability. The shortest length where the LME has converged to the regional mean with sufficiently low variance is considered the window of stationarity (first-order). This window length covers the temporal dynamics of the signal. The measures calculated for different time windows are, thus, the first moment m_1, and its variability is calculated using the second moment m_2. Due to software implementation constraints (block coding in GNURadio) and the limitation in the data throughput, the maximum number of windows is fixed to eight in the implemented estimator. Each of the eight time windows $(T_1, T_2, \cdots, T_8)$, has a corresponding time series of local means $m_{1k}^{T_i}[l]$ and local second-order moments $m_{2k}^{T_i}[l]$. Figure F.1 depicts the hierarchy of $m_{1k}^{T_i}[l]$. The index l indicates the block we consider, where $l \in \{0, 1, \ldots, T/T_i - 1\}$. Equation (F.3) shows how to calculate the values.

$$m_{1k}^{T_i}[l] = \frac{1}{T_i} \sum_{n=0}^{T_i-1} |z_k[n + l \cdot T_i]| \,. \tag{F.3}$$

Doubling the window length in each step $T_{i+1} = 2T_i$ and using square averaging windows allows for a very efficient implementation of the algorithm.

To analyse the variability of $m_{1k}^{T_i}[l]$, the second moment is used. There is a $m_{2k}^{T_i}$ for each time window calculated as

$$m_{2k}^{T_i} = \frac{1}{T/T_i} \sum_{l=0}^{T/T_i-1} \mid m_{1k}^{T_i}[l] \mid^2 \,. \tag{F.4}$$

Substituting $m_{1k}^{T_i}[l]$ in (F.3), we have:

$$\mid m_1^{T_i}[l] \mid^2 = \left| \frac{1}{T_i} \sum_{n=0}^{T_i-1} z_k[n + l \cdot T_i] \right|^2 = \frac{1}{T_i^2} \sum_{n=0}^{T_i-1} \sum_{m=0}^{T_i-1} z_k[n + l \cdot T_i] \cdot z_k[m + l \cdot T_i]. \tag{F.5}$$

In addition, substituting Equation (F.5) in Equation (F.4), $m_{2k}^{T_i}$ can be calculated as

$$m_{2k}^{T_i} = \frac{1}{T/T_i} \sum_{l=0}^{T/T_i-1} \frac{1}{T_i^2} \sum_{n=0}^{T_i-1} \sum_{m=0}^{T_i-1} z_k[n + l \cdot T_i] \cdot z_k[m + l \cdot T_i]. \tag{F.6}$$

The values of $m_{2k}^{T_i}$ for different T_i depend on the specific signal analysed (see Appendix Section F.7). The algorithm implemented provides: (1) an overall mean m_{1k}, (2) overall average power m_{2k}, and (3) measurements of variability of the local mean for different time windows $m_{2k}^{T_i}$.

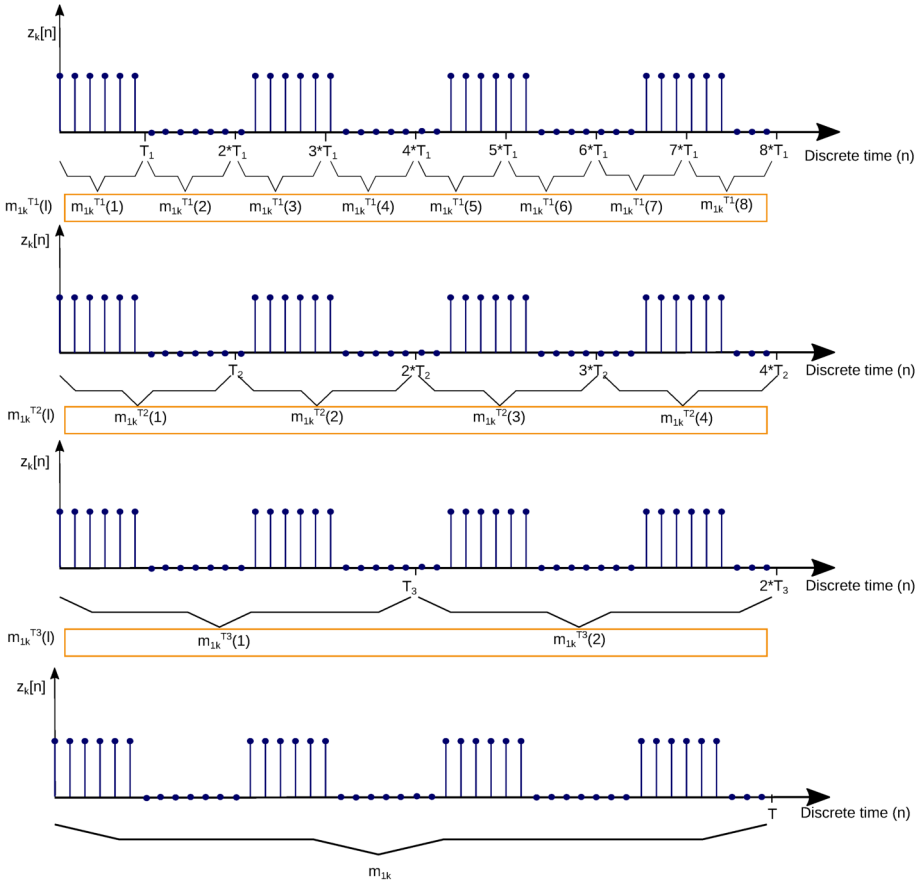

Figure F.1: Calculation of the local means $m_{1k}^{T_i}$ and the overall (m_{1k}).

F.3.3 Coefficient of Variation

The coefficient of variation (CV) is a standardised measure of dispersion defined by the ratio of the standard deviation and the mean. The CV for the envelope for frequency bin k is

$$c_k = \frac{\sqrt{m_{2k} - (m_{1k})^2}}{m_{1k}}. \tag{F.7}$$

To estimate the window of first-order stationarity, the CV is calculated to analyse the variability of the LME. This standard measure of dispersion is defined as the ratio between the standard deviation of the LME and its mean. Using the output parameters of the algorithm presented, the CV for frequency bin k and time window T_i can be calculated as

$$c_k^{T_i} = \frac{\sqrt{m_{2k}^{T_i} - (m_{1k})^2}}{m_{1k}}. \tag{F.8}$$

For sufficiently long windows (large T), the coefficient of variation c_k^T converges to zero as $m_{2k}^T \rightarrow (m_{1k})^2$. The CV is here used to find the required window length to obtain a local mean sufficiently close to the true mean of the envelope. This window length T_s is considered the window of stationarity in this paper. The limit of convergence is set at -10 dB; thus, if $(c^{T_s})^2 < 0.1$, then each T_s long local average is considered long enough to include a sufficiently varied selection of samples to form a consistent mean.

For a constant envelope signal, $c = 0$. Then, each observed sample is a good representation of the mean. For independent samples (white noise), the coefficient of variation for a window of length T is obtained in Equation (F.9) by inserting the second-order moment m_{2k}^T from Equation (F.20) into Equation (F.8).

$$c_k^T = \frac{\sqrt{\left((m_{1k})^2 + \frac{m_{2k} - (m_{1k})^2}{T}\right) - (m_{1k})^2}}{m_{1k}} = \frac{1}{\sqrt{T}} \cdot \frac{\sqrt{m_{2k} - (m_{1k})^2}}{m_{1k}} = \frac{c_k}{\sqrt{T}}. \tag{F.9}$$

For a complex AWGN, the envelope is Rayleigh distributed and the relationship between the moments, $m_1 = \sqrt{\frac{\pi}{4} m_2}$, renders a coefficient of variation of

$$c_k = \frac{\sqrt{m_{2k} \cdot \left(1 - \frac{\pi}{4}\right)}}{\sqrt{m_{2k} \cdot \frac{\pi}{4}}} = \sqrt{\frac{4}{\pi} - 1} \approx 0.52. \tag{F.10}$$

Hence, for AWGN, an average window of just three samples is sufficient to obtain a CV below −10 dB, and only 27 samples to obtain it below −20 dB.

F.4 Measurement Setup

In this section, the setup for the simulations, hardware-in-the-loop (flatsat), and satellite measurements is explained, including the configuration of the measurement software.

One measurement is defined as one C++ programme execution, and a *measurement set* contains a group of measurements. Each measurement has a *duration* and generates a file with date and time as filename. The measurements within a set have a periodicity (time between the start time of two consecutive measurements).

The configuration of the measurements is presented in Table F.1. The center frequency was chosen based on the lowest frequency in the UHF amateur radio band measured in Reference [48], [60]. In addition, the frequency 435 MHz is in the middle of the ground radar band 420–450 MHz. To reduce software computational power, the sampling frequency was 600 kSps, rounding up the minimum value (521 kSps). To satisfy the Nyquist criterion and avoid aliasing, the RF bandwidth shall be, at least, half of the sampling frequency [91]. The bandwidth setting was chosen to be 200 kHz so that there is a margin with regard to Nyquist; the sampling frequency is then three times the bandwidth.

The measurement duration should be long enough to find stationarity, but short enough not to measure the spatial variability due to the satellite's

Table F.1: Configuration parameters for simulations, as well as flatsat and in-orbit measurements.

Parameters	Values
RF centre frequency (MHz)	435.00
RF bandwidth (kHz)	200.00
Sampling frequency (kSps)	600
Duration (s)	5
Period between measurements (s)	60
Frequency bins	128
Time windows (ms)	0.21, 0.43, 0.85, 1.71, 3.41, 6.83, 13.6, and 27.3
Number of outputs	10
Number of bits	32

movement. The duration was five seconds as a trade-off. This interval corresponds to a movement of a 0.3° angle from nadir (center of Earth). The time between measurements is one minute, which defines the spatial resolution. To resolve the 3° beamwidth (rounding up) used by type A space-tracking radars, a corresponding spatial sampling is performed. Thus, measurements were one minute apart.

There is no maximum bandwidth for the 435 MHz according to the International Amateur Radio Union (IARU) band plan [199], but the Norwegian band plan recommends between 12–20 kHz [200]. Therefore, the frequency resolution should be higher than these values and traded-off against the data size to downlink since the number of frequency bins is proportional to the data size. The number used was 128 to obtain a frequency resolution better than 5 kHz. The resolution for time variability is determined by the first time window, chosen to be 0.21 ms, since it is lower than the shortest pulse width of the radars mentioned in Section F.1. The smallest step between windows, which is 2, was chosen for this first round of measurement campaigns. The maximum number of outputs and number of bits was configured to obtain better temporal variation resolution and reduce bit quantisation errors.

To verify the implementation of the proposed estimator, it was first tested on a set of simulated signals describing different possible interference scenarios using the same configuration. The same scenarios were then tested on the TOTEM SDR in the flatsat setup, generating the signals with another SDR to verify the hardware.

F.4.1 Simulation Setup

The algorithm was developed and tested using an iterative approach. Simulations were the first step to verify the software implementation of the measurement algorithm. The simulations were developed in C++ using GNURadio libraries. The setup consists of a transmitter and a receiver implemented in software. The transmitter sends simulated interference (test signals) and the receiver runs the measurement algorithm.

The test signals used to validate the algorithm were based on the interference environment that can be encountered by a satellite in LEO using the UHF band (430–440 MHz). The four types of signals that were used in testing and validation are: *AWGN*, *Continuous Wave (CW)*, *pulse wave*, and a *chirp* signal. When there are many independent random processes, an AWGN model can be used. A CW is a stationary signal; thus, it can be used to measure full stationarity. Pulsed signals and chirps are chosen because radiolocation is a primary service in the 420–450 MHz band and are expected to be found.

F.4.2 Flatsat Setup

The next step for verification and validation was to include target hardware in the loop. The main components of the flatsat setup were two SDRs: the Ettus USRP-2901 SDR and the TOTEM SDR. The USRP was used as a transmitter of the test signals. The transmitter software was run on GNURadio companion which is controlled by a desktop computer remotely via Secure SHell (SSH). The version of the TOTEM SDR used in the lab is an upgraded version of the SDR in LUME-1. It was used as the receiver, and it ran the measurement software. The TOTEM SDR encompasses a Xilinx

Zynq 7020 System on Chip (SoC) running an embedded Linux system [13], allowing remote access via SSH. The measurement results are saved in files and copied to a computer for analysis.

The lab setup is shown in Figure F.2. The USRP is connected to Computer #1 through USB and the SMA transmitter port of the SDR is connected to a 30 dB attenuator to avoid damaging the receiver with strong signals. The output of the attenuator is connected to a 3 dB power splitter. One output of the splitter is connected to the RF port of TOTEM, and the other to a spectrum analyser (Rohde & Schwarz FSV). The power supply provides 5 V to the TOTEM. Computer #2 controls TOTEM and Computer #1 remotely.

The same test signals used in simulations are transmitted by the USRP, properly upconverted to the frequency range which this TOTEM is designed for (430–440 MHz), mixing them with a Local Oscillator (LO). To avoid the effect produced by the LO leakage, the signals (except the chirp) are transmitted with an offset (100 kHz) with respect to the centre frequency, configured in the USRP. The chirp is not shifted 100 kHz because it would be outside the 3 dB bandwidth.

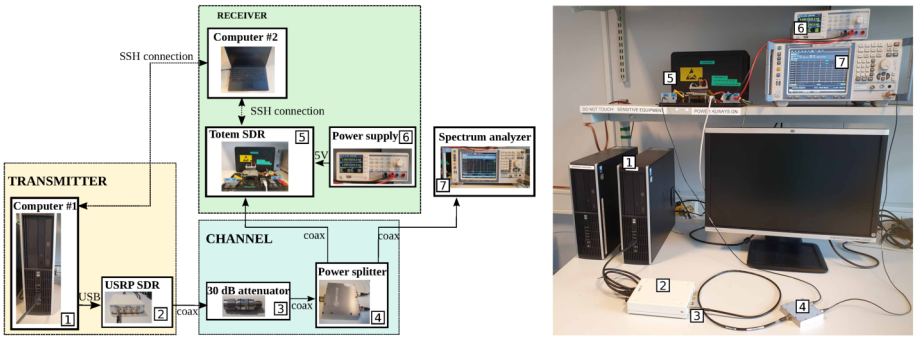

Figure F.2: Flatsat setup. The USRP is used as the transmitter for test signals, and the TOTEM SDR (Software-Defined Radio) is the receiver.

F.4.3 Satellite Setup

In this article, we present the first measurement results using the algorithm described on-board the LUME-1 satellite. The measurement areas were decided based on where interference has previously been reported in the UHF amateur radio band (America, Europe, north of Africa, and the Middle East) [46], [48], [60]; over areas where there are known radar sources and can be of interest to Norway (the Arctic) [44]; and areas in the ocean (South Pacific and South Atlantic). All measurements are referred to as interference over populated areas, except for the last category. The latter are named noise measurements over non-populated areas because the spectra measured had lower power and because there are lower population concentrations.

The Concept of Operations (CONOPS) for the measurement campaigns is as follows:

1. **Plan schedule**. The date and time of passes where the satellite is over the areas of interest are estimated using the Python library *pyorbital* and the corresponding Two-Line Element (TLE) from Celestrak [183].

2. **Upload schedule**. When there is availability over the ground station, the schedule for the measurements is uploaded to the satellite. The schedule includes the date and time to execute the command to run the measurement software, the command, and its parameters.

3. **Run measurement**. TOTEM is turned on and the measurement software runs for five seconds every minute for 10 min. Afterwards, TOTEM is turned off until the next measurement set.

4. **Downlink data**. After all measurements are carried out, the UHF transmitter is turned on to downlink the measurement files.

The size of each data file depends on the number of frequency bins (M), the number of bits per sample (n_b), and the number of outputs of the software (n_u): $M \cdot n_b \cdot n_u$.

In Table F.2, the data budget for the measurement algorithm described in this paper, with the configuration of Section F.4, is compared to raw

spectrum monitoring with the same parameters for five seconds and for one minute continuously. By raw spectrum monitoring, we refer to a spectrogram (commonly known as waterfall plot), which is a representation of the power spectrum of a signal as it changes in time. The on-board processing software provides a data reduction of 203,400 times compared to the 10 min waterfall and 1920 times compared to the five-second waterfall.

Table F.2: Data budget to show how the on-board processing software dramatically reduces the data size to be downlinked compared to standard waterfalls.

	(A) Our Software	**(B) 10 min Waterfall**	**(C) 5 s Waterfall**
Sampling frequency (kSps)	600	600	600
Number of frequency bins	128	128	128
Freq. resolution (kHz/bin)	4.7	4.7	4.7
Number of bits	32	32	32
Number of parameters	10	-	-
kBytes per measurement	51.2	11,520,000	96,000
MBytes per measurement	**0.05**	11,520	96

Assuming an available downlink rate of 1 kbps, the time estimated to downlink one set of 10 measurements is shown in Table F.3. The number of days to downlink is estimated assuming an average of one pass per day with average five minutes for the 4.8 kbps configuration.

Table F.3: Downlink time for the data output of the on-board processing software compared to standard waterfalls.

	(A) Our Software	**(B) 10 min Waterfall**	**(C) 5 s Waterfall**
Net time (h)	0.11	3200	26.6
Effective days	**1.4**	38,400	320

F.5 Results

First, the validation of theory, simulations, and flatsat results are presented. Second, the in-orbit results obtained from measurements during the first half of 2021 are presented.

F.5.1 Validation of Theory, Simulations and Flatsat Results

The test signals described in Section F.4.1 are used to validate the measurement algorithm. The results analysed are: *average power* (m_{2k}); the variation of m_{2k} from the smallest time window to the largest normalised, referred to as *normalised LME second moment*; and the difference of m_{2k} between consecutive windows normalised ($m_{2k}^{T_i} - m_{2k}^{T_{i+1}}$), named *bin difference*.

The results obtained when measuring different input signals: AWGN; a CW; a pulsed signal with pulses 5 ms long and repetition period of 16.67 ms; and a chirp signal with pulses 5 ms long, repetition period of 16.67 ms, and 300 kHz bandwidth are shown in Figure F.3–Figure Figure F.5, respectively. All results are measured with the configuration in Table F.1. The average power spectrum (m_{2k}) is plotted for AWGN (Figure F.3a), a CW (Figure F.3b), a pulsed signal (Figure F.3c), and a chirp signal (Figure F.3d). The signals generated are the same both for simulations and measurements with the flatsat.

The main differences between the simulation results (blue lines) and the flatsat results (red lines) are the filter, whose frequency response can be seen in Figure F.3a, when transmitting AWGN, and the measured noise. In the simulation, the spectrum is flat because the noise transmitted is white (all frequencies are affected in the same way). When the noise is transmitted in the flatsat setup, the spectrum measured is not completely flat because of the receive filter. The filter is configured to have a bandwidth of 200 kHz for the AD9364 transceiver chip. Nevertheless, the measured 3 dB bandwidth is larger (from 434.75 to 435.25 MHz), so this is the band analysed in the remainder of the paper (indicated by vertical black dotted lines). The TOTEM in the lab setup was calibrated for the spectral power

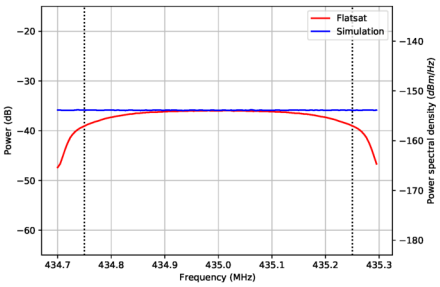

(a) AWGN (Additive White Gaussian Noise).

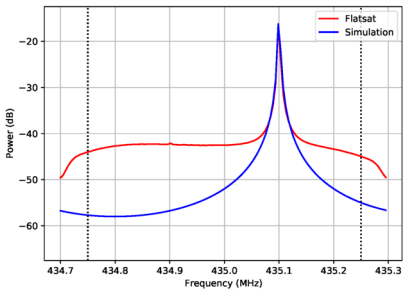

(b) Complex CW (Continuous Wave) transmitted.

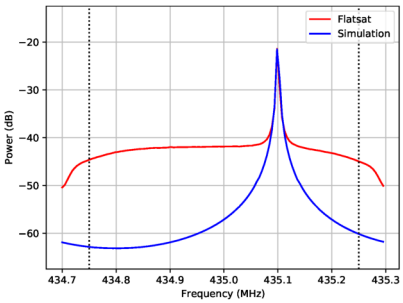

(c) Complex pulse (5 ms long and period 16.67 ms) transmitted.

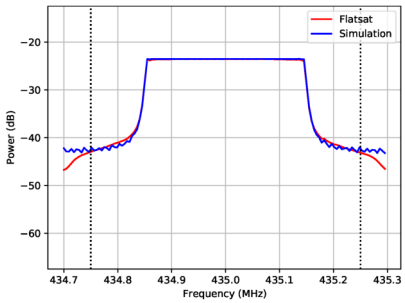

(d) Complex chirp (300 kHz wide, 5 ms long, and period 16.67 ms) transmitted.

Figure F.3: Test signal comparison of spectrum of average power in simulations (blue curves) and the median of 10 measurements with the flatsat (red curves). Black dotted lines indicate the 3 dB bandwidth of the receive filter.

density, but, for the TOTEM on LUME-1, there is no power calibration available. Measured power on LUME-1 is a relative measure and is displayed in dB.

In both the CW simulations and flatsat results (Figure F.3b), there is one peak at 435.1 MHz. This peak is expected since a complex tone is transmitted at 100 kHz and modulated onto the 435 MHz carrier. In the pulsed case (Figure F.3c), there is one peak at around 435.1 MHz since the transmitted signal was also shifted 100 kHz from the centre frequency. For a 5 ms long pulse, the sidelobes appear at multiples of 0.2 kHz, but there is not enough frequency resolution (4.7 kHz) to distinguish them. The spectrum of

a chirp signal with 300 kHz bandwidth can be seen in Figure F.3d. The chirp was directly modulated onto the RF carrier at 435 MHz, without shifting it 100 kHz, so that it could fit in the 3 dB bandwidth of the receiver.

To detect at which time window a signal becomes stationary, the time statistics of the moments can be analysed. In Figure F.4, the normalised LME second moment, for different signals, is shown. It compares theoretical results (blue dashed lines), simulation results for all frequency bins (blue circles), and flatsat results (all frequency bins in black asterisks, and the bin with the highest power with a red cross). It shows that the time variability of the local averages decreases when the window size increases. In the AWGN case (Figure F.4a), the normalised second moment for LME decreases following the result in Equation (F.23) and converges to $\pi/4$ after some time for all frequency bins. For the CW (Figure F.4b), the values are stable and do not change significantly with the time windows since a CW is a stationary signal at all time scales for the bin with the carrier, which is the bin with the highest power. The rest of the bins are the sidelobes of the signal. The lower the sidelobes, the lower signal to noise ratio, and the signal approaches the properties of an AWGN.

The pulsed signal curve (Figure F.4c) changes the behaviour considerably, depending on whether the time window is smaller than the pulse length (T_p) and/or the pulse repetition period (T_r). When the time window is larger than the pulse repetition period, the curve flattens out. The last two data points in the curve correspond to 13.6 ms and 27.3 ms, and, since the curve is converging, it indicates that the pulse repetition period is in that range. The indication in the graph is validated since the pulse repetition period is 16.67 ms. To be able to obtain a better estimation of the period, more time windows would be needed.

In Figure F.5, the difference between the values of consecutive windows normalised is shown. For the AWGN, the curve has a decreasing exponential trend, and, for the CW, the values are zero for the highest frequency bin. There should not be any variation between time windows for a continuous signal. In the case of the pulsed signal, the peak is in between the fifth ($T_5 = 3.4$ ms) and sixth point ($T_6 = 6.8$ ms). Since the pulse transmitted was 5 ms long, the curve is as expected. Furthermore, all theoretical, simulation, and flatsat values in Figure F.5 are similar, validating the algorithm.

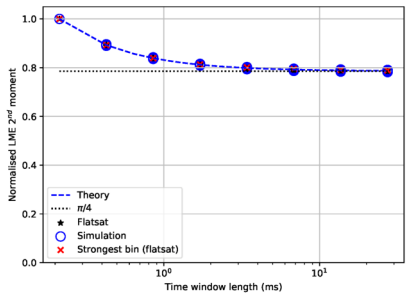

(a) Normalised Local Mean Estimator (LME) second moment for AWGN.

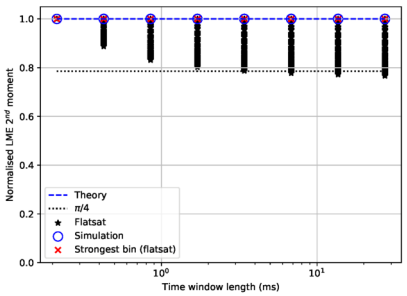

(b) Normalised LME second moment for a CW.

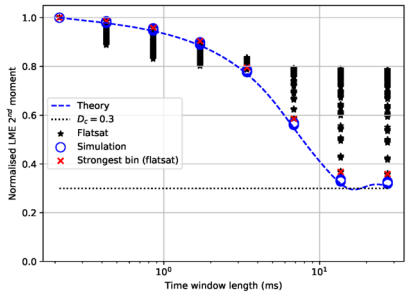

(c) Normalised LME second moment for a complex pulse.

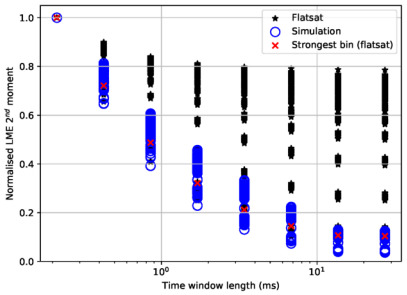

(d) Normalised LME second moment for a complex chirp.

Figure F.4: Comparison of the normalised LME second moment in theory, simulations and measurements with the flatsat. The pulse and the chirp signal have a pulse length of 5 ms and a period of 16.67 ms.

F.5.2 In-Orbit Results

The first in-orbit measurement was performed in December 2020. Three more measurement campaigns were carried out in the first half of 2021 during the months of February, May, and June. Each measurement set consisted of 10 individual calls to the measurement software as previously explained. In total, 300 individual measurements were executed. The main areas that the measurements covered were the South Pacific, South Atlantic, North America, Europe, and the Arctic.

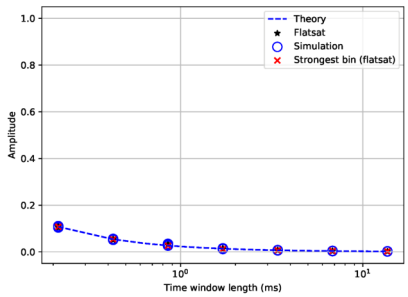

(a) AWGN bin difference.

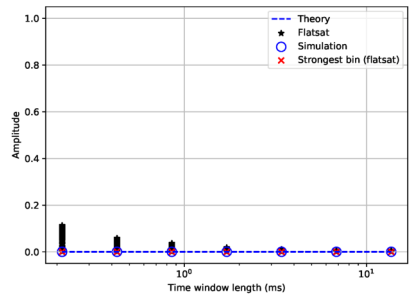

(b) CW bin difference.

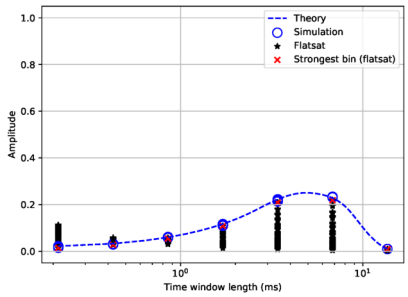

(c) Complex pulse bin difference.

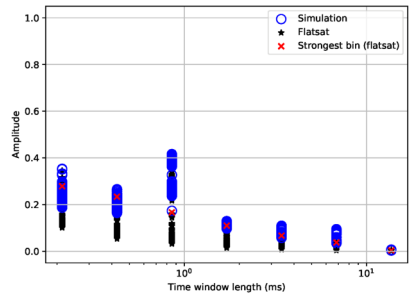

(d) Complex chirp bin difference.

Figure F.5: Comparison of bin difference in theory, simulations and measurements with the flatsat. The pulse and the chirp signal have a pulse length of 5 ms and a period of 16.67 ms.

Measurements over Non-Populated Areas

To analyse in-orbit interference measurements, it is important to measure over non-populated areas to estimate the noise floor. Since absolute power levels cannot be obtained from the satellite, these measurements can be used as a lower bound for the power. The estimation of the in-orbit noise floor can be compared to the AWGN measurements with the flatsat setup to verify that the spectrum shape is as expected.

The measurements over non-populated areas were taken over the South Pacific and South Atlantic, as shown in Figure F.6a. In total, 60 measurements were performed in this area, but five of them contained CW interference (red circles in the map). Thus, they were grouped with the

measurements over populated areas since they were obtained close to the South American coast.

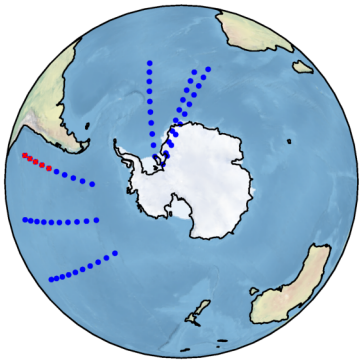

(a) Sub-satellite points for measurements over non-populated areas (blue circles) and close to populated areas (red circles).

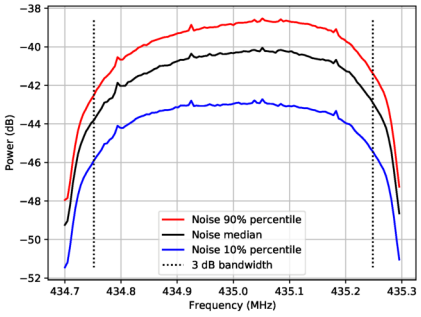

(b) Spectrum of average power (m_{2k}).

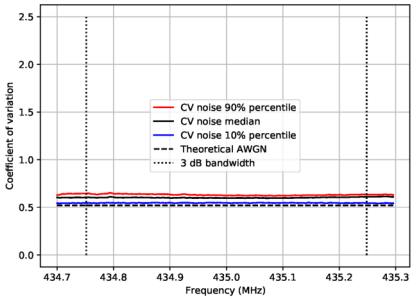

(c) Coefficient of variation (CV). A high coefficient indicates high spread in the measured envelope.

Figure F.6: Time-frequency behaviour of measurements over non-populated areas.

The average power spectrum (m_{2k}) was estimated over five seconds for each of the measurements. In Figure F.6b, the 90% percentile, median, and 10% percentile of the average power for each bin of all average power spectra are shown. The shape of the spectrum is very similar to the result obtained in the lab (Figure F.3a). In the bandwidth of interest (434.8–

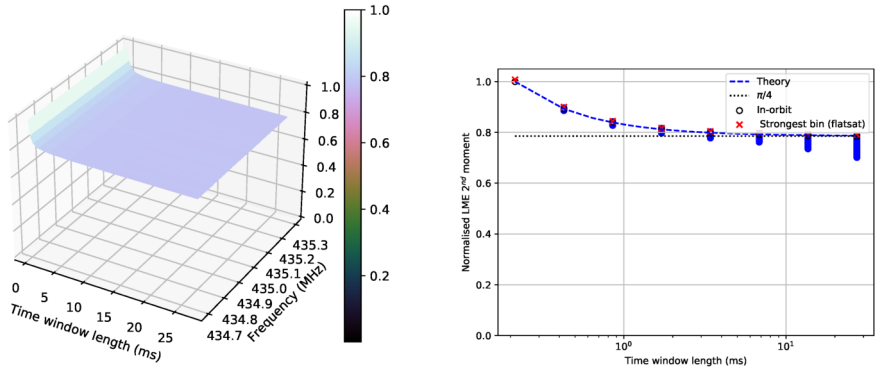

(a) Normalised LME second moment for different time windows in 3D.

(b) Normalised LME second moment for different time windows in 2D.

Figure F.7: Time behaviour of measurements over non-populated areas.

435.2 MHz), the median value of all measurements and all frequency bins is −41 dB. The 10% percentile is −44 dB, and the 90% percentile is −39 dB, including all frequency bins. In Figure F.6c, the coefficient of variation c_k was calculated using Equation (F.7) and compared to the theoretical value of AWGN in Equation (F.10), which is approximately 0.52. The CV for noise in-orbit measurement is similar to that of the AWGN but slightly higher for the median and the 90% percentile.

The variability of the LME as a function of averaging window length was also measured (Figure F.7). All measurements have similar temporal behaviour, so a representative example of the normalised LME second moment for all the frequencies is presented in Figure F.7a. The normalised LME second moment follows the AWGN time behaviour converging to approximately $\pi/4$. This trend can also be seen in Figure F.7b, where the normalised LME second moment was plotted for all frequency bins of all noise floor measurements (blue circles). The blue dashed line represents the theoretical trend for the AWGN, the red crosses show the highest bin measured in the flatsat setup, and the dotted line $\pi/4$. The in-orbit results show a slightly higher deviation from the flatsat results for AWGN for longer windows.

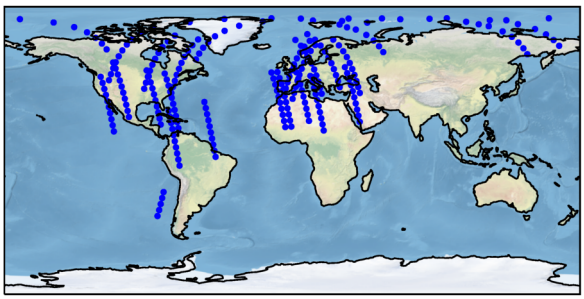

(a) Sub-satellite points for measurements over populated areas.

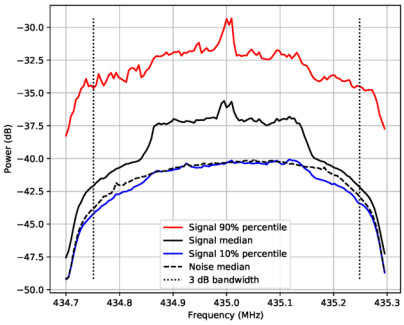

(b) Spectrum of average power (m_{2k}).

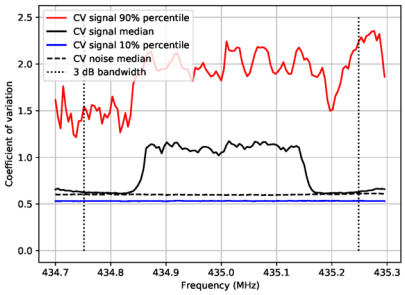

(c) CV. A high CV indicates high spread in the measured envelope.

Figure F.8: Time-frequency behaviour of measurements over populated areas.

Measurements over Populated Areas

The measurements performed close to populated areas are shown in Figure F.8a, and they are referred to as interference measurements hereafter. The 90% (red line) and 10% percentile (blue line) and the median (black continuous line) of all average power spectra measured over populated areas are compared to the median of the noise measurements over non-populated areas (black dashed line) plotted in Figure F.8b. The 10% percentile signal spectrum has about the same power level as the noise median spectrum.

A band-limited signal of around 300 kHz of low power can be observed in the 10% percentile signal spectrum, but it is more visible in the signal median and the 90% percentile spectrum as it has higher power. Since the band-limited signals appear clearly in the signal median, they are present

at least in half of the measurements. Furthermore, the 90% percentile spectrum has around 7 dB higher power than the median in the centre frequency and there seems to be a wide-band signal in addition to the band-limited signal.

The dispersion of the spectra can be analysed using the CV in Figure F.8c. The 10% percentile is close to the median of the CV for noise measurements. The CV for the signal median and the signal 90% percentile have a different tendency to that of the noise measurements. The CV in these cases is higher, which means the dispersion is higher and the probability for communication to be hit by interference significantly larger than the average power is higher than for AWGN. In the CV for the median, we observe that the increase of the dispersion is band-limited, as seen in the average power spectrum (Figure F.8b), while, for the 90% percentile, the band-limited signal is combined with other wide-band signals with even higher dispersion.

The Empirical Cumulative Density Function (ECDF) of the measured interference power of all frequency bins shows the probability of getting hit by an interference no larger than a certain power. The ECDF for the interference is estimated for three regions $R1$–$R3$ covering West and East Europe and northern Africa, together with the Middle East (Figure F.9). In the map shown in Figure F.9a, the northern parts of the plot are between 35° and 70° (marked with crosses in the map and with dashed lines in the plot), and the southern part is between 0° and 35° (circles in the map and a blue continuous line in the plot). Each of the northern regions represents 35° of longitude, while the southern region represents 70° of longitude. The points in the map represent the sub-satellite points where the satellite measured received power. The power of all frequency bins within the 3 dB bandwidth is included to estimate the ECDFs (Figure F.9b). As a reference, the red curve is the distribution of all regions.

There is a clear difference between the interference experienced in the regions in the north ($R1$ and $R2$) and south ($R3$). The region $R3$ is affected in less than 20% of the points by signals with a power higher than −38 dB. The power increases about 7 dB for regions $R1$ and and 6 dB in $R2$ for 20% of the points in relation to region $R3$. In general, the sub-satellite points with lower latitude experience less interference because they were acquired over less populated areas. Nevertheless, their distribution is different from the noise distribution (dotted black line).

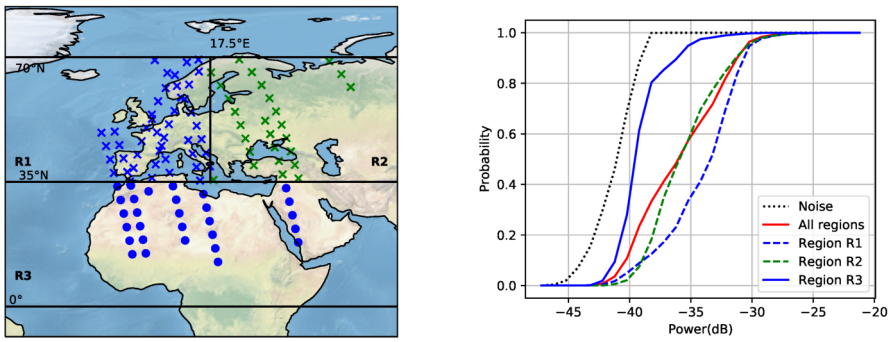

(a) Measurement locations over several orbits. The northern regions cover 35° of longitude and latitude; and the southern region, 70° of longitude and 35° of latitude.

(b) Empirical Cumulative Density Function (ECDF) of received power over the three regions and all frequency bins within the 3 dB bandwidth, including the noise floor measurements (black dotted line). The blue continuous line is linked to the blue circles in the map and dashed lines to crosses. Red line is the ECDF of all the points in the map.

Figure F.9: Power distribution over Europe, northern Africa, and the Middle East.

Figure F.10 shows the results of the same procedure applied to the measurements carried out over America, redefining the areas of interest. The coastal regions ($R4$, $R6$ and $R7$) cover 40° of longitude, while the middle region ($R5$) covers 30°. The latitude limits are 0°, 35°, and 70°, as shown in the map. The interference levels are lower than in Figure F.9b. The regions that are more affected by the interference are $R4$ and $R6$. Around 20% of the points in these regions experience an interference level higher than −36 dB. Furthermore, two different behaviours can be observed in region $R6$: 57% of the points experience interference levels above −38 dB, while the rest of the points follow a different trend with lower power. The regions $R5$ and $R7$ follow a distribution that is not so different from the noise (dotted black line).

One representative example of a measurement where the band-limited signal can be seen in the average power spectrum is shown in Figure F.11a, obtained close to Greenland. Two types of interference signals can be distinguished: one narrow-band at 434.74 MHz and the band-limited signal

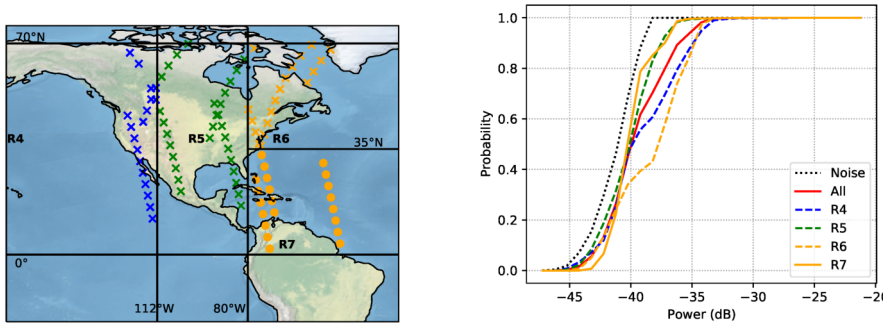

(a) Measurement locations over several orbits. The regions $R4$, $R6$ and $R7$ cover 40° of longitude; and the middle region $R5$ covers 30°. $R4$ and $R5$ cover 70° of latitude; and $R6$ and $R7$, 35°.

(b) ECDF of received power over the four regions, including the noise floor measurements (black dotted line). The yellow continuous line is linked to the circles in the map and dashed lines to crosses. The red line is the ECDF of all the points in the map.

Figure F.10: Power distribution over America divided in four regions. The colour blue is for western, green for central, and orange for eastern areas.

with a bandwidth around 300 kHz, which is about 7 dB higher than the rest of the spectrum. At the same time, the CV indicates that the band-limited signal has a higher spread as CV increases up to 2.6. The temporal behaviour of the frequency bins differs (Figure F.11b,c). When analysing both figures, we can see the main behaviour of the band-limited signal converging to about 0.25. The edges of the spectrum are a combination of noise and the sidelobes of the band-limited signal and converge to around 0.6.

Window of Stationarity

To analyse the first-order stationarity of the interference measurements, the window of stationarity is estimated at the −10 dB level for the CV (see Section F.3). The measurements have been divided into four regions (Figure F.12a): South Pacific and South Atlantic (named the Antarctic), America, the Arctic, and Europe. In this section, when we refer to Europe, we include the north of Africa and the Middle East. The estimation of the window of stationarity over the frequencies has been divided into two parts: the frequencies that are within the band-limited interference (434.83–

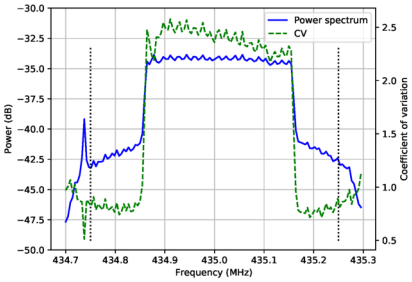

(a) Average power spectrum (m_{2k}) and coefficient of variation. If there was no time variability in the mean, it would be zero.

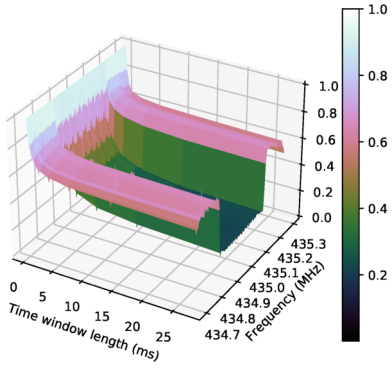

(b) Normalised LME second moment for different time windows for all frequency bins in 3D.

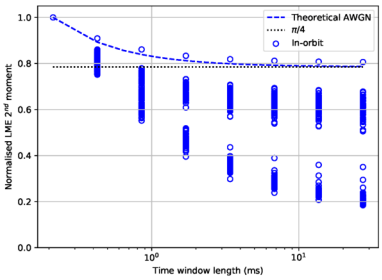

(c) Normalised LME second moment for different time windows for all frequency bins.

Figure F.11: Example of a five second measurement with different types of signals over Greenland.

435.19 MHz); and the ones outside but within the 3 dB bandwidth (434.75–434.83 MHz and 435.19–435.25 MHz).

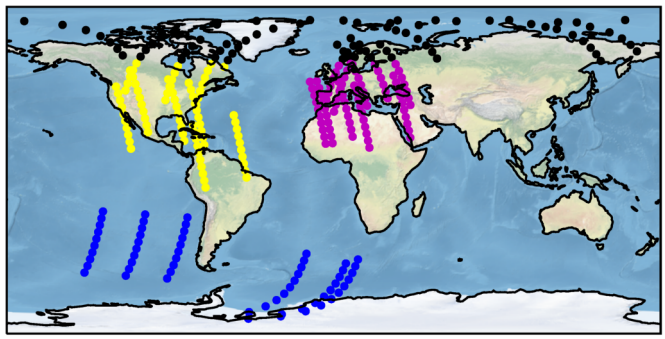

(a) Measurement locations grouped into four categories: Antarctic (blue), America (yellow), Arctic (black), and Europe (magenta).

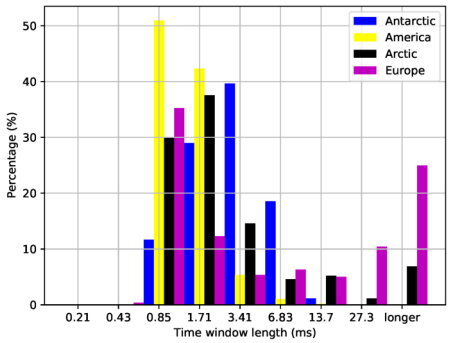

(b) Histogram of stationarity window per region (outside band-limited interference bandwidth).

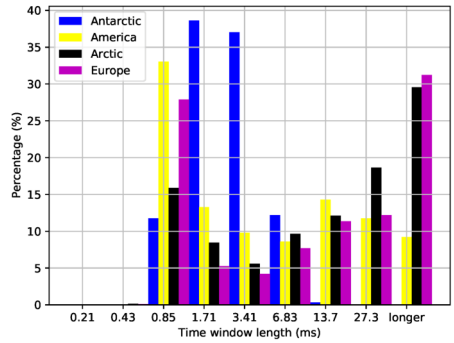

(c) Histogram of stationarity window per region (within band-limited interference bandwidth).

Figure F.12: Window of stationarity results of in-orbit measurements.

In Figure F.12b, the window of stationarity for frequencies outside the band-limited signal is shown. Most measurements have a window of stationarity below 6.83 ms, particularly the Antarctic measurements. The only regions that have stationarity windows longer than 27.31 ms are Europe and the Arctic.

In Figure F.12c, the frequency bins analysed are the ones within the band-limited interference. For the Antarctic measurements, there is no big change.

For the rest of the regions, the window of stationarity increases for more measurements. About 29% of the Arctic measurements have a window of stationarity longer than 27.3 ms. For America and Europe, it is around 9% and 31%, respectively. There is a considerable difference for measurements over America between Figure F.12b,c, since the largest window of stationarity in Figure F.12b is 6.83 ms, and, in Figure F.12c, it is longer than 27.3 ms.

Interference with Time Structure

In the measurements performed, interference with time structure was observed in different areas. Figure F.13a shows the sub-satellite points where different types of interference were detected visually. There are two types of interference with time structure: band-limited (red crosses) and wide-band (black circles). Interference with no time structure is marked with blue stars, and the position of the type A ground radars in the 420–450 MHz band, according to Reference [44], is marked with black triangles and numbers.

The band-limited interference was observed where the radars are present, and the bandwidth is consistent with the chirp bandwidth of these radars for the search mode (100–350 kHz for radar type A [44]). The bandwidth of the interference was estimated automatically based on two different parameters: the average power spectrum (m_{2k}) and the ratio of moments, $(m_{1k})^2/m_{2k}$. Both show similar results as depicted in Figure F.13b. Where the algorithm did not detect a signal, the bandwidth was set to zero. It can be seen that the m_{2k} approach has slightly lower performance when the interference has low power compared to the noise. In these cases, the estimation of the bandwidth has a better performance when using the ratio of moments approach. Figure F.13c shows the CV of the envelope for the cases where band-limited interference was visually detected. It was estimated by calculating the median of c_k over the bandwidth where the band-limited interference was detected. The cases where the ratio is zero are due to the same reason as before, i.e., where the bandwidth was not detected automatically, the CV was set to zero. The CV gives an indication of the spread and dispersion of the envelope. For AWGN, the CV is 0.52 since the spread in envelope is low. In Figure F.13c, the CV is higher than the AWGN and up to 2.6. This means that the dispersion of the envelope is higher, and the probability of getting hit by stronger than average interference is higher

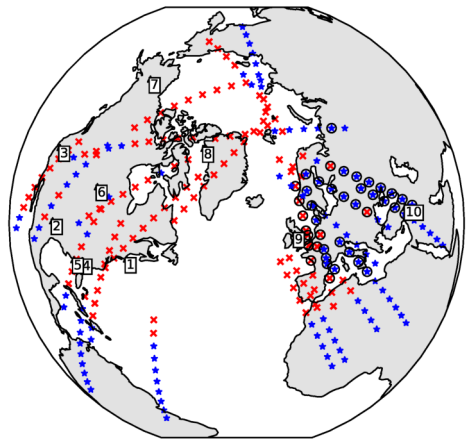

(a) Measurement location where band-limited interference (red crosses) and wide-band interference (black circles) with time structure was detected by visual analysis, rest of locations (blue stars), ground radar locations (black triangles with numbers) [44], [45]. 1: Massachusetts (U.S.), 2: Texas (U.S.), 3: California (U.S.), 4: Georgia (U.S.), 5: Florida (U.S.), 6: North Dakota (U.S.), 7: Alaska (U.S.), 8: Thule (Greenland), 9: Fylingdales Moore (United Kingdom), 10: Pirinclik (Turkey).

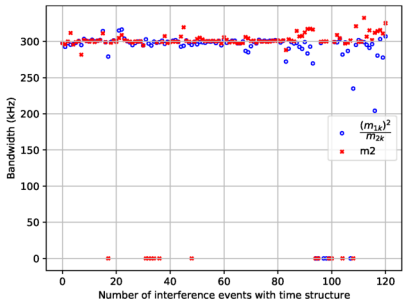

(b) Automatic bandwidth estimation using two parameters: the ratio of moments, $(m_{1k})^2/m_{2k}$; and the average power spectrum (m_{2k}). The cases with zero bandwidth corresponds to when the automatic detection failed.

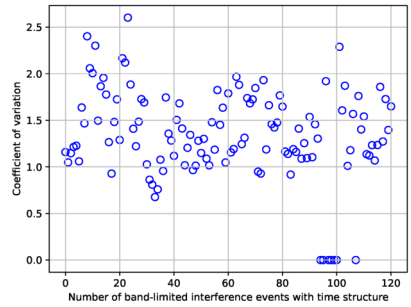

(c) The median of the CV over the bandwidth of the automatically detected band-limited interference. The cases with zero correspond to when the automatic detection failed. A high coefficient indicates high spread in the measured envelope.

Figure F.13: Detection of band-limited interference, estimation of bandwidth, and CV.

than if it was an AWGN with the same average power.

F.6 Discussion

The interference measured over non-populated areas has similar behaviour to the AWGN behaviour both in frequency and time. The in-orbit spectrum measured (Figure F.6b) shows the frequency response of the system that was measured in the lab (Figure F.3a). The measurements over non-populated areas can be used as an in-orbit relative noise floor and justify the use of heatmaps over these areas since the behaviour is close to Gaussian. In the power spectrum, there is a variation that can be caused by the tumbling of the satellite that introduces a variation in antenna gain and polarisation, as well as a variation in internal temperature. On several of the measurement tracks, the satellite moved from daylight (highest internal temperature) to eclipse (lowest internal temperature). This could also be the explanation why the temporal behaviour is not completely Gaussian; perhaps there is a slow variation of internal temperature causing this difference.

For the populated areas, the power levels of the interference are higher than the noise floor. In these areas, there can be a lot of interference sources, such as ground stations for different satellites and amateur radio activity. The results show that the measured interference over different regions has different frequency and time behaviour. There are different types of interference: some have AWGN statistics, others show CW temporal behaviour, and the last type has a pulsed tendency (both band-limited and wide-band). The AWGN is predominant on the edges of the frequency response where no other signals are present. The narrow-band signals (CW) can be beacons from radio amateurs and would be possible to locate with more measurements.

The interference that has roughly 300 kHz bandwidth has higher power than the noise floor and different statistics than CW and AWGN. This signal requires a longer time window to obtain a consistent estimate of the average envelope than the AWGN. It is consistently present over the areas where there are known type A radars. The frequency band measured in this paper is 435 MHz and is exactly in the middle of the band for ground

radars (420–450 MHz), so it is expected to see some of that behaviour. The bandwidth also matches the chirp bandwidth for the search mode of type A radars used for space-tracking (100–350 kHz) [44].

There was also another type of interference with time structure detected over central Europe. However, this interference has a bandwidth higher than what can be seen with the configuration of these measurements (higher than 500 kHz). This interference could be caused by the radar chirps from the tracking mode (1 MHz wide), but it can also be a different source.

The time behaviour measured shows high variability within five seconds. Average power is a useful measure to design a system that works for the average interference environment, but it does not take the temporal structure and dispersion of the interference into account. The CV can be helpful to estimate how much time variability the signal has. The CV is a measure of dispersion. So, if a band has significant power above the general noise floor and the CV is high, the peak power is much higher than the average power. The high CV observed over Europe, the Arctic, and the coastlines of North America indicates a much larger spread in amplitude than for AWGN. A communication system designed to cope with AWGN at the noise levels given by a heatmap fails under these circumstances. The stationarity measurements and the CV show that the interference is not AWGN over populated areas.

The window of stationarity can be used as the required length of an interleaver to obtain average coding performance for each interleaved interval. Even though a lot of measurements are required to increase the reliability of the estimation of the length of this window, we can identify regional trends. For frequencies in the range 434.75–434.83 MHz and 435.19–435.25 MHz, the length could be less than 14 ms for most cases and regions. For the Arctic and Europe, longer lengths are needed for more reliability. In the band 434.83–435.19 MHz, there is a significant portion of measurements over America, Europe, and the Arctic, where window lengths longer than 27 ms are needed.

The results presented are part of the measurement campaigns performed in the first half of 2021. Calibration measurements to estimate absolute power levels are planned for the next phase. A ground station will transmit test signals, such as a CW, with a known power to calibrate the in-orbit

power results. Furthermore, global measurements will be performed to obtain an overall view of the interference environment. These measurements will have a lower frequency resolution to decrease the data size of the campaign. The center frequency will also be modified to observe the frequency variability. It is important that future measurements include ECDF measurements of the interference IQ samples, as well as temporal characteristics to enable the choice of the right countermeasures to obtain robust uplink communication.

F.7 Conclusions

In this article, we have presented an algorithm that can measure frequency and time characteristics of in-orbit interference with low downlink data rate requirements. The method is validated through theoretical analysis, simulations and hardware-in-the-loop testing, and executed in-orbit measurements on the LUME-1 satellite. The studied frequency band was the UHF amateur radio frequencies commonly used for TT&C of small satellites. The in-orbit interference measurements were carried out over the South Pacific, South Atlantic, North America, Europe, North Africa, the Middle East, and the Arctic during the spring of 2021.

As expected, higher interference levels were generally detected over populated areas. Three different time behaviours were distinguished: AWGN, narrow band CW, and pulsed. The pulsed behaviour was seen by analysing the variation of the local mean of the average envelope as a function of window length. High values of the coefficient of variation were estimated in regions with band-limited interference that have significant power over the general noise floor. For that interference, the peak power is much higher than the average power. This interference was observed over areas with known type A ground radars in the UHF band around 435 MHz, and the observed bandwidth of 300 kHz is consistent with the chirp bandwidth for radar search mode [44]. Furthermore, wide-band interference with pulsed behaviour was measured over Europe, but the bandwidth could not be estimated due to the limited bandwidth of 500 kHz in the measurements.

A global measurement campaign is planned to provide a world overview of

the interference environment in the selected band. Calibration measurements using a ground station transmitting to the satellite will enable the use of absolute power levels. Furthermore, different centre frequencies will also be studied, and ECDF measurements of the IQ samples will be planned to obtain the proper interference statistics to design the counter-measures required to improve the reliability of the satellite uplink in the UHF amateur radio band.

Author contribution Conceptualisation, G.Q.-D., T.E., and F.A.A.; methodology, G.Q.-D. and T.E.; software, G.Q.-D.; validation, G.Q.-D. and D.H.d.M.; formal analysis, G.Q.-D. and T.E.; investigation, G.Q.-D., J.M.L.A., A.G.M., and F.A.A.; resources, F.A.A., A.G.M., D.H.d.M., and J.M.L.A.; data curation, G.Q.-D.; writing—original draft preparation, G.Q.-D.; writing—review and editing, G.Q.-D., T.E., F.A.A., J.M.L.A., and D.H.d.M.; visualisation, G.Q.-D.; supervision, T.E. and F.A.A.; project administration, T.E.; funding acquisition, T.E. and F.A.A. All authors have read and agreed to the published version of the manuscript.

Funding The work of the Norwegian University of Science and Technology (NTNU) is supported by the Norwegian Research Council (Grant No. 270959), the Norwegian Space Agency, and the Centre of Autonomous Marine Operations and Systems (NTNU AMOS). The work of the University of Vigo has been funded by Programa de Cooperación Transfronteriza INTERREG V-B SUDOE (Fondos FEDER) under the project "Wildfire picosatellite constellation & uavs remote sensing: active fire mapping and management" (Grant No. FIRE-RS, SOE1/P4/E0437) and by Ministerio de Economía y Competitividad— Programa Estatal de Investigación, Desarrollo e Innovación Orientada a los Retos de la Sociedad under the project "Development of a small satellite for spectrum monitoring and validation of robust communications" (Grant No. ESP2016-79184-R).

Institutional review Not applicable.

Informed consent Not applicable.

Data availability The data presented in this study are available on request from the corresponding author.

Conflicts of interest The authors declare no conflict of interest. The funders had no role in the design of the study, in the collection, analyses, or interpretation of data, in the writing of the manuscript, or in the decision to publish the results.

Acknowledgments Gara Quintana Díaz wishes to acknowledge the help of her colleagues, Roger Birkeland and Jens Abraham, and Nicolás Molina Padrón for useful discussions of ideas and results.

Appendix. Properties of Local Mean Envelope of a Stationary Stochastic Process

A discrete-time envelope $z[n]$ is generated by a stationary stochastic process with mean μ_z and variance σ_z^2. The first-order moment is $m_1 = \mathbb{E}\{z[n]\} = \mu_z$, and the second-order moment is $m_2 = \mathbb{E}\{z[n]^2\} = \sigma_z^2 + \mu_z^2$. The length T ($T \in \{0, 1, 2, \ldots\}$) sliding local average of the envelope $z[n]$ can be obtained as

$$u[n] = h[n] * z[n], \tag{F.11}$$

where $h[n]$ is the square window Finite Impulse Response (FIR) filter normalized with the length T to get the average,

$$h[n] = \begin{cases} 1/T, & \text{for } n = 1, \ldots, T \\ 0, & \text{else.} \end{cases} \tag{F.12}$$

The LME is obtained as $u[n]$ sub-sampled by a factor T. The moments of $u[n]$ are hence the moments for the LME. The first-order moment (mean) of the LME is the mean of $u[n]$, which is μ_z. The second-order moment depends on the length T. To obtain it, we study the correlation function for $u[n]$, the filtered stochastic signal

$$r_u[k] = \mathbb{E}\{u[n] \cdot u[n+k]\} = r_h[k] * r_z[k], \tag{F.13}$$

where $r_z[k]$ is the correlation for the envelope $z[n]$, and

$$r_h[k] = h[k] * h[k] = \begin{cases} \dfrac{T-|k|}{T^2}, & \text{for } -T \leq k \leq T \\ 0, & \text{else.} \end{cases} \tag{F.14}$$

As $z[n]$ is real valued and $z[n] \geq 0$ then $r_z[k] = r_z[-k]$ and $r_u[k] \geq 0$. The second-order moment for $u[n]$, denoted m_2^T, is obtained as $r_u[0]$

$$\begin{aligned} m_2^T = r_u[0] = r_h[k] * r_z[k]|_{k=0} &= \sum_{k=-\infty}^{\infty} r_h[k] \cdot r_z[0-k] \\ &= \frac{1}{T}\left\{ r_z[0] + \frac{2}{T}\sum_{k=1}^{T}(T-k)\cdot r_z[k] \right\}. \end{aligned} \tag{F.15}$$

For $T = 1$, we obtain $m_2^1 = m_2$, which is the power of the signal. Hence, the LME has the mean $\mu_u = \mu_z = m_1$ and the variance $\sigma_u^2 = m_2^T - (m_1)^2$, where the second-order moment is given in Equation (F.15).

By normalising the LME second-order moment by the power of the signal, we obtain the moment ratio as

$$\frac{m_2^T}{m_2} = \frac{1}{T} + \frac{2}{T^2}\sum_{k=1}^{T}(T-k)\cdot\frac{r_z[k]}{r_z[0]}. \tag{F.16}$$

The ratio starts at 1 for $T = 1$ and converges to $\dfrac{(m_1)^2}{m_2}$ for large T, as for a sufficiently large T the LME is equal to the mean of the envelope. How fast the ratio converges depends on the correlation function $r_z[k]$. If the correlation function falls off fast, the m_2^T will converge fast. We use the coefficient of variation to evaluate the convergence of the LME.

Example Signal: Constant Envelope

A signal with constant envelope $z[n] = a$, as a CW, has a constant envelope correlation $r_z[k] = a^2$. The ratio in Equation (F.16) is then $\dfrac{(m_2^T)^2}{m_2} = 1$, for all T.

Example Signal: Square Pulse

For a square pulse wave that is on with magnitude a for a duration T_p with a period T_r, the envelope correlation is periodic $r_z[k] = r_z[k - T_r]$. For $T_p < T_r/2$, the correlation is:

$$r_z[k] = \begin{cases} a^2 \cdot \dfrac{T_p - k}{T_p}, & \text{for } |k| < T_p \\ 0, & \text{for } T_p < |k| < T_r - T_p. \end{cases} \tag{F.17}$$

The moment ratio, Equation (F.16), of a pulse converges to the duty cycle:

$$\lim_{T\to\infty} \frac{m_2^T}{m_2} = \frac{(m_1)^2}{m_2} = \frac{\left(\dfrac{T_p}{T_r} \cdot a\right)^2}{\dfrac{T_p}{T_r} \cdot a^2} = \frac{T_p}{T_r}. \tag{F.18}$$

Example Signal: White Signal

For a signal with independent but equally distributed samples, the correlation is

$$r_z[k] = \mathbb{E}\{z[n] \cdot z[n+k]\} = \begin{cases} \mathbb{E}\{z^2[n]\} = m_2, & \text{for } k = 0 \\ \mathbb{E}\{z[n] \cdot z[n+k]\} = (m_1)^2 & \text{for } k \neq 0 \end{cases}. \tag{F.19}$$

Inserting this correlation into Equation (F.15), the second-order moment for the LME for a white signal is obtained as

$$m_2^T = (m_1)^2 + \frac{m_2 - (m_1)^2}{T} = \mu_z^2 + \frac{\sigma_z^2}{T}. \tag{F.20}$$

For large T, the second-order moment m_2^T converges to the squared mean of the envelope.

For an AWGN, the samples are zero mean complex normal distributed, and the envelope has a Rayleigh distribution. The $\mathbb{E}\{z^2[n]\} = m_2$ is the

power of the signal. The mean of the envelope is

$$m_1 = \mu_z = \mathbb{E}\{z[n]\} = \sqrt{\frac{\pi}{4} \cdot m_2}, \tag{F.21}$$

and the variance is

$$\sigma_z^2 = m_2 - \mu_z^2 = m_2 \cdot \left(1 - \frac{\pi}{4}\right). \tag{F.22}$$

The normalised second moment given in Equation (F.16) is then

$$\frac{m_2^T}{m_2} = \frac{\pi}{4} + \frac{1}{T} \cdot \left(1 - \frac{\pi}{4}\right), \tag{F.23}$$

which converges to

$$\lim_{T \to \infty} \frac{m_2^T}{m_2} = \frac{(m_1)^2}{m_2} = \frac{\pi}{4} \tag{F.24}$$

for large T.

G In-orbit Interference Measurements and Analysis in the VDES-band with the NorSat-2 Satellite

The text of the following paper is added as a chapter and re-formatted for better readability:

G. Quintana-Díaz, R. Birkeland, L. Løge, E. Andersen, A. Bolstad and T. Ekman, 'In-orbit Interference Measurements and Analysis in the VDES-band with the NorSat-2 Satellite,' in *IEEE Aerospace Conference [accepted]*, 2022

Abstract Maritime activity in the Arctic is increasing, triggering a need for better communication infrastructure. With limited terrestrial infrastructure available, satellite services are essential for distributing maritime safety information, such as ice and weather information, navigational augmentation data, and basic communication to vessels operating in the vulnerable Arctic environment. The VHF Data Exchange System (VDES) is a new communication system for ships, extending the successful Automatic Identification System (AIS). VDES has a satellite component (VDE-SAT) which will extend the terrestrial-based coastal coverage to global coverage. Measurements and analysis of the in-orbit radio environment are needed to improve the robustness and reliability of the VDE-SAT system. Knowledge and understanding of the in-orbit interference will allow the development of appropriate interference mitigation techniques. This paper presents preliminary in-orbit measurement results and analysis of the radio environment in the VDE-SAT frequencies in the 157.2875 – 157.3375 MHz band. The measurements were carried out using the VDE-SAT payload on-board the Norwegian NorSat-2 satellite. We analyze the time-frequency characteristics of interference by studying two types of statistics on the raw in-phase

and quadrature samples: the general temporal dynamic of the interference, characterised using the Local Mean Envelope (LME) for different averaging window lengths; and the interference duration and periodicity. Both these views play a role when choosing suitable countermeasures to get robust communications. The coefficient of variation on the LME is used to study the dispersion. Data from two measurement campaigns over the Arctic area from May 2021 are analysed using these two methods, and the initial results are presented.

G.1 Introduction

Global warming is affecting the Arctic and the temperature is rising at even higher rates than the rest of the world [4]. The ice is melting and some predictions indicate there could be ice-free summers in this century [25]. Ship traffic routes will constantly change due to ice melting, and navigation of these areas will be difficult without frequently updated ice charts. Thus, increased connectivity and reliable communication to ships in the Arctic is needed [2], and terrestrial communication is seldom available. Therefore, satellite services will play a key role in this scenario, as they provide digital communication to vessels far from coastal infrastructure.

The Automatic Identification System (AIS) is a maritime communication system used for ship safety and navigation aid [202] that also has a satellite component to increase coverage. The main focus of the AIS is to avoid vessel collisions by broadcasting the position, speed, and course of all ships above a given size. All nearby ships can then follow the navigational status of the transmitter on their navigation system. Furthermore, AIS data can be used for different purposes, like search-and-rescue operations [203], as well as estimating sea pollution from ships [204], fighting illegal fishing, among many others. However, the success of the AIS system resulted in a huge increase of users, overloading the system in areas with high maritime traffic [205]. Thus, the International Association of Lighthouse Authorities (IALA) and its members started developing the VHF Data Exchange System (VDES) to offload the data traffic of the AIS and to provide new capabilities, such as ship-to-ship messaging [206] and distribution of ice charts to aid navigation [65]. The VDES standard was approved in 2015 and is formed

by three services: AIS, Application Specific Messages (ASM) and VHF Data Exchange (VDE) [207], [208]. The ASM channels are used to send predefined messages to report weather conditions, safety and navigational purposes [209]. VDE is more flexible and has a terrestrial component (VDE-TER) and a satellite component (VDE-SAT). Both VDE types, as well as ASM, support Adaptive Coding and Modulation (ACM), allowing for changing modulation and error correction codes while adapting to varying communication conditions.

Choosing the right modulation and error coding is vital to increase the data throughput effectively. This selection depends on channel and interference behaviour in the frequency band used. For the VHF maritime propagation channel, there have been some studies on the empirical path loss [210], [211] and signal propagation at sea [212]. A channel model for VDE-SAT is presented in [63]. The first VDE-SAT downlink measurements were performed in November 2017 using the NorSat-2 satellite [64]. Three different types of VDES signals, in addition to a Continuous Wave (CW), were transmitted from the satellite: Binary Phase Shift Keying (BPSK)/Code Division Multiple Access (CDMA), $\pi/4$-Quadrature Phase Shift Keying (QPSK) and 8-Phase Shift Keying (PSK). The signals were received on two vessels and raw In-Phase and Quadrature (IQ) samples were recorded. Initial analysis of the variation of the carrier-to-noise-density ratio (C/N_o) for each signal type over a pass was carried out in [64]. In [65], the variation of the downlinked CW signal power and Doppler shift was analysed for more than a 100 passes. The typical carrier received power on-board a vessel was -118 dBm for the measurements performed. Further analysis on the beacon power distribution and fading distribution estimations can be found in [66]. However, all these VDE-SAT measurement results have focused on the downlink performance. The interference environment encountered when satellites receive messages from vessels is still not characterised. This is needed to establish a reliable two-way communication.

In this paper, we present a preliminary analysis of the time-frequency characteristics of the radio interference in the lower leg of the uplink VDE-SAT frequency band (157.2875 – 157.3375 MHz) over the Arctic area. Two measurement campaigns on two consecutive days were performed with the NorSat-2 satellite, where IQ samples were recorded for post-processing using the Local Mean Envelope (LME) method and a pulse detection algorithm. The results of this project can be used to plan future measurements with

NorSat-2 or other satellites. Measurement results can be used to optimise waveforms in the VDES standard.

The remainder of the manuscript is structured as follows. First, the NorSat-2 satellite and the analysis method are described, as well as the measurement planning and configuration. Second, the results of the measurement campaigns are presented. Finally, the conclusions are presented.

G.2 Method

In this section, the measurement strategy, and the analysis methods are explained. Two algorithms to measure time and frequency characteristics of interference are described.

G.2.1 The NorSat-2 satellite

NorSat-2 was launched in July 2017, and was built by University of Toronto Institute for Aerospace Studies (UTIAS) for the Norwegian Space Agency (NOSA) [213]. It has two main objectives: primarily, to collect AIS data from ships and forward it to Norwegian users, mainly the Norwegian Coastal Administration (NCA). Secondary, to demonstrate the use of the VDE-SAT with a VDE-SAT payload owned by Space Norway, and developed by Kongsberg Seatex. The VDE-SAT payload is based on Software-Defined Radio (SDR) technology and is connected to a folded dipole Yagi-Uda VHF antenna with three cross elements providing 8 dBi gain.

The SDR payload can also be used to measure the in-orbit radio environment in the VDES bands by storing the raw IQ samples recorded. To measure the radio environment, the satellite will be listening without transmitting. The samples will be downloaded and processed on ground with different algorithms to, for example, detect and characterize any measured interference. In the next section, two different algorithms to analyse interference will be presented.

G.2.2 Local Mean Envelope (LME)

The LME method is a low-complexity algorithm that measures both time and frequency characteristics of a signal [88]. Firstly, Discrete Fourier Transforms (DFTs) of the incoming IQ data are calculated throughout the measurement duration. Secondly, the mean of the envelope for each frequency bin is estimated throughout all the measurement duration, as well as the average power in the same time frame. The time variability comes from estimating the local mean envelopes for different time window lengths for each frequency bin. The coefficient of variation (CV) is used to calculate the dispersion of the data and the first-order stationarity window.

G.2.3 Detection of pulsed interference

A simple algorithm to automatically detect pulsed interference and their characteristics (pulse length and pulse period) was implemented. The absolute value of the complex signal formed by the raw IQ samples recorded is calculated and a median filter is applied to smooth out the signal. After smoothing the signal, signal pulses can be detected. The minimum detectable pulse length is approximately 7 μs and the minimum detectable pulse period was 0.7 ms due to the configuration of the algorithm. The edges of the pulses yield the pulse length, and its period is estimated as the difference of the position where the pulses were detected.

G.2.4 Measurement planning

The main target of interest is the Arctic Ocean, where VDE-SAT can be used to distribute ice charts and help increase maritime safety. Ten different measurement tracks centered at Bjørnøya/Bear Island (Norway) were recorded in May 2021. The raw IQ data captured by the SDR onboard NorSat-2 was saved for post-processing on ground. Each track is referred to as *one session* and lasted approximately 10-12 minutes. Five sessions were recorded on the 5^{th} of May (S13-S17) and the next five sessions were executed the next day at similar times (S18-S22) so that the tracks were close to each other, see Figure G.1.

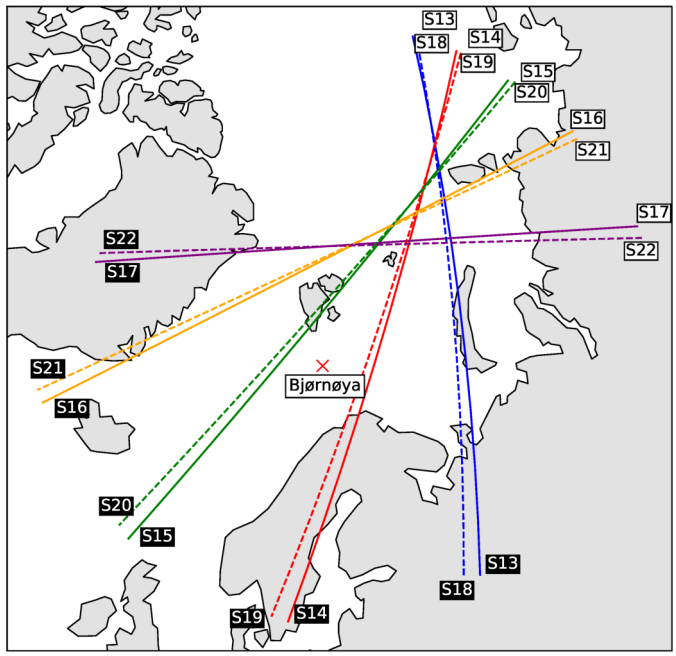

Figure G.1: Measurement tracks. Tracks S13-S17 were recorded on 5th May 2021 and S18-S22 on 6th May 2021. White squares indicate where the satellite started the track and black squares where it ended.

G.2.5 Measurement configuration

The measurement configuration used in these campaigns is summarised in Table G.1. The center frequency chosen was the nominal uplink frequency for VDE-SAT in the lower leg to measure the interference received by the satellite, and the bandwidth corresponds to the channel bandwidth of VDE-SAT [206]. The Automatic Gain Control (AGC) was deactivated to keep the same gain for all measurement points. All power values relate to the output of the VHF antenna. The satellite was configured to point the satellite antenna towards the horizon in the direction of Bjørnøya (Norway) in all passes, so the antenna was tracking that target for the measurements. The measurements were carried out without the satellite transmitting any signal to be able to measure the noise and interference environment.

Table G.1: Measurement configuration

Parameter	Value
Center frequency (MHz)	157.3125
Bandwidth (kHz)	50
Sampling rate (kSps)	134.4
Number of bits per sample	8

G.3 Measurement results

To get an overview of the measured power (interference) in the different sessions, the Empirical Cumulative Density Function (ECDF) of instantaneous power received for each session is calculated using the raw IQ samples (Figure G.2). The sessions that follow similar tracks in the two consecutive days, are plotted with the same colour. Continuous lines indicate sessions taken the 5^{th} May and dashed lines, 6^{th} May. It can be seen that lines with the same colour have very similar power distributions, which means that the distribution of instantaneous power over those locations did not change considerably from the first measurement day to the second. The tracks *S13* and *S18* show slightly less power than the rest. However, all measured tracks have a similar distribution of instantaneous power. These measurements give an indication of the power distribution, but more measurements are necessary to address time variability over larger time scales. The steps that appear in the ECDFs are due to the 8 bit quantization. Most of the power values lie on the lowest bits.

The percentiles of average power spectrum density during one-second segments of all measurement sessions are shown in Figure G.3. The drop in power at 157.2875 and 157.3375 MHz coincides with the 50 kHz bandwidth configured. However, this drop is much bigger for the 10% percentile spectrum (15 dB) than for the 50% (median) or 90% percentile, 5 and 3 dB. There is a big dispersion in the spectra. Within the configured bandwidth, there is about 15 dB less power density in the 10% percentile compared to the median, and 4 dB less from the median to the 90% percentile. Thus, 50% of the power spectral density averages are above -142 dBm/Hz in the considered bandwidth. Furthermore, there is a narrow-band signal in the center of the band.

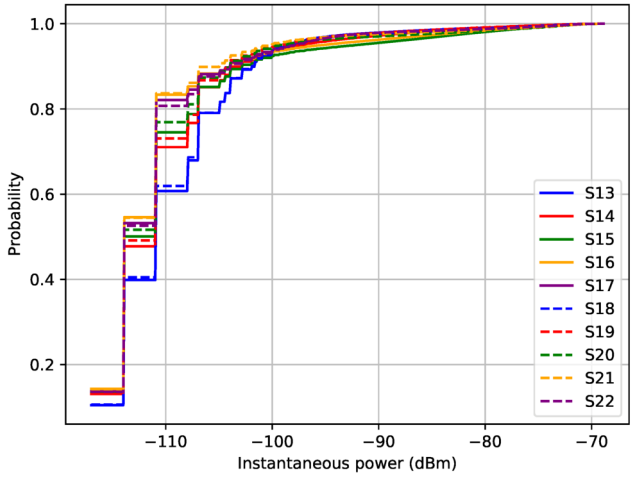

Figure G.2: Empirical Cumulative Density Function (ECDF) of instantaneous power received over the tracks. Same colour indicate similar tracks performed in two consecutive days. The tracks of the first day are in continuous lines and the second day, in dashed lines.

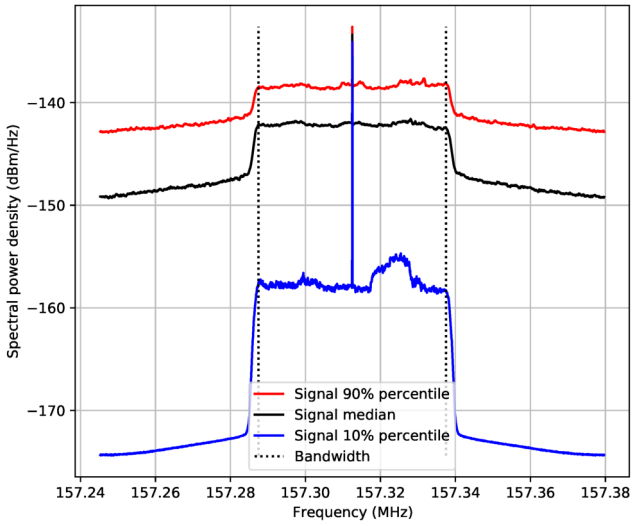

Figure G.3: Average power spectral density percentiles.

The coefficient of variation c_k was calculated to analyse the dispersion of the data and compare it with the CV of Additive White Gaussian Noise (AWGN). As it can be seen in Figure G.4, there are different frequency behaviours. The narrow-band signal has a CV close to zero, indicating low dispersion in the envelope. Since the signal is narrow-band, does not vary in time, and is in the center of the band, it is most likely the local oscillator of the receiver. For the 10% percentile, the CV out of band is the same as the one for AWGN, and within the bandwidth, the CV is slightly higher. However, for the median and 90% percentile, the CV out of band is higher than the one in-band. The CV in-band is also much higher than for the 10% percentile, indicating that the measured interference is be pulsed. The signals out of band are more attenuated than the one in-band due to the 50 kHz digital filter, and they have a larger dispersion. The difference between Figure G.4a and Figure G.4b is that the first one uses segments of 2048 samples to calculate the DFT, which is equivalent to 15 ms of signal; and the second one uses segments of 32 samples (0.24 ms). Hence, in Figure G.4a the variability within 15 ms cannot be appreciated in the CV, whereas in Figure G.4b the CV is higher, indicating that there was a high variability within 15 ms.

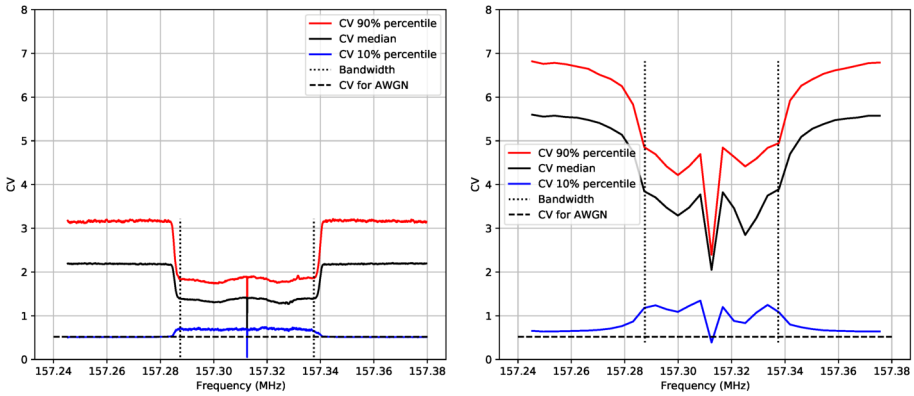

(a) CV calculated from DFT segments of 2048 frequency bins (15 ms).

(b) CV calculated from DFT segments of 32 frequency bins (0.2 ms).

Figure G.4: CV. A high CV indicates high spread in the measured envelope.

In satellite communications, time variability on the order of seconds implies spatial variability since the satellite is orbiting the Earth. In Figure G.5a,

the tracks have been divided into four regions according to the average local power while avoiding rapid changes between region: $R1$ from -100 dBm to -95 dBm, $R2$ from -95 dBm to -90 dBm, $R3$ from -110 dBm to -100 dBm, and $R4$ from -115 dBm to -110 dBm. The power is the sum of the average power in the frequency bins within the bandwidth. The ECDFs of this power measure over the regions are presented in Figure G.5b. The red curve represents the ECDF of the power of all regions. Region $R2$ (black), where all tracks crossed each other, shows the highest interference in the measurements. The ECDF of the region $R1$ (yellow) shows less power than region $R2$, but higher than the two other regions, and it does not appear in all tracks. Region $R3$ shows less power than the previous regions and is present in the second part of the tracks. Finally, the magenta region appears at the beginning of tracks $S13/S18$ and $S14/S19$, and at the end of $S16/S21$ and $S17/S22$. This region receives very little power.

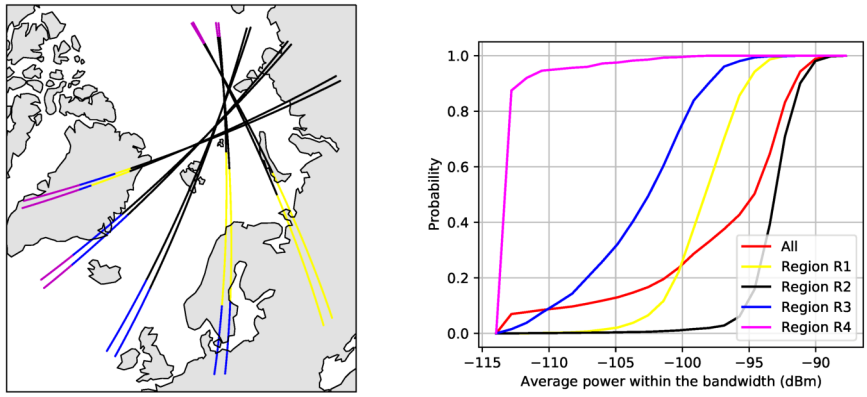

(a) Sub-satellite points grouped into four regions chosen based on the average local power.

(b) ECDF of average power within the bandwidth.

Figure G.5: Power distribution of measurement tracks divided into four regions.

Using the LME method and the CV, the window of stationarity has been calculated for each region (Figure G.6). In this paper, we define first-order stationarity as when the coefficient of variation of the local means is below -10 dB as in [88]. When the CV of the local mean of a specific window reaches this convergence, that window is referred to as the stationarity window. The shortest window for region $R1$ is 0.95 ms, for a tiny percentage of points. The percentage slowly increases when the windows are larger, but

almost 55% of the points have a window of stationarity longer than 121.9 ms. This means that there is high variability between long local means of the signal envelope and that the one-second measurement has non-stationary statistics. Region $R2$ has even a larger percentage of points (around 76 %) with a stationarity window longer than 121.9 ms. This percentage of points for windows smaller than 61 ms is very low, increasing to 7.5% for 61 ms and 16% for 121.9 ms. Region $R3$ has a slightly higher percentage of points in shorter windows, as compared to region $R2$, having almost 39% of the points with a stationarity window longer than 121.9 ms. The trend changes in the region $R4$ where about 67% of the points have a stationarity window close to 0.95 ms, and the rest have different windows. It seems that a time window of 0.95 ms is long enough to have similar statistics and be stationary in this region.

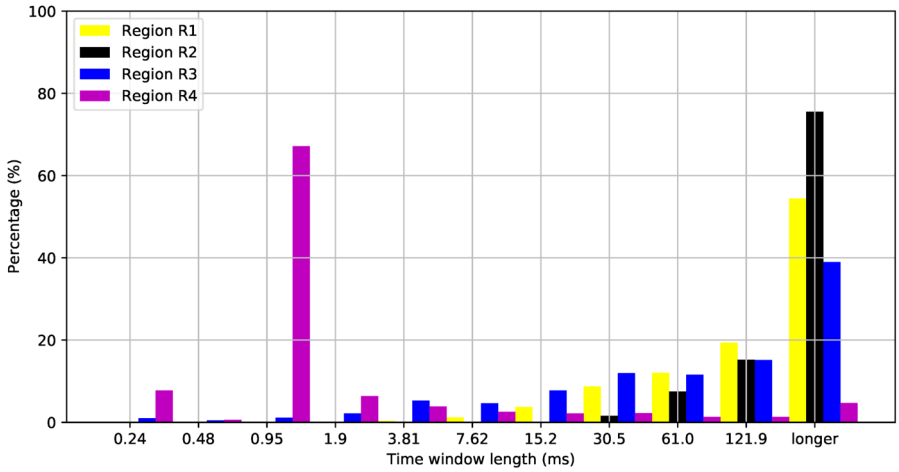

Figure G.6: Histogram of stationarity window per region (within the bandwidth).

Visual analysis confirms that the interference detected has a pulsed structure. In Figure G.7, a segment of the in-phase signal captured in track $S13$ at different time scales is shown as an example of the interference encountered. In the largest time scale, several interference pulses of different amplitudes can be seen. When zooming in on that time scale, the pulse structure is recognised. Different pulses can be seen with different pulse periods. In the smallest time scale, zooming in on a typical 1.6 ms pulse, the time structure of the pulse can be seen and the amplitude varies within the pulse length.

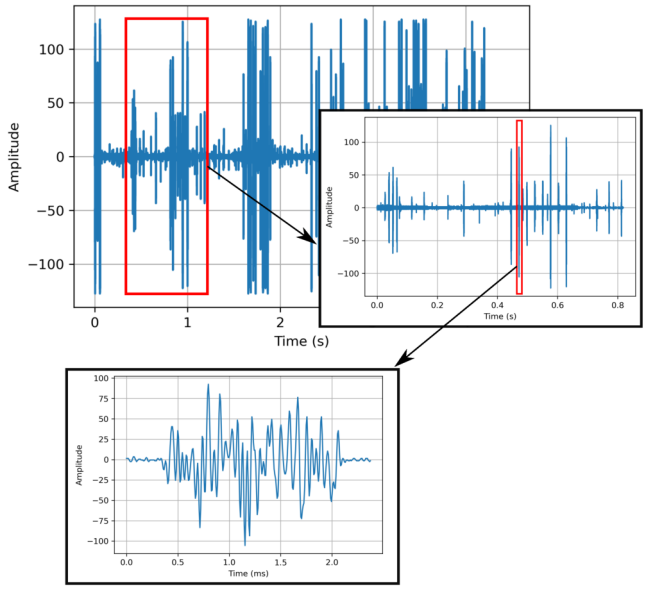

Figure G.7: In-phase signal at different time scales.

An algorithm to detect pulses was applied to the time data of each session, as explained in section G.2.3, to gather statistics of interference characteristics. An algorithm to detect pulse lengths and pulse periods was applied to the IQ data of each session, as explained in section 2, to gather statistics of interference characteristics. In Figure G.8, the pulse length (red dots) and its corresponding period with respect to the next pulse (blue dots) in track $S13$ are plotted against the number of pulses detected in the session. In the large time scale picture, a cloud of pulse periods ranging from almost zero to 1700 ms can be seen, whereas the pulse length dots are all aligned throughout the track. The longest pulse periods can be neglected in this analysis, since the detection algorithm would detect long periods if after a pulse train the next pulse train is far away, due to the differentiation of position explained in section G.2.3. If the time axis is zoomed in, the pulse characteristics are shown more clearly. This segment corresponds to the same segment shown in the second zoom-in picture of Figure G.7. The pulse length is still a continuous row of dots with a value of approximately 1.6 ms. However, the pulse period varies even in a short time scale, changing from 26 ms to 13 ms and 52 ms in this particular example.

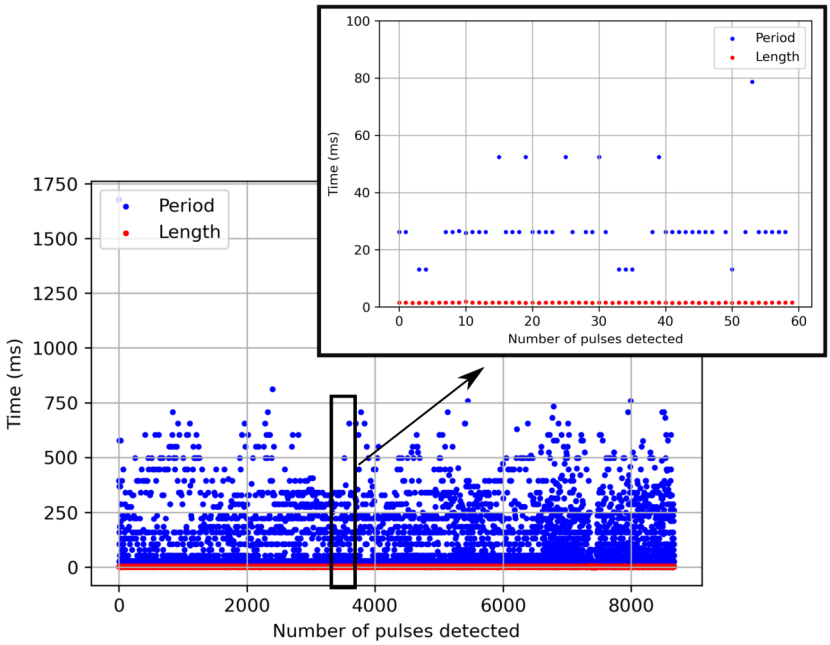

Figure G.8: Pulse period pattern at different time scales.

To verify that the pulse period is consistent throughout all the measurements, the distribution of the pulse length of detected pulses in each region is depicted in Figure G.9. All regions have a similar distribution, where almost all pulses have a length of approximately 1.6 ms, within the studied bandwidth. Regions $R1$ and $R2$ have a small percentage of pulses with a shorter length.

The ECDF of the pulse period estimated for detected pulses in the different regions is depicted in Figure G.10. In region $R4$, 48% of the pulses detected have a period lower than 53 ms, and in the region $R3$, 56%. The percentages for regions $R2$ and $R1$ are 81% and 72%. In $R4$, lower signal power was detected which would mean a lower signal-to-noise ratio (the pulses being the signal in this case). Hence, it is reasonable that the detected pulse period is longer as some pulses are missed. In general, the most common periods are 13 ms (3% in $R3$ and $R4$, 12% in $R1$ and 14% in $R2$), 26 ms (34% in $R4$, 11% in $R3$, 42% in $R1$ and 59% in $R2$), 41 ms and 52 ms, which would mean a duty cycle of 12.3%, 6%, 3.8% and 3% with the pulse length

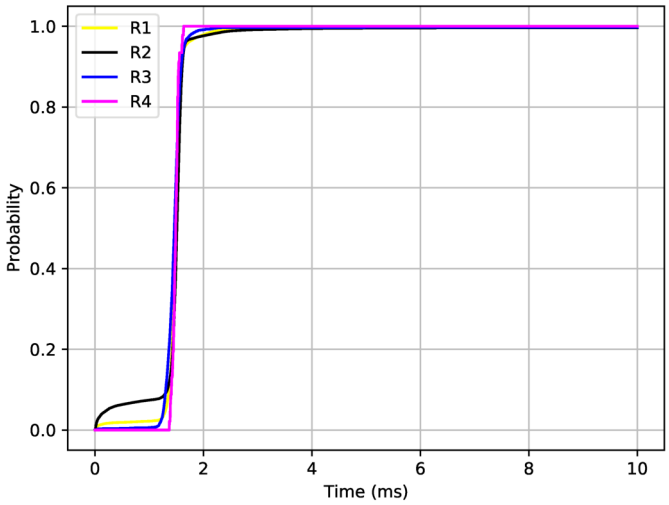

Figure G.9: ECDF of pulse length detected in the different regions.

of 1.6 ms. The pulse period changes throughout the measurement with a train of pulses of one period and then another train of a different number of pulses of a different period as shown in Figure G.8, but no clear pattern has been detected.

G.4 Discussion

When uplinking information in the VDE-SAT band, the detected pulses will interfere with the signal. Instantaneous interference power of up to -70 dBm has been detected, but it could have been higher. The configuration limited the maximum power that could be measured. Observed VDE-SAT signal power from previous experiments was between -90 and -110 dBm. Hence, the interference is between 20 and 40 dB above the desired signal. CDMA has been successfully applied as a mitigation, but other possible countermeasures could be applied. The worst-case is when the pulses have a period of 13 ms. If the transmitted packet length was 13 ms, the pulses were 1.6 ms long and the period between pulses was 13 ms, 12% of the packet would be lost to interference. Error-correcting codes must then account for losing this 12% of data. In addition, the header needs to be protected

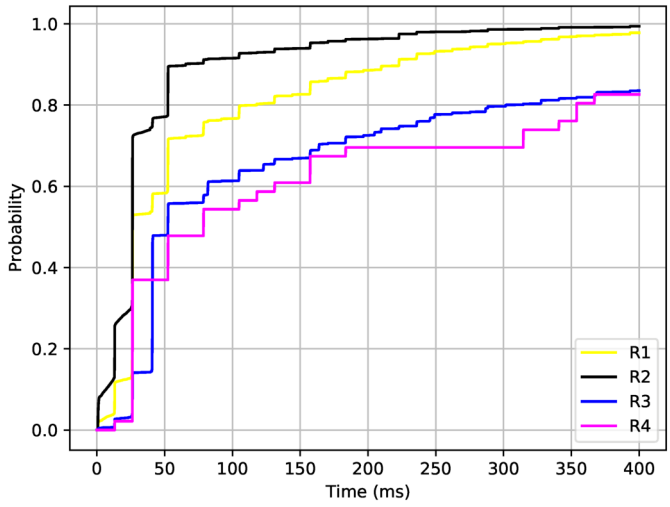

Figure G.10: ECDF of pulse period detected in the different region.

against these errors. An interleaver with a depth that matches or exceeds the pulse length can be used to spread out the burst errors in different parts of the packet. Furthermore, the communication system could be improved from a worst-case design by changing parameters (modulation, coding and waveform) depending on the region.

In this paper we provided a preliminary time-frequency analysis of the in-orbit interference measured in a small area of the Arctic, but more measurements are needed to obtain reliable interference statistics both at different time scales and larger areas. Furthermore, the data used had only 8 bits which reduces the resolution. Interference power could be higher than reported here, so measurements with more bits and different dynamic ranges would be desired.

A long measurement campaign would enable the first step of increasing the data throughout by selecting different communication parameters and improving the waveforms in the standard depending on which area the satellite is over. ACM can be challenging due to fast variations of the uplink interference, as seen in this article. However, it can be tested in the future.

G.5 Conclusion

In this article, we presented the results of a preliminary measurement campaign of in-orbit interference in the lower leg of the VDE-SAT frequency band (157.2875-157.3375 MHz) using the NorSat-2 satellite. Raw IQ data was captured for ten satellite passes in May 2021 over the Arctic area around Bjørnøya/Bear Island (Norway). The data was processed using the LME method to analyze its time and frequency variability, and an algorithm for pulse detection to characterize interference characteristics.

High levels of pulsed interference covering the full measured bandwidth were detected in the measurement area with instantaneous uplink interference power up to -70 dBm, which is 20 to 40 dB above the uplink signal power. The power can be even higher but due to the small dynamic range in the measurements, the maximum power measured is limited by the measurement configuration. Detected interference varied both within a short time scale and within different regions. The statistics of the interference were highly variable even within one second. The window of stationarity of first-order of the data was estimated for different regions. Most of the measured points have a stationarity window longer than 121.9 ms for most regions, but for the region that received the least interference power, the window is 0.95 ms for 67% of the points. The main measured interference source is pulsed and has a pulse length of about 1.6 ms and the most common pulse periods detected were 13, 26, 41 and 52 ms.

From the measurements analyzed in this paper, it seems that the VDE-SAT communication system should be configured either for the worst-case over a larger area or be adaptive within smaller areas to maximise data throughput. The first step would be to fix communication parameters in different regions. As an example, the pulse length can be used as the minimum depth of an interleaver to spread out errors in the frame and enable error correction after burst events. However, more measurements are necessary to provide more reliable statistics over larger areas and longer time.

Acknowledgments This work was supported by the Research Council of Norway through the Centers of Excellence funding scheme, Grant 223254 - Center for Autonomous Marine Operations and Systems (AMOS) and

the Research Council of Norway through the IKTPLUSS programme grant 270959 (MASSIVE), and the project TIN21024 by the NOSA. Further, the authors would like to acknowledge the support of NOSA and NCA, especially for providing payload space onboard Norsat-2 for the Space Norway owned VDE-SAT payload, and European Space Agency (ESA) for supporting activities related to the development of VDES. G. Q. D. would like to thank her colleague Jens Abraham, and Nicolás Molina Padrón for useful discussions.

Bibliography

[1] Y. B. Zikria, R. Ali, M. K. Afzal and S. W. Kim, 'Next-generation internet of things (iot): Opportunities, challenges, and solutions,' *Sensors*, vol. 21, no. 4, 2021. DOI: 10.3390/s21041174.

[2] Arctic Economic Council, *Arctic Connectivity Working Group 2021*, 2021.

[3] M. Ding, S. Wang and W. Sun, 'Decadal climate change in ny-ålesund, svalbard, a representative area of the arctic,' *Condensed Matter*, vol. 3, no. 2, 2018. DOI: 10.3390/condmat3020012.

[4] V. A. Semenov, 'Modern Arctic Climate Research: Progress, Change of Concepts, and Urgent Problems,' *Izvestiya, Atmospheric and Oceanic Physics*, vol. 57, no. 1, pp. 18–28, 2021. DOI: 10.1134/S0001433821010114.

[5] *U.S. Geological Survey - Water Science School | How Much Water is There on Earth?* https://www.usgs.gov/special-topic/water-science-school/science/how-much-water-there-earth?qt-science_center_objects=0#qt-science_center_objects, accessed on 16/11/2021.

[6] R. Birkeland, 'Freely drifting cubesat constellations for improving coverage for arctic sensor networks,' in *2017 IEEE International Conference on Communications (ICC)*, May 2017, pp. 1–6. DOI: 10.1109/ICC.2017.7997293.

[7] L. R. Haury, J. A. McGowan and P. H. Wiebe, 'Patterns and processes in the time-space scales of plankton distributions,' in *Spatial Pattern in Plankton Communities*, J. H. Steele, Ed. Boston, MA: Springer US, 1978, pp. 277–327. DOI: 10.1007/978-1-4899-2195-6_12.

[8] A. Ferreira, F. Py, J. Pinto *et al.*, 'Advancing multi-vehicle deployments in oceanographic field experiments,' *Autonomous Robots*, vol. 43, Aug. 2019. DOI: 10.1007/s10514-018-9810-x.

[9] E. Honoré-Livermore, R. Birkeland and C. Haskins, 'Addressing the Sustainable Development Goals with a System-of-Systems for Monitoring Arctic Coastal Regions,' in *INCOSE International Symposium (ISSN 2334-5837)*, http://dx.doi.org/10.1002/j.2334-5837.2020.00743.x, vol. 30, 2020, pp. 604–619.

[10] N. R. Council, *Science at Sea: Meeting Future Oceanographic Goals with a Robust Academic Research Fleet*. Washington, DC: The National Academies Press, 2009. DOI: 10.17226/12775.

[11] M. J. Costa, J. Pinto, P. S. Dias *et al.*, 'Field report: Exploring fronts with multiple robots,' in *2018 IEEE/OES Autonomous Underwater Vehicle Workshop (AUV)*, 2018.

[12] E. Alarcón, A. A. Sanchez, C. Araguz *et al.*, 'Design and optimization of a polar satellite mission to complement the copernicus system,' *IEEE Access*, vol. 6, pp. 34 777–34 789, 2018. DOI: 10.1109/ACCESS.2018.2844257.

[13] G. Quintana-Díaz, R. Birkeland, E. Honoré-Livermore and T. Ekman, 'An sdr mission measuring uhf signal propagation and interference between small satellites in leo and arctic sensors,' in *33rd Annual AIAA/USU Conference on Small Satellites*, 2019.

[14] J. Dixon, C. Politis, C. Wijting, W. Mohr, C. Legutko and J. Jian, 'Considerations in the choice of suitable spectrum for mobile communications,' in *OUTLOOK Visions and research directions for the Wireless World*, vol. 2, 2008.

[15] CCSDS, 'TM Synchronization and Channel Coding—Summary of Concept and Rationale,' *CCSDS Green Book*, no. November 2012, 2012.

[16] *GOMspace | Software Defined Radio*, https://gomspace.com/Shop/payloads/software-defined-radio.aspx, accessed on 13/04/2018.

[17] *TOTEM Motherboard Datasheet*, Alén Space, 2018.

[18] Ettus Research, *USRP E310 EMBEDDED SDR*, http://www.ettus.com/content/files/USRP_E310_Product_Sheet.pdf, accessed 16/12/2017, 2015.

[19] *AstroSDR – Rincon Research Corporation*, https://www.rincon.com/shop/space-systems/astrosdr-family/, accessed on 13/04/2018.

[20] Lime Microsystems, *Lime SDR*, https://www.crowdsupply.com/lime-micro/limesdr, 2017.

[21] *HackRF One Wiki*, https://github.com/mossmann/hackrf/wiki/HackRF-One, accessed on 13/04/2018.

[22] *USRP N210 Software Defined Radio (SDR) - Ettus Research*, https://www.ettus.com/product/details/UN210-KIT, accessed on 13/05/2018.

[23] L. Fernandez, J. A. Ruiz-de-Azua, A. Calveras and A. Camps, 'On-demand satellite payload execution strategy for natural disasters monitoring using lora: Observation requirements and optimum medium access layer mechanisms,' *Remote Sensing*, vol. 13, no. 19, 2021. DOI: 10.3390/rs13194014.

[24] J. Overpeck, K. Hughen, D. Hardy *et al.*, 'Arctic environmental change of the last four centuries,' *Science*, vol. 278, no. 5341, pp. 1251–1256, 1997. DOI: 10.1126/science.278.5341.1251.

[25] N. Wunderling, M. Willeit, J. F. Donges and R. Winkelmann, 'Global warming due to loss of large ice masses and Arctic summer sea ice,' *Nature Communications*, vol. 11, no. 1, p. 5177, 2020. DOI: 10.1038/s41467-020-18934-3.

[26] M. Geoffroy, J. Berge, S. Majaneva *et al.*, 'Increased occurrence of the jellyfish Periphylla periphylla in the European high Arctic,' *Polar Biology*, vol. 41, no. 12, pp. 2615–2619, 2018. DOI: 10.1007/s00300-018-2368-4.

[27] P. E. Renaud, M. Daase, N. S. Banas *et al.*, 'Pelagic food-webs in a changing arctic: A trait-based perspective suggests a mode of resilience,' *ICES Journal of Marine Science*, vol. 75, no. 6, pp. 1871–1881, 2018.

[28] E. Lancheros, A. Camps, H. Park *et al.*, 'Selection of the key earth observation sensors and platforms focusing on applications for polar regions in the scope of copernicus system 2020–2030,' *Remote Sensing*, vol. 11, no. 2, 2019. DOI: 10.3390/rs11020175.

[29] J. Berge, M. Geoffroy, G. Johnsen, F. Cottier, B. Bluhm and D. Vogedes, 'Ice-tethered observational platforms in the arctic ocean pack ice,' *IFAC-PapersOnLine*, vol. 49, no. 23, pp. 494–499, 2016, 10th IFAC Conference on Control Applications in Marine Systems CAMS 2016. DOI: https://doi.org/10.1016/j.ifacol.2016.10.484.

[30] A. Zolich, P. R. De La Torre, S. Rodwell, M. Geoffroy, G. Johnsen and J. Berge, 'An ice-tethered buoy for fish and plankton research,' in *OCEANS 2018 MTS/IEEE Charleston*, 2018, pp. 1–7. DOI: 10.1109/OCEANS.2018.8604603.

[31] M. Centenaro, C. E. Costa, F. Granelli, C. Sacchi and L. Vangelista, 'A survey on technologies, standards and open challenges in satellite iot,' *IEEE Communications Surveys Tutorials*, vol. 23, no. 3, pp. 1693–1720, 2021. DOI: 10.1109/COMST.2021.3078433.

[32] *Myriota*, https://myriota.com/common-questions/, accessed 05/10/2021, 2021.

[33] *Connect to the world with Hiberband*, https://hiber.global/hiberband/, accessed 05/10/2021, 2021.

[34] R. Birkeland, 'On the use of micro satellites as communication nodes - in an arctic sensor network,' Ph.D. dissertation, Norwegian University of Science and Technology, 2019.

[35] ITU-R: Recommendation ITU-R P.618-13, 'Propagation data and prediction methods required for the design of Earth-space telecommunication systems,' ITU, Tech. Rep., 2017.

[36] P. A. Bernhardt and C. L. Siefring, 'New satellite-based systems for ionospheric tomography and scintillation region imaging,' *Radio Science*, vol. 41, no. 5, 2006. DOI: https://doi.org/10.1029/2005RS003360. eprint: https://agupubs.onlinelibrary.wiley.com/doi/pdf/10.1029/2005RS003360.

[37] A. W. Yau and H. G. James, 'CASSIOPE Enhanced Polar Outflow Probe (e-POP) Mission Overview,' *Space Science Reviews*, vol. 189, no. 1, pp. 3–14, 2015. DOI: 10.1007/s11214-015-0135-1.

[38] J. Vierinen, J. Norberg, M. S. Lehtinen *et al.*, 'Beacon satellite receiver for ionospheric tomography,' *Radio Science*, vol. 49, no. 12, pp. 1141–1152, 2014. DOI: https://doi.org/10.1002/2014RS005434. eprint: https://agupubs.onlinelibrary.wiley.com/doi/pdf/10.1002/2014RS005434.

[39] V. Chu, P. Sweeney, J. Paffett and M. Sweeting, 'Characterising error sequences of the low earth orbit satellite channel and optimisation with hybrid-arq schemes,' in *IEEE GLOBECOM 1998 (Cat. NO. 98CH36250)*, vol. 5, 1998, 2930–2935 vol.5. DOI: 10.1109/GLOCOM.1998.776610.

[40] C. T. Phua, L. C. L., I. Gosling and K. Arichandran, 'Leo Satellite Channel Measurements at UHF Frequencies,' in *Proceedings of the Euro-Asia Space Week on Cooperation in Space*, 1999.

[41] ITU-R: Report ITU-R SA.2348-0, 'Current practice and procedures for notifying space networks currently applicable to nanosatellites and picosatellites,' ITU, Tech. Rep., 2015.

[42] International Telecommunication Union, *Radio Regulations*. ITU, 2008, pp. 47–100.

[43] M. Toyoshima and A. Matas, 'Spectrum frequency allocation issues and concerns for small satellites,' *Handbook of Small Satellites: Technology, Design, Manufacture, Applications, Economics and Regulation*, pp. 283–293, 2020.

[44] ITU-R: Recommendation ITU-R M.1462-1, *Characteristics of and protection criteria for radars operating in the radiolocation service in the frequency range 420-450 MHz*, 2019.

[45] ITU-R: Recommendation ITU-R SA.1260-1, *Feasibility of sharing between active spaceborne sensors and other services in the range 420-470 MHz*, 2017.

[46] G. Quintana-Diaz, D. Nodar-López, A. González Muíño, F. Aguado Agelet, C. Cappelletti and T. Ekman, 'Detection of radio interference in the uhf amateur radio band with the serpens satellite,' *Advances in Space Research*, vol. 69, no. 2, pp. 1159–1169, 2022. DOI: https://doi.org/10.1016/j.asr.2021.10.017.

[47] United States Air Force, 'Pave paws early warning radar operation project continued operation of the solid-state phased-array radar system (sspars) also known as pave phased array warning systems (paws) cape cod air force station ma,' United States Air Force, Tech. Rep., 2009.

[48] M. Buscher, *Investigations on the current and future use of radio frequency allocations for small satellite operations*. Universitätsverlag der TU Berlin, 2019, vol. 7.

[49] ITU-R: Report ITU-R SA.2425, 'Studies to accommodate requirements in the space operation service for non-geostationary satellites with short duration missions,' ITU, Tech. Rep., 2015.

[50] European Space Agency (ESA), *ESA Artes frequency monitoring*, https://artes.esa.int/projects/board-spectrum-monitoring-obsm, 2016.

[51] European Space Agency, *On-board Interference Geo-location System (ARTES 5.1 5A.037)*, https://artes.esa.int/funding/onboard-interference-geolocation-system-artes-51-5a037-0, 2016.

[52] European Space Agency (ESA), *Spectrum Monitoring Mission Feasibility Assessment(ARTES FPE 1B.129)*, https://artes.esa.int/funding/spectrum-monitoring-mission-feasibility-assessment-artes-fpe-1b129, 2016.

[53] European Space Agency, *Radio Frequency Analytics Applications (ARTES)*, https://business.esa.int/funding/call-for-proposals-artes-satcom-apps/radio-frequency-analytics-applications, 2021.

[54] R. Zeif, A. Hörmer, M. Kubicka, M. Henkel and O. Koudelka, 'From OPS-SAT to PRETTY Mission: A Second Generation Software Defined Radio Transceiver for Passive Reflectometry,' in *2020 International Conference on Broadband Communications for Next Generation Networks and Multimedia Applications (CoBCom)*, 2020, pp. 1–8.

[55] K. Sarda, R. E. Zee, D. CaJacob and N. G. Orr, 'Making the Invisible Visible: Precision RF-Emitter Geolocation from Space by the HawkEye 360 Pathfinder Mission,' in *Proceedings of the 32nd Annual AIAA/USU Conference on Small Satellites*, "Logan UT, USA", 2018.

[56] Aurora Insight Inc., *Aurora Insight*, https://aurorainsight.com/.

[57] *Space Powered Signal & Geospatial Intelligence | Kleos*, https://kleos.space/, accessed on 22/12/2021.

[58] *Iluminate the world | Umbra*, https://umbra.space/, accessed on 22/12/2021.

[59] *Amber Space-Based Maritime Domain Intelligence Solutions | Horizon Technologies*, https://horizontechnologies.eu/products/cubesat/, accessed on 22/12/2021.

[60] S. Busch, P. Bangert, S. Dombrovski and K. Schilling, 'UWE-3, in-orbit performance and lessons learned of a modular and flexible satellite bus for future pico-satellites,' *Acta Astronautica*, vol. 117, pp. 73–89, 2015. DOI: 10.1016/j.actaastro.2015.08.002.

[61] F. Aguado Agelet, D. Nodar López and A. González Muiño, 'Preliminary noise measurements campaign carried out by HUMSAT-D during 2014,' in *ITU Conference and Workshop on the Small Satellite Regulation and Communication Systems*, Mar. 2015, pp. 1–21.

[62] G. Giambene, I. Gomez, T. de Cola, R. Sebastian and M. S. Rahman, 'Satellite forward vdes channel modeling and impact on higher-layer performance,' *International Journal of Satellite Communications and Networking*, vol. n/a, no. n/a, DOI: https://doi.org/10.1002/sat.1430. eprint: https://onlinelibrary.wiley.com/doi/pdf/10.1002/sat.1430.

[63] L. E. Bråten, V. Arneson, K. Svenes, T. Eriksen and Ø. Olsen, 'Channel Modelling for VHF Data Exchange System via Satellite,' in *12th European Conference on Antennas and Propagation (EuCAP 2018)*, IET, 2018.

[64] H.-C. Haugli, L. Løge, N. Alagha *et al.*, 'The VHF data exchange system (VDES) and Norsat-2 satellite testing,' *35th AIAA International Communications Satellite Systems Conference, ICSSC 2017*, no. 204009, 2017. DOI: 10.2514/6.2017-5419.

[65] T. Eriksen, L. Braten, A. N. Skauen *et al.*, 'VDE-SAT–Preliminary verification results for proposed satellite component of new maritime communication system,' in *Proc. 4S Symp.*, 2018, pp. 1–14.

[66] L. E. Bråten, T. Eriksen, A. N. Skauen, A. Bjernevik, H. C. Haugli and L. Lege, 'On the VHF radio channel for the data exchange system via satellite (VDE-SAT); experimental results from the NorSat-2 satellite experiment,' in *36th International Communications Satellite Systems Conference (ICSSC 2018)*, IET, 2018, pp. 1–8.

[67] J. Querol, A. Perez and A. Camps, 'A Review of RFI Mitigation Techniques in Microwave Radiometry,' *Remote Sensing*, vol. 11, no. 24, 2019. DOI: 10.3390/rs11243042.

[68] J. Lahtinen, J. Uusitalo, T. Ruokokoski and J. Ruoskanen, 'Evaluation and comparison of RFI detection algorithms,' in *2016 14th Specialist Meeting on Microwave Radiometry and Remote Sensing of the Environment (MicroRad)*, 2016, pp. 62–67. DOI: 10.1109/MICRORAD.2016.7530505.

[69] S. Misra and P. de Matthaeis, 'Passive Remote Sensing and Radio Frequency Interference (RFI): An Overview of Spectrum Allocations and RFI Management Algorithms [Technical Committees],' *IEEE Geoscience and Remote Sensing Magazine*, vol. 2, no. 2, pp. 68–73, 2014. DOI: 10.1109/MGRS.2014.2320879.

[70] W. Emery and A. Camps, 'Chapter 4 - Microwave Radiometry,' in *Introduction to Satellite Remote Sensing*, Elsevier, 2017, pp. 131–290. DOI: https://doi.org/10.1016/B978-0-12-809254-5.00004-X.

[71] A. M. Wyglinski, R. Getz, T. Collins and D. Pu, *Software-defined radio for engineers*. Artech House, 2018.

[72] J. Mitola, 'The software radio architecture,' *IEEE Communications magazine*, vol. 33, no. 5, pp. 26–38, 1995.

[73] *SDR-1001| High performance, compact software-defined radio | Cesium*, https://www.cesiumastro.com/products/sdr, accessed on 02/01/2022.

[74] *SWIFT Software Defined Radios for CubeSats*, https://www.tethers.com/software-defined-radios/, accessed on 31/03/2022.

[75] *FUNcube Dongle*, http://www.funcubedongle.com/, accessed on 13/04/2018.

[76] *RTL-SDR.COM | About RTL-SDR*, https://www.rtl-sdr.com/, accessed on 13/04/2018.

[77] *EPIQ Solutions*, https://epiqsolutions.com/, accessed on 02/01/2022.

[78] *Nuand | bladeRF Software Defined Radio*, https://www.nuand.com/, accessed on 13/04/2018.

[79] *ADALM PLUTO | Software-Defined Radio Active Learning Module | Analog Devices*, https://www.analog.com/en/design-center/evaluation-hardware-and-software/evaluation-boards-kits/adalm-pluto.html, accessed on 02/01/2022.

[80] *AD9361 Datasheet and Product Info | Analog Devices*, http://www.analog.com/en/products/rf-microwave/integrated-transceivers-transmitters-receivers/wideband-transceivers-ic/ad9361.html, accessed on 13/04/2018.

[81] *AD9364 Datasheet and Product Info | Analog Devices*, http://www.analog.com/en/products/rf-microwave/integrated-transceivers-transmitters-receivers/wideband-transceivers-ic/ad9364.html, accessed on 13/04/2018.

[82] *Matchstiq SDR Platform*, https://www.epiqsolutions.com/matchstiq/, accessed on 10/04/2018.

[83] NTNU SmallSat Lab, *Mission: Hyper Spectral Camera*, https://www.ntnu.edu/ie/smallsat/mission-hyper-spectral-camera, accessed on 03/06/2019.

[84] G. Santilli, C. Vendittozzi, C. Cappelletti, S. Battistini and P. Gessini, 'CubeSat constellations for disaster management in remote areas,' *Acta Astronautica*, vol. 145, pp. 11–17, 2018. DOI: 10.1016/j.actaastro.2017.12.050.

[85] G. Muíño and A. Agelet, 'Cubesat Constellations For Sensor Data Acquisition,' in *IAA Cubesat Brasilia*, 2014.

[86] G. Fernandes, M. Bueno dos Santos, J. Almeida, S. VD and N. PRM, 'Thermal tests for cubesat in brazil: Lessons learned and the challenges for the future,' in *67th International Astronautical Congress (IAC)*, Sep. 2016.

[87] F. Pérez-Lissi, F. Aguado-Agelet, A. Vázquez *et al.*, 'FIRE-RS: Integrating land sensors, cubesat communications, unmanned aerial vehicles and a situation assessment software for wildland fire characterization and mapping,' in *69th International Astronautical Congress*, 2018.

[88] G. Quintana-Diaz, T. Ekman, J. M. Lago Agra, D. Hurtado de Mendoza, A. González Muíño and F. Aguado Agelet, 'In-Orbit Measurements and Analysis of Radio Interference in the UHF Amateur Radio Band from the LUME-1 Satellite,' *Remote Sensing*, vol. 13, no. 16, 2021. DOI: 10.3390/rs13163252.

[89] T. Eriksen, Ø. Helleren, A. N. Skauen *et al.*, 'In-orbit AIS performance of the Norwegian microsatellites NorSat-1 and NorSat-2,' *CEAS Space Journal*, vol. 12, no. 4, pp. 503–513, 2020. DOI: 10.1007/s12567-019-00289-1.

[90] Semiconductor Components Industries, LLC, *AND9354 - AX5042 Programming Manual*, 2016.

[91] A. V. Oppenheim, *Signals & systems*, eng, 2nd ed., ser. Prentice-Hall signal processing series. Upper Saddle River, N.J: Prentice-Hall, 1997.

[92] S. K. Endresen, 'A method for measuring temporal properties of uplink interference in satellite communication,' M.S. thesis, Norwegian University of Science and Technology, 2021.

[93] L. Stankovic, *Time-frequency signal analysis with applications*, eng, Boston, 2013.

[94] G. Quintana-Díaz and R. Birkeland, 'Software-defined radios in satellite communications,' in *Small Satellites, System & Services Symposium (4S)*, 2018.

[95] NASA, 'Small Spacecraft Technology State of the Art,' no. February, pp. 1–197, 2014. DOI: NASA/TPâĂŞ2014âĂŞ216648. arXiv: TPâĂŞ2014âĂŞ216648 [NASA].

[96] I. Simms William Herbert, K. Varnavas and E. Eberly, *High speed, low cost telemetry access from space development update on programmable ultra lightweight system adaptable radio (pulsar)*, eng, Aug. 2014.

[97] *Software Defined Radio - Lime Micro*, http://www.limemicro.com/products/software-defined-radio/, accessed on 13/04/2018.

[98] E. Grayver, A. Chin, J. Hsu, S. Stanev, D. Kun and A. Parower, 'Software defined radio for small satellites,' in *2015 IEEE Aerospace Conference*, Mar. 2015, pp. 1–9. DOI: 10.1109/AERO.2015.7118901.

[99] O. Ceylan, A. Caglar, H. B. Tugrel *et al.*, 'Satellites,' *IEEE microwave magazine*, no. 03, pp. 26–33, 2016. DOI: 10.1109/MMM.2015.2505700.

[100] E. Baceski, S. Gökçebağ, A. Erdem *et al.*, 'Havelsat: A software defined radio experimentation cubesat,' in *2015 7th International Conference on Recent Advances in Space Technologies (RAST)*, Jun. 2015, pp. 831–834. DOI: 10.1109/RAST.2015.7208455.

[101] *Gunter's Space Page - Information on spaceflight, launch vehicles and satellites*, http://space.skyrocket.de/, accessed on 13/04/2018.

[102] A. G. Guerra, A. S. Ferreira, M. Costa, D. Nodar-López and F. Aguado Agelet, 'Integrating small satellite communication in an autonomous vehicle network: A case for oceanography,' *Acta Astronautica*, vol. 145, pp. 229–237, 2018. DOI: https://doi.org/10.1016/j.actaastro.2018.01.022.

[103] M. P. Angert, B. M. Bubnash, R. J. Hearty *et al.*, 'Advancements in hardware design for the frontier radio used for the solar probe plus mission,' in *Aerospace Conference, 2017 IEEE*, IEEE, 2017, pp. 1–11.

[104] C. B. Haskins, M. P. Angert, E. J. Sheehi, W. P. Millard, N. Adams and J. R. Hennawy, 'The Frontier Software-Defined Radio for the Solar Probe Plus Mission,' pp. 1–11, 2016.

[105] S. K. Johnson, R. C. Reinhart and T. J. Kacpura, 'CoNNeCT's approach for the development of three Software Defined Radios for space application,' *2012 IEEE Aerospace Conference*, pp. 1–13, 2012. DOI: 10.1109/AERO.2012.6187147.

[106] M. Bosco, P. Tortora and D. Cinarelli, 'Alma Mater Ground Station transceiver: A software defined radio for satellite communications,' *2014 IEEE Metrology for Aerospace (MetroAeroSpace)*, pp. 549–554, 2014. DOI: 10.1109/MetroAeroSpace.2014.6865986.

[107] M. R. Maheshwarappa, 'Software defined radio (sdr) architecture for concurrent multi-satellite communications,' Ph.D. dissertation, University of Surrey, 2016.

[108] J. C. Juang, C. T. Tsai and J. J. Miau, 'A software-defined radio approach for the implementation of ground station receivers,' *Small Satellites for Earth Observation*, pp. 293–298, 2008. DOI: 10.1007/978-1-4020-6943-7_27.

[109] Ø. Karlsen, 'Ground station considerations for the amos satellite programme,' master thesis, Norwegian Univesity of Science and Technology (NTNU), 2017.

[110] A. Løfaldli and R. Birkeland, 'Implementation of a software defined radio prototype ground station for cubesats,' in *Proceedings of the ESA Small Satellites and Services Symposium*, 2016. DOI: DOI:10.13140/RG.2.1.1806.0408.

[111] *Mare incognitum*, http://www.mare-incognitum.no/, accessed 20/05/2021.

[112] Arctic Council Task Force on Telecommunications Infrastructure in the Arctic, 'Telecommunications Infrastructure in the Arctic; A Circumpolar Assessment,' May 2017.

[113] R. Birkeland, 'An overview of existing and future satellite systems for arctic communication,' *Proceedings of ESA Small Satellites Systems and Services 2014*, 2014.

[114] C. Haskins, 'Systems engineering analyzed, synthesized, and applied to sustainable industrial park development,' Ph.D. dissertation, Norwegian University of Science and Technology (NTNU), 2008.

[115] *Iridium Certus | Iridium Satellite Communications*, https://www.iridium.com/services/iridium-certus/, accessed on 20/05/2019.

[116] R. Birkeland, D. Palma and A. Zolich, 'Integrated smallsats and unmanned vehicles for networking in remote locations,' in *Proceedings of The 68th International Astronautical Congress*, 2017.

[117] J. Großhans, H. Quan, A. Balke, A. Lohse and A. Maaß, 'SALSAT - An innovative nanosatellite for spectrum analysis based on SDR technology,' in *69th International Astronautical Congress (IAC)*, Oct. 2018, pp. 1–5.

[118] R. Birkeland, G. Quintana-Díaz, E. Honoré-Livermore, T. Ekman, F. A. Agelet and T. A. Johansen, 'Development of a multi-purpose SDR payload for the HYPSO-2 satellite,' in *IEEE Aerospace Conference [accepted]*, 2022.

[119] M. E. Grøtte, R. Birkeland, E. Honoré-Livermore *et al.*, 'Ocean color hyperspectral remote sensing with high resolution and low latency–the hypso-1 cubesat mission,' *IEEE Transactions on Geoscience and Remote Sensing*, pp. 1–19, 2021. DOI: 10.1109/TGRS.2021.3080175.

[120] E. F. Prentice, M. E. Grøtte, F. Sigernes and T. A. Johansen, 'Design of a hyperspectral imager using cots optics for small satellite applications,' in *International Conference on Space Optics*, 2021.

[121] The Nansen Legacy, *The Nansen Legacy*, https://arvenetternansen.com, accessed on 10/11/2021.

[122] M. W. Maier, 'Architecting principles for systems-of-systems,' *Systems Engineering*, vol. 1, no. 4, pp. 267–284, 1998.

[123] A. Dallolio, G. Quintana-Diaz, E. Honoré-Livermore, J. L. Garrett, R. Birkeland and T. A. Johansen, 'A satellite-usv system for persistent observation of mesoscale oceanographic phenomena,' *Remote Sensing*, vol. 13, no. 16, 2021. DOI: 10.3390/rs13163229.

[124] A. G. C. Guerraa, F. Francisco, J. Villate, F. A. Agelet, O. Bertolami and K. Rajan, 'On small satellites for oceanography: A survey,' *Acta Astronautica*, vol. 127, 404 to 423, 2016. DOI: j.actaastro.2016.06.007.

[125] B. Denby and B. Lucia, 'Orbital Edge Computing: Nanosatellite Constellations as a New Class of Computer System,' in *ASPLOS '20: Proceedings of the Twenty-Fifth International Conference on Architectural Support for Programming Languages and Operating Systems*, 2020. DOI: 10.1145/3373376.3378473.

[126] Y. Wang, J. Yang, X. Guo and Z. Qu, 'Satellite edge computing for the internet of things in aerospace,' *Sensors*, vol. 19, no. 20, 2019. DOI: 10.3390/s19204375.

[127] Y. Zeng, Q. Wu and R. Zhang, 'Accessing From the Sky: A Tutorial on UAV Communications for 5G and Beyond,' *Proceedings of the IEEE*, vol. 107, no. 12, pp. 2327–2375, 2019. DOI: 10.1109/JPROC.2019.2952892.

[128] W. Zhang, Y. Li, Z. Zhang and Z. Feng, 'A pattern-reconfigurable aircraft antenna with low wind drag,' *IEEE Transactions on Antennas and Propagation*, vol. 68, no. 6, pp. 4397–4405, 2020. DOI: 10.1109/TAP.2020.2975262.

[129] A. Zolich, D. Palma, R. Birkeland and Y. Jiang, *A multi-hop intermittent wireless sensor network with unmanned aerial vehicles and satellite links for the Arctic*, Presentation at ReCAMP Flagship Workshop, 5 - 6 April 2016, Tromsø, Norway, Abstract available at: http://www.asuf.no/wp-content/uploads/2016/03/ReCAMP2016_AbstractsBook.pdf, 2016.

[130] R. Birkeland and D. Palma, 'Freely drifting small-satellite swarms for sensor networks in the arctic,' in *Third International Congress on Information and Communication Technology*, X.-S. Yang, S. Sherratt, N. Dey and A. Joshi, Eds., Singapore: Springer Singapore, 2019, pp. 175–190. DOI: 10.1007/978-981-13-1165-9_16.

[131] D. Palma and R. Birkeland, 'Enabling the internet of arctic things with freely-drifting small-satellite swarms,' *IEEE Access*, vol. 6, pp. 71 435–71 443, 2018. DOI: 10.1109/ACCESS.2018.2881088.

[132] E. Honoré-Livermore, R. Birkeland and C. Haskins, 'Addressing the sustainable development goals with a system-of-systems for monitoring arctic coastal regions,' *INCOSE International Symposium*, vol. 30, no. 1, pp. 604–619, 2020. DOI: https://doi.org/10.1002/j.2334-5837.2020.00743.x. eprint: https://onlinelibrary.wiley.com/doi/pdf/10.1002/j.2334-5837.2020.00743.x.

[133] D. Mohney, *The 2018 summer of satellite iot – 18 startups, over 1,600 satellites*, https://www.spaceitbridge.com/the-2018-summer-of-satellite-iot-18-startups-over-\1600-satellites.htm, accessed on 05/10/2021.

[134] C. Schoenberger and B. Upbin, *The internet of things*, http://www.forbes.com/global/2002/0318/092.html, Mar. 2002.

[135] E. Honoré-Livermore, A. Dallolio, R. Birkeland, D. D. Langer, C. Haskins and T. A. Johansen, 'MBSE modeling of a SoS with a small satellite and autonomous surface vessels for persistent coastal monitoring,' in *2021 16th International Conference of System of Systems Engineering (SoSE)*, 2021, pp. 156–161. DOI: 10.1109/SOSE52739.2021.9497470.

[136] O. Kodheli, E. Lagunas, N. Maturo *et al.*, 'Satellite communications in the new space era: A survey and future challenges,' *IEEE Communications Surveys Tutorials*, vol. 23, no. 1, pp. 70–109, 2021. DOI: 10.1109/COMST.2020.3028247.

[137] E. Kulu, *Nanosats Database*, https://www.nanosats.eu/, accessed 05/10/2021, 2021.

[138] E. Kulu, *Newspace index*, https://www.newspace.im/, accessed 05/10/2021, 2021.

[139] Alen Space, *Small satellite payloads*, https://alen.space/nanosatellite-payloads/, Jan. 2021.

[140] S. Bakken, E. Honore-Livermore, R. Birkeland *et al.*, 'Software Development and Integration of a Hyperspectral Imaging Payload for HYPSO-1,' in *Submitted to IEEE SICE SII 2022*, Submitted, 2022.

[141] S. Bakken, R. Birkeland, J. L. Garrett *et al.*, 'Testing of Software-Intensive Hyperspectral Imaging Payload for the HYPSO-1 CubeSat,' in *Submitted to IEEE SICE SII 2022*, Submitted, 2022.

[142] I. H. Onarheim, T. Eldevik, L. H. Smedsrud and J. C. Stroeve, 'Seasonal and regional manifestation of arctic sea ice loss,' *Journal of Climate*, vol. 31, no. 12, pp. 4917–4932, 2018.

[143] International Ocean Colour Coordinating Group, *Why Ocean Colour? The Societal Benefits of Ocean-Colour Technology*. Dartmouth, Canada: IOCCG, 2008, vol. 7.

[144] IOCCG, *Observation of Harmful Algal Blooms with Ocean Colour Radiometry*. Darthmouth, Canada: IOCCG, 2021, vol. 20.

[145] International Ocean Colour Coordinating Group, *Remote Sensing of Ocean Colour in Coastal, and Other Optically-Complex, Waters*. Dartmouth, Canada: IOCCG, 2000, vol. 3.

[146] P. McGillivary, J. Borges de Sousa, R. Martins, K. Rajan and F. Leroy, 'Integrating autonomous underwater vessels, surface vessels and aircraft as persistent surveillance components of ocean observing studies,' in *2012 IEEE/OES Autonomous Underwater Vehicles (AUV)*, Sep. 2012, pp. 1–5. DOI: 10.1109/AUV.2012.6380734.

[147] IOCCG, *Uncertainties in Ocean Colour Remote Sensing*, ser. Reports of the International Ocean-Colour Coordinating Group. Darthmouth, Canada: IOCCG, 2019, vol. 18.

[148] L. L. Sousa, F. López-Castejón, J. Gilabert *et al.*, 'Integrated monitoring of mola mola behaviour in space and time,' *PLOS one*, vol. 11, no. 8, Aug. 2016. DOI: http://dx.doi.org/10.1371/journal.pone.0160404.

[149] M. J. Costa, J. Pinto, P. S. Dias *et al.*, 'Field report: Exploring fronts with multiple robots,' in *2018 IEEE/OES Autonomous Underwater Vehicle Workshop (AUV)*, 2018, pp. 1–7. DOI: 10.1109/AUV.2018.8729780.

[150] R. Hine, S. Willcox, G. Hine and T. Richardson, 'The wave glider: A wave-powered autonomous marine vehicle,' in *OCEANS 2009*, Oct. 2009, pp. 1–6. DOI: 10.23919/OCEANS.2009.5422129.

[151] *Naval Technology C-Enduro Long Endurance ASV*, https://www.naval-technology.com/projects/c-enduro-autonomous-surface-vehicle/. (visited on 11/08/2021).

[152] P. Johnston and M. Poole, 'Marine surveillance capabilities of the AutoNaut wave-propelled unmanned surface vessel (USV),' in *OCEANS 2017 - Aberdeen*, Jun. 2017, pp. 1–46. DOI: 10.1109/OCEANSE.2017.8084782.

[153] K. M. Schmidt, S. Swart, C. Reason and S.-A. Nicholson, 'Evaluation of Satellite and Reanalysis Wind Products with In Situ Wave Glider Wind Observations in the Southern Ocean,' *Journal of Atmospheric and Oceanic Technology*, vol. 34, no. 12, pp. 2551–2568, Dec. 2017. DOI: 10.1175/JTECH-D-17-0079.1. eprint: https://journals.ametsoc.org/jtech/article-pdf/34/12/2551/3386322/jtech-d-17-0079_1.pdf.

[154] N. Goebel, S. Frolov and C. Edwards, 'Complementary use of wave glider and satellite measurements: Description of spatial decorrelation scales in chl-a fluorescence across the pacific basin,' *Methods in Oceanography*, vol. 10, Aug. 2014. DOI: 10.1016/j.mio.2014.07.001.

[155] A. M. Madni and M. Sievers, 'System of systems integration: Fundamental concepts, challenges and opportunities,' in *Advances in Systems Engineering*, J. Hsu and R. Curran, Eds., vol. 252, Reston, Virginia, USA: American Institute of Aeronautics and Astronautics, 2016, pp. 1–34.

[156] R. Gomes, J. Straub, A. Jones *et al.*, 'An interconnected network of uas as a system-of-systems,' in *2017 IEEE/AIAA 36th Digital Avionics Systems Conference (DASC)*, 2017, pp. 1–7.

[157] R. Zhang, B. Song, Y. Pei and Q. Yun, 'Improved method for subsystems performance trade-off in system-of-systems oriented design of uav swarms,' *Journal of Systems Engineering and Electronics*, vol. 30, pp. 720–737, 2019.

[158] M. LaSorda, J. M. Borky and R. M. Sega, 'Model-based architecture and programmatic optimization for satellite system-of-systems architectures,' *System Engineering*, vol. 21, 2018.

[159] M. Berger, J. Moreno, J. A. Johannessen, P. F. Levelt and R. F. Hanssen, 'Esa's sentinel missions in support of earth system science,' *Remote Sensing of Environment*, vol. 120, pp. 84–90, 2012, The Sentinel Missions - New Opportunities for Science. DOI: https://doi.org/10.1016/j.rse.2011.07.023.

[160] Z. Malenovský, H. Rott, J. Cihlar *et al.*, 'Sentinels for science: Potential of sentinel-1, -2, and -3 missions for scientific observations of ocean, cryosphere, and land,' *Remote Sensing of Environment*, vol. 120, pp. 91–101, 2012, The Sentinel Missions - New Opportunities for Science. DOI: https://doi.org/10.1016/j.rse.2011.09.026.

[161] I. Ogashawara, L. Li and M. J. Moreno-Madriñán, 'Slope algorithm to map algal blooms in inland waters for Landsat 8/Operational Land Imager images,' *Journal of Applied Remote Sensing*, vol. 11, no. 1, pp. 1–18, 2016. DOI: 10.1117/1.JRS.11.012005.

[162] *CLS Group. ARGOS.* https://www.argos-system.org/. (visited on 11/03/2021).

[163] I. Fer and D. Peddie, 'Near surface oceanographic measurements using the sailbuoy,' in *2013 MTS/IEEE OCEANS - Bergen*, Jun. 2013, pp. 1–15. DOI: 10.1109/OCEANS-Bergen.2013.6607969.

[164] A. Dallolio, B. Agdal, A. Zolich, J. A. Alfredsen and T. A. Johansen, 'Long-endurance green energy autonomous surface vehicle control architecture,' in *OCEANS*, Seattle, Washington., 2019.

[165] R. Jha, 'Wave Measurement Methodology and Validation from Wave Glider Unmanned Surface Vehicles,' in *2018 OCEANS - MTS/IEEE Kobe Techno-Oceans (OTO)*, 2018, pp. 1–7. DOI: 10.1109/OCEANSKOBE.2018.8558815.

[166] Y. Zhang, B. Kieft, C. Rueda *et al.*, 'Autonomous front tracking by a Wave Glider,' in *OCEANS 2016 MTS/IEEE Monterey*, 2016, pp. 1–4. DOI: 10.1109/OCEANS.2016.7761070.

[167] Y. Zhang, B. Kieft, B. W. Hobson *et al.*, 'Persistent sampling of vertically migrating biological layers by an autonomous underwater vehicle within the beam of a seabed-mounted echosounder,' *IEEE Journal of Oceanic Engineering*, vol. 46, no. 2, pp. 497–508, 2021. DOI: 10.1109/JOE.2020.2982811.

[168] H. Cheyne, C. Key, M. Satter, M. Ornee and C. Clark, 'Multi-channel acoustic data acquisition and telemetry on an autonomous vehicle for marine mammal monitoring,' in *2013 OCEANS - San Diego*, 2013, pp. 1–5. DOI: 10.23919/OCEANS.2013.6740997.

[169] P. R. Hill, A. Kumar, M. Temimi and D. R. Bull, 'HABNet: Machine Learning, Remote Sensing-Based Detection of Harmful Algal Blooms,' *IEEE Journal of Selected Topics in Applied Earth Observations and Remote Sensing*, vol. 13, pp. 3229–3239, 2020. DOI: 10.1109/JSTARS.2020.3001445.

[170] J. Fjeldtvedt, M. Orlandić and T. A. Johansen, 'An efficient real-time fpga implementation of the ccsds-123 compression standard for hyperspectral images,' *IEEE Journal of Selected Topics in Applied Earth Observations and Remote Sensing*, vol. 11, no. 10, pp. 3841–3852, 2018. DOI: 10.1109/JSTARS.2018.2869697.

[171] ESA and EUMETSAT, 'S3 product notice - olci,' EUMETSAT, Tech. Rep., 2019.

[172] D. Manolakis, M. Pieper, E. Truslow, T. Cooley, M. Brueggeman and S. Lipson, 'The remarkable success of adaptive cosine estimator in hyperspectral target detection,' in *Algorithms and Technologies for Multispectral, Hyperspectral, and Ultraspectral Imagery XIX*, International Society for Optics and Photonics, vol. 8743, 2013, p. 874 302.

[173] Đ. Bošković, M. Orlandić and T. A. Johansen, 'A reconfigurable multi-mode implementation of hyperspectral target detection algorithms,' *Microprocessors and Microsystems*, vol. 78, p. 103 258, 2020.

[174] M. N. Sweeting, 'Modern small satellites-changing the economics of space,' *Proceedings of the IEEE*, vol. 106, no. 3, pp. 343–361, Mar. 2018. DOI: 10.1109/JPROC.2018.2806218.

[175] A. Zolich, D. Palma, K. Kansanen *et al.*, 'Survey on communication and networks for autonomous marine systems,' *Journal of Intelligent & Robotic Systems volume*, vol. 95, pp. 789–813, 2019. DOI: https://doi.org/10.1007/s10846-018-0833-5.

[176] M. Ludvigsen, P. S. Dias, S. Ferreira *et al.*, 'Autonomous network of heterogeneous vehicles for marine research and management,' in *IEEE Oceans 2016 – Monterey, CA*, Sep. 2016.

[177] J. Pinto, P. S. Dias, R. Martins, J. Fortuna, E. Marques and J. Sousa, 'The LSTS toolchain for networked vehicle systems,' in *OCEANS - Bergen, 2013 MTS/IEEE*, Jun. 2013, pp. 1–9. DOI: 10.1109/OCEANS-Bergen.2013.6608148.

[178] I. Bekmezci, I. Sen and E. Erkalkan, 'Flying ad hoc networks (fanet) test bed implementation,' in *2015 7th International Conference on Recent Advances in Space Technologies (RAST)*, Jun. 2015, pp. 665–668. DOI: 10.1109/RAST.2015.7208426.

[179] C. Rodriguez, H. Boiardt and S. Bolooki, 'CubeSat to Commercial Intersatellite Communications: Past, present and Future,' in *IEEE Aerospace Conference*, 2016.

[180] V. J. Riot, L. M. Simms and D. Carter, 'Lessons Learned Using Iridium to Communicate with a CubeSat in Low Earth Orbit,' *Journal of Small Satellites*, vol. 10, no. 1, pp. 995–1006, 2021.

[181] J.-L. Voirin, S. Bonnet, V. Normand and D. Exertier, 'From initial investigations up to large-scale rollout of an mbse method and its supporting workbench: The thales experience,' *INCOSE International Symposium*, vol. 25, no. 1, pp. 325–340, 2015.

[182] E. Honoré-Livermore, A. Dallolio, R. Birkeland, D. D. Langer, C. Haskins and T. A. Johansen, 'Mbse modeling of a sos with a small satellite and autonomous surface vessels for persistent coastal monitoring,' in *16th Annual Conference on System of Systems Engineering*, ser. Series MBSE modeling of a SoS with a small satellite and autonomous surface vessels for persistent coastal monitoring, Virtual, 2021.

[183] *CelesTrak*, https://celestrak.com/, accessed on 18/06/2021.

[184] G. Hallegraeff, H. Enevoldsen and A. Zingone, 'Global harmful algal bloom status reporting,' *Harmful Algae*, vol. 102, p. 101 992, 2021, Global Harmful Algal Bloom Status Reporting. DOI: https://doi.org/10.1016/j.hal.2021.101992.

[185] D. Scavia, J. David Allan, K. K. Arend *et al.*, 'Assessing and addressing the re-eutrophication of lake erie: Central basin hypoxia,' *Journal of Great Lakes Research*, vol. 40, no. 2, pp. 226–246, 2014. DOI: https://doi.org/10.1016/j.jglr.2014.02.004.

[186] M. von der Ohe, 'Small satellite TT&C allocations below 1 GHz: outcome of ITU WRC-19,' *CEAS Space Journal*, vol. 12, no. 4, pp. 565–571, 2020. DOI: 10.1007/s12567-020-00310-y.

[187] ITU-R: Report ITU-R SA.2312-0, 'Characteristics, definitions and spectrum requirements of nanosatellites and picosatellites, as well as systems composed of such satellites,' ITU, Tech. Rep., 2014.

[188] F. Aguado, R. Tubío, D. Nodar, A. Castro, E. V. Vivas and W. Balogh, 'HUMSAT / DEMO – The first CubeSat for the HUMSAT constellation,' in *UN/Japan Nano-Satellite Symposium*, 2012, pp. 1–5.

[189] *Marconissta*, https://marconissta.com/.

[190] HawkEye 360, *RFGeo™ - HawkEye 360*, https://www.he360.com/products/rfgeo/.

[191] Consultative Committee for Space Data Systems: CCSDS 101.0-B-6, *CCSDS recommendation for telemetry channel coding*, 2002.

[192] C. C. Chan, A. Al-Hourani, J. Choi, K. M. Gomez and S. Kandeepan, 'Performance modeling framework for iot-over-satellite using shared radio spectrum,' *Remote Sensing*, vol. 12, no. 10, 2020. DOI: 10.3390/rs12101666.

[193] B. A. Homssi, A. Al-Hourani, Z. Krusevac and W. S. T. Rowe, 'Machine learning framework for sensing and modeling interference in iot frequency bands,' *IEEE Internet of Things Journal*, vol. 8, no. 6, pp. 4461–4471, 2021. DOI: 10.1109/JIOT.2020.3026819.

[194] Z. Lin, M. Lin, T. de Cola, J.-B. Wang, W.-P. Zhu and J. Cheng, 'Supporting iot with rate-splitting multiple access in satellite and aerial-integrated networks,' *IEEE Internet of Things Journal*, vol. 8, no. 14, pp. 11 123–11 134, 2021. DOI: 10.1109/JIOT.2021.3051603.

[195] Z. Lin, M. Lin, B. Champagne, W.-P. Zhu and N. Al-Dhahir, 'Secure and energy efficient transmission for rsma-based cognitive satellite-terrestrial networks,' *IEEE Wireless Communications Letters*, vol. 10, no. 2, pp. 251–255, 2021. DOI: 10.1109/LWC.2020.3026700.

[196] M. Jia, X. Gu, Q. Guo, W. Xiang and N. Zhang, 'Broadband hybrid satellite-terrestrial communication systems based on cognitive radio toward 5g,' *IEEE Wireless Communications*, vol. 23, no. 6, pp. 96–106, 2016. DOI: 10.1109/MWC.2016.1500108WC.

[197] *The SALSAT Mission by TU Berlin: from Berlin into Space*, https://www.tu.berlin/en/research/themenportal-forschen/2020/juli/salsat-mission/, TU Berlin.

[198] *GOMspace | NanoCom ANT430*, https://gomspace.com/shop/subsystems/communication-systems/nanocom-ant430.aspx. (visited on 30/11/2020).

[199] International Amateur Radio Union (IARU), *IARU Region 1 UHF band plan*, https://www.iaru-r1.org/wp-content/uploads/2021/03/UHF-Bandplan.pdf, 2020.

[200] Norwegian Radio Relay League (NRRL), *Norwegian band plan 70 cm (432 – 438 MHz)*, https://www.nrrl.no/images/bandplaner/BP2016-70cm.pdf, 2017.

[201] G. Quintana-Díaz, R. Birkeland, L. Løge, E. Andersen, A. Bolstad and T. Ekman, 'In-orbit Interference Measurements and Analysis in the VDES-band with the NorSat-2 Satellite,' in *IEEE Aerospace Conference [accepted]*, 2022.

[202] International Association of Lighthouse Authorities (IALA), *IALA GUIDELINE 1082 AN OVERVIEW OF AIS Edition 2.0*, 2016.

[203] I. Varlamis, K. Tserpes and C. Sardianos, 'Detecting Search and Rescue Missions from AIS Data,' in *2018 IEEE 34th International Conference on Data Engineering Workshops (ICDEW)*, 2018, pp. 60–65. DOI: 10.1109/ICDEW.2018.00017.

[204] D. Chen, Y. Zhao, P. Nelson *et al.*, 'Estimating ship emissions based on AIS data for port of Tianjin, China,' *Atmospheric Environment*, vol. 145, pp. 10–18, 2016. DOI: https://doi.org/10.1016/j.atmosenv.2016.08.086.

[205] ITU-R, 'Automatic identification system VHF data link loading,' *Rep. ITU-R M.2287-0*, vol. 0, 2013.

[206] IALA, 'VHF Data Exchange System (VDES),' *G1117*, no. December, pp. 1–20, 2017.

[207] F. Lázaro, R. Raulefs, W. Wang, F. Clazzer and S. Plass, 'VHF Data Exchange System (VDES): an enabling technology for maritime communications,' *CEAS Space Journal*, vol. 11, no. 1, pp. 55–63, 2019. DOI: 10.1007/s12567-018-0214-8.

[208] N. Molina, F. Cabrera, V. Araña and M. Tichavska, 'An overview about the physical layer of the vhf data exchange system (vdes),' in *Computer Aided Systems Theory – EUROCAST 2019*, R. Moreno-Díaz, F. Pichler and A. Quesada-Arencibia, Eds., Cham: Springer International Publishing, 2020, pp. 67–74.

[209] International Maritime Organization (IMO), *Guidance on the use of AIS Application-Specific Messages*, 2010.

[210] R. I.-R. P.1546-6, *Method for point-to-area predictions for terrestrial services in the frequency range 30 MHz to 3 000 MHz P Series Radiowave propagation*, 2009.

[211] I. J. Timmins and S. O'Young, 'Marine communications channel modeling using the finite-difference time domain method,' *IEEE Transactions on Vehicular Technology*, vol. 58, no. 6, pp. 2626–2637, 2009. DOI: 10.1109/TVT.2008.2010326.

[212] C. Y. D. Sim, 'The propagation of VHF and UHF radio waves over sea paths,' Ph.D. dissertation, University of Leicester, Jan. 2002.

[213] L. M. Bradbury, D. Diaconu, S. Molgat Laurin *et al.*, 'NorSat-2: Enabling advanced maritime communication with VDES,' *Acta Astronautica*, vol. 156, pp. 44–50, 2019. DOI: https://doi.org/10.1016/j.actaastro.2018.10.030.

This page is intentionally left blank